

EARTHQUAKE SOURCE MECHANISMS AND THREE-DIMENSIONAL WAVEFIELD
SIMULATIONS IN ALASKA

By

Vipul Silwal, M.S.

A Dissertation Submitted in Partial Fulfillment of the Requirements
for the Degree of

Doctor of Philosophy

in

Geophysics

University of Alaska Fairbanks

August 2018

© 2018 Vipul Silwal

APPROVED:

Dr. Carl Tape, Committee Chair

Dr. Douglas Christensen, Committee Member

Dr. Michael West, Committee Member

Dr. Natalia Ruppert, Committee Member

Dr. Jeffrey Freymueller, Committee Member

Dr. Paul McCarthy, Chair

Department of Geosciences

Dr. Anupma Prakash, Interim Dean

College of Natural Science and Mathematics

Dr. Michael Castellini, *Dean of the Graduate School*

Abstract

This thesis presents: (1) a set of earthquake source mechanism catalogs for Alaska and (2) a three-dimensional seismic velocity model of Alaska. The improved earthquake sources are used within the velocity model for generating synthetic seismograms, which are then compared with recorded seismograms to assess the quality of the velocity model.

An earthquake source mechanism can be modeled as a moment tensor, which is a 3×3 symmetric matrix. We estimate the moment tensor for earthquakes by comparing observed waveforms (body waves and surface waves) with synthetic waveforms computed in a layered model. The improved moment tensor solutions are obtained by utilizing both the body waves and surface waves at as many broadband stations as possible. Further improvement in the inversion technique is obtained by (1) implementation of L1 norm in waveform misfit function and (2) inclusion of first-motion polarity misfit in the misfit function. We also demonstrate a probabilistic approach for quantifying the uncertainty in a moment tensor solution.

Moment tensors can be used for understanding the tectonics of a region. In the Cook Inlet and Susitna region, west of Anchorage, we determined moment tensor solutions for small-to-intermediate magnitude ($M \geq 2.5$) crustal earthquakes. Analyzing these small earthquakes required us to modify the misfit function to include first-motion polarity measurements, in addition to waveform differences. The study was complemented with the probabilistic hypocenter estimation of large historical earthquakes ($M_w \geq 5.8$) to assess their likelihood of origin as crustal, intraslab, or subduction interface. The predominance of thrust faulting mechanisms for crustal earthquakes indicate a compressive regime within the crust of south-central Alaska.

Wavefield simulations are performed in three regions of Alaska: the southern Alaska region of subduction, the eastern Alaska region with the accreting Yakutat microplate, and the interior Alaska region containing predominantly strike-slip faulting, including the Minto Flats fault zone. Our three-dimensional seismic velocity model of Alaska is an interpolated body-wave arrival time model from a previous study, embedded with major sedimentary basins (Cook Inlet, Susitna, Nenana), and with a minimum shear wave velocity threshold of 1000 m/s. Our comparisons between data and synthetics quantify the misfit that arises from different parts of each model. Further work is needed to comprehensively document the regions within each model that give rise to the observed misfit. This would be a step toward performing an iterative adjoint tomographic inversion in Alaska.

Table of Contents

	Page
Title Page	i
Abstract	iii
Table of Contents	v
List of Figures	ix
List of Tables	xiii
List of Appendices	xv
Acknowledgements	xvii
Chapter 1 Introduction	1
1.1 A brief introduction to moment tensors	2
1.2 Overview of Chapters	2
1.2.1 Contributions to published works	3
Chapter 2 Seismic moment tensors and estimated uncertainties in southern Alaska¹	11
2.1 Abstract	11
2.2 Introduction	11
2.3 Methods	14
2.3.1 Selection of events and processing of waveforms	14
2.3.2 Cut-and-paste (CAP) approach	15
2.3.3 Grid-search moment tensor inversion	16
2.3.4 Misfit function	18
2.3.5 Scaling the misfit function	19
2.4 Estimation of uncertainties	19
2.4.1 Quantification of uncertainty	20
2.4.2 Samples of the posterior probability	21
2.5 Example waveform fits and uncertainty analyses	21
2.5.1 Full analysis for example event	21
2.5.2 Additional earthquake examples	23
2.6 Moment tensor catalog, Part I (21 events)	23
2.6.1 The effect of using bad stations	24
2.6.2 The effect of ignoring body waves	25
2.6.3 The effect of using fewer stations	25
2.6.4 Improvement over existing catalogs	25
2.6.5 The effect of using either body waves or surfaces waves	25

	Page
2.6.6 Additional comparisons	25
2.7 Moment tensor catalog, Part II (85 events)	26
2.8 Discussion	27
2.8.1 The confidence curve $\mathcal{P}(V)$	27
2.8.2 The misfit function scale factor k	28
2.8.3 Finding the ‘best’ moment tensor solution	28
2.8.4 Comparison of catalogs	29
2.9 Summary	30
2.10 Acknowledgments	31
Chapter 3 Crustal earthquakes in the Cook Inlet and Susitna region of southern Alaska¹	61
3.1 Abstract	61
3.2 Introduction	61
3.3 Hypocenter estimation of historical earthquakes	63
3.3.1 The 1933, 1943, and 1954 earthquakes	64
3.4 Moment tensor inversions for modern crustal earthquakes	65
3.4.1 Event selection for moment tensor inversions	66
3.4.2 Moment tensor inversion method	66
3.4.3 Misfit function	67
3.4.4 Results	68
3.5 Hypocenter relocation of modern crustal seismicity	69
3.6 Discussion	70
3.6.1 Structures and active tectonics in the Cook Inlet and Susitna region	70
3.6.2 Implications of minor earthquakes for active faults	72
3.6.3 Structures responsible for 1933, 1943, and 1954 earthquakes	74
3.7 Summary	75
3.8 Summary of felt reports for 1933, 1943, and 1954 earthquakes	77
3.9 Acknowledgments	79
Chapter 4 Seismic wavefield simulations within a three-dimensional seismic velocity model for Alaska¹	107
4.1 Abstract	107
4.2 Introduction	107
4.3 Three target regions of mainland Alaska	109
4.4 Earthquake sources for simulation	110

4.4.1	Event selection	110
4.4.2	Moment tensor inversion	111
4.5	Construction of seismic velocity model	111
4.6	Meshing	112
4.6.1	Topography smoothing	113
4.7	Wavefield simulations and minimum resolvable period	113
4.8	Wavefield simulations and comparison with data	115
4.8.1	1D-3D comparison	115
4.9	Discussion	115
4.9.1	Minimum resolvable period test	115
4.9.2	Effect of 3D structure on seismic waveforms	116
4.10	Summary	117
Chapter 5	Conclusion	139
5.1	Code Development	140
5.2	Future work	141
Appendices	145

List of Figures

	Page
1.1 Tectonic setting and seismicity in southern Alaska	5
1.2 Moment tensor solution and waveform comparisons for the example event	6
1.3 Snapshots of a 3D wavefield simulation	7
2.1 Tectonic setting and the broadband station coverage of southern Alaska	36
2.2 Seismotectonic setting of south-central Alaska	37
2.3 Workflow for our uncertainty analysis	38
2.4 Construction of the confidence curve $\mathcal{P}(V)$	39
2.5 Moment tensor solution and waveform comparisons for 20090407201255351	40
2.6 Grid search for the best-fitting depth for 20090407201255351	42
2.7 Summary of the moment tensor solution 20090407201255351	43
2.8 Uncertainty measure for an event with good station coverage	45
2.9 Uncertainty measure for an event with poor station coverage	46
2.10 Moment tensor solution and waveform fits for 20071003140612444	47
2.11 Waveform fits for 20071003140612444 using AEC moment tensor solution	49
2.12 Effect of using L1 and L2 norms	51
2.13 Effect of using L1 norm on different data sets for 21 events	52
2.14 Confidence parameter \mathcal{P}_{AV} versus probability density $p(M_0)$	53
2.15 Comparison between AEC moment tensor, AEC fault plane and our catalog	54
3.1 Tectonic setting and physiography of south-central Alaska	83
3.2 Seismicity in south-central Alaska	85
3.3 Gravity data and estimated basement depths for the Cook Inlet and Susitna region .	86
3.4 Major earthquakes ($M_w \geq 5.8$) in the Cook Inlet and Susitna region	87
3.5 Station coverage for estimating the epicenters for the 1933, 1943, 1954 earthquakes .	88
3.6 Estimated epicenters for the 1933, 1943, and 1954 earthquakes	89
3.7 Estimated depth to slab for three historical earthquakes	90
3.8 Moment tensor solutions in Cook Inlet and Susitna region from previous studies .	91
3.9 Waveform fits for a $M_w 4.2$ crustal earthquake in the Susitna region	92
3.10 Impact of using different weights for the polarity misfit on moment tensor solution .	93
3.11 Moment tensor solutions for crustal earthquakes in three subregions	94
3.12 Comparison between moment tensors in this study and an existing catalog	95
3.13 Relocation of hypocenters using a double-difference approach	96

	Page
4.1 Seismotectonic setting and simulation regions of Alaska	119
4.2 Moment tensor sources in three simulation regions	120
4.3 2 km velocity slice from Eberhart-Phillips et al. (2006)	121
4.4 Effect of smoothing topography and minimum resolvable period of mesh elements .	122
4.5 Effect of smoothing topography on waveforms in Interior Alaska	123
4.6 Snapshots of a 3D wavefield simulation in southern Alaska	124
4.7 Minimum resolvable period test for Cook Inlet mesh	125
4.8 Minimum resolvable period across all stations in Cook Inlet mesh	126
4.9 Effect of including basin on waveforms in Cook Inlet mesh	127
4.10 Comparison between 1D and 3D velocity model of southern Alaska	128
4.11 Effect on seismic waves traversing through the Cook Inlet basin	129
4.12 Effect of Wrangells on seismic waveforms	130
4.13 Data-synthetic comparison of seismic waveforms in Interior Alaska	131
5.1 Comparison of earthquake sources used in Chapter 2 and Chapter 3	142
A.1 Southern Alaska seismicity	155
A.2 Waveform amplitude ratios between observed data and synthetics	156
A.3 spurce-station time-shift plot for the example event	157
A.4 Waveform fits for 20071003140612444 for AEC moment tensor	158
A.5 Waveform fits for 20081118195651180 at CAP solution	159
A.6 Waveform fits for 20081118195651180 at AEC first-motion solution (M_w fixed)	160
A.7 Waveform fits for 20081118195651180 at AEC first-motion solution (M_w search)	161
A.8 Waveform fits for 20090210074254600 at CAP solution	162
A.9 Waveform fits for 20090210074254600 at AEC first-motion solution (M_w search)	163
A.10 Waveform fits for 20090210074254600 at AEC first-motion solution (M_w fixed)	164
A.11 Extended uncertainty analysis for 20090407201255351 (M_{110})	165
A.12 Extended uncertainty analysis for 20090407201255351 (M_{011})	166
A.13 Extended uncertainty analysis for 20090407201255351 (M_{101})	167
A.14 Extended uncertainty analysis for 20090407201255351 (M_{112})	168
A.15 Extended uncertainty analysis for 20090407201255351 (M_{012})	169
A.16 Effect of using L2 norm on different data sets for 21 events	170
A.17 Uncertainty analysis for example 20090407201255351 with M_x ad reference	171
A.18 Uncertainty analysis for example 20090407201255351 with $-M_0$ as reference	172
A.19 Moment tensors in southern Alaska from various catalogs	173

A.20 Improvement in moment tensor solution obtained	174
B.1 Station reward factor used in the misfit function	182
B.2 Effect on number of stations on moment tensor solution (Nstn = 3 and 7)	183
B.3 Effect on number of stations on moment tensor solution (Nstn = 9)	184
B.4 Effect on number of stations on moment tensor solution (Nstn = 10)	185
B.5 Waveform fits using polarity weight $m = 0.0$	186
B.6 Waveform fits using polarity weight $m = 0.5$	187
B.7 Waveform fits using polarity weight $m = 0.9$	188
B.8 Event selection for moment tensor inversion	189
B.9 Depth distribution of events in the Cook Inlet and Susitna region	190
B.10 Variation in seismicity with depth	191
B.11 Seismicity, moment tensors and basement depths in three subregions	192
B.12 Variation in relocation vector with depth	193
B.13 Changes in depths due to relocation	194
B.14 Felt reports for the 1933, 1943, and 1954 earthquakes	195
C.1 Event selection for simulation in the Cook Inlet mesh	204
C.2 Event selection for simulation in the Interior mesh	205
C.3 Event selection for simulation in Wrangell mesh	206
C.4 Nodes used for the tomographic inversion by Eberhart-Phillips et al. (2006)	207
C.5 Eberhart-Phillips et al. (2006) nodes at depth= 2 km	208
C.6 Vp and Vs at E2006 nodes in layer 1, depth = 1 km above the sea level	209
C.7 Vp and Vs at E2006 nodes in layer 2, depth = 2 km below the sea level	210
C.8 Vp and Vs at E2006 nodes in layer 3, depth = 6 km below the sea level	211
C.9 Vp and Vs at E2006 nodes in layer 4, depth = 15 km below the sea level	212
C.10 Vp and Vs at E2006 nodes in layer 5, depth = 24 km below the sea level	213
C.11 Vp and Vs at E2006 nodes in layer 6, depth = 33 km below the sea level	214
C.12 Vp and Vs at E2006 nodes in layer 7, depth = 48 km below the sea level	215
C.13 Horizontal interpolation of E2006 nodes	216
C.14 Effect of smoothing the topography in three simulation regions	217
C.15 Effect of topographic smoothing on the Interior mesh	218
C.16 Effect of topographic smoothing at AK.ALC2.Z – Wrangell	219
C.17 Effect of topographic smoothing – Wrangell	220
C.18 Effect of velocity thresholding without basin – Interior	221
C.19 Effect of velocity thresholding with basin – Interior	222
C.20 Effect of velocity thresholding without basin – Cook Inlet	223

C.21 Effect of velocity thresholding with basin – Cook Inlet	224
C.22 Effect of velocity thresholding with basin – Cook Inlet	225

List of Tables

	Page
2.1 Moment tensor labels used in the study	32
2.2 Comparison of different moment tensors	32
2.3 Summary of inversion results for the example event (20090407201255351)	33
2.4 Momnet tensor catalog, Part I	34
2.5 ω difference between our preferred solution (M_{111}) and other datasets	35
3.1 Earthquake selection for three target subregions and for the full region	80
3.2 Earthquakes $M \geq 5.8$ in the Cook Inlet and Susitna region	81
3.3 Depths, with uncertainties, for the earthquakes in Table 3.2	82
4.1 Parameters for selecting earthquakes within the three subregions	117
4.2 Comparison among the three simulation regions in Alaska	118
A.1 scak velocity model for southern Alaska	150
A.2 Discretized grid for moment tensor grid search	150
A.3 Comparison tests for Part I catalog	151
A.4 Summary of comparisons between various solutions with the expected solution M_{111}	154
A.5 Text file of moment tensor solutions	154
B.1 Origin info for 1933, 1943 and 1954 earthquakes from various sources.	179
B.2 Moment tensor solutions for 9 crustal earthquakes in the Beluga region	179
B.3 Moment tensor solutions for 22 crustal earthquakes in the Upper Cook Inlet region .	180
B.4 Moment tensor solutions for 22 crustal earthquakes in the Susitna region	181
C.1 Seismic networks used in the study	198
C.2 Moment tensor solutions for 20 earthquakes in the Cook Inlet mesh	199
C.3 Moment tensor solutions for 20 earthquakes in the Interior mesh	200
C.4 Moment tensor solutions for 20 earthquakes in the Wrangell mesh	201
C.5 Expected and actual minimum resolvable periods for meshes of Alaska	202
C.6 Comparison of simulation time for meshes of Alaska	203

List of Appendices

	Page
Appendix A Supplemental Information for Chapter 2 (Seismic moment tensors and estimated uncertainties in southern Alaska)	145
A.1 ScholarWorks@UA collection	145
A.2 Methods	145
A.2.1 Waveform selection criteria	145
A.2.2 Time shifts	146
A.2.3 Variance Reduction	146
A.3 Results	147
A.3.1 Extended analysis for the example event	147
A.3.2 Two small events	147
A.3.3 Comparison between moment tensor catalogs	147
Appendix B Supporting Information for Chapter 3 (Crustal earthquakes in the Cook Inlet and Susitna region of southern Alaska)	175
B.1 Misfit reward factors	175
B.1.1 Waveform reward factor for longer time windows and a broader bandpass .	175
B.1.2 Station reward factor for using more stations	176
Appendix C Supporting Information for Chapter 4 (Seismic wavefield simulations within a three-dimensional seismic velocity model for Alaska)	197

Acknowledgements

I am not sure if I can thank Carl Tape enough. Carl has set the standard for good science, commitment to work, and an example of how to collaborate with students and peers.

I was fortunate to have Natalia Ruppert in my committee. In some aspects I was revisiting her PhD thesis: “Seismological constraints on tectonics of southern and central Alaska: Earthquake locations and source mechanisms (2001),” however, this time with a different dataset and approach. She has been a point of contact for questions ranging from Alaska tectonics to database structures.

I would also like to thank members of Alaska Earthquake Center (AEC). This thesis could not have been possible without their persistent effort to maintain and expand the station coverage. Also thanks to Doug Christensen, Geoff Abers, and Carl Tape for temporary deployments of BEAAR (1999–2000), MOOS (2006–2008), FLATS (2014–2019), and SALMON (2015–2017). (The oldest and largest earthquake in our moment tensor catalog occurred in Minto Flats, and its solution would not have been possible without the BEAAR stations.) It would have been hard to perform moment tensor inversions without the data!

A major part of the thesis involved building tools for data extraction and processing, and moment tensor codes. This was made possible only with the combined effort of Celso Alvizuri. Thanks to Celso for numerous brainstorming and debugging sessions over the years. The third manuscript which deals with minimum resolvable period in Alaska actually has its roots in Ulrika Cahayani Miller’s Masters thesis. The third manuscript would not have been possible without the help and guidance of Ryan Modrak. The quantification of uncertainty in the first manuscript was made possible only due to the theoretical efforts by Walt Tape.

Other members of the group—Kyle Smith, Cole Richards, and Ulrika Cahayani—have been helpful in providing feedback and in discussions. Thanks to Joshua Purba and Qingping Yu for helping expand the moment tensor catalog and improving the moment tensor inversion workflow, and also for providing the opportunity to mentor. I appreciate the constant help and support from Research Computing Systems at the Geophysical Institute, especially David Covey for maintaining the lab machines, and Kevin Galloway for answering numerous cluster-related questions.

I would also like to thank coauthors Anthony Lomax for collaborating on the study of crustal earthquakes in Alaska, Emanuele Casarotti for helping with meshing, and Lion Krischer for data extraction and python related support.

This work was supported by grants from National Science Foundation, Alaska Earthquake Center, U. S. Geological Survey (Earthquake Hazards Program), Air Force Research Laboratory, and one semester of teaching assistantship from UAF Physics Department. I also benefited from

scholarships and travel support from Earthscope, Alaska Geological Society, Geophysical Society of Alaska, Society of Exploration Geophysics, and IRIS.

Lastly, and perhaps most importantly, thanks to my parents and brothers for their support and motivation. Thanks to Alaska and friends for the memories.

Chapter 1

Introduction

We now have a fair understanding of the earth structure and how it has evolved at a large scale: a spherically symmetric, layered model of earth; a solid inner core surrounded by liquid outer core and a slowly convecting, rocky mantle; plate tectonics driven by descending slabs at subduction zones and convection in the mantle. Even three dimensional models estimated using different datasets agree at the largest scales. However, things are complicated as we try to investigate smaller-scale features. These smaller features are the ones that we can observe with our naked eyes, such as mountains, volcanoes, and sedimentary basins. To look beneath the surface, we rely on indirect techniques to infer—or, image—using data recorded at the surface.

In this thesis, we aim toward understanding the structure of Alaska. There are about seven major tectonic plates. Of these, the Pacific plate subducts under the North-American plate forming the Alaska-Aleutian subduction zone. This subduction has been going on for millions of years, however, our understanding of plate tectonics is fairly new, about half a century (Benioff et al., 1961). As the Pacific plate subducts, it sticks to the North American plate until it accumulates enough stress to overcome the frictional locking, and then it slips in the form of large megathrust earthquakes, such as 1964 M_w 9.2. Three of the world’s 15 largest earthquakes have occurred in the Alaska-Aleutian subduction zone. This constant northwest motion of the Pacific plate also radiates stress inwards causing earthquakes in continental Alaska.

The Alaska-Aleutian subduction zone is one the world’s largest and tectonically most active plate margins. Megathrust subduction earthquakes like that of 1964, and the tsunami generated thereof, are the prime consideration of hazard focused studies in southern Alaska. However, including intraplate earthquakes and faults can provide us with improved hazard assessment (Haeussler et al., 2000; Graves et al., 2011). The study of these earthquakes provides insight into the stress regime of the region (Ruppert, 2008), delineation of new seismic zones, and estimating the largest possible earthquake that can occur in the region.

In this thesis, we perform three main tasks to further our understanding of earthquake mechanisms and structure of Alaska:

1. Improve earthquake source inversion techniques and demonstrate an approach for uncertainty estimation.
2. Use source mechanisms of crustal earthquakes for understanding the tectonics of south-central Alaska.
3. Investigate the effects of structure on the regional seismic wavefield, by simulating seismic waves in a three-dimensional model of Alaska.

These topics comprise the themes of the thesis and correspond, respectively, to the three chapters. The improvement in the moment tensor inversion technique is demonstrated in Chapter 2 and Chapter 3. An application of source mechanism for explaining the tectonics of south-central Alaska is presented in Chapter 3. Parts of this thesis also contributed towards understanding the transtensional tectonics of Nenana basin (Silwal, 2015a; Tape et al., 2015). Throughout the thesis we acknowledge the effect of structure, particularly of the Cook Inlet basin and the subducting Pacific slab, when comparing observed seismograms with synthetics for source inversion in south-central Alaska. In Chapter 4 we make a more focused effort of understanding this observed-and-synthetics mismatch by using a three-dimensional model of Alaska. A more detailed overview of each chapter is presented in Section 1.2.

1.1 A brief introduction to moment tensors

Earthquakes in general occur on a fault by shear dislocation, which can be modeled as a double couple moment tensor. A double couple moment tensor is a 3×3 symmetric matrix whose eigenvalues are $(\lambda, 0, -\lambda)$. We are concerned with estimating the magnitude and orientation (strike, dip, rake) of the moment tensor. Alternative terms for double couple moment tensors are ‘fault-plane solution’ or ‘focal mechanism.’ Our approach to moment tensor estimation can also be applied to ‘full’ moment tensors, which contain an additional two parameters. The full moment tensor representation allows for modeling oblique opening across faults (e.g., Aki & Richards, 1980; Dufumier & Rivera, 1997; Minson & Dreger, 2008; Tape & Tape, 2013).

Throughout this thesis, we perform moment tensor inversion using the ‘cut-and-paste’ (CAP) method of Zhu & Helmberger (1996). CAP uses both surface waves and body waves from seismic waveforms filtered over relatively short periods, for example 3–10 s of Tan et al. (2006) or 5–100 s of Zhu & Helmberger (1996). The body wave measurements are for the ‘Pnl’ waveform, which includes multiple paths that follow the arrival of the direct P (Helmberger & Engen, 1980); this is measured on the vertical and radial components. The surface wave measurements target the Rayleigh wave (vertical and radial components) and the Love wave (transverse component) (Figure 1.2). The best moment tensor solution is achieved by minimizing the misfit between filtered recorded data \mathbf{u} and synthetics \mathbf{s} , for different sections of seismogram (discussed in detail in Chapter 2):

$$\phi_{ij}(M) = \left[(\mathbf{u}_{ij} - \mathbf{s}_{ij}(M))^T \mathbf{W}_{ij} (\mathbf{u}_{ij} - \mathbf{s}_{ij}(M)) \right]^{1/2} \quad (1.1)$$

1.2 Overview of Chapters

Chapter 2 aims at providing a high-quality moment tensor catalog for southern Alaska. The improvements in moment tensor solutions are achieved by using more data and an improved

methodology. We demonstrated that using an L1 norm in the misfit function will provide more stable moment tensor solutions (Silwal & Tape, 2016). We also introduce an approach for quantifying and visualizing the uncertainty in a double couple moment tensor solution using a probabilistic approach. This approach was further extended to quantify the uncertainty in full moment tensor solution by Alvizuri et al. (2018). The moment tensor catalog generated is available at ScholarWorks@UA (Silwal, 2015b).

Chapter 3 is a more focused study in which we analyze the crustal seismicity (depth ≤ 30 km) in the Cook Inlet and Susitna region (Silwal et al., 2018). The active folds and faults in this region have the potential of generating M_w 6–7 magnitude earthquakes. Combined with the amplification of the seismic waves due to the basin, such earthquakes pose a significant hazard to nearby cities such as Anchorage. We select 11 historical earthquakes $M_w \geq 5.8$. We also recompute the locations for major historical earthquakes in the region using a non-linear least square approach (Lomax et al., 2018). Moment tensor inversion of smaller earthquakes and double-difference relocation suggest that the region is pre-dominantly in a thrust setting. The moment tensor catalog generated is available at ScholarWorks@UA (Silwal, 2018a).

For the moment tensor inversions in Chapters 2 and 3, we assumed that the material properties of earth vary only with depth. This is a reasonable assumption if one is interested only in the large scale features of earth. If we want to understand the effect on seismic waves due to the small-scale features such as basins, the subducting Pacific slab, the accreting Yakutat block and the topography, then we need to use a 3D velocity model that contains the appropriate details. Figure 1.3 shows the effect of basins on the seismic wavefield.

In **Chapter 4** our aim is to provide a 3D reference velocity model which could be used as the initial model for an iterative tomographic inversion. The validation of different seismic velocity models is the focus of this chapter. This involves testing different meshes—such as the effects of topography smoothing on simulations—and testing different models—such as the effects of including basin and setting a minimum allowable velocity. We also perform detailed comparisons of minimum resolved period of the synthetics and the simulation time for different runs, both of which plays important roles in deciding which model to choose.

1.2.1 Contributions to published works

Here we document parts of this PhD thesis that have contributed to published manuscripts.

1. The ScholarWorks@UA collection of Silwal (2015b) for Silwal & Tape (2016) in Chapter 2.
2. The ScholarWorks@UA collections of Silwal (2018a) and Lomax et al. (2018) for Silwal et al. (2018) in Chapter 3.

3. The ScholarWorks@UA collection of Silwal (2015a) for Tape et al. (2015) (second author Silwal). This includes moment tensor results for 15 earthquakes in the Minto Flats fault zone. The similarity among moment tensors provided support for the Minto Flats fault zone as a left-lateral strike slip fault.
4. The ScholarWorks@UA collection of Silwal (2018b) for Tape et al. (2018) (third author Silwal). This includes moment tensors results for 6 events in the Minto Flats fault zone, as well as a more detailed analysis of the influence of source duration and choice of bandpass on the moment tensor results.
5. The moment tensor inversion results for the 2012 triggered earthquake in Tape et al. (2013). The initial analysis of this earthquake appeared in my Master's thesis (Silwal, 2012). I provided slightly revised moment tensor results for this earthquake in Tape et al. (2015) and in Tape et al. (2018).
6. The moment tensor inversion results in Figure B1 of Tape et al. (2017) (third author Silwal). This is for the 2000-02-03, M_w 5.5, earthquake on the Kaltag fault.
7. Code developments used in Alvizuri et al. (2018). The polarity + waveform misfit function described and used in Silwal et al. (2018) was also used in Alvizuri et al. (2018) (second author Silwal).

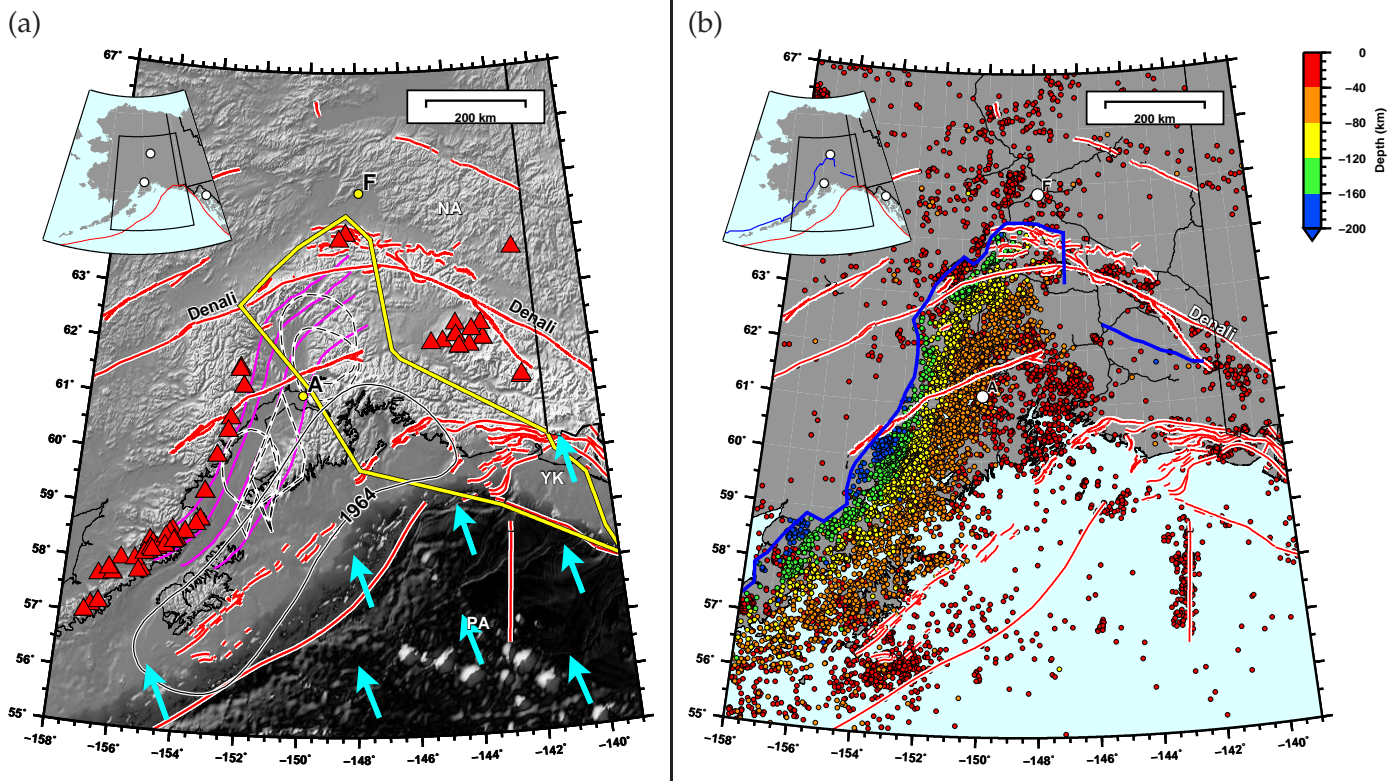


Figure 1.1: (a) Active tectonic setting of the Aleutian–Alaskan subduction zone, south-central Alaska. The rectangle in the middle shows the main study region. Cyan arrows shows the plate vectors for the subducting Pacific plate (PA) under the North American plate (NA) (Bird, 2003). Magenta curves are the 40 km, 60 km, 80 km, and 100 km contours of the top of the Pacific plate (Li et al., 2013). Yellow bounded region denotes the surface and subsurface extent of the Yakutat block (YK) (Eberhart-Phillips et al., 2006). Red triangles represent active volcanoes. Black dashed lines are inferred slow slip from various sources (Ohta et al., 2006; Wei et al., 2012; Fu & Freymueller, 2013; Li et al., 2016). Also marked is the aftershock zone of the 1964 M_w 9.2 earthquake. Labeled cities: Anchorage (A) and Fairbanks (F). (b) Alaska Earthquake Center (AEC) catalog: $M_w \geq 2$, 1990-01-01 to 2017-01-01, colored by depth. The red lines are the active faults from Koehler et al. (2012). The blue line is the lateral extent of slab seismicity, digitized from the full AEC catalog. These figures are part of Silwal et al. (2018).

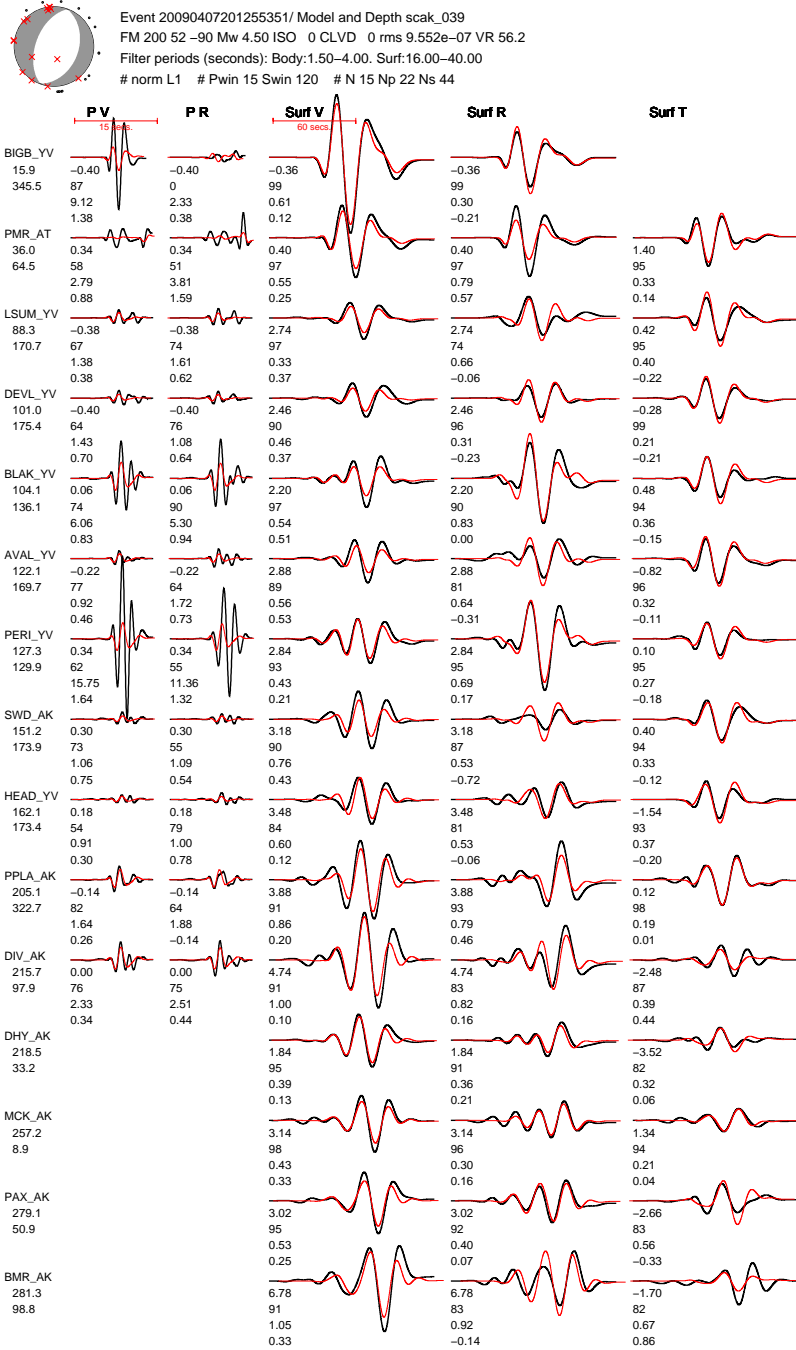


Figure 1.2: Moment tensor solution and waveform comparisons for an example event in Anchorage, April 7, 2009. Waveform fit between the data (black) and the synthetics (red). The waveforms at each station are cut into 5 components (PV, PR, Rayleigh R, Rayleigh V, SH) and the matching is done by applying a different filter to body and surface waves. Number below the waveforms are, from top to bottom, (1) time shift required for matching the synthetics with the data; (2) maximum cross-correlation percentage between data and synthetics; (3) the percentage of the total misfit; (4) log amplitude between data and synthetics in each window. Number below the station name are distance and azimuth. This figure is part of Silwal & Tape (2016).

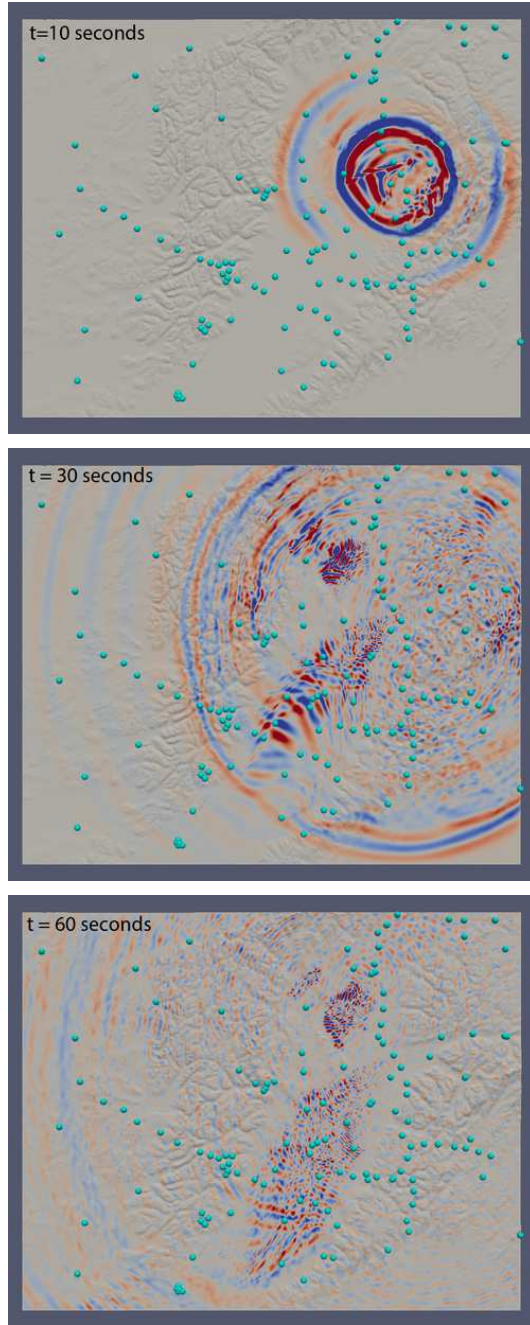


Figure 1.3: Snapshots of a 3D wavefield simulation showing the influence of the Cook Inlet and Susitna basin on the seismic wavefield. Simulation is performed for the 2009-04-07 Anchorage event for which the source was obtained from (Silwal & Tape, 2016). Colors represent the vertical component of simulated ground velocity. Cyan circles denote broadband stations.

References

- Aki, K. & Richards, P. G., 1980. *Quantitative Seismology, Theory and Methods*, W. H. Freeman, San Francisco, Calif., USA.
- Alvizuri, C., Silwal, V., Krischer, L., & Tape, C., 2018. Estimation of full moment tensors, including uncertainties, for nuclear explosions, volcanic events, and earthquakes, *J. Geophys. Res. Solid Earth*, **123**, doi:10.1029/2017JB015325.
- Benioff, H., Press, F., & Smith, S., 1961. Excitation of the free oscillations of the Earth by earthquakes, *J. Geophys. Res.*, **66**, 605–619.
- Bird, P., 2003. An updated digital model of plate boundaries, *Geochem. Geophys. Geosyst.*, **4**, 1027, doi:10.1029/2001GC000252.
- Dufumier, H. & Rivera, L., 1997. On the resolution of the isotropic component in moment tensor inversion, *Geophys. J. Int.*, **131**, 595–606.
- Eberhart-Phillips, D., Christensen, D. H., Brocher, T. M., Hansen, R., Ruppert, N. A., Haeussler, P. J., & Abers, G. A., 2006. Imaging the transition from Aleutian subduction to Yakutat collision in central Alaska, with local earthquakes and active source data, *J. Geophys. Res.*, **111**, B11303, doi:10.1029/2005JB004240.
- Fu, Y. & Freymueller, J. T., 2013. Repeated large Slow Slip Events at the south central Alaska subduction zone, *Earth Planet. Sci. Lett.*, **375**, 303–311.
- Graves, R., Jordan, T. H., Callaghan, S., Deelman, E., Field, E., Juve, G., Kesselman, C., Maechling, P., Mehta, G., Milner, K., Okaya, D., Small, P., & Vahi, K., 2011. CyberShake: A physics-based seismic hazard model for southern California, *Pure App. Geophys.*, **168**, 367–381.
- Haeussler, P. J., Bruhn, R. L., & Pratt, T. L., 2000. Potential seismic hazards and tectonics of the upper Cook Inlet basin, Alaska, based on analysis of Pliocene and younger deformation, *Geol. Soc. Am. Bull.*, **112**(9), 1414–1429.
- Helberger, D. V. & Engen, G. R., 1980. Modeling the long-period body waves from shallow earthquakes at regional ranges, *Bull. Seismol. Soc. Am.*, **70**, 1699–1714.
- Koehler, R. D., Farrell, R.-E., Burns, P. A. C., & Combellick, R. A., 2012. Quaternary faults and folds in Alaska: A digital database, Alaska Div. Geol. Geophys. Surv. Miscellaneous Publication 141, 31 p., 1 sheet, scale 1:3,700,000.

Li, J., Abers, G. A., Kim, Y., & Christensen, D., 2013. Alaska megathrust 1: Seismicity 43 years after the great 1964 Alaska megathrust earthquake, *J. Geophys. Res.*, **118**, 4861–4871, doi:10.1002/jgrb.50358.

Li, S., Freymueller, J., & McCaffrey, R., 2016. Slow slip events and time-dependent variations in locking beneath Lower Cook Inlet of the Alaska-Aleutian subduction zone, *J. Geophys. Res. Solid Earth*, **121**, 1060–1079, doi:10.1002/2015JB012491.

Lomax, A., Silwal, V., & Tape, C., 2018. Hypocenter estimation for 14 earthquakes in south-central Alaska (1929–1975), ScholarWorks@UA at <http://hdl.handle.net/11122/8380>: descriptor file and zipped set of text files for each earthquake.

Minson, S. E. & Dreger, D. S., 2008. Stable inversions for complete moment tensors, *Geophys. J. Int.*, **174**, 585–592, doi:10.1111/j.1365-246X.2008.03797.x.

Ohta, Y., Freymueller, J. T., Hreinsdóttir, S., & Suito, H., 2006. A large slow slip event and the depth of the seismogenic zone in the south central Alaska subduction zone, *Earth Planet. Sci. Lett.*, **247**, 108–116.

Ruppert, N. A., 2008. Stress map for Alaska from earthquake focal mechanisms, in *Active Tectonics and Seismic Potential of Alaska*, vol. 179 of **Geophysical Monograph**, pp. 351–367, eds Freymueller, J. T., Haeussler, P. J., Wesson, R., & Ekström, G., Am. Geophys. Un., Washington, D.C.

Silwal, V., 2012. *Seismic Moment Tensor Inversion in Alaska using Body and Surface Waves*, Master's thesis, Indian Institute of Technology, Kharagpur.

Silwal, V., 2015a. Seismic moment tensor catalog for Minto Flats fault zone (2000–2014), ScholarWorks@UA at <http://hdl.handle.net/11122/6267> (last accessed 2016-01-22): descriptor file, text file of catalog, composite figures of waveform fits and depth searches.

Silwal, V., 2015b. Seismic moment tensor catalog for southern Alaska, ScholarWorks@UA at <http://hdl.handle.net/11122/6025> (last accessed 2016-01-22): descriptor file, text file of catalog, figures with waveform fits, depth searches, and uncertainty analyses.

Silwal, V., 2018a. Seismic moment tensor catalog for crustal earthquakes in the Cook Inlet and Susitna region of southern Alaska, ScholarWorks@UA at <http://hdl.handle.net/11122/8383>: descriptor file, text file of catalog, figures with waveform fits, and input weight files.

Silwal, V., 2018b. Seismic moment tensors for six events in the Minto Flats fault zone, 2012–2016, ScholarWorks@UA at <http://hdl.handle.net/11122/8253>: descriptor file, text file of catalog, figures with waveform fits, and input weight files.

Silwal, V. & Tape, C., 2016. Seismic moment tensors and estimated uncertainties in southern Alaska, *J. Geophys. Res. Solid Earth*, **121**, 2772–2797, doi:10.1002/2015JB012588.

Silwal, V., Tape, C., & Lomax, A., 2018. Crustal earthquakes in the Cook Inlet and Susitna region of southern Alaska, *Tectonophysics* (submitted).

Tan, Y., Zhu, L., Helmberger, D. V., & Saikia, C. K., 2006. Locating and modeling regional earthquakes with two stations, *J. Geophys. Res.*, **111**, B01306, doi:10.1029/2005JB0037750.

Tape, C., West, M., Silwal, V., & Ruppert, N., 2013. Earthquake nucleation and triggering on an optimally oriented fault, *Earth Planet. Sci. Lett.*, **363**, 231–241, doi:10.1016/j.epsl.2012.11.060.

Tape, C., Silwal, V., Ji, C., Keyson, L., West, M. E., & Ruppert, N., 2015. Transtensional tectonics of the Minto Flats fault zone and Nenana basin, central Alaska, *Bull. Seismol. Soc. Am.*, **105**(4), 2081–2100, doi:10.1785/0120150055.

Tape, C., Lomax, A., Silwal, V., Agnew, J. D., & Brettschneider, B., 2017. The 1904 M_s 7.3 earthquake in central Alaska, *Bull. Seismol. Soc. Am.*, **107**(3), 1147–1174, doi:10.1785/0120160178.

Tape, C., Holtkamp, S., Silwal, V., Hawthorne, J., Kaneko, Y., Ampuero, J. P., Ji, C., Ruppert, N., Smith, K., & West, M. E., 2018. Earthquake nucleation and fault slip complexity in the lower crust of central Alaska, *Nature Geoscience*, **11**, 536–541, doi:10.1038/s41561-018-0144-2.

Tape, W. & Tape, C., 2013. The classical model for moment tensors, *Geophys. J. Int.*, **195**, 1701–1720, doi:10.1093/gji/ggt302.

Wei, M., McGuire, J. J., & Richardson, E., 2012. A slow slip event in the south central Alaska Subduction Zone and related seismicity anomaly, *Geophys. Res. Lett.*, **39**, L15309, doi:10.1029/2012GL052351.

Zhu, L. & Helmberger, D., 1996. Advancement in source estimation techniques using broadband regional seismograms, *Bull. Seismol. Soc. Am.*, **86**(5), 1634–1641.

Chapter 2

Seismic moment tensors and estimated uncertainties in southern Alaska¹

2.1 Abstract

We present a moment tensor catalog of 106 earthquakes in southern Alaska, and we perform a conceptually based uncertainty analysis for 21 of them. For each earthquake, we use both body waves and surface waves to do a grid search over double couple moment tensors and source depths in order to find the minimum of the misfit function. Our uncertainty parameter or, rather, our confidence parameter, is the average value of the curve $\mathcal{P}(V)$, where $\mathcal{P}(V)$ is the posterior probability as a function of the fractional volume V of moment tensor space surrounding the minimum-misfit moment tensor. As a supplemental means for characterizing and visualizing uncertainties, we generate moment tensor samples of the posterior probability. We perform a series of inversion tests to quantify the impact of certain decisions made within moment tensor inversions and to make comparisons with existing catalogs. For example, using an L1 norm in the misfit function provides more reliable solutions than an L2 norm, especially in cases when all available waveforms are used. Using body waves in addition to surface waves, as well as using more stations, leads to the most accurate moment tensor solutions.

2.2 Introduction

The seismic moment tensor, visualized as a beachball, represents the radiation pattern for a point-source earthquake and plays an important role within the field of seismology (e.g., Isacks et al., 1968). Moment tensors are used to interpret the style of faulting and deformation in active tectonic settings, they are used within seismic wavefield simulations to estimate ground motions in a particular region, and they are used within earthquake-based tomographic inversions that seek to improve seismic velocity models. Despite these fundamental purposes, there have been few insights into how to characterize the uncertainty of moment tensors (Riedesel & Jordan, 1989; Valentine & Trampert, 2012; Käufl et al., 2014; Stähler & Sigloch, 2014). In this paper we apply a new approach for estimating uncertainties (Tape & Tape, 2016) to a set of 21 earthquakes in southern Alaska (Figures 2.1 and 2.2). We also present moment tensor solutions for an additional 85 smaller earthquakes to form a catalog of 106 events.

We could have chosen any set of recorded earthquakes for our uncertainty analysis, but southern Alaska provides several advantages. First it is a region of active tectonics and high seismicity rates (Figure A.1) with events occurring throughout the crust and within the slab down to depths of 200 km. Second there is a good network of broadband seismic stations, especially during the

¹Published as: Silwal, V. and Tape, C., 2016. Seismic moment tensors and estimated uncertainties in southern Alaska, *J. Geophys. Res. Solid Earth*, 121, 2772–2797, doi:10.1002/2015JB012588.

time period of interest. Third there are two existing moment tensor catalogs using two different techniques (Section 2.3.1); this allows us to compare different inversion algorithms and to compare the various choices made within these algorithms. Finally we are interested in better understanding the tectonics of this region, and we are interested in using our moment tensors within a tomographic inversion using earthquakes, wavefield simulations, and adjoint methods (e.g., Tape et al., 2009). One of the most prominent tectonic features within our region of interest (Figure 2.1) is the Cook Inlet forearc basin, one of the largest in the world. The basin poses challenges when performing waveform fits between data and synthetics at the stations in and around the basin.

In our study we assume that each earthquake is a shear dislocation that can be modeled as a double couple moment tensor. A double couple moment tensor is a 3×3 symmetric matrix whose eigenvalues are $(\lambda, 0, -\lambda)$. We are concerned with estimating the magnitude and orientation (strike, dip, rake) of the moment tensor. Alternative terms for double couple moment tensors are ‘fault-plane solution’ or ‘focal mechanism.’ Our approach to moment tensor estimation can also be applied to ‘full’ moment tensors, which contain an additional two parameters. The full moment tensor representation allows for modeling oblique opening across faults (e.g., Aki & Richards, 1980; Dufumier & Rivera, 1997; Tape & Tape, 2013).

Seismic moment tensors are routinely estimated using different approaches, which can be divided into two broad categories on the basis of data used:

1. high-frequency body waves measurements, such as the polarity of (first-motion) P waves or the amplitude ratios of S to P waves. These observations can be extracted readily from catalogs containing P and S arrival times. Two examples of codes that estimate double couple moment tensors from these data are HASH (Hardebeck & Shearer, 2002) and FPFIT (Reasenberg & Oppenheimer, 1985).
2. filtered seismic waveforms. Other moment tensor inversions involve comparing filtered synthetic waveforms with filtered recorded waveforms. Typically some portion of the full waveform is used (e.g., P wave or surface wave). Examples of this approach are GCMT (Ekström et al., 2012), TDMT (Dreger et al., 1998; Dreger & Woods, 2002), CAP (Zhu & Helmberger, 1996), and W-phase (Duputel et al., 2012).

The method of Dreger et al. (1998) is the most widely used algorithm for regional moment tensor determination. This method (Time Domain Moment Tensor INVersion Code, TDMT_INV), which uses relatively long-period surface waves (10–50 s) has been implemented in Alaska (Ratchkovski & Hansen, 2002), western Canada (Ristau et al., 2007), southern California (Clinton et al., 2006), Japan (Fukuyama et al., 1998; Fukuyama & Dreger, 2000), New Zealand (Ristau, 2008), Spain (Rueda & Mezcua, 2005), and Italy (Scognamiglio et al., 2009), and probably elsewhere. The al-

gorithm constrains moment tensors to be deviatoric. The Alaska Earthquake Center (AEC) uses TDMT to produce their moment tensor catalog, including 21 analyzed in our study. We use the notation M_{AEC} to denote a moment tensor in the AEC moment tensor catalog derived using TDMT.

An example of an algorithm that uses first-motion polarities to determine double couple moment tensors is FPFIT (Reasenberg & Oppenheimer, 1985). This algorithm uses weighted sum of first-motion polarity differences (between observed and predicted) to find the global minimum and local minima. The uncertainty in each solution parameter is estimated using the 90% confidence interval for the normalized misfit function (0 to 1). The AEC routinely uses FPFIT to estimate double couple moment tensors for earthquakes, including 85 analyzed in our study. We use the notation M_{fm} to denote a moment tensor from the AEC first-motion catalog derived using FPFIT.

The ‘cut-and-paste’ (CAP) method of Zhu & Helmberger (1996) uses both surface waves and body waves from seismic waveforms filtered over relatively short periods, for example 3–10 s of Tan et al. (2006) or 5–100 s of Zhu & Helmberger (1996). The body wave measurements are for the ‘Pnl’ waveform which includes multiple paths that follow the arrival of the direct P (Helmberger & Engen, 1980); this is measured on the vertical and radial components. The surface wave measurements target the Rayleigh wave (vertical and radial components) and the Love wave (transverse component). Based on catalog comparisons in Tape et al. (2009, Appendix D), as well as our desire to fit as much of the seismic wavefield as possible, we chose to use CAP within this study. Details on CAP are presented in Sections 2.3.2–2.3.4.

Most of the inversion methods discussed above do not have a clear approach for estimating uncertainties in moment tensors. The most common method for estimating uncertainties involves ‘bootstrapping’, which involves resampling the data and reinverting the moment tensor repeatedly to obtain a set of possible solutions (e.g., Nayak & Dreger, 2014; Ross et al., 2015).

Part of the challenge in estimating uncertainties is that the properties of the moment tensor space under consideration are not obvious. The notion of uniformly distributed moment tensors, and the closely related notion of volumes in moment tensor space, need to be clarified. For us the space of moment tensors under consideration is the set of all double couples. For this set Tape & Tape (2015) show that uniform orientations give uniformly distributed moment tensors.

We calculate a new uncertainty curve, or rather ‘confidence curve,’ $\mathcal{P}(V)$, for each of 21 earthquakes. The function $\mathcal{P}(V)$, to be defined precisely in Section 2.4.1, describes how the posterior probability is concentrated around a selected reference tensor within moment tensor space. For example, $\mathcal{P}(0.1) = 0.9$ means that 90% of the probability is contained within the 10% volume fraction around the reference moment tensor. The curve $\mathcal{P}(V)$ is calculated from the posterior probability and the fractional volume in moment tensor space. The probability density p is scaled from

a waveform difference misfit function Φ as $p(M) \propto \exp(-\Phi(M))$. Associated with the curve $\mathcal{P}(V)$ are two useful scalar quantities: (1) the slope of the curve at the origin. It is proportional to the probability density at the reference moment tensor. (2) the area \mathcal{P}_{AV} under the curve, which is the average value of $\mathcal{P}(V)$. It gives a single measure of confidence.

Our study produces a moment tensor catalog of 106 events in southern Alaska. The catalog is divided into two parts, as explained in Section 2.3.1: Part I (Table 2.4) and Part II (Table A.5). In Section 2.3 we describe our moment tensor inversion, including the estimation of uncertainties. Section 2.5.1 presents our uncertainty analysis for a single earthquake. Section 2.6 summarizes a set of comparative inversions for the 21 events. It is intended to provide insights into some of the choices made within moment tensor inversions.

We suggest two alternatives to reading the paper from start to finish. If you are primarily interested in our approach to estimating moment tensor uncertainties, then please focus on Sections 2.4, 2.5.1, and 2.8. If you are primarily interested in our assessment of the impact of various decisions made within moment tensor inversions—e.g., type of norm, body waves or surface waves, number of stations—then please see Sections 2.3.4 and 2.6.

2.3 Methods

Our objective is to obtain the highest-quality catalog of moment tensors in southern Alaska, primarily for future purposes of earthquake-based seismic tomographic inversion. Our study is centered on data acquired by the MOOS (Multidisciplinary Observations Of Subduction) array in the Kenai Peninsula region of south-central Alaska (Christensen et al., 2008). This array had up to 34 broadband stations active between 2007-8-15 and 2009-8-15 and provides the best coverage for studying earthquakes in this region. We also include all permanent broadband stations that were active during this time period; a map of stations is shown in Figure 2.1. All earthquakes in this study occurred within the bounding box of latitude $[58^\circ, 62.5^\circ]$ and longitude $[-154^\circ, -146^\circ]$ (Figure 2.2).

2.3.1 Selection of events and processing of waveforms

In addition to estimating the best possible moment tensors in southern Alaska, we are interested in performing comparative studies with existing catalogs. The Alaska Earthquake Center (AEC) maintains two moment tensor catalogs:

1. AEC moment tensor catalog. This catalog contains deviatoric moment tensors for $M_w \geq 4$ earthquakes. The moment tensors, which we denote by M_{AEC} , are estimated using the TDMT code (Pasmanos et al., 1996; Dreger et al., 1998).

2. AEC first-motion catalog. This catalog contains double couple moment tensors for $M_w \geq 3.0$ earthquakes. The moment tensors, which we denote by M_{fm} , are estimated using the FPFIT code (Reasenberg & Oppenheimer, 1985).

We use these two catalogs as a basis for selecting events in this study. The two catalogs form two parts of our composite catalog of 106 earthquakes:

1. Part I catalog: all 21 events from the AEC moment tensor catalog within our region (Figure 2.2) and time period of interest. We perform our uncertainty analysis on these events. By focusing on the events in the AEC moment tensor catalog, we can perform direct comparisons between two moment tensor inversion methods: CAP (used here) and TDMT (used by AEC).
2. Part II catalog: 85 events from the AEC first-motion catalog with magnitude $M_w \geq 3.5$ and within our region and time period of interest. For several of the smaller Part II catalog events we use first-motion polarity observations in order to help constrain the solution. We do not calculate confidence curves for the 85 events, mainly because our current formulation of the misfit function—and subsequent confidence curve—does not consider first-motion polarities. Our primary goal for the Part I events is to obtain the most reliable moment tensor solutions and to compare them with the solutions obtained by AEC using P-wave polarities only.

We acquired three-component broadband seismic waveforms from the Alaska Earthquake Center and from the MOOS waveform database (Christensen et al., 2008). For each event we extracted 300 s of waveforms from stations within 500 km of epicentral distance (Figure 2.1). Waveform processing, including instrument deconvolution between periods 0.04–100 s (using a 2-pole Butterworth bandpass filter), was performed using the GISMO Waveform Toolbox for MATLAB (Reyes & West, 2011). Additional bandpass filtering was applied within the moment tensor grid search algorithm.

2.3.2 Cut-and-paste (CAP) approach

The cut-and-paste moment tensor inversion approach of Zhao & Helmberger (1994) and Zhu & Helmberger (1996) is named for its cutting of sections of synthetic seismograms and pasting them on corresponding portions of observed seismograms. A key feature is that each section of synthetic seismogram is allowed to be time shifted to best match the observed seismogram. By using different time shifts, CAP accounts for some of the errors associated with the seismic velocity

model that is assumed. For example, for a given station we might expect a different time shift between data and synthetics for the P wave, Rayleigh wave, and Love wave. Allowing for different time shifts is especially important when considering a second feature of CAP: different bandpass filters are generally applied to body waves and surface waves.

The seismic waveforms are rotated radial, transverse, and vertical components and are divided into five time windows of body and surface waves:

1. PV: vertical component of the P wave
2. PR: radial component of the P wave
3. SurfV: vertical component of the Rayleigh wave
4. SurfR: radial component of the Rayleigh wave
5. SurfT: transverse component of the Love wave

Any of these time windows can be excluded based on the waveform selection criteria (Section A.2.1).

In our inversions we use three time shifts: one for PV and PR, one for SurfV and SurfR, and one for SurfT. For the 21 Part I events in our catalog (Table 2.4) we filtered body waves between 1.5–4.0 s and allowed a maximum time shift of ± 2 s, and we filtered surface waves between 16–40 s and allowed a maximum time shift of ± 10 seconds. For the 85 smaller Part II events in the catalog, we made adjustments to the bandpass filters and time shifts. Our goal was to fit as much of the wavefield as possible, both in terms of the broadest bandpass and the greatest sections of time.

2.3.3 Grid-search moment tensor inversion

In a grid search moment tension inversion, one looks for the minimum of a misfit function Φ between observed and synthetic seismograms. The CAP approach is distinguished by the details of how Φ is assembled from pieces of filtered seismic waveforms. Our synthetic seismograms are computed using a frequency-wavenumber method based on the Thomson-Haskell Propagator matrix method (Haskell, 1964; Zhu & Rivera, 2002). We use the same layered seismic velocity model that is used by the Alaska Earthquake Center for moment tensor inversions and for locating earthquakes (Table A.1). Once a misfit function is established, the approach to finding the minimum of the misfit function is a straightforward grid search over the space of model parameters.

We consider five model parameters: earthquake depth z , earthquake magnitude m , and moment tensor orientation: strike κ , rake σ , and dip θ . We assume that the earthquakes occur as shear faulting without opening; hence our moment tensors are double couples. We fix the epicenter and origin time as those from the AEC catalog.

The search ranges for our parameters are:

- depth z : $z_{\text{AEC}} - 35 \leq z \leq z_{\text{AEC}} + 35$, where z_{AEC} is the depth in the AEC moment tensor catalog
- magnitude m : search within ± 1 unit of the AEC moment tensor catalog magnitude
- strike κ : $0^\circ \leq \kappa < 360^\circ$
- rake σ : $-90^\circ \leq \sigma \leq 90^\circ$
- $h = \cos \theta$: $0 \leq h \leq 1$, corresponding to dip θ ranging from 0° to 90°

The use of h instead of dip angle θ allows us to obtain uniformly distributed orientations by choosing κ , σ , and h uniformly (Kagan, 1991; Tape & Tape, 2012). Uniformly distributed orientations give uniformly distributed double couple moment tensors (Tape & Tape, 2015).

While our grid search involves five parameters, most of the post-processing uncertainty analysis involves only the three parameters (κ, σ, h) that describe the moment tensor orientation. For each earthquake our unknown model vector is

$$\mathbf{m} = (\kappa, \sigma, h, m, z)^T. \quad (2.1)$$

Our goal is to search over this parameter space to obtain the model vector $\mathbf{m}_0 = (\kappa_0, \sigma_0, h_0, m_0, z_0)$ that minimizes the misfit Φ . We let M_0 be the corresponding moment tensor:

$$M_0 = M(\kappa_0, \sigma_0, h_0, m_0, z_0) \quad (2.2)$$

(The moment tensor M_0 is not to be confused with the scalar seismic moment, also usually denoted by M_0 .)

We can find M_0 either by using a regular grid of points or by using random points. The values of M_0 in our catalog (e.g., Table 2.4) are based on the regular grid search; the intervals are listed in Table A.2. Alternatively we could have found M_0 from the set of random points used in our uncertainty analysis. The workflow in Figure 2.3 starts by generating 100,000 random points in the space of κ - σ - h . We then choose a regular grid for searching over depth and magnitude (Table A.2). We evaluate the misfit function Φ at the moment tensors to obtain the minimum.

Our analysis of uncertainties begins at this stage, with both the magnitude $m = m_0$ and the depth $z = z_0$ fixed; the analysis therefore only involves the moment tensor orientation, which is determined by (κ, σ, h) .

2.3.4 Misfit function

Let $\mathbf{s}(M)$ represent a predicted time series for a moment tensor M . We can think of $\mathbf{s}(M)$ as a forward model that will input a moment tensor and output a time series of ground motion on the surface. The underlying physics is wave propagation in a simple layered medium.

Our misfit function measures the difference between recorded seismograms ('data') and modeled seismograms ('synthetics'). Each station records ground motions in three components, which are recorded on three seismograms. Let \mathbf{u} represent a discretized time series of one component of the seismometer-recorded ground velocity, so u_k would be the ground velocity at time t_k . The goal is to find the M that minimizes the difference between \mathbf{u} and $\mathbf{s}(M)$.

Seismograms at each station are split into different time windows. We use i for the time window index and j for the station index. We adopt the commonly used L2 norm as a measure of misfit between data and synthetic waveforms. The L2-norm waveform difference within a single time window is given by

$$\phi_{ij}(M) = \left[(\mathbf{u}_{ij} - \mathbf{s}_{ij}(M))^T \mathbf{W}_{ij} (\mathbf{u}_{ij} - \mathbf{s}_{ij}(M)) \right]^{1/2} \quad (2.3)$$

where the matrix \mathbf{W}_{ij} is a weighting matrix that can be thought of as an inverse data covariance matrix (e.g., Aster et al., 2013). For our purposes it is a diagonal square matrix with the same weight factor w_{ij} on the diagonal. This gives the flexibility of adjusting the weights for any time window.

We define a misfit function for each earthquake. Each earthquake is recorded by N_s stations. Each seismogram at each station is split into five time windows (PV, PR, SurfV, SurfR, SurfT). We consider two norms for the misfit function, which we refer to as L1 and L2:

$$\Phi_{L1}(M) = \sum_{j=1}^{N_s} \sum_{i=1}^5 \phi_{ij}(M) \quad (2.4)$$

$$\Phi_{L2}(M) = \sum_{j=1}^{N_s} \sum_{i=1}^5 \phi_{ij}^2(M) \quad (2.5)$$

Equation (2.5) is actually the square of an L2 norm and is what was implemented in the CAP code of Zhu & Helmberger (1996). We are not directly comparing values of these two norms, rather we are comparing the moment tensors that give the minima. The L1 norm is less sensitive to outliers than the L2 norm (Aster et al., 2013). The moment tensor that minimizes $\Phi_{L1}(M)$ may be very different from the one that minimizes $\Phi_{L2}(M)$, as we will see later in Section 2.6.1.

In the explanation and notation above we have omitted some details. Each waveform within a synthetic seismogram is time-shifted to match the data. Furthermore, the data and synthetics are filtered (identically) over a specified bandpass. Finally, there is a built-in weighting of waveforms

by source-station distance that allows the more distant stations to have influence comparable to closer stations (Zhu & Helmberger, 1996).

2.3.5 Scaling the misfit function

We define a scaled version Φ of the L1-norm misfit function by

$$\Phi(M) = \frac{k}{u_{L1}} \Phi_{L1}(M) = \frac{k}{u_{L1}} \sum_{j=1}^{N_s} \sum_{i=1}^5 \phi_{ij}(M). \quad (2.6)$$

where u_{L1} is defined in terms of the observed waveforms by

$$u_{L1} = \left(\sum_{j=1}^{N_s} \sum_{i=1}^5 [\mathbf{u}_{ij}^T \mathbf{W}_{ij} \mathbf{u}_{ij}] \right)^{1/2} \quad (2.7)$$

The reason we need a scale factor in the misfit function is that, as with most seismological studies, the errors in the data are poorly known. If we had a good estimate for errors in the data, then our weighting matrix for each time window, \mathbf{W}_{ij} , could be represented by the inverse data covariance matrix. Furthermore, if we knew how the uncertainties varied with each source-station path, then we could incorporate this information explicitly within the summations in Equations (2.4) and (2.5). Because these quantities are unknown, we account for the lack of information with the scale factor k/u_{L1} .

The constant k is the same for all events. The scaling by k/u_{L1} does not impact our best-fitting moment tensors M_0 , but it does impact our uncertainty analysis; we return to this topic in Section 2.8.2.

2.4 Estimation of uncertainties

Our uncertainty analysis is summarized in Figure 2.3 and described below. The notion of distance in the space of moment tensors is important. The (angular) distance between two moment tensors $X = (x_{ij})$ and $Y = (y_{ij})$ is defined in terms of their euclidean inner product:

$$\angle(X, Y) = \cos^{-1} \frac{X \cdot Y}{\|X\| \|Y\|}, \quad (2.8)$$

where $X \cdot Y = \sum_{i,j=1}^3 x_{ij} y_{ij}$ and where $\|X\| = \sqrt{X \cdot X}$.

The moment tensor for the global minimum of the misfit function is denoted by M_0 . We define $\omega(M)$ to be the distance from M_0 to M :

$$\omega(M) = \angle(M_0, M) \quad (2.9)$$

The angle $\omega(M)$ ranges from $\omega(M_0) = 0^\circ$ to $\omega(-M_0) = 180^\circ$.

Our moment tensor space is taken to be the set of all double couple moment tensors with fixed norm (i.e., fixed magnitude). We denote it by \mathbb{M} . The probability density p on \mathbb{M} is defined from the misfit function by (Tarantola, 2005)

$$p(M) = \frac{1}{a} e^{-\Phi(M)}, \quad a = \int_{\mathbb{M}} e^{-\Phi(M)} dM, \quad (2.10)$$

where, for us, $\Phi(M) = \Phi(\mathbf{m}(\kappa, \sigma, h, m_0, z_0))$ and $M = M(\kappa, \sigma, h)$. The probability that the true moment tensor for the earthquake is in a given subset \mathbb{A} of \mathbb{M} is the integral of p over \mathbb{A} :

$$P(\mathbb{A}) = \frac{\int_{\mathbb{A}} e^{-\Phi(M)} dM}{\int_{\mathbb{M}} e^{-\Phi(M)} dM} \quad (2.11)$$

We sometimes refer to the probability P as the posterior probability. The ‘prior’ probability would then be the homogeneous probability, that is, the fractional volume.

2.4.1 Quantification of uncertainty

Our confidence curve $\mathcal{P}(V)$ is from Tape & Tape (2016). The curve depends on a reference moment tensor, which will usually be the moment tensor M_0 with lowest misfit (or highest probability density). To define $\mathcal{P}(V)$, we first let $\mathbb{N}(\omega)$ be the neighborhood of M_0 consisting of moment tensors within angular radius ω of it. We then let $\hat{P}(\omega)$ and $\hat{V}(\omega)$ be the probability and fractional volume of $\mathbb{N}(\omega)$. Then $\mathcal{P}(V)$ is defined to be the probability that the true moment tensor for the earthquake lies in the neighborhood of M_0 that has volume V . That is, as illustrated in Figure 2.4,

$$\mathcal{P}(V) = \hat{P}(\omega) \text{ when } \hat{V}(\omega) = V \quad (2.12)$$

The confidence curve $\mathcal{P}(V)$ shows to what extent the probability in moment tensor space is concentrated around the tensor M_0 . For a high quality event, we would expect $\mathcal{P}(V)$ to be near unity for some small V ; equivalently, the curve $\mathcal{P}(V)$ should resemble the Greek letter Γ .

The average value of $\mathcal{P}(V)$ is

$$\mathcal{P}_{AV} = \int_0^1 \mathcal{P}(V) dV \quad (2.13)$$

The closer \mathcal{P}_{AV} is to unity, the better.

To calculate $\mathcal{P}(V)$ from Equation (2.12), we need both $\hat{V}(\omega)$ and $\hat{P}(\omega)$. To get $\hat{V}(\omega)$ (approximately), we can construct a sequence M_1, M_2, \dots, M_N of uniformly distributed moment tensors in \mathbb{M} ; according to Tape & Tape (2015), this can be done by choosing each of the corresponding κ_i, σ_i, h_i uniformly. Uniformity of the moment tensors M_i in \mathbb{M} means that subsets of \mathbb{M} having equal volumes should contain equal numbers of the M_i . Since $\hat{V}(\omega)$ is the fractional volume of $\mathbb{N}(\omega)$, then

$$\hat{V}(\omega) \approx \frac{n(\omega)}{N}, \quad (2.14)$$

where $n(\omega)$ is the number of the M_i with $\angle(M_0, M_i) \leq \omega$. Thus the fractional volume $\hat{V}(\omega)$ is found by counting the number of moment tensors M_i within the expanding neighborhood defined by ω .

Finding $\hat{P}(\omega)$ is only slightly more involved. Since $\hat{P}(\omega)$ is the probability of the set $\mathbb{N}(\omega)$, it is given by Equation (2.11) with $\mathbb{N}(\omega)$ in place of \mathbb{A} . Using M_1, M_2, \dots, M_N as before, we can replace the ratio of the integrals in Equation (2.11) with a ratio of sums:

$$\hat{P}(\omega) \approx \frac{\sum_{\angle(M_0, M_i) \leq \omega} e^{-\Phi(M_i)}}{\sum_{i=1}^N e^{-\Phi(M_i)}} \quad (2.15)$$

Notice that if the probability P were the homogeneous probability, for which the function p would be constant, then Equation (2.15) would reduce to Equation (2.14), and $\hat{P}(\omega)$ would coincide with $\hat{V}(\omega)$.

The fractional volume $\hat{V}(\omega)$ depends neither on M_0 nor on the earthquake. Its derivative $\hat{V}'(\omega)$ has a mesa-like shape. Values of $\hat{V}'(\omega)$ are tabulated in Appendix A of Tape & Tape (2016).

2.4.2 Samples of the posterior probability

There is an alternate perspective on the calculation of $\hat{P}(\omega)$. It begins with the generation of a large number of samples of the posterior probability. This is done by starting with a set of uniformly distributed moment tensors and applying the rejection method (von Neumann, 1951; Tarantola, 2005). The fraction of the resulting moment tensors M with $\angle(M_0, M) \leq \omega$ is then $\hat{P}(\omega)$. Since $\hat{P}(\omega)$ can be interpreted in terms of samples of the posterior probability, then so can $\mathcal{P}(V)$. For example, $\mathcal{P}(0.1) = 0.8$ means that 80% of the posterior samples are concentrated in only 10% of the volume around M_0 .

We use samples of the posterior to further characterize and visualize uncertainties associated with our moment tensor solutions. This is best seen in the context of a real example, described next.

2.5 Example waveform fits and uncertainty analyses

2.5.1 Full analysis for example event

We show the complete results for one of the 21 events in the Part I. The event occurred on 2009-04-07 just northwest of Anchorage, Alaska. Results for this event are shown in Figures 2.5–2.7. Results for the other 20 Part I events are in Silwal (2015).

A subset of waveform fits for our moment tensor inversion are shown in Figure 2.5; the full set of waveform fits are in Silwal (2015). The observed waveforms are plotted in black, and the synthetic waveforms are red. In this example the body waves are filtered 1.5–4.0 s and the surface

waves are filtered 16–40 s. The synthetic seismograms have been time-shifted by the time shift listed beneath each seismogram pair (Section 2.3.2).

For this event the value of the scaled misfit function (Eq. 2.6) at the global minimum is $\Phi(M_0) = 27.00$ and the probability density (Eq. 2.10) is $p(M_0) = 3.30$. (A related measure, variance reduction, is discussed in Section A.2.3.) The waveform fits in Figure 2.5 are good but not exceptional: the probability $p(M_0) = 3.30$ is exactly in the middle of the 21 events listed in Table 2.4.

Figure 2.6 shows the grid search over depth for this event. The depth increment in the grid search is 2 km. For each depth we search over the full space of orientations and magnitudes to obtain the best-fitting moment tensor. For this event, the best-fitting moment tensor has magnitude $M_w 4.5$ and occurs at depth 39 km; for comparison, the AEC catalog depth is 33 km, and the AEC moment tensor catalog depth is 45 km.

Figure 2.7 is a summary of the uncertainty analysis for the event. This analysis is performed after we have determined the best-fitting depth and magnitude for the event, and after we have evaluated the misfit function throughout the space of moment tensor orientations. Three cross sections of the strike-rake-dip ‘brick’ are shown in Figure 2.7b, with colors giving values of the misfit function Φ . Each section contains the solution M_0 (white star), which is at strike 205° , dip 49° , rake -85° . Also shown are contours of the angular distance ω from M_0 (Eq. 2.9). They do not correspond to distances in the brick and may at first look peculiar. For example, in the strike-rake cross section the two seemingly separate dark blue patches are close to each other when considered in moment tensor space, as shown by their small values of ω . In moment tensor space, the two patches are parts of a single small neighborhood of M_0 . The three light blue patches near the right edge of the strike-rake section are parts of a single small neighborhood of $-M_0$ when considered in moment tensor space. Incidentally, there are never any repeated moment tensors strictly inside the strike-rake-dip ‘brick’; repetitions can only occur on the boundary (Tape & Tape, 2012).

Our uncertainty analysis contains two parts. In the first part (Figure 2.7e-f and lower left of Figure 2.3) we calculate the confidence curve $\mathcal{P}(V)$ and, from it, the confidence parameter \mathcal{P}_{AV} : The fractional volume curve $\hat{V}(\omega)$ and the probability curve $\hat{P}(\omega)$ (blue and green, respectively, in Figure 2.7e) are calculated from Equations (2.14) and (2.15). Then $\mathcal{P}(V)$ (Figure 2.7f) is calculated from $\hat{V}(\omega)$ and $\hat{P}(\omega)$ using Equation (2.12). The area under the confidence curve gives the average value of $\mathcal{P}(V)$ (Eq. 2.13), which in this example is $\mathcal{P}_{AV} = 0.95$.

The second part of our uncertainty analysis uses samples of the posterior probability, which we generate using the rejection method. Two hundred posterior samples are plotted in the misfit-vs- ω plot in Figure 2.7c as green dots; they can be compared with the blue background, which is the corresponding plot for ‘prior’ samples, that is, for uniformly distributed moment tensors.

The curves $\hat{P}(\omega)$ and $\hat{P}'(\omega)$ (green in Figures 2.7d,e) can both be interpreted in terms of posterior samples: For a large set of posterior samples, $\hat{P}(\omega)$ is the fraction of them within angular distance ω of M_0 , and $\hat{P}'(\omega)d\omega$ is the fraction of them whose angular distance from M_0 is between ω and $\omega+d\omega$. A normalized histogram of values $\angle(M_0, M)$ for posterior samples M would therefore have the curve $\hat{P}'(\omega)$ as its upper boundary. In each of Figure 2.7c-e, the green color pertains to the posterior probability, and blue pertains to the prior probability, that is, to fractional volume.

A set of 2000 posterior samples is used to plot distributions of strike, dip, and rake in Figure 2.7g. There are two distributions (green and black), since there are two sets of strike-rake-dip angles for each moment tensor. The global minimum M_0 is plotted as a beachball in (h) along with P-T axes for 200 posterior samples. Beachballs for 20 posterior samples are shown in Figure 2.7i. Stähler & Sigloch (2014) offered a similar perspective by averaging posterior beachballs to get a ‘Bayesian beach ball’.

2.5.2 Additional earthquake examples

In Figures 2.8 and 2.9 we show condensed versions of the uncertainty analysis for two events that are outside our region of interest and not in our catalog. These examples suggest the range in quality of solutions that we might expect in Alaska, and they provide some reference for the values of \mathcal{P}_{AV} . The first event, a slab earthquake beneath the Alaska Range, represents one of the best possible data sets for a moment tensor inversion in Alaska. For this 2014 earthquake there is complete azimuthal coverage, with 76 stations used in the inversion. The $\mathcal{P}(V)$ curve resembles Γ , and $\mathcal{P}_{AV} = 0.98$ is nearly unity (good).

The second event, a crustal earthquake in northwestern Alaska (near Noatak), has poor data coverage, with almost all stations situated within a 60° azimuth of the source. For this event the curve $\mathcal{P}(V)$ is near the 45° line (Figure 2.9f), indicating that M_0 is not a reliable solution. This earthquake was well-recorded globally, and the GCMT solution indicated a normal-fault mechanism with $M_w 5.7$, whereas the (unreliable) solution in Figure 2.9 is a strike-slip mechanism with $M_w 5.2$. Smaller events, which, like the Noatak earthquake, are near the margins of the Alaska regional network, will not appear in global moment tensor catalogs. In such cases we will need to rely on assessing the confidence of our regional moment tensor solutions.

In Figures 2.10–2.11 we compare the moment tensor solution and waveform fits from our catalog with those from the AEC moment tensor catalog. The moment tensor in Figure 2.10 clearly provides better waveform fits, and it results in a larger variance reduction (39% versus 25%). Among the 21 Part I events, the event in Figure 2.10 had the largest difference ($\omega = 54^\circ$) from the solution in the AEC moment tensor catalog. A visual inspection of the beachballs in Figures 2.10–2.11 shows

that these solutions are quite different and would imply two different tectonic interpretations for this M_w 5.0 earthquake.

2.6 Moment tensor catalog, Part I (21 events)

There are 21 events in the AEC moment tensor catalog that occurred within our region during the time period of interest. For each of these events we perform a range of inversions with different subsets of data, in order to quantify the influence of various factors on the estimated model parameters and their uncertainties. The different types of inversions and comparisons are listed in Tables 2.1 and 2.2. We note that the 21 events are all high-quality events: $M_w \geq 4$ recorded by dozens of stations at regional distances. The inferences we make in the comparisons below may not generalize to the smaller Part II events.

Implicit in these comparisons is our choice of the ‘best’ moment tensor, which we take to be the one whose synthetic seismograms fit the most observed seismograms (this is explained in Section 2.8.3). This corresponds to the M_{111} case in Table 2.1. We can then measure the angular difference between another moment tensor to M_{111} .

We use Table 2.3 to explain the different inversions for the example event. The different subsets of data produce similar moment tensors, as indicated by $\omega \leq 26^\circ$ from M_{111} . However two cases (M_{110} and M_{101}) have low values of $p(M_0)$ and \mathcal{P}_{AV} , and we would not consider these to be reliable solutions. The table also shows the distance of the two AEC catalog moment tensors, M_{AEC} and M_{fm} , from M_{111} . Table 2.3 is reproduced for the other Part I catalog events in Table A.3. The information in Table A.3 is presented in abridged form in Table 2.5. We will refer to these results while discussing the six comparisons listed in Table 2.2.

2.6.1 The effect of using bad stations

Manual review and selection of waveforms can be an extremely time-consuming part of seismological studies. We expect there to be differences between data and synthetics. Some differences are due to errors in representing the earthquake source or Earth structure, while other differences are due to inherent errors in the observed waveforms for a particular earthquake and a particular station at a particular time. We generally do not know what the estimated errors are in the observed waveforms, but we have some idea of errors in our synthetic seismograms due to errors in our assumed Earth model. For example, in our region the presence of Cook Inlet basin produces larger amplitudes and larger time shifts for source-station paths that interact with the basin. Therefore some systematic amplitude anomalies may be expected.

Our motivation for using the L1 misfit function (Eq. 2.6), rather than the L2 misfit function, was to reduce the effort of manually reviewing waveform comparisons (Maceira et al., 2000; Aster

et al., 2013; Tarantola, 2005). In Figure 2.12 we show inversion results for 21 events for four cases: L1 with good waveforms, L1 with all waveforms, L2 with good waveforms, L2 with all waveforms. We find that: (1) the L2 norm fails dramatically for some events (red beachballs), (2) the L1 norm gives stable results even when bad stations are not thrown out. Except for Figure 2.12, all the results presented in this study (Tables 2.4 and A.5) are based on using the L1 norm in the misfit function (Eq. 2.6).

2.6.2 The effect of ignoring body waves

The effect of ignoring body waves can be seen by comparing the columns of M_{111} with those of M_{011} in Table 2.5. The angular differences range from 0° (3 events) to $\geq 50^\circ$ (2 events). The two anomalous events here are both $M_w \geq 5.0$; one is a slab event to the west with decent station coverage, the other is a crustal event to the southwest with relatively poor station coverage. A further analysis could provide insights into the scenarios where using body waves is particularly important for obtaining the correct moment tensor solution.

2.6.3 The effect of using fewer stations

The effect of using fewer stations, while using both body waves and surface waves, can be seen by comparing case M_{111} with M_{112} . The comparison shows that there are significant differences (5 events with $\omega \geq 50^\circ$) in the moment tensor solution when we use fewer stations. In practice it is not easy to determine which station will ‘pull’ the solution toward the true solution. Our tabulation implies that using as many stations as possible is desirable. It is important to have good azimuthal coverage of stations, but we did not systematically investigate this.

2.6.4 Improvement over existing catalogs

We can also compare the angular difference from our preferred solution (M_{111}) to the moment tensors in the two AEC catalogs (M_{AEC} and M_{fm}) (Table 2.5). For the 21 Part I events the differences with the AEC moment tensor catalog are generally small ($\omega < 30^\circ$), with one exception (20071003140612444: $\omega = 54^\circ$) highlighted in Figures 2.10–2.11. We discuss catalog comparisons in Section 2.8.4.

2.6.5 The effect of using either body waves or surfaces waves

From Figure 2.13 we see that moment tensor solutions obtained using only surface waves (M_{011}) are consistently better than solutions obtain using only body waves (M_{101}). Furthermore the confidence measure \mathcal{P}_{AV} is higher for the surface-wave-only solutions (Table A.3).

2.6.6 Additional comparisons

When considering only surface waves, there is a small effect of adding more stations. This can be seen in Figure 2.13 for the columns M_{012} (few stations) and M_{011} (more stations). This possibly justifies the practice of using a small (<10) subset of stations for surface-wave-only moment tensor inversion (e.g., Dreger et al., 2000; Ratchkovski & Hansen, 2002; Clinton et al., 2006).

For completeness we also compare the effect of using a different inversion code with same the seismograms. This is achieved by performing a CAP inversion (M_{012}) using the same stations and same bandpass filter as those used in the AEC moment tensor catalog (M_{AEC}). Any differences would arise from the minor differences (e.g., how time windows are cut, how stations are weighted by distance) between the CAP algorithm that we use and the TDMT algorithm that is used by AEC. The differences shown in the M_{012} and M_{AEC} columns in Figure 2.13 are small, as we would hope. Note that much of the visual difference arises from comparing a double couple moment tensor (M_{012}) to a deviatoric but non-double-couple moment tensor.

2.7 Moment tensor catalog, Part II (85 events)

Part I of our moment tensor catalog contains 21 events. For each event we performed a grid search over depth, an uncertainty analysis, and a series of comparison inversions (Section 2.6). Table 2.4 lists the moment tensor parameters, and Silwal (2015) contains figures of waveform fits, depth grid searches, and uncertainty analyses.

We performed moment tensor inversions for an additional 85 events that make up Part II of our catalog. These events were the largest events within the AEC first-motion catalog (but not within the AEC moment tensor catalog) that occurred during the time period of interest (Section 2.3). For these smaller events we decided to use a limited number of first-motion polarity measurements to help guide the inversion by excluding moment tensors that fail to match the polarities. The moment tensor parameters are listed in Table A.5, and waveform fits are provided in Silwal (2015). In principle it should be possible to perform the uncertainty analyses for a misfit function that uses both waveform differences and first-motion polarities. It would be interesting to see the \mathcal{P}_{AV} curves for earthquakes with worse data than the high-quality events in Part I. The example in Figure 2.9 suggests that the uncertainty analysis could provide insights into local minima in the misfit function that may occur.

In the supporting materials we provide waveform fits for two Part II catalog events (Figures A.5–A.7 and Figures A.8–A.10). These examples show the challenges associated with moment tensor inversions for events with lower signal-to-noise ratios (like smaller events): the waveform fits for two very different moment tensors appear to be qualitatively comparably good. An un-

certainty analysis would benefit these events, as would a detailed investigation of the inclusion of first-motion polarities along with the waveforms.

2.8 Discussion

2.8.1 The confidence curve $\mathcal{P}(V)$

We provide several examples to elucidate the confidence curve $\mathcal{P}(V)$. In all of them we are dealing with double couple moment tensors. The normalized eigenvalues are therefore $\hat{\Lambda} = (1, 0, -1)/\sqrt{2}$, and the fractional volume curve $\hat{V}(\omega)$ takes the shape of a mesa. (The curve will change for full moment tensors or for a different choice of $\hat{\Lambda}$ (Tape & Tape, 2016).)

The calculation of $\mathcal{P}(V)$ is shown in Figure 2.4. While the curve itself is our indicator of confidence, we also rely on two scalar quantities derived from it. The first is the average \mathcal{P}_{AV} of $\mathcal{P}(V)$; this is the area under $\mathcal{P}(V)$. The second is the slope of $\mathcal{P}(V)$ at the origin, which is proportional to the probability density at M_0 . Traditionally, an estimated moment tensor M would be considered good if the curve $\mathcal{P}(V)$ were steep at the origin. Our philosophy in this paper is that we need to look at the rest of the curve $\mathcal{P}(V)$ as well; it should be Γ -shaped if M is truly reliable.

We present three examples of $\mathcal{P}(V)$ curves in Figures 2.7, 2.8, and 2.9. Two are for high-quality solutions, where the curves resemble a Γ shape, while one is a low-quality solution, where the curve is close to the 45° line, $\mathcal{P}(V) = V$.

Figure 2.14 shows \mathcal{P}_{AV} versus $p(M_0)$ for our 21 events and for all the cases listed in Table 2.1. The modest correlation seen in the figure suggests that high confidence may reasonably be expected for high $p(M_0)$. In geometrical terms, if $\mathcal{P}(V)$ starts at the origin with a high slope (high $p(M_0)$), then there is a good chance that $\mathcal{P}(V)$ will result in a Γ shape with its area near 1. Yet it is no guarantee, as illustrated by the Noatak event (Figure 2.9). But the main message of Figure 2.14 is that for a given value of the misfit function at the global minimum $\Phi(M_0)$ —or, more appropriately, the value of the probability density $p(M_0)$ —we can expect a wide range of values in \mathcal{P}_{AV} . As we might have hoped in our endeavor, \mathcal{P}_{AV} provides useful information about the probability density that is not available from just the information at M_0 .

Thus far we have chosen to calculate $\mathcal{P}(V)$ for the global minimum of misfit (or highest probability density) M_0 . But we can calculate $\mathcal{P}(V)$ for any reference tensor M , and in some cases it may be useful to do so. In the supporting materials we show the uncertainty analysis for our example event when choosing the reference moment tensor to be the maximum misfit solution M_x (Figure A.17) and then again when it is the opposite $-M_0$ of the minimum misfit solution (Figure A.18). For M_x the slope of $\mathcal{P}(V)$ at the origin is near zero, as expected, yet the average confidence is $\mathcal{P}_{AV} = 0.66$, which, although it is not good, it is not as bad as one might expect.

One might have hoped that the worst fitting point would also have low confidence (as hinted by Figure 2.14), but we can understand why this is not the case. If we examine cross sections of the misfit function (Figure A.18b), we can see that, as expected, the misfit goes down as we look in any direction away from the moment tensor with maximum misfit. But $\angle(M_x, M_0) = 74^\circ$, so M_x ‘sees’ the region of high probability around M_0 at an angular distance of only about 74° . The curve $\mathcal{P}(V)$ therefore rises steeply for $V \approx \hat{V}(74^\circ) = 0.308$.

The confidence curve for $-M_0$ is always a 180° rotation of the confidence curve for M_0 (Tape & Tape, 2016). Since in this example the confidence curve for M_0 resembles a Γ (Figure 2.7f), then the confidence curve for $-M_0$ resembles a backwards L. And since \mathcal{P}_{AV} for M_0 was 0.95, \mathcal{P}_{AV} for $-M_0$ is only 0.05. The reason for this low value is that as we move away from $-M_0$ in any direction in moment tensor space, we do not encounter the concentrated probability near M_0 until we are nearly 180° from $-M_0$, at which point the $\mathcal{P}(V)$ curve shoots up toward 1 to make the backwards L.

2.8.2 The misfit function scale factor k

The scale factor k (Eq. 2.6) in the misfit function Φ is arbitrary, and it will systematically alter $\mathcal{P}(V)$. If k is near zero, then the probability density will be nearly constant, $\mathcal{P}(V)$ will be nearly the 45° line, and the moment tensor orientations (depicted in Figure 2.7h-i) will be nearly random. As k increases, $\mathcal{P}(V)$ will sharpen toward a Γ shape, \mathcal{P}_{AV} will correspondingly increase (assuming that $\mathcal{P}(V)$ was at least slightly favorable to begin with), and the moment tensor orientations will become more consistent. This is a reminder that one can only meaningfully compare $\mathcal{P}(V)$ (and \mathcal{P}_{AV}) for different earthquakes when the misfit function is the same. In our study we fix k to be the same for all events, and then our results give a relative measure of confidence among all events in the catalog. A similar qualification faces any moment tensor catalog or any study that attempts to compare results from different catalogs (using different misfit functions).

2.8.3 Finding the ‘best’ moment tensor solution

We have discussed three factors in determining the quality of a moment tensor solution:

1. the ‘amount’ of the wavefield that is fit within the moment tensor inversion
2. the confidence curve $\mathcal{P}(V)$ and its average \mathcal{P}_{AV}
3. the difference between observed and synthetic waveforms

The normalized waveform difference is represented by probability density $p(M_0)$ and geometrically depicted by the slope $\mathcal{P}'(0)$ of the confidence curve for M_0 . Our comparison tests in Sec-

tion 2.6, tabulated in Table A.4, show how $p(M_0)$ tends to decrease as we include more stations, more seismic phases (like body waves), and shorter-period waveforms in the inversion (see also Zahradník & Custódio (2012)). Yet what we want is to fit more of the seismic wavefield, and we cannot simply assume that the moment tensor with the largest $p(M_0)$ is the better solution. Our guide for establishing our preferred solution M_{111} is to fit the most waveforms, rather than just to achieve the lowest waveform difference (highest $p(M_0)$). In principle it should be possible to adapt the misfit function to up-weight the amount of time of seismograms used in waveform fitting.

The confidence curve provides insights into the concentration of the posterior probability near M_0 . In the case of the Noatak earthquake (Figure 2.9), the steep slope of $\mathcal{P}(V)$ at zero implies a high probability density (low misfit) at M_0 . Yet the confidence curve reveals that M_0 is not a reliable solution.

2.8.4 Comparison of catalogs

The availability of two different catalogs from the Alaska Earthquake Center allows us to make comparisons with the solutions from our catalog. At the simplest level, we can compare the angular differences among moment tensors for the same event in each catalog. Figure 2.15a shows a comparison between the AEC moment tensor catalog (M_{AEC}) and the AEC first-motion catalog (M_{fm}) for the 21 Part I events in our study. These can be seen in Table 2.5 and in Figure 2.13 (last two columns), and it is clear that in some cases there are notable differences. Keep in mind that the techniques for estimating these moment tensors are very different: one technique uses long-period ($T > 16$ s for $M_w > 4$) surface waves, while the other technique uses first-motion P polarities from raw waveforms.

A direct comparison between our catalog and the AEC moment tensor catalog is shown in Figure 2.15b for 21 events. A direct comparison between our catalog and the AEC first-motion catalog is shown in Figure 2.15c for 85 events. We identify a small discrepancy in magnitudes between our moment tensors and the magnitudes in the AEC catalog (Figure 2.15d); the average difference 0.2 agrees with Ruppert & Hansen (2010). Figure A.19 shows these different moment tensor catalogs in map view.

We designed this study to provide more than just angular measures between moment tensors in two catalogs. Some of our tests in Section 2.6 allow us to quantify the influence of different choices that are made within a particular approach. To perform one-to-one comparisons, we evaluate the AEC moment tensor (M_{AEC}) using the same misfit function as was used to obtain our solution (M_{CAP}). By design, the misfit $\Phi(M_{AEC})$ will always be greater than $\Phi(M_{CAP})$, since M_{AEC} is a point within the global grid search. Our assumption in Section 2.8.3 is that M_{CAP} is the best

solution because it fits the most of the seismic wavefield; therefore M_{AEC} will be a worse solution, and we can quantify this difference.

2.9 Summary

We present a catalog of 106 moment tensors in southern Alaska. In order to isolate the impact of decisions made in moment tensor algorithms—stations, bandpass filter, seismic phases, weights, norm in misfit function—we perform a series of tests in Section 2.6. Our main assumption is that the ‘best’ solution (Section 2.8.3) is the one that fits the most of the seismic wavefield, in terms of number of stations, number of seismic phases, and broadest range of periods (notably shortest periods). We compare 21 of our moment tensor solutions with those in the Alaska Earthquake Center (AEC) moment tensor catalog, and we compare 85 with the AEC first-motion catalog. We have an inherent advantage over the AEC catalogs in that we use data from the MOOS deployment. We nevertheless can test the influence of choices within the moment tensor inversion by using the same stations as those used in the AEC inversion. Our comparisons are based on the matrix angle between moment tensors; for example $\omega = \angle(M_{CAP}, M_{AEC})$ is the angle between our preferred solution derived from the CAP (Zhu & Helmberger, 1996) and the AEC moment tensor solution derived from TDMT (Dreger & Woods, 2002; Ratchkovski & Hansen, 2002).

When comparing two moment tensors, ‘close enough’ depends strongly on how one intends to use the information. If one is interested in understanding the tectonics of a region, then it may be enough to say, for example, that an earthquake is a normal-fault mechanism. In that case $\omega < 50^\circ$ may be acceptable. If, however, one is performing a tomographic inversion based on amplitude and traveltimes differences, or if one is interested in calculating ground motions from a 3D wavefield simulation, then it is important to have the best possible moment tensor; this will minimize the propagation of errors from the moment tensor to the seismic velocity structure, or to the ground motion predictions. For these purposes one might want the moment tensor to be $\omega < 20^\circ$ of the true solution. Our motivation for this study is to use this catalog for a tomographic inversion using wavefield simulations and adjoint methods (e.g., Tape et al., 2009; Lee et al., 2014). Our improved moment tensor catalog will allow us to more confidently associate differences in traveltimes and amplitudes with structural differences within a 3D reference Earth model. An additional consideration in such studies is whether to perform additional moment tensor inversions using the 3D reference model (Liu et al., 2004; Chen et al., 2005; Covellone & Savage, 2012; Zhu & Zhou, 2016).

Three summary points are as follows:

1. We present an improved catalog of moment tensors in southern Alaska. We use both body waves and surface waves from as many broadband stations as possible (both permanent and

temporary). Examples in Section 2.6 show that using more stations and using body waves, in addition to surface waves, can substantially improve the moment tensor solutions. For 33 (out of 106) events, our moment tensor differed from the AEC first-motion solution by $\omega \geq 50^\circ$ (Figure 2.15).

2. We demonstrate that using an L1 norm in the misfit function will provide more stable moment tensor solutions (Section 2.3.4 and Section 2.6.1). This should allow for less manual (or automatic) thresholding of bad stations, which could be valuable in operational settings. The modification to the misfit function in the code is trivial.
3. We introduce an approach for quantifying and visualizing the uncertainty in a double couple moment tensor solution (Section 2.4 and Figure 2.7). The confidence curve $\mathcal{P}(V)$ in Figure 2.7f is shaped like a Γ for a high-quality event, and it is close to the 45° line for a low-quality event. The slope of $\mathcal{P}(V)$ at the origin is related to the probability density at the best-fitting moment tensor, and the area under the curve $\mathcal{P}(V)$ provides the average confidence (Tape & Tape, 2016). Results for 21 events are presented in Silwal (2015) and summarized in Table 2.4.

2.10 Acknowledgments

We thank Geoff Abers and Doug Christensen for collecting the seismic waveform data from the MOOS project (Christensen et al., 2008; Li et al., 2013). Seismic waveforms were obtained from the Alaska Earthquake Center, and they are also available from the IRIS Data Management Center. This project was supported by the Alaska Earthquake Center (V. Silwal) and by a grant from the National Science Foundation (EAR 1251971). We benefitted from discussions with Celso Alvizuri, Natalia Ruppert, Michael West, and Walt Tape. We thank two anonymous reviewers for their constructive feedback.

Table 2.1: Moment tensor labels used in the study to distinguish among inversions using different subsets of waveform data. The three indices in the label M_{abc} represent the choice of body waves ($a = 0, 1$), the choice of surface waves ($b = 0, 1$), and the choice of stations ($c = 0, 1, 2$). The index c covers three cases: $c = 0$ is for all available stations, $c = 1$ is a subset of stations that pass our waveform selection criteria, and $c = 2$ is a smaller subset of stations used for the inversions in the AEC moment tensor catalog. See Section 2.6 for details.

Label	Description
M_{111}	using both body and surface waves at selected stations
M_{011}	using only surface waves at selected stations
M_{101}	using only body waves at selected stations
M_{112}	using both body and surface waves at stations used in AEC moment tensor catalog
M_{012}	using only surface waves at stations used in AEC moment tensor catalog
M_{110}	using both body and surface waves at all stations
M_{AEC}	AEC moment tensor catalog (should be close to M_{012})
M_{fm}	AEC first-motion catalog

Table 2.2: Examples of comparisons between different sets of moment tensors listed in Table 2.3. See Section 2.6 for details.

misfit function	Analysis
M_{111} vs M_{110}	effect of using bad stations (for testing multiple norms)
M_{111} vs M_{011}	effect of ignoring body waves
M_{111} vs M_{112}	effect of using fewer stations (both body and surface waves)
M_{111} vs M_{AEC}	improvement over existing catalog
M_{101} vs M_{011}	effect of using either body waves or surface waves
M_{012} vs M_{011}	effect of adding more stations (only surface waves)
M_{012} vs M_{AEC}	effect of using a different inversion method with the same seismograms
M_{AEC} vs M_{fm}	comparison between two catalogs (AEC moment tensor and AEC first motion)

Table 2.3: Summary of inversions for the example event (20090407201255351) for the L1 misfit function using different subsets of data. $\omega = \angle(M_{111}, M)$, where M is a different moment tensor solution. Previously published catalog results are included as M_{AEC} and M_{fm} ; for these events, no $p(M_0)$ and \mathcal{P}_{AV} are listed, since we did not perform the inversion. Table A.3 contains similar results for the other Part I events in the catalog. See Figure 2.7 (M_{111}) and Figures A.11–A.15 (M_{110} , M_{011} , M_{101} , M_{112} , M_{012}) for the uncertainty analysis for each case M_{abc} .

misfit function (see Table 2.1)		depth km	M_w	ω deg	$p(M_0)$	\mathcal{P}_{AV}
L1	M_{111}	39	4.5	–	3.30	0.95
L1	M_{110}	39	4.4	26	0.04	0.52
L1	M_{011}	41	4.5	9	9.26	0.98
L1	M_{101}	39	4.6	21	2.26	0.77
L1	M_{112}	39	4.5	10	2.27	0.95
L1	M_{012}	47	4.6	10	10.44	0.98
L1	M_{AEC}	45	4.6	17	–	–
L1	M_{fm}	33	4.5	32	–	–

Table 2.4: Moment tensor catalog, Part I (21 out of 106 events), generated by CAP using body waves and surface waves. The depth is obtained from grid search and is based on variations in the amplitudes of waveforms (e.g., Figure 2.6). The AEC catalog depth, derived from P and S travel times, is listed in parentheses. The last three columns are the maximum probability density ($p(M_0)$), the confidence parameter (\mathcal{P}_{AV}), and the number of stations used in the inversion (N_s). See Table A.5 for the complete catalog of 106 events. Additional inversions with these events are tabulated in Table 2.5.

label	eid	lat	lon	strike	dip	rake	M_w	depth, km	$p(M_0)$	\mathcal{P}_{AV}	N_s
1	20070911234634153	61.53	-151.53	80	40	80	4.4	94 (100.9)	3.19	0.89	37
2	20070919112226549	61.38	-146.11	225	62	-70	4.5	47 (30.8)	2.35	0.92	42
3	20071003140612444	58.28	-151.29	45	83	60	5.0	32 (45.5)	4.38	0.88	45
4	20071010180326301	59.96	-147.41	40	87	5	4.2	27 (11.8)	1.56	0.90	44
5	20071128235703849	61.91	-151.13	35	83	65	4.9	69 (69.6)	7.65	0.97	48
6	20080314093821771	61.07	-152.64	265	28	90	5.1	139 (143.7)	8.28	0.94	38
7	20080327230745201	59.01	-152.17	240	90	-25	5.1	65 (68.5)	1.66	0.90	28
8	20080828231418631	62.12	-149.60	220	76	-30	4.2	54 (43.0)	4.36	0.95	33
9	20080918194353069	59.50	-152.79	75	58	65	4.6	81 (90.2)	0.88	0.78	29
10	20081228071310738	62.35	-151.05	90	54	50	4.6	82 (89.3)	4.28	0.95	21
11	20090124180950811	59.43	-152.89	70	76	55	5.8	105 (97.9)	1.33	0.85	35
12	20090215193500098	61.60	-146.33	80	40	-55	4.5	43 (37.2)	1.80	0.93	59
13	20090223000427175	58.92	-153.63	60	80	75	4.9	81 (87.8)	11.76	0.94	18
14	20090317011333066	60.24	-152.15	60	58	60	4.3	96 (90.1)	0.75	0.78	13
15	20090407201255351	61.45	-149.74	205	50	-85	4.5	39 (33.0)	3.30	0.95	25
16	20090414171427415	60.16	-153.06	145	40	75	4.3	111 (117.8)	0.89	0.83	29
17	20090430045457938	58.99	-151.31	40	28	-45	4.8	40 (52.7)	5.52	0.89	41
18	20090524094004552	59.78	-153.25	70	54	40	4.6	109 (125.5)	2.02	0.89	32
19	20090622192805162	61.94	-150.70	25	50	-20	5.4	62 (64.6)	4.30	0.94	57
20	20090626164820729	61.91	-150.64	25	35	-25	4.2	56 (59.5)	7.72	0.95	27
21	20090730223910267	59.93	-151.09	220	20	15	4.6	60 (44.1)	3.62	0.94	23
Fig. 2.8	20140416202423770	62.89	-149.91	110	69	30	4.9	72 (82.9)	1.77	0.98	76
Fig. 2.9	20140418184418152	63.93	-145.77	340	86	0	5.2	20* (20)	12.29	0.61	54

* For the Noatak event the inversion was performed at the AEC catalog depth.

Table 2.5: Angular difference ω between our preferred solution (M_{111}) and solutions obtained using different waveform datasets. The column labels are described in Table 2.1. See Figure 2.13 for the corresponding beachballs. See Table A.3 for details, including values of $p(M_0)$ and \mathcal{P}_{AV} .

Event		$\omega = \angle(M_{111}, M)$							
		M_{111}	M_{110}	M_{011}	M_{101}	M_{112}	M_{012}	M_{AEC}	M_{fm}
20070911234634153	(1)	–	0	16	0	37	15	21	12
20070919112226549	(2)	–	22	18	23	20	31	34	21
20071003140612444	(3)	–	13	62	119	55	61	54	67
20071010180326301	(4)	–	10	7	53	41	41	19	20
20071128235703849	(5)	–	29	0	12	16	0	4	77
20080314093821771	(6)	–	10	50	0	53	43	32	67
20080327230745201	(7)	–	0	8	68	19	8	11	19
20080828231418631	(8)	–	0	10	14	19	19	14	13
20080918194353069	(9)	–	19	11	56	151	10	8	27
20081228071310738	(10)	–	18	26	17	21	26	25	27
20090124180950811	(11)	–	10	10	52	20	10	30	29
20090215193500098	(12)	–	0	12	36	17	17	25	27
20090223000427175	(13)	–	10	0	110	0	10	26	25
20090317011333066	(14)	–	31	0	59	55	13	17	19
20090407201255351	(15)	–	26	9	21	10	10	17	32
20090414171427415	(16)	–	10	27	125	50	20	24	21
20090430045457938	(17)	–	0	10	118	28	16	25	65
20090524094004552	(18)	–	13	24	0	43	24	29	27
20090622192805162	(19)	–	0	10	24	10	10	13	13
20090626164820729	(20)	–	13	19	10	14	30	25	20
20090730223910267	(21)	–	28	10	29	36	30	17	28

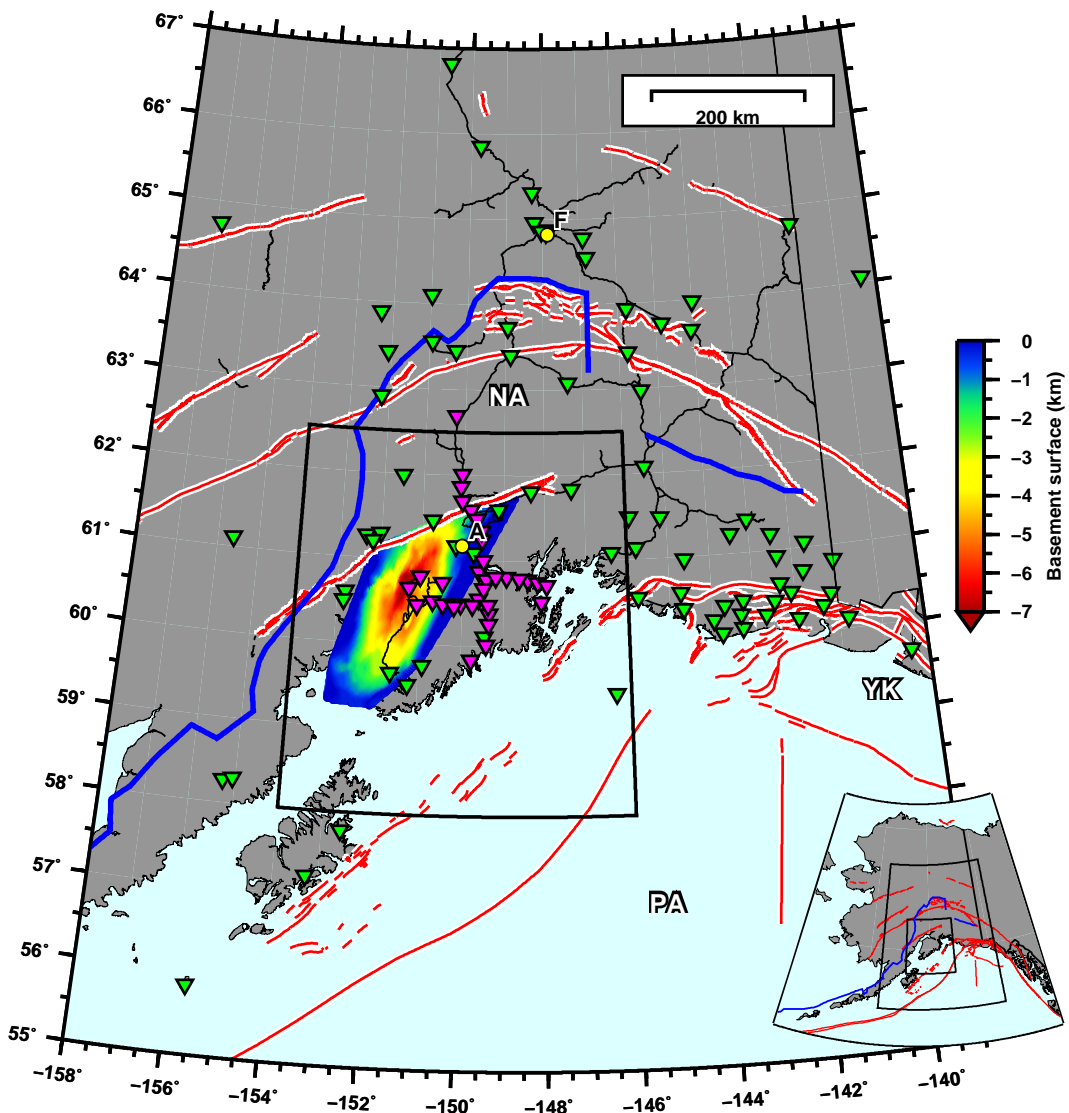


Figure 2.1: Broadband station coverage for the time period of this study, 2007-8-15 to 2009-8-15. The permanent stations in the regional network are plotted green; the MOOS stations are plotted magenta. Stations within 500 km of each epicenter were used for computing the moment tensor solution. The Tertiary basement surface of Cook Inlet basin is color-coded for depth (Shellenbaum et al., 2010). Labels: A = Anchorage, F = Fairbanks, PA = Pacific plate, NA = North American plate, YK = Yakutat block. See Figure A.1 for the seismicity distribution in the region. See Figure 2.2 for the moment tensor beachballs inside the study region (inner box).

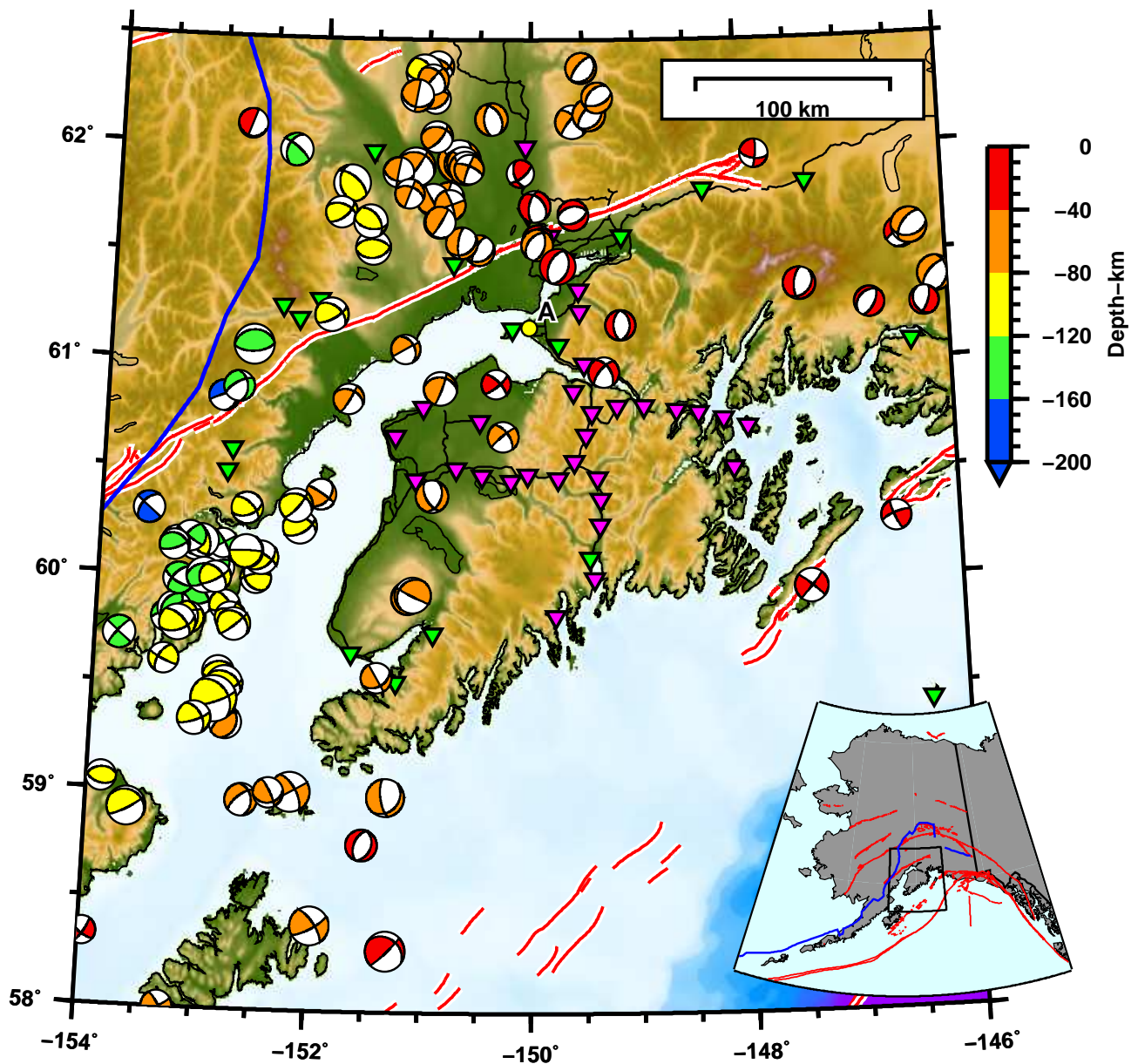


Figure 2.2: Seismotectonic setting of south-central Alaska showing the 106 moment tensor solutions obtained in this study. Our catalog contains all earthquakes in this region from 2007-8-15 to 2009-8-15 with $M_w \geq 3.5$ and for which an AEC first-motion solution was available. Inverted green triangles are the permanent stations in Alaska during this time period, and magenta are the temporary stations deployed during the MOOS array (Christensen et al., 2008; Li et al., 2013). The heavy blue line marks the lateral extent of slab seismicity and the red lines delineate the active faults (Koehler et al., 2012).

A. Evaluate misfit function between observed and synthetic seismograms

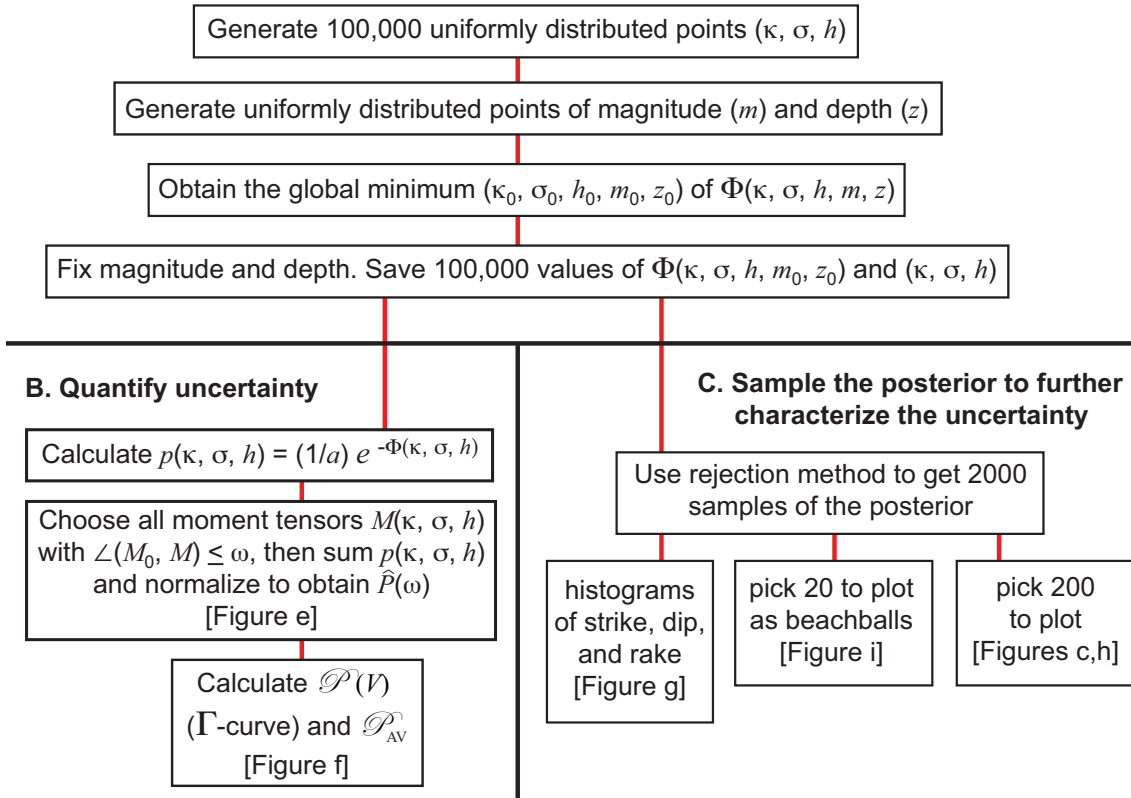


Figure 2.3: Workflow for our uncertainty analysis, such as in Figure 2.7. The model parameters for the moment tensor inversion are the strike angle κ , the rake (or slip) angle σ , cosine of the dip angle ($h = \cos \theta$), the magnitude (m), and depth z , all with ranges as specified in Section 2.3.3. The uncertainty analysis (parts B and C) begins when we have determined the magnitude and depth of the moment tensor M_0 at the global minimum of the misfit function.

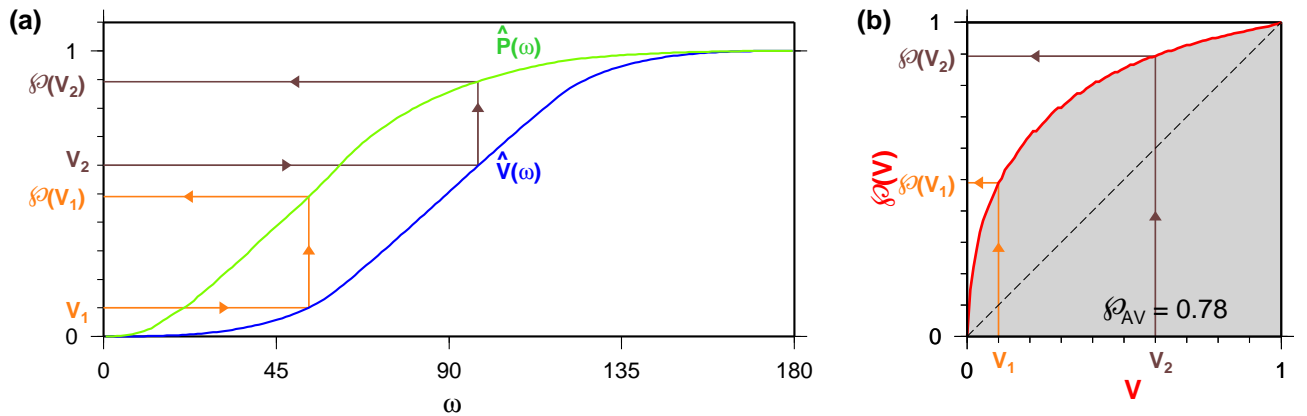
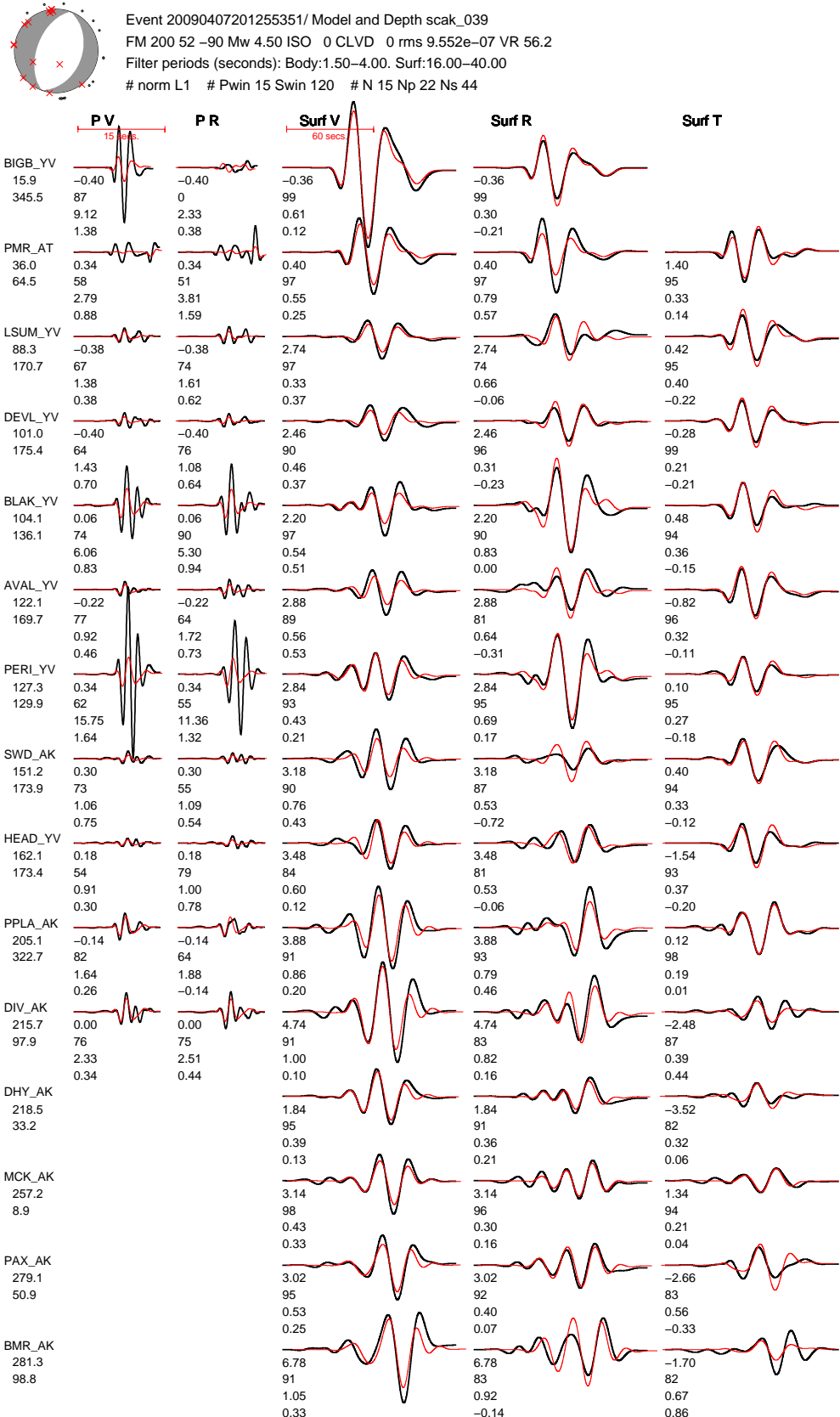


Figure 2.4: Construction of the confidence curve $\mathcal{P}(V)$ for a moment tensor M_0 . (a) The fractional volume and probability curves $\hat{V}(\omega)$ and $\hat{P}(\omega)$. The value $\mathcal{P}(V)$ is defined in terms of $\hat{V}(\omega)$ and $\hat{P}(\omega)$ by requiring that $\mathcal{P}(V) = \hat{P}(\omega)$ when $\hat{V}(\omega) = V$, as indicated by the arrows. The number $\hat{V}(\omega)$ is the fractional volume of the neighborhood $\mathbb{N}_{M_0}(\omega)$ of moment tensors within angular distance ω of M_0 , and $\hat{P}(\omega)$ is likewise the probability of $\mathbb{N}_{M_0}(\omega)$. Hence $\mathcal{P}(V)$ is the probability that the true moment tensor for the earthquake lie in the neighborhood of M_0 that has volume V ; large $\mathcal{P}(V)$ for small V is desirable. (b) The confidence curve $\mathcal{P}(V)$. The orange and brown trajectories correspond to those in (a). The area under the curve is our confidence parameter \mathcal{P}_{AV} . The 45° line (dashed) would be $\mathcal{P}(V)$ if the probability had been homogeneous.

Figure 2.5: [FOLLOWING PAGE] Moment tensor solution and waveform comparisons for the example event in this study. Each column is a different section of the three-component waveform: PV = vertical component P wave, PR = radial component P wave, SurfV = vertical component Rayleigh wave, SurfR = radial component Rayleigh wave, SurfT = transverse component Love wave. The stations are ordered by increasing epicentral distance from the top row. The observed waveforms are plotted in black, the synthetic waveforms are plotted in red. The body waves are filtered 1.5–4.0 s, and the surface waves are filtered 16–40 s. The numbers below each station name are the station epicentral distance (top) and station azimuth (bottom). The four numbers below each pair of waveforms are, from top to bottom, (1) the cross-correlation time shift $\Delta T = T_{\text{obs}} - T_{\text{syn}}$ required for matching the synthetics $s(t)$ with the data $u(t)$ (a positive time-shift means that the synthetics arrive earlier than the data); (2) the maximum cross-correlation percentage between $u(t)$ and $s(t - \Delta T)$; (3) the percentage of the total misfit; and (4) the amplitude ratio $\ln(A_{\text{obs}}/A_{\text{syn}})$ in each time window. The four header lines are described in Silwal (2015).



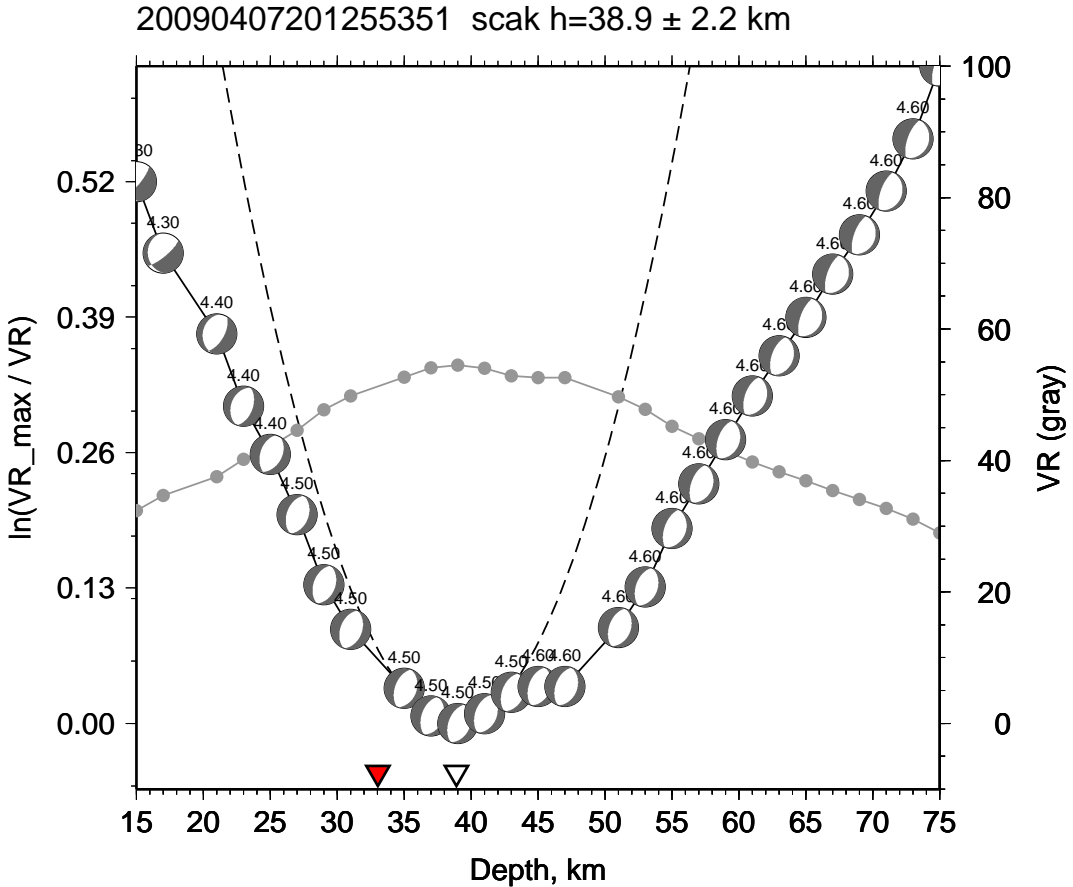
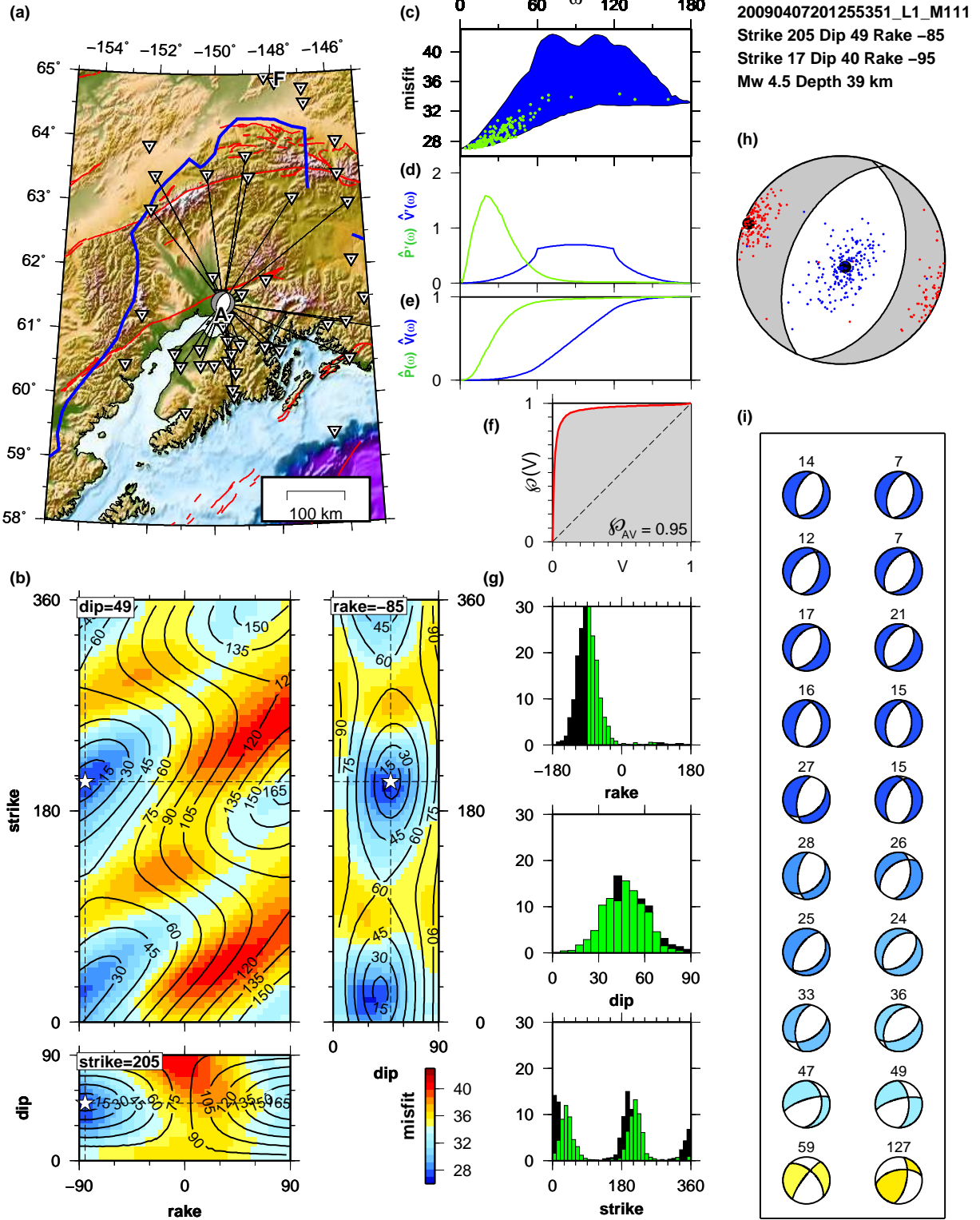


Figure 2.6: Grid search for the best-fitting depth for the event in Figure 2.7. The red arrow marks the AEC catalog depth, and the white arrow marks the depth obtained from our moment tensor inversion. The gray line with solid circles denotes the variance reduction (VR) for the moment tensor solution obtained at that particular depth (scale at right). The best solution occurs at the maximum in variance reduction $VR_{\max} = 56.2$. The beachballs are plotted at the value of $\ln(VR_{\max}/VR)$, which gives the variance reduction relative to the maximum (scale at left). Note that the orientation and magnitude are free to change for each depth; for this event we see that deeper depths produce larger magnitude estimates (4.6 vs 4.4), as we would expect. The black dashed line is the best-fitting parabola, which is used for estimating the uncertainty in depth; here the best-fitting depth is 39 ± 2 km. The long tick marks on the x -axis mark the layer boundaries in the 1D model (Table A.1) used in the moment tensor inversions.

Figure 2.7: [FOLLOWING PAGE] Summary of the moment tensor solution M_0 for an earthquake near Anchorage. The moment tensor M_0 is the moment tensor with minimum misfit. The set of moment tensors under consideration is the set of double couples. (a) Map showing the earthquake source and the station coverage. The stations used in calculating the misfit are identified with ray paths. (b) Colored map of misfit $\Phi(M)$, shown on sections of strike-rake-dip space that pass through the strike-rake-dip point for M_0 (white star). The black curves are not contours of misfit Φ but rather contours of ω , where $\omega(M) = \angle(M_0, M)$ is the angular distance from M_0 to M . (c) A two-dimensional summary of the three-dimensional plot of misfit in (b). The blue region consists of all pairs $(\omega(M), \Phi(M))$. The green dots are pairs $(\omega(M), \Phi(M))$ for 200 posterior samples. (d) The curves $\hat{P}'(\omega)$ and $\hat{V}'(\omega)$. (e) The curves $\hat{V}(\omega)$ and $\hat{P}(\omega)$; they are used to construct the confidence curve $\mathcal{P}(V)$ in (f), as explained in Figure 2.4. (f) The confidence curve $\mathcal{P}(V)$ for M_0 . The more the curve resembles the shape of a capital gamma (Γ), the better. The shaded area is the average confidence \mathcal{P}_{AV} . (g) Strike, rake, and dip for a set of 2000 posterior samples. There are two possible fault normal and slip vector pairs for a double couple; green indicates the pair having its coordinates in the strike-rake-dip box in (b), and black indicates its conjugate. (h) Beachball for M_0 . The two big black dots are the P-T axes of M_0 , and the small red and blue dots are the P-T axes of 200 posterior samples. (i) 20 posterior samples. The number above each beachball M is its angular distance $\omega(M)$ from M_0 , and the color of the ball gives its relative misfit, using the same color scale as in (b).



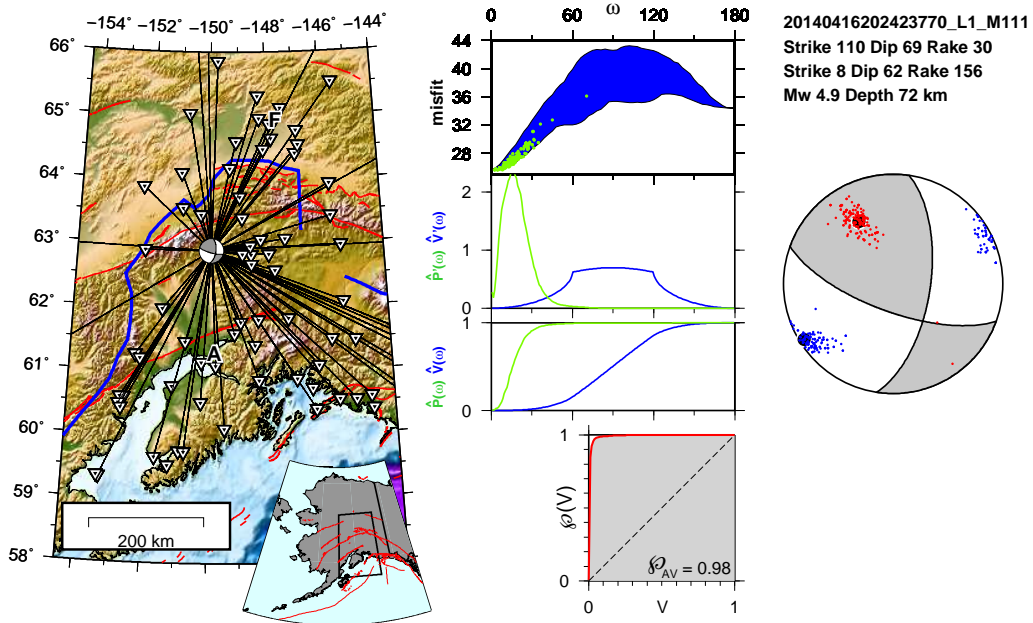


Figure 2.8: Uncertainty analysis for an event with good station coverage. The figure is like the upper diagram in Figure 2.7, but for an earthquake near Denali, Alaska. The $\mathcal{P}(V)$ curve resembles a Γ and gives high confidence ($\mathcal{P}_{AV} = 0.98$) for M_0 . See Section 2.5.2 for details.

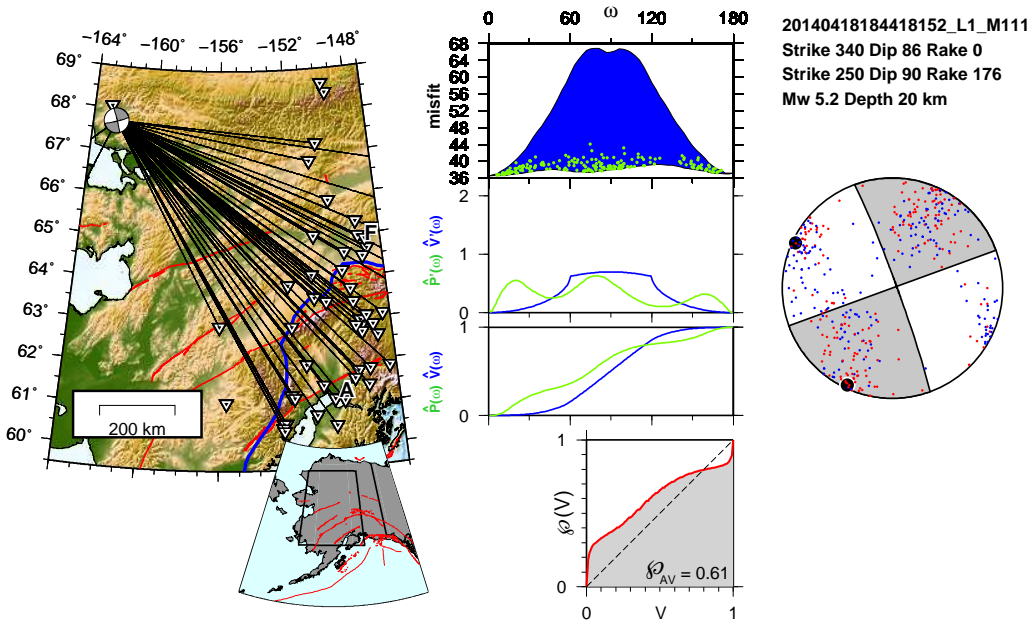


Figure 2.9: Uncertainty analysis for an event with poor station coverage. The figure is like the upper diagram in Figure 2.7, but for an earthquake near Noatak, Alaska. Examining the curve $\hat{P}'(\omega)$, we see that the probability is widely distributed over moment tensor space, which leads to a low confidence ($P_{AV} = 0.61$) for M_0 . The closeness of $P(V)$ to the 45° line (dashed) is another indication that M_0 is not a reliable solution. See Section 2.5.2 for details.

Figure 2.10: [FOLLOWING PAGE] Moment tensor solution and waveform fits at a subset of 11 stations for event 20071003140612444 (depth 32 km, M_w 5.0). The angle between this solution and the AEC moment tensor catalog solution is 56°. See Figure A in Silwal (2015) for the waveform fits for the full set of 45 stations. See Figure 2.11 for the waveform fits when using the AEC moment tensor. See Figure 2.7 caption for details.

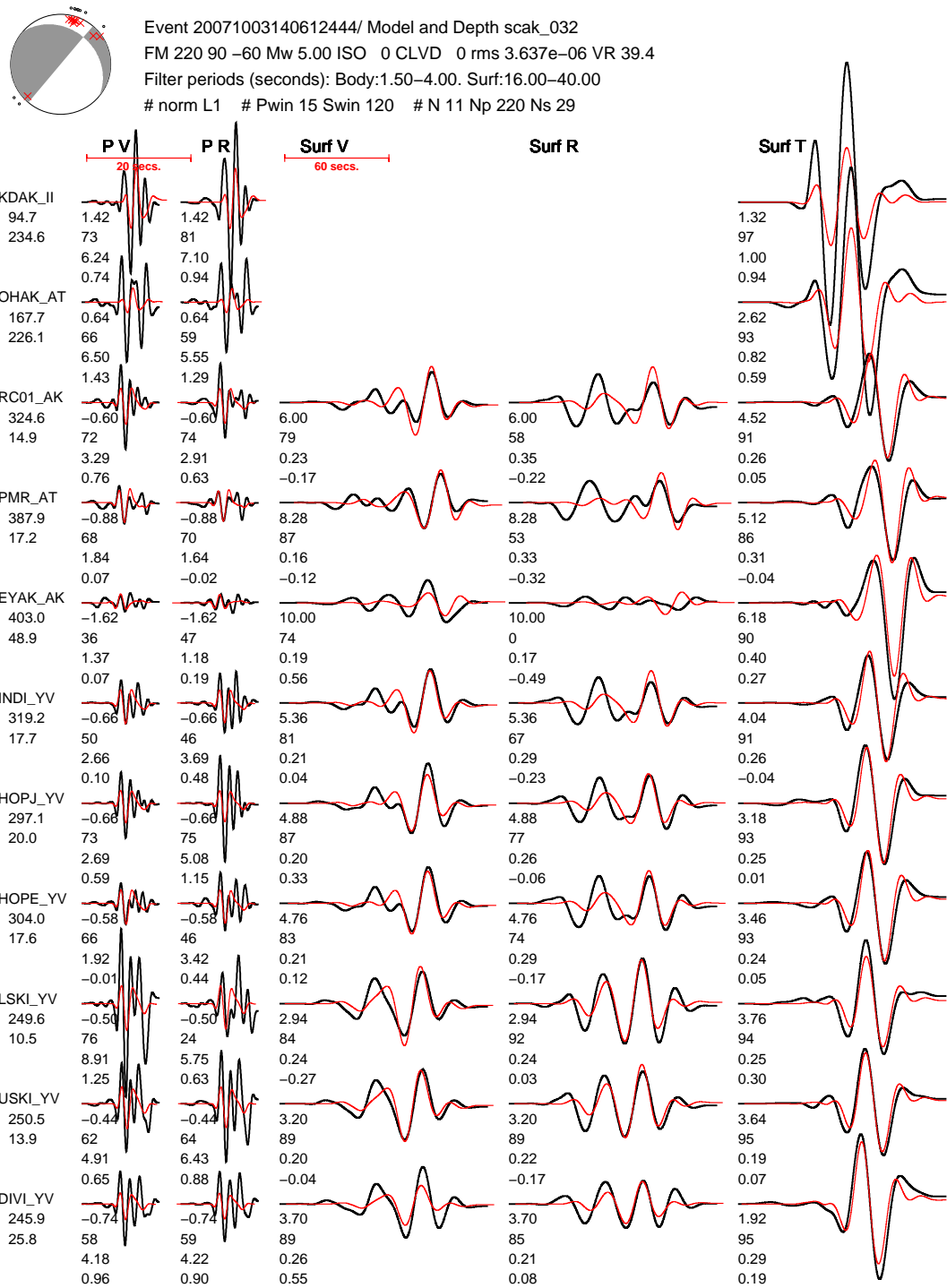


Figure 2.10

Figure 2.11: Same as Figure 2.10, but showing synthetic waveforms for the moment tensor and depth (40 km) in the AEC moment tensor catalog. Our preferred moment tensor solution in Figure 2.10, obtained using both body and surface waves, provides better waveform fits (CAP VR = 39%; AEC VR = 25%). Here we allow the magnitude of the AEC moment tensor to vary in order to achieve the best possible waveform fits for this fixed hypocenter and orientation; the best-fitting magnitude of M_w 4.6 is much lower than M_w 5.0 in Figure 2.10. See Figure A.4 for the AEC waveform fits when the magnitude is fixed to be the AEC magnitude.

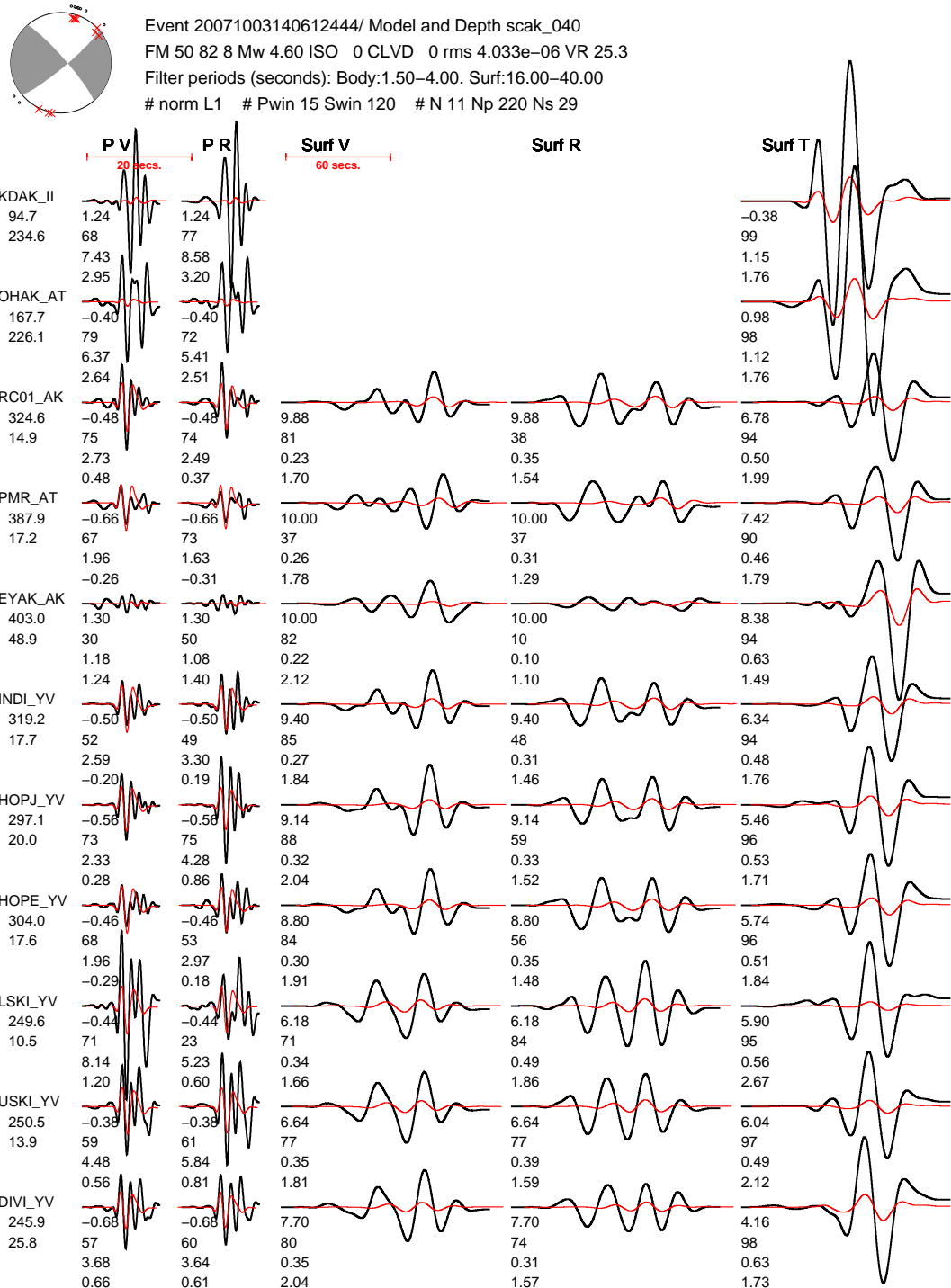


Figure 2.11

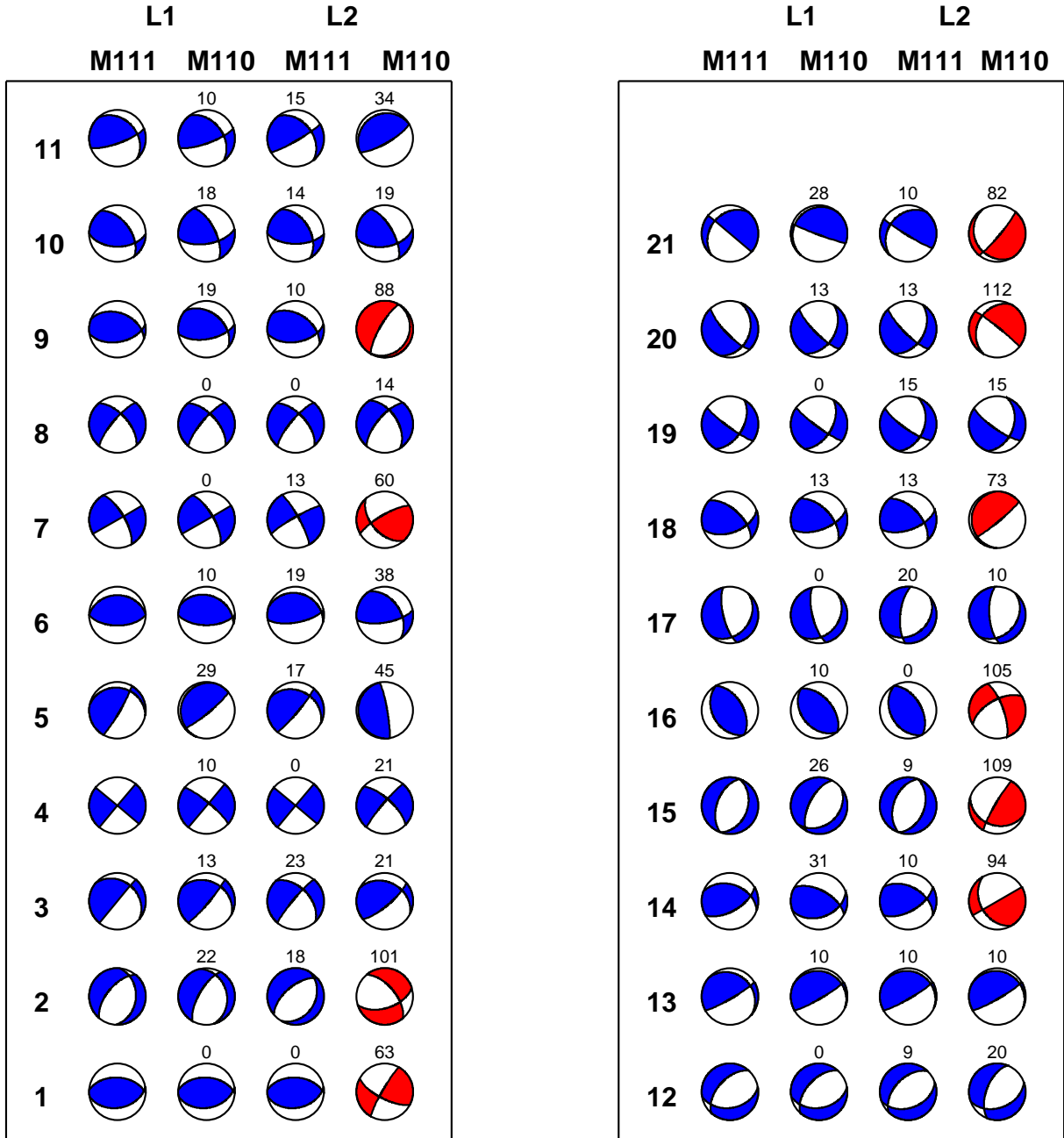


Figure 2.12: The effect of using an L1 versus an L2 norm in the misfit function for the 21 Part I events. Column 1: using only the best stations (M_{111}) and applying the L1 norm. Column 2: using all stations (M_{110}) and applying the L1 norm. Column 3: using only the best stations (M_{111}) and applying the L2 norm. Column 4: using all stations (M_{110}) and applying the L2 norm. The number above each beachball is the angle ω to the preferred beachball in column 1; if $\omega \geq 50^\circ$, then the ball is colored red and is considered to be significantly wrong.

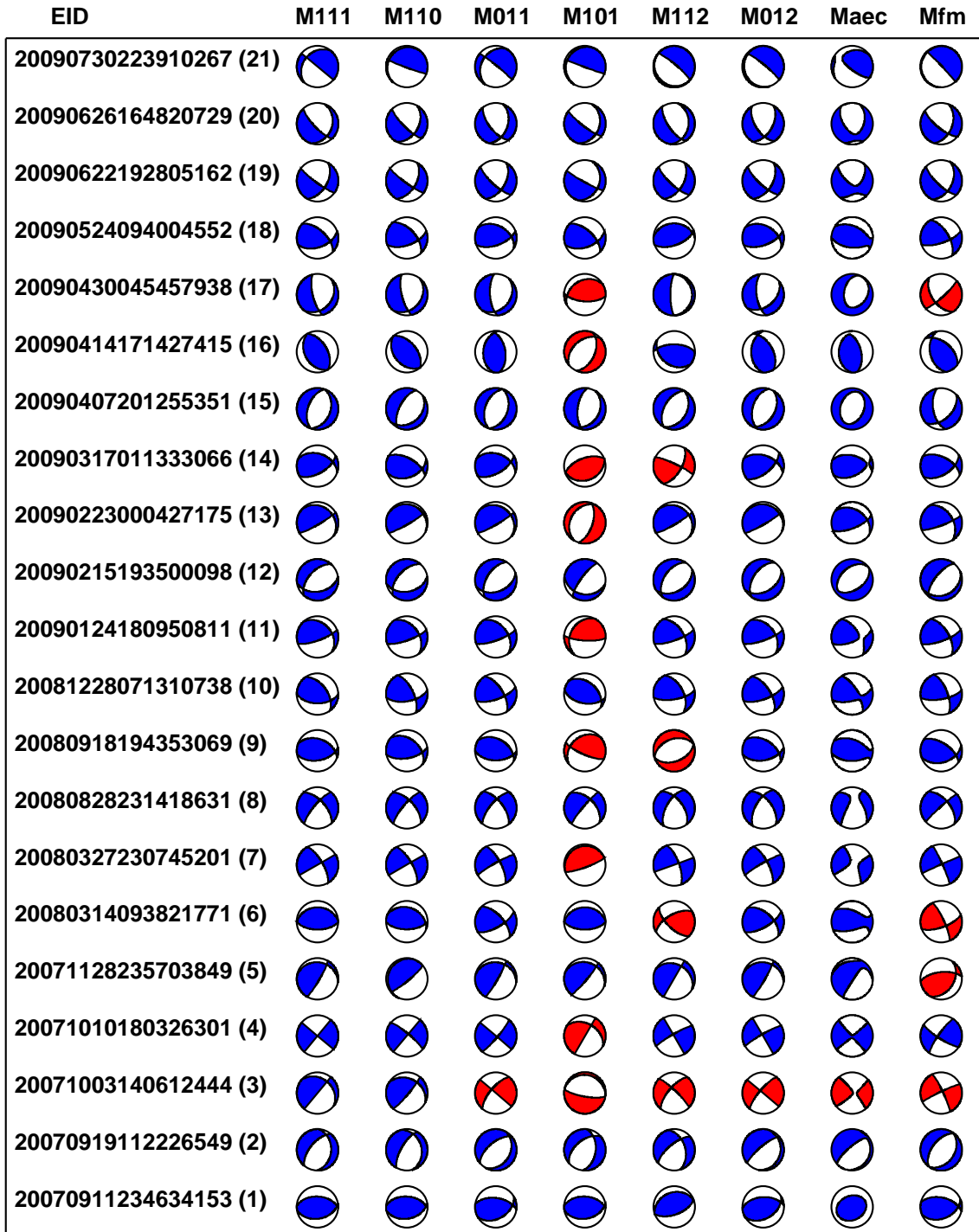


Figure 2.13: Beachballs obtained using different data sets and applying an L1 norm. See Tables 2.1 and 2.2 for comparing the differences between different columns. The solution used in our catalog (Table 2.4) is M_{111} (the first column). The last two columns show the moment tensors in the Alaska Earthquake Center catalogs (M_{AEC} and M_{fm}). A beachball is colored red if it is $\omega \geq 50^\circ$ from the M_{111} solution.

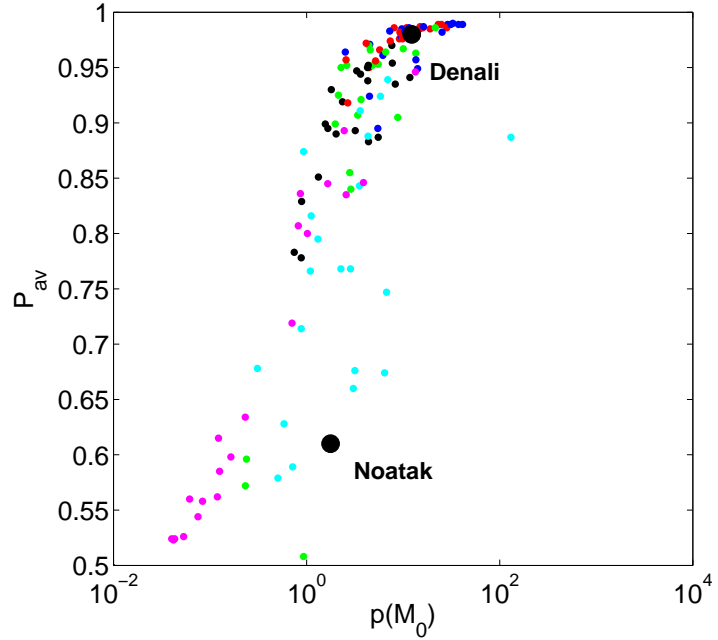


Figure 2.14: Confidence parameter \mathcal{P}_{AV} versus probability density $p(M_0)$ for the 21 Part I catalog events for inversions performed with different subsets of data (see Table 2.1): M_{111} (black), M_{011} (red), M_{101} (cyan), M_{112} (green), M_{012} (blue), M_{110} (magenta). The plot reveals some correlation between \mathcal{P}_{AV} and log-scaled $p(M_0)$, though in general a range of \mathcal{P}_{AV} values are possible for any given $p(M_0)$. See Figure 2.13 for the set of beachballs corresponding to the dots in this figure. Values for the black dots (M_{111}) are listed in Table 2.4; the two large black dots are for the Denali (Figure 2.8) and Noatak (Figure 2.9) events.

Figure 2.15: [FOLLOWING PAGE] Comparison among three moment tensor catalogs for earthquakes in this study: (1) the Alaska Earthquake Center moment tensor catalog (M_{AEC}), (2) the AEC first-motion catalog (M_{fm}), and (3) our catalog (M_{CAP}). The difference between two moment tensors for the same event is quantified by the matrix angle ω between the closest double-couple moment tensors. (Only the M_{AEC} moment tensors allow for a non-double-couple component.) (a) $\omega = \angle(M_{CAP}, M_{AEC})$: AEC first-motion solution vs AEC moment tensor for the 21 Part I events. This shows the influence of using long-period waveforms or first-motion polarities. These results are computed directly from the AEC catalogs. (b) CAP moment tensor vs AEC moment tensor for the 21 Part I events. (c) CAP moment tensor vs AEC first-motion solution for all 106 events. The differences are larger than those in (b), likely because the set of 106 events includes smaller events than the higher-quality, larger events in (b). Larger uncertainties in either the CAP solutions or the AEC first-motion solutions will result in larger differences between the two sets of solutions. (d) Differences in magnitude, $m_{CAP} - m_{AEC}$, for all 106 events in the catalog. The average difference in magnitude is 0.2, indicating that our CAP magnitude estimates tend to be larger than those from AEC. It is possible that these differences are partly due to how the magnitudes are determined: m_{CAP} is measured as moment magnitude (M_w) and m_{AEC} is measured as local magnitude (M_l).

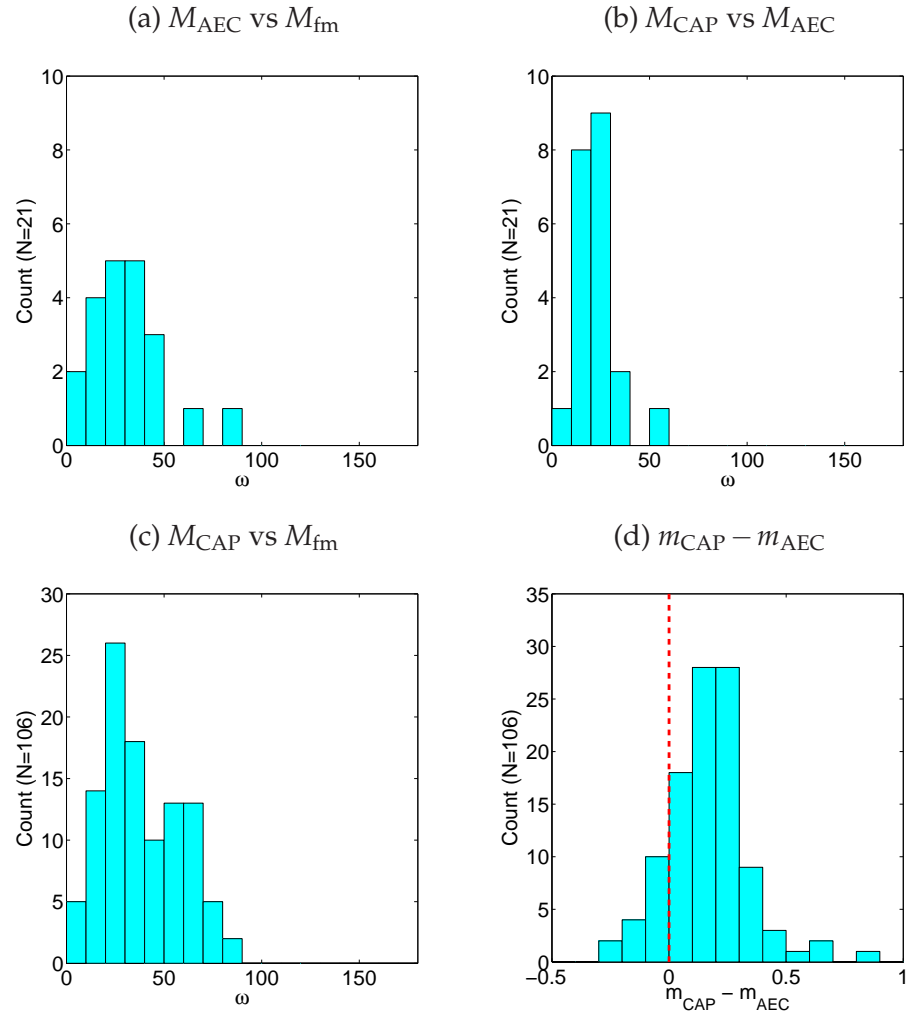


Figure 2.15

References

- Aki, K. & Richards, P. G., 1980. *Quantitative Seismology, Theory and Methods*, W. H. Freeman, San Francisco, Calif., USA.
- Aster, R. C., Borchers, B., & Thurber, C. H., 2013. *Parameter Estimation and Inverse Problems*, Elsevier, Waltham, Mass., USA, 2nd edn.
- Chen, P., Jordan, T. H., & Zhao, L., 2005. Finite-moment tensor of the 3 September 2002 Yorba Linda earthquake, *Bull. Seismol. Soc. Am.*, **95**(3), 1170–1180, doi:10.1785/0120040094.
- Christensen, D., Abers, G., & Freymueller, J., 2008. Multidisciplinary observations of subduction (MOOS) experiment in south-central Alaska, in *Eos Trans. Am. Geophys. Un.*, vol. 89(53), Abstract U51B-0041.
- Clinton, J. F., Hauksson, E., & Solanki, K., 2006. An evaluation of the SCSN moment tensor solutions: Robustness of the M_w magnitude scale, style of faulting, and automation of the method, *Bull. Seismol. Soc. Am.*, **96**(5), 1689–1705, doi:10.1785/0120050241.
- Covellone, B. M. & Savage, B., 2012. A quantitative comparison between 1D and 3D source inversion methodologies: Application to the Middle East, *Bull. Seismol. Soc. Am.*, **102**(5), 2189–2199, doi:10.1785/0120110278.
- Dreger, D. & Woods, B., 2002. Regional distance seismic moment tensors of nuclear explosions, *Tectonophysics*, **356**, 139–156, doi:10.1016/S0040-1951(02)00381-5.
- Dreger, D., Uhrhammer, R., Pasanos, M., Franck, J., & Romanowicz, B., 1998. Regional and far-regional earthquake locations and source parameters using sparse broadband networks: A test on the Ridgecrest sequence, *Bull. Seismol. Soc. Am.*, **88**(6), 1353–1362.
- Dreger, D. S., Tkalcic, H., & Johnson, M., 2000. Dilational processes accompanying earthquakes in the Long Valley Caldera, *Science*, **288**, 122–125.
- Dufumier, H. & Rivera, L., 1997. On the resolution of the isotropic component in moment tensor inversion, *Geophys. J. Int.*, **131**, 595–606.
- Duputel, Z., Rivera, L., Kanamori, H., & Hayes, G., 2012. W phase source inversion for moderate to large earthquakes, *Geophys. J. Int.*, **189**, 1125–1147.

- Ekström, G., Nettles, M., & Dziewoński, A. M., 2012. The global GCMT project 2004–2010: Centroid-moment tensors for 13,017 earthquakes, *Phys. Earth Planet. Inter.*, **200-201**, 1–9, doi: 10.1016/j.pepi.2012.04.002.
- Fukuyama, E. & Dreger, D. S., 2000. Performance test of an automated moment tensor determination system for the future “Tokai” earthquake, *Earth Planets Space*, **52**, 383–392, doi: 10.1186/BF03352250.
- Fukuyama, E., Ishida, M., Dreger, D. S., & Kawai, H., 1998. Automated seismic moment tensor determination by using on-line broadband seismic waveforms, *Zisin (J. Seis. Soc. Japan)*, **51**, 149–156.
- Hardebeck, J. L. & Shearer, P. M., 2002. A new method for determining first-motion focal mechanisms, *Bull. Seismol. Soc. Am.*, **92**(6), 2264–2276, doi:10.1785/0120010200.
- Haskell, N., 1964. Total energy and energy spectral density of elastic wave radiation from propagating faults, *Bull. Seismol. Soc. Am.*, **54**, 1811–1842.
- Helberger, D. V. & Engen, G. R., 1980. Modeling the long-period body waves from shallow earthquakes at regional ranges, *Bull. Seismol. Soc. Am.*, **70**, 1699–1714.
- Isacks, B., Oliver, J., & Sykes, L. R., 1968. Seismology and the new global tectonics, *J. Geophys. Res.*, **73**, 5855–5899.
- Kagan, Y. Y., 1991. 3-D rotation of double-couple earthquake sources, *Geophys. J. Int.*, **106**, 709–716, doi:10.1111/j.1365-246X.1991.tb06343.x.
- Käufl, P., Valentine, A. P., O'Toole, T. B., & Trampert, J., 2014. A framework for fast probabilistic centroid-moment-tensor determination—involution of regional static displacement measurements, *Geophys. J. Int.*, **196**, 1676–1693, doi:10.1093/gji/ggt473.
- Koehler, R. D., Farrell, R.-E., Burns, P. A. C., & Combierick, R. A., 2012. Quaternary faults and folds in Alaska: A digital database, Alaska Div. Geol. Geophys. Surv. Miscellaneous Publication 141, 31 p., 1 sheet, scale 1:3,700,000.
- Lee, E.-J., Chen, P., Jordan, T. H., Maechling, P. B., Denolle, M. A. M., & Beroza, G. C., 2014. Full-3-D tomography for crustal structure in Southern California based on the scattering-integral and the adjoint-wavefield methods , *J. Geophys. Res. Solid Earth*, **119**, 6421–6451, doi:10.1002/2014JB011346.

Li, J., Abers, G. A., Kim, Y., & Christensen, D., 2013. Alaska megathrust 1: Seismicity 43 years after the great 1964 Alaska megathrust earthquake, *J. Geophys. Res.*, **118**, 4861–4871, doi:10.1002/jgrb.50358.

Liu, Q., Polet, J., Komatitsch, D., & Tromp, J., 2004. Spectral-element moment tensor inversions for earthquakes in southern California, *Bull. Seismol. Soc. Am.*, **94**(5), 1748–1761, doi: 10.1785/012004038.

Maceira, M., Ammon, C. J., & Herrmann, R. B., 2000. Faulting parameters of the September 25, 1998 Pymatuning, Pennsylvania earthquake, *Seismol. Res. Lett.*, **71**(6), 742–752.

Nayak, A. & Dreger, D. S., 2014. Moment tensor inversion of seismic events associated with the sinkhole at Napoleonville salt dome, Louisiana, *Bull. Seismol. Soc. Am.*, **104**(4), 1763–1776, doi: 10.1785/0120130260.

Pasyanos, M. E., Dreger, D. S., & Romanowicz, B., 1996. Toward real-time estimation of regional moment tensors, *Bull. Seismol. Soc. Am.*, **86**(5), 1255–1269.

Ratchkovski, N. A. & Hansen, R. A., 2002. New constraints on tectonics of interior Alaska: Earthquake locations, source mechanisms, and stress regime, *Bull. Seismol. Soc. Am.*, **92**(3), 998–1014, doi:10.1785/0120010182.

Reasenberg, P. & Oppenheimer, D., 1985. FPFIT, FPPILOT and FPPAGE: Fortran computer programs for calculating and displaying earthquake fault-plane solutions, Open-File Report 85-739.

Reyes, C. G. & West, M. E., 2011. The Waveform Suite: A robust platform for manipulating waveforms in MATLAB, *Seismol. Res. Lett.*, **82**, 104–110, doi:10.1785/gssrl.82.1.104.

Riedesel, M. A. & Jordan, T. H., 1989. Display and assessment of seismic moment tensors, *Bull. Seismol. Soc. Am.*, **79**(1), 85–100.

Ristau, J., 2008. Implementation of routine regional moment tensor analysis in New Zealand, *Seismol. Res. Lett.*, **79**(3), 400–415, doi:10.1785/gssrl.79.3.400.

Ristau, J., Rogers, G. C., & Cassidy, J. F., 2007. Stress in western Canada from regional moment tensor analysis, *Can. J. Earth Sci.*, **44**, 127–148, doi:10.1139/E06-057.

Ross, Z. E., Ben-Zion, Y., & Zhu, L., 2015. Isotropic source terms of San Jacinto fault zone earthquakes based on waveform inversions with a generalized CAP method, *Geophys. J. Int.*, **200**, 1267–1278, doi:10.1093/gji/ggu460.

Rueda, J. & Mezcua, J., 2005. Near-real-time seismic moment-tensor determination in Spain, *Seismol. Res. Lett.*, **76**(4), 455–465, doi:10.1785/gssrl.76.4.455.

Ruppert, N. A. & Hansen, R. A., 2010. Temporal and spatial variations of local magnitudes in Alaska and Aleutians and comparison with body-wave and moment magnitudes, *Bull. Seismol. Soc. Am.*, **100**(3), 1174–1183, doi:10.1785/0120090172.

Scognamiglio, L., Tinti, E., & Michelini, A., 2009. Real-time determination of seismic moment tensor for the Italian region, *Bull. Seismol. Soc. Am.*, **99**(4), 2223–2242, doi:10.1785/0120080104.

Shellenbaum, D. P., Gregersen, L. S., & Delaney, P. R., 2010. Top Mesozoic unconformity depth map of the Cook Inlet Basin, Alaska, Alaska Div. Geol. Geophys. Surv. Report of Investigation 2010-2, 1 sheet, scale 1:500,000, available at <http://www.dggs.alaska.gov/pubs/id/21961> (last accessed 2016-10-30).

Silwal, V., 2015. Seismic moment tensor catalog for southern Alaska, ScholarWorks@UA at <http://hdl.handle.net/11122/6025> (last accessed 2016-01-22): descriptor file, text file of catalog, figures with waveform fits, depth searches, and uncertainty analyses.

Stähler, S. C. & Sigloch, K., 2014. Fully probabilistic seismic source inversion – Part 1: Efficient parameterisation, *Solid Earth*, **5**, 1055–1069, doi:10.5194/se-5-1055-2014.

Tan, Y., Zhu, L., Helmberger, D. V., & Saikia, C. K., 2006. Locating and modeling regional earthquakes with two stations, *J. Geophys. Res.*, **111**, B01306, doi:10.1029/2005JB0037750.

Tape, C., Liu, Q., Maggi, A., & Tromp, J., 2009. Adjoint tomography of the southern California crust, *Science*, **325**, 988–992, doi:10.1126/science.1175298.

Tape, W. & Tape, C., 2012. A geometric setting for moment tensors, *Geophys. J. Int.*, **190**, 476–498, doi:10.1111/j.1365-246X.2012.05491.x.

Tape, W. & Tape, C., 2013. The classical model for moment tensors, *Geophys. J. Int.*, **195**, 1701–1720, doi:10.1093/gji/ggt302.

Tape, W. & Tape, C., 2015. A uniform parameterization of moment tensors, *Geophys. J. Int.*, **202**, 2074–2081, doi:10.1093/gji/ggv262.

Tape, W. & Tape, C., 2016. A confidence parameter for seismic moment tensors, *Geophys. J. Int.*, **205**, 938–953, doi:10.1093/gji/ggw057.

Tarantola, A., 2005. *Inverse Problem Theory and Methods for Model Parameter Estimation*, SIAM, Philadelphia, Penn., USA.

Valentine, A. P. & Trampert, J., 2012. Assessing the uncertainties on seismic source parameters: Towards realistic error estimates for centroid-moment-tensor determinations, *Phys. Earth Planet. Inter.*, **210–211**, 36–49, doi:10.1016/j.pepi.2012.08.003.

von Neumann, J., 1951. Various techniques used in connection with random digits, in *Monte Carlo Method*, vol. 12 of **Applied Mathematics Series**, pp. 36–38, U.S. Dept. Commerce Nat. Bureau Standards, Summary written by G. E. Forsythe.

Zahradník, J. & Custódio, S., 2012. Moment tensor resolvability: Application to southwest Iberia, *Bull. Seismol. Soc. Am.*, **102**(3), 1235–1254, doi:10.1785/0120110216.

Zhao, L.-S. & Helmberger, D. V., 1994. Source estimation from broadband regional seismograms, *Bull. Seismol. Soc. Am.*, **84**(1), 91–104.

Zhu, L. & Helmberger, D., 1996. Advancement in source estimation techniques using broadband regional seismograms, *Bull. Seismol. Soc. Am.*, **86**(5), 1634–1641.

Zhu, L. & Rivera, L. A., 2002. A note on the dynamic and static displacements from a point source in multilayered media, *Geophys. J. Int.*, **148**, 619–627, doi:10.1046/j.1365-246X.2002.01610.x.

Zhu, L. & Zhou, X., 2016. Seismic moment tensor inversion using 3D velocity model and its application to the 2013 Lushan earthquake sequence, *Physics and Chemistry of the Earth* (in press), doi:10.1016/j.pce.2016.01.002.

Chapter 3

Crustal earthquakes in the Cook Inlet and Susitna region of southern Alaska¹

3.1 Abstract

Several large ($M \geq 6$) earthquakes have occurred in the vicinity of Anchorage, Alaska, within the past century. The presence of the underlying subducting Pacific plate makes it difficult to determine the origin of these older earthquakes as either crustal, slab, or the subduction plate interface. We perform a seismological study of historical and modern earthquakes within the Cook Inlet and Susitna region, west of Anchorage. We first estimate hypocenters for historical large earthquakes in order to assess their likelihood of origin as crustal, slab, or plate interface. We then examine modern crustal seismicity to better understand the style of faulting and the location of active structures, including within (and beneath) the Cook Inlet and Susitna basins. We perform double-couple moment tensor inversions using high frequency body waves (1–10 Hz) for small to moderate ($M \geq 2.5$) crustal earthquakes (depth ≤ 30 km) occurring from 2007 to 2017. Our misfit function combines both waveforms differences as well as first-motion polarities in order to obtain reliable moment tensor solutions. The three focus regions—Beluga, upper Cook Inlet, and Susitna—exhibit predominantly thrust mechanisms for crustal earthquakes, indicating an overall compressive regime within the crust that is approximately consistent with the direction of plate convergence. Mechanisms within upper Cook Inlet have strike directions aligned with active anticlines previously identified in Cook Inlet from active-source seismic data. Our catalog of moment tensors is helpful for identifying and characterizing subsurface faults from seismic lineaments and from faults inferred from subsurface images from active-source seismic data.

3.2 Introduction

The active tectonics of south-central Alaska is governed primarily by the northwestern subduction of the Pacific plate beneath the North America plate (Figure 3.1). This setting is one of the most seismically active regions in the world, having produced the $M_w 9.2$ 1964 earthquake. It includes pervasive earthquakes in the slab, down to depths of 200 km, as well as crustal seismicity spanning a broad zone of intraplate deformation (Figure 3.2) (Page et al., 1991; Bird, 2003). Many of the earthquakes—both large and small—are not clearly associated with any geologically mapped active faults. With improved locations of earthquakes and improved characterization of the style of faulting from these earthquakes, we can better assess the active faults in the region. Here we perform a seismological study of a tectonically complex region of south-central Alaska to improve our understanding of active tectonics and seismic hazards in the region.

¹In review at *Tectonophysics*: Silwal, V., Tape, C., and Lomax, A., 2018. Crustal earthquakes in the Cook Inlet and Susitna region of southern Alaska.

The Pacific plate subducts to the northwest under south-central Alaska (Figure 3.1a). Attached to the Pacific plate to the east is the Yakutat microplate, identified as an oceanic plateau, that is colliding and subducting beneath Alaska (Plafker et al., 1978; Eberhart-Phillips et al., 2006; Christeson et al., 2010). The subducting Pacific/Yakutat plate is interpreted to be responsible for the extremely shallow angle of subduction ($< 5^\circ$), far inland, as well as for the lack of volcanism (Eberhart-Phillips et al. (2006); Rondenay et al. (2010)).

We focus on the Cook Inlet and Susitna region, which spans the western margin of the Pacific/Yakutat plate (Figure 3.1a). The region, outlined in Figure 3.1, contains several notable tectonic elements. The subduction interface (Li et al., 2013) exhibits a clear kink from a westward-dipping slab to a northwestern-dipping slab (Ratchkovski & Hansen, 2002) (Figure 3.1a). The interface ranges from a depth of 40 km in the southeast, beneath the Kenai peninsula, to a depth of 100 km in the northwest, beneath the Alaska Range. The southeast corner also marks the approximate downdip extent of the 1964 $M_w 9.2$ earthquake (Davies et al., 1981; Ichinose et al., 2007). Slow slip and tectonic tremor have been identified on the deeper sections of the interface, from about 40 km to 80 km (Ohta et al., 2006; Wei et al., 2012; Fu & Freymueller, 2013; Li et al., 2016). The crustal thickness inferred from receiver functions is ~ 30 km in the northern region (Veenstra et al., 2006), implying that these deeper slow slip events would arise from contact with subcrustal mantle.

The dynamics of underlying subduction provide context for characterizing crustal structures and crustal earthquakes, which are the target of this study. Within the Cook Inlet and Susitna region are two mapped active faults: the Pass Creek fault and the Castle Mountain fault. The earliest reference of the Pass Creek fault (PCF) appears in Capps (1913), who reported “some thousands of feet” (p. 36) of displacement across the fault. Dover (1992) interpreted the PCF as a thrust fault but marked it as poorly constrained. Using interferometric synthetic aperture radar (IFSAR) elevation data, Haeussler et al. (2017) inferred the PCF to be a northwest dipping thrust fault and that it “appears likely that the scarp is a result of at least several surface-rupturing earthquakes” (p. 1471). They estimated the fault has a slip-rate of ~ 0.5 mm/yr and has the potential of producing a $M6.9 \pm 0.3$ earthquake if the complete 37 km of the fault plane ruptured.

The Castle Mountain and Lake Clark fault system extends 500 km, from Lake Clark in the southwest and into the Talkeetna mountains to the northeast (Grantz, 1966). The fault was interpreted as a right-lateral strike-slip fault (Grantz, 1966; Willis et al., 2007), but recent analyses have identified compressional structures across the fault, as well as a lack of definitive lateral offset indicators (Koehler & Carver, 2018). The Susitna section of the fault is the only section classified as active, based on geomorphic evidence (Koehler et al., 2012). A paleoseismic study by Haeussler et al. (2002) used data from nine trenches along the fault near Houston, Alaska. They identified

four major earthquakes in the past 2800 years, indicating a recurrence interval of \sim 700 years. The two largest historical earthquakes in the region, in 1933 and 1943, appear to have occurred near, but not on, the fault (Doser & Brown, 2001). Based on the Global Centroid Moment Tensor catalog, which started in 1976 (Dziewonski et al., 1981; Ekström et al., 2012), the largest earthquake on the fault in the past 40 years occurred in the northeastern most section as a M_w 5.8 right-lateral earthquake in 1984.

Physiographically the Cook Inlet and Susitna region is marked by the presence of two major sedimentary basins (Figure 3.3): the Cook Inlet basin south of the Castle Mountain fault, and the Susitna basin north of the fault (Figure 3.1b)). These basins are surrounded by mountains: the Talkeetna mountains to the east, the Alaska Range to the northwest, the Tordrillo mountains to the west, and the Kenai mountains to the south. Additional faults and folds have been identified within 3D active-source seismic data in Cook Inlet and Susitna basins (Bruhn & Haeussler, 2006; Lewis et al., 2015; Haeussler et al., 2017).

We conduct a seismological study that spans three different methods and three sets of earthquakes in the Cook Inlet and Susitna region. First, in Section 3.3 we estimate the hypocenters of the largest earthquakes ($M_w \geq 5.8$) that have occurred since the start of the instrumental era in 1904 (Gutenberg & Richter, 1954). We use globally recorded arrival times of P and S waves, in addition to traveltimes predictions in a spherically symmetric Earth model, within a probabilistic inversion for hypocenter and origin time. Second, in Section 3.4 we use P waveforms and first-motion polarities to estimate focal mechanisms for crustal earthquakes $M_w \geq 2.5$. This procedure is challenging on account of the lack of large earthquakes that are available. Third, in Section 3.5 we relocate seismicity ($M \geq 1.5$, 1990–2017) using arrival time data and a double-difference relocation algorithm (Waldhauser & Ellsworth, 2000). The results from these three analyses reveal a predominance of thrust faulting in the crust, consistent with structural inferences from subsurface images, but differing from the strike-slip mechanisms previously estimated from the large historical earthquakes. Widespread seismicity and different styles of faulting provide challenges for characterizing different scenarios for future large earthquakes in this region.

3.3 Hypocenter estimation of historical earthquakes

At least 12 major events ($M_w \geq 5.8$) have occurred in the Cook Inlet and Susitna region since the start of instrumental era in 1904. Table 3.2 summarizes previous publications of the magnitudes for these earthquakes. For larger earthquakes we use the Global Centroid Moment Tensor (GCMT) catalog (Dziewonski et al., 1981; Ekström et al., 2012) for events since 1976 and the ISC-GEM catalog (Storchak et al., 2013; International Seismological Centre, 2018) for events before 1976. The ISC-GEM catalog provides relocated hypocenters (Engdahl et al., 1998; Bondár & Storchak, 2011)

and magnitude estimates (Giacomo et al., 2015). In recent years, it has expanded its coverage of historical earthquakes to lower magnitudes. Doser and colleagues have estimated hypocenters, magnitudes, and mechanisms for many historical earthquakes in south-central Alaska (Doser, 2006, 2005; Doser & Brown, 2001; Flores & Doser, 2005).

Depth estimates of the hypocenters and of the subduction interface provide a starting point for interpreting the earthquakes as either crustal, interface, or intraslab. Table 3.3 reveals a mix of crustal and intraslab (or interface) earthquakes. Interestingly, the occurrence of earthquakes in the crust versus the slab appears to have changed with time, as shown in Figure 3.4. Prior to 1950 most earthquakes were crustal; after 1950 all four earthquakes were in the slab. This pattern was previously noted (Doser & Brown, 2001) and is apparent over a larger region. Doser & Brown (2001) speculated that stress changes from the 1964 M_w 9.2 earthquake were responsible for the shift from crustal to slab earthquakes.

We use a nonlinear probabilistic approach to estimate the hypocenters of the 11 pre-1976 earthquakes $M_w \geq 5.8$ in the region (Table 3.2). The code, NonLinLoc, uses an efficient global sampling algorithm to obtain an estimate of the probability density function (pdf) in 3D space for the hypocenter location (Lomax et al., 2000). The pdf (and the likelihood) is computed using the misfit between the observed and theoretical arrival times for teleseismic stations. Theoretical travel times are computed for a spherical earth with the ak135 velocity model (Kennett et al., 1995) using the TauP Toolkit (Crotwell et al., 1999). Recorded arrival times are obtained from the International Seismological Centre (International Seismological Centre, 2015).

Our full results for all 11 historical earthquakes are presented in Lomax et al. (2018); next we highlight three of the largest earthquakes.

3.3.1 The 1933, 1943, and 1954 earthquakes

We present results from three $M_w > 6$ earthquakes in the Cook Inlet and Susitna region: 1933-04-27 M_w 6.8, 1943-11-03 M_w 7.3, and 1954-10-03 M_w 6.4 (Table 3.2). These earthquakes were widely felt across south-central Alaska, including Kodiak, to the southwest, and at least as far north as Fairbanks, which is about 400 km from the epicenters. Section 3.8 summarizes felt reports of these earthquakes. The 1933 earthquake toppled telegraph lines around Anchorage, broke storefront windows in Anchorage, and shook houses off foundations in Old Tyonek. The 1954 earthquake produced minor landslides over the highway, damaged a section of railroad, and damaged structures in Anchorage and the western Kenai peninsula. Although having the largest magnitude of the three earthquakes, the 1943 earthquake did not lead to any reported damage in the region. By comparison, the maximum shaking intensities in Anchorage—which is approximately equidistant from the three earthquakes—were MMI 6 (1933), MMI 5 (1943), and MMI 8 (1954) (Section 3.8;

Brockman et al. (1988)). These discrepancies could arise from influences of 3D structure on ground motion, from source effects (radiation pattern or directivity), and from possible inconsistencies in the MMI values (e.g., are the MMI values from the same place in Anchorage?).

The seismicity cross sections in Figure 3.2b-c provide context for these three earthquakes. The plots show our maximum likelihood (MLL) hypocenters for the three earthquakes in the context of modern seismicity and estimated subsurface interfaces (subduction and Moho). From these results alone, it appears that the 1933 and 1943 earthquakes are crustal, while the 1954 earthquake was likely intraslab, though we cannot rule out the subduction interface as a possibility (Table 3.3). We discuss this further in Section 3.6.3.

Station coverage and traveltimes residuals for our MLL hypocenters (and origin times) are shown in Figure 3.5. Figure 3.6 shows our posterior epicenters for the three earthquakes. These ‘clouds’ are approximately 30 km by 40 km and convey the uncertainty associated with the epicenter estimation. For each posterior hypocenter we calculate its vertical distance to the subduction interface, and these differences are then plotted as histograms in the bottom row of Figure 3.7. These distributions provide critical uncertainties for the interpretation of the earthquakes as crustal, subduction interface, or intraslab. For example, Figure 3.7c (bottom) makes the case for the 1954 earthquake as intraslab. (However, note that we do not have uncertainties for the subduction geometry models, including the one we have chosen to use (Li et al., 2013)).

3.4 Moment tensor inversions for modern crustal earthquakes

A double couple moment tensor is a 3×3 symmetric matrix whose eigenvalues are $(\lambda, 0, -\lambda)$. We are concerned with estimating the magnitude and orientation (strike, dip, rake) of the moment tensor, which we also refer to as the ‘source mechanism’. Alternative terms for double couple moment tensors are ‘fault-plane solution’ or ‘focal mechanism.’ The strike, dip, and rake define the moment tensor orientation, as well as one of the two possible fault planes.

Three catalogs of moment tensors are summarized in Figure 3.8: (a) Doser & Brown (2001): large $M_w > 6$ historical (pre-1964) earthquakes; (b) the GCMT catalog (Dziewonski et al., 1981; Ekström et al., 2012): post-1976 earthquakes, predominantly $M_w > 5.3$; (c) crustal earthquakes from the Alaska Earthquake Center fault-plane catalog: predominantly $M_I > 3$. We also considered the focal mechanism catalog of Li et al. (2013), which includes 117 earthquakes over a one-year period of the MOOS deployment (2007-8). Almost all of these earthquakes are within the slab or to the southeast of our focus region.

Within the Cook Inlet and Susitna region, we observe two historical crustal earthquakes (1933, 1943) and zero crustal earthquakes since 1976 (GCMT: Dziewonski et al. (1981); Ekström et al. (2012)). There is one event in the GCMT catalog that is ≤ 30 km depth, plotted as a red beachball

near Anchorage in Figure 3.8b. The depth is listed as 15 km in the GCMT catalog, but the Alaska Earthquake Center (AEC) earthquake catalog, using all available regional data, lists 31 km for the depth, which would likely be an intraslab origin (not crustal) for the earthquake. The GCMT magnitude of M_w 5.3 is near the completeness level for the catalog, which indicates that there is limited global data for estimating the moment tensor. This might explain the large discrepancy between the moment tensor from GCMT and the one from the Alaska Earthquake Center, as shown in Figure 3.6.

Focal mechanisms for crustal earthquakes since 1990 are available from Alaska Earthquake Center. The mechanisms are estimated from first-motion polarities, and they vary widely across the region. Our primary motivation was to use enhanced methods, including waveforms, and enhanced station coverage from the past decade, to estimate moment tensors.

3.4.1 Event selection for moment tensor inversions

We consider earthquakes in the Cook Inlet and Susitna region shallower than 30 km and occurring between 2007-08-15 and 2017-01-01. From the spatial distribution of crustal seismicity (Figure B.10), we identified three sub-regions to select events for moment tensor inversions: Beluga region, Upper Cook Inlet region, and Susitna region (Table 3.1 and Figure B.8). The time period of event selection, 2007–2017, spans two seismic experiments in the region: MOOS (2007–2009) (Li et al., 2013; Abers & Christensen, 2006) and SALMON (2015–2017) (Tape et al., 2017, 2015) and also includes new stations from the EarthScope Transportable Array (TA) in Alaska (2014–2019). Station coverage is a primary factor on the reliability of our moment tensor solutions. Events in 2010, following the end of MOOS, have poor station coverage. Events starting in 2015 have the best coverage due to SALMON and TA networks.

We selected 53 events for moment tensor inversions: 9 from the Beluga region, 22 from the Upper Cook Inlet region, and 22 from the Susitna region. Hypocenters and origin times were obtained from the AEC catalog. These were fixed for the moment tensor inversions. Analyst-reviewed P arrival times and polarities were used for stations in the permanent network (AK, AT, AV). For stations in temporary networks (MOOS, SALMON, TA), we picked the P arrival times and assigned polarities.

3.4.2 Moment tensor inversion method

Estimating a moment tensor for an earthquake involves comparing observed waveforms with synthetic waveforms calculated for an assumed moment tensor for an assumed model of Earth structure. We use the same layered seismic velocity model used by the Alaska Earthquake Cen-

ter for moment tensor inversions and for locating earthquakes; see Table S1 of Silwal & Tape (2016). We use the ‘cut-and-paste’ approach to estimate moment tensors for earthquakes (Zhao & Helmberger, 1994; Zhu & Helmberger, 1996; Zhu & Rivera, 2002). In this approach, each three-component seismogram is cut into two body wave windows and three surface wave windows. Different bandpass filters are applied to the body waves and surface waves. The same procedures are applied to synthetic seismograms, which are then quantitatively compared with the recorded seismograms, via a misfit function. As demonstrated in Silwal & Tape (2016), the choices within the misfit function can have a significant impact on the estimated best-fitting moment tensor. Our previous studies (Silwal & Tape, 2016; Alvizuri & Tape, 2016) employed a simplified treatment of first-motion polarities that is generalized here.

Within the grid-search moment tensor inversion, the synthetic seismograms are aligned with the observed seismograms by applying time shifts to the synthetic waveforms that minimize the misfit between synthetic and observed waveforms. In many cases, this minimization can result in time shifts that are unreasonable, based on comparisons with a larger set of measurements. In these cases of cycle skipping, the synthetic waveforms are aligned on the wrong portion of the observed waveforms. The challenges of cycle-skipping and time shifts have been discussed previously Alvizuri & Tape (2016); Alvizuri et al. (2018). In our study we specify the observed P onset times, which effectively eliminates the need for time shifts.

Figure 3.9 shows a moment tensor inversion result for one of 22 crustal earthquakes in the Susitna region. Its relatively large magnitude (M_w 4.2) allows us to use surface waves, in addition to body waves. For all the other events, only P waves (and P polarities) were used. The example shows the basic approach to comparing recorded waveforms (black) with synthetic waveforms (red) generated using a layered Earth model and a moment tensor source. Significant differences in shapes between data and synthetics are attributed to complexities in 3D Earth structure that are not modeled by the synthetics. For this event, the recorded waveforms to the southwest are influenced by Cook Inlet basin, as well as by Susitna basin from the source region. Some of these differences in structure between our assumed 1D model and real 3D Earth structure are encapsulated by the time shift maps shown in Figure 3.9.

3.4.3 Misfit function

Small earthquakes ($M_w < 3.5$) do not produce large signals at low frequencies. Therefore we are forced to use higher frequency waveforms, which are sensitive to 3D structural heterogeneities. Most regional networks do not have enough stations to capture the detailed effects of 3D structure on the wavefield. As used in previous studies Ford et al. (2012); Guilhem et al. (2014); Chiang et al. (2014); Wéber (2018), first-motion polarity measurements (i.e., up or down) can be used to stabilize

the waveform misfit function. Below we define our misfit function that combines waveforms differences and polarity differences.

The L1-norm waveform misfit is given by

$$\Phi_w(M) = \sum_{j=1}^{N_s} \sum_{i=1}^5 \left[(\mathbf{u}_{ij} - \mathbf{s}_{ij}(M))^T \mathbf{W}_{ij} (\mathbf{u}_{ij} - \mathbf{s}_{ij}(M)) \right]^{1/2} \quad (3.1)$$

where N_s is the number of stations used, i is the window index for a seismogram, j is the station index for an event, \mathbf{u} is a discretized recorded seismogram, $\mathbf{s}(M)$ is a discretized synthetic seismogram for moment tensor M , \mathbf{W}_{ij} is a square weighting matrix with the same dimension as the number of time points. As discussed in Section B.1, we choose \mathbf{W}_{ij} to be a constant-valued diagonal matrix with a weight factor that takes into account the duration of the time window, the width of the bandpass, and a user-specified weight. Recent approaches have considered non-diagonal weighting matrices based on estimated noise at each station Stähler & Sigloch (2016); Mustać & Tkalčić (2016, 2017).

The polarity misfit is given by

$$\Phi_p(M) = \frac{1}{2} \sum_{j=1}^{N_p} |p_j - t_j(M)| \quad (3.2)$$

where p is the observed polarity, t is the theoretical polarity for the moment tensor M , and N_p is the number of stations at which first-motion polarity is picked. p and t can either be +1 (up) or -1 (down), so that the polarity misfit for a station is either 0 or 1.

The total misfit is a weighted sum of the normalized waveform and polarity misfit

$$\Phi(M) = h(N_s) \left(m \frac{\Phi_p(M)}{N_p} + (1-m) \frac{\Phi_w(M)}{\|\mathbf{u}\|_{L1}} \right) \quad (3.3)$$

where the waveform misfit normalization $\|\mathbf{u}\|_{L1}$ is same as given in equation 7 of Silwal & Tape (2016), m is the weight given to the polarity misfit, and $h(N_s)$ is the station reward factor (see Section B.1). Figure 3.10 shows the impact of using different weights for the polarity misfit on moment tensor solution. The Supporting Information includes text and figures to illustrate the roles of different variables in the misfit function. This misfit function was also used in Alvizuri et al. (2018); Alvizuri & Tape (2018) for full moment tensor inversions.

3.4.4 Results

Our moment tensor inversion results for 53 crustal earthquakes in the three sub-regions (Table 3.1) are presented in Tables B.2–B.4, in Figure 3.11, and in Silwal (2018). The sub-regions exhibit predominantly thrust earthquake mechanisms that are consistent with the plate convergence direction of 339° (N21W) (Bird, 2003). Specifically, the T axes of the mechanisms are near vertical, and

the P axes of the mechanisms are near horizontal and point in the northwest direction of plate convergence.

In Figure 3.12 we compare our moment tensor results, which use P waveforms and first-motion polarities, with a catalog of mechanisms (AECfp) produced by the Alaska Earthquake Center that uses first-motion polarities only (fpfit: Reasenberg & Oppenheimer (1985)). For the time period 2007-08-15 to 2017-01-01 and depths ≤ 30 km, the AECfp catalog contains 46 earthquakes, 26 of which were examined in our study. The additional earthquakes in the AEC catalog were ones that were either not within our three sub-regions or were excluded by us due to low signal-to-noise levels for waveforms (Section 3.4.1). Therefore the comparison in Figure 3.12 is between a set of 53 moment tensors derived from P waveforms and a set of 46 derived from P polarities. The result in Figure 3.12a, which includes 27 that are not in (b), is a more coherent pattern of thrust faulting, whereas Figure 3.12b shows predominantly strike-slip faulting. This suggests that the inclusion of waveforms, as in our study, may help discriminate among strike-slip and thrust mechanisms in cases where P polarities alone cannot isolate the mechanism. Specifically, the moment tensor for a north-striking thrust fault dipping 45° (west or east) can be rotated 90° about its P-axis; this will result in a strike-slip moment tensor that is significantly overlapping with the original moment tensor (as quantified by $\omega = \angle(M_1, M_2) = 60^\circ$, which is much less than the maximum of 180°). Although the mechanisms look different, they are not easily constrained by seismic data, and a formal assessment of uncertainties could elucidate this point (Silwal & Tape, 2016). Of course, better station coverage would also help discriminate between the strike-slip and thrust mechanisms. By examining small, shallow earthquakes, we are unlikely to have the ray path coverage near the center of the source mechanisms. For shallow events, the upward ray paths cover a small region of the surface, where we are unlikely to have a station. For small events, the downward ray paths have too-small signal-to-noise by the time they reach distant stations. Station coverage for the source mechanisms is best viewed in the beachball plots in Silwal (2018).

3.5 Hypocenter relocation of modern crustal seismicity

We apply the double-difference hypocenter relocation method of Waldhauser & Ellsworth (2000) to crustal seismicity in the Cook Inlet and Susitna region. The double difference method relies on minimizing the difference between observed and theoretical travel-times for pairs of earthquakes at each station. The method, especially when used in conjunction with waveform cross correlations, has been effective in collapsing diffuse clouds of seismicity onto strikingly sharp fault-like features; meanwhile other diffuse clouds remain diffuse (Hauksson & Shearer, 2005; Shearer et al., 2005). The changes in the locations are also used to reduce the systematic errors due to the model, which could be used to improve the tomography models (Zhang & Thurber, 2003).

Our work expands on the results of Ratchkovsky et al. (1998), who relocated crustal earthquakes with $ml > 2.0$ and depths ≤ 50 km in southern Alaska occurring during 1988–1996 using the joint hypocenter determination (JHD) method (Douglas, 1967). They classified their results into five regions, one of which coincides with our target region: “Shallow North American intraplate earthquakes (0–25 km) located to the west of 149° W” (p. 96). Their results revealed diffuse seismicity within the crust.

We used a much larger data set, spanning from 1990-01-01 to 2017-01-01, and a more robust double-difference hypocenter relocation method (Waldhauser & Ellsworth, 2000). We used crustal events (depth ≤ 30 km) with $M_l \geq 1.5$ occurring between 1990-01-01 and 2017-01-01 (Table 3.1). With these selection criteria, we started with 5726 events from the AEC catalog. The final relocated catalog, after removing 35 (depth > 40 km) events, contained 4748 earthquakes. The changes between the initial hypocenter and final hypocenter are displayed in Figures B.13 and B.12. The mean change in epicenter is about 5 km and the standard deviation of depth changes is about 5.95 km.

In general, after relocation the diffuse seismicity remains diffuse (Figure 3.13). Similar results were obtained for relocations in the Los Angeles basin by Hauksson & Shearer (2005). Hauksson & Shearer (2005) explained the diffuse hypocenters as a effect of complex 3D brittle structure with interlaced strike-slip faults and thrust faults. The main lineament in our study region, within the Beluga region, is rotated toward a N-S alignment after relocation (Figure 3.13). Future efforts using new stations and waveform cross-correlation measurements could improve our results.

3.6 Discussion

Here we summarize our seismological results in the context of previous work within the three regions of interest (Table 3.1). We then discuss implications for active faults and larger earthquakes in the region.

3.6.1 Structures and active tectonics in the Cook Inlet and Susitna region

Beluga region

The Beluga region (Figure 3.11a) is physiographically marked by a triangular-shaped feature which we describe as the Beluga “interlowland region” (BILR), after Saltus et al. (2016). The BILR comprises four small mountains, each on the order of 1000 m in elevation: Mount Susitna, Little Mount Susitna, unnamed (south of Wolf Lakes), and Beluga Mountain. The BILR is bounded to the northeast by the Susitna basin and the Beluga Mountain fault, to the south by Castle Moun-

tain fault and the Cook Inlet basin, and to the west by a north-south physiographic low that is the drainage for the Talachulitna river, which flows north.

The Beluga region (Figure 3.11a) contains a seismic lineament named the Talachulitna seismic zone (TSZ) by Flores & Doser (2005). The TSZ is approximately aligned with the western margin of the BILR, near the Talachulitna river. Flores & Doser (2005) interpreted the TSZ to be dipping steeply to the northeast (their Fig. 4c). The scatter in their results—and ours (Figure 3.11a)—prevents us from identifying any alignment with depth.

Earthquake mechanisms are challenging to estimate for the TSZ. Flores & Doser (2005) tabulated one focal mechanism in this zone (AF2; their Table 2), from the AEC focal mechanism catalog, but the current AEC catalog has only five events (Figure 3.12b), none of which pre-date 2005. We present moment tensors for 9 events, all of which are shallower than 12 km (Table B.2). The mechanisms have considerable variation, with a predominance of thrust faulting consistent with east-west compression (Figure 3.11a).

Regional geophysical data and geological data provide context for the active seismicity. The BILR is mainly composed of Cenozoic and Mesozoic intrusive rocks (Ridgway et al., 2012; LePain et al., 2015) that are adjacent to Cenozoic sedimentary basins to the north (Susitna), west (Beluga), and south (Cook Inlet) (Figure 3.1b). Hackett (1977) and Saltus et al. (2016) used gravity data and magnetic data to identify the Beluga Mountain fault on the northern front of the BILR as a thrust fault dipping southwest; however recent fault kinematic data do not support a thrust interpretation Gillis et al. (2015). The Beluga Mountain fault does not appear to be seismically active or connected with the Talachulitna seismic zone.

Examining Figure 3.11a, we speculate that the Talachulitna seismic zone represents a north-striking, east-dipping thrust fault system that may represent some weakness within the crustal block north of the Castle Mountain fault and west of Susitna basin. This weakness, aligned with the western margin of the BILR, could accommodate some regional compression and contribute to uplift of the BILR.

Upper Cook Inlet region

Earthquakes in the Upper Cook Inlet region occur beneath Cook Inlet basin, a large, long-lived forearc sedimentary basin whose Tertiary strata have a maximal thickness of 7.6 km and overlie a Mesozoic section of approximately 8 km (Fisher & Magoon, 1978; Shellenbaum et al., 2010; LePain et al., 2013). It is bounded by the Aleutian Range to west, the Alaska Range and Talkeetna Mountains to the north, and the Kenai and Chugach Mountains to the east (see Figure 3.1). The Castle Mountain Fault to the north separates the Cook Inlet basin from the adjoining Susitna basin. The

similarities in structures of Cook Inlet and Susitna basins suggests that their histories are linked (LePain et al., 2013).

The 22 events in our study (Figure 3.11b, Table B.3) mostly have depths in the 10–20 km range, placing them either within the Mesozoic strata or the crystalline basement. The crust within Upper Cook Inlet (north of West Foreland) is more seismically active than the Lower Cook Inlet; this is possibly related to the underlying subduction of the Yakutat microplate (Eberhart-Phillips et al., 2006; Haeussler, 2008).

Folds in Cook Inlet are complex, discontinuous structures with variable shape and vergence that probably developed by right-transpressional deformation on oblique-slip faults extending downward into the Mesozoic strata beneath the Tertiary basin (Haeussler et al., 2000). A discussion of the complex folding and faulting structures in the basin can be found in Fisher & Magoon (1978); Haeussler & Saltus (2011).

Our moment tensor inversions for 22 events reveal thrust fault mechanisms whose strike angles are generally aligned with the Cook Inlet anticlines (Haeussler et al., 2000; Koehler et al., 2012) (Figure 3.11b). The simplest explanation is that the anticline structures, identified within active-source seismic data, arise from NW–SE thrust faulting identified from modern earthquakes.

Susitna region

The Susitna region exhibits diffuse seismicity with the larger earthquakes (22 in this study) exhibiting thrust fault mechanisms (Figure 3.11c, Table B.4). These mechanisms, with NW–SE P-axes, are consistent with the convergence direction of N21W (Bird, 2003) between the Pacific and North America plates. They are also consistent with the interpretation of subsurface compressional structures in the region Saltus et al. (2016).

The earthquakes in the Susitna region occur within a tectonically complicated region. The region is marked by the Susitna basin (Figure 3.3b) Kirschner (1988); Wilson et al. (2009), which is bounded by the Alaska Range to the north, the Talkeetna Mountains to the east, the BILR (and Beluga Mountain fault) to the west, and the Castle Mountain fault to the south. The crustal earthquakes are vertically bounded by the overlying Susitna basin and the underlying subducting Pacific plate. The Pacific plate exhibits two transitions in this region: (1) a kink in its geometry (e.g., Figure 3.6), from western dipping to more northwestern dipping (Ratchkovski & Hansen, 2002) and (2) an interpreted transition from normal subducting crust in the west to overthickened Pacific/Yakutat crust in the east (Figure 3.1a). It is possible that either of these slab-related features contributes to the concentration of crustal seismicity in the eastern part of the Susitna region.

Comparison between the crustal earthquakes and the basement surface (Figure B.11c) reveals several earthquakes below the deepest part of Susitna basin and within the uppermost 10 km. It

is possible that these earthquakes occur on deeper extensions of the structures mapped within the subsurface basin structures (Lewis et al., 2015; Haeussler et al., 2017). The diffuse seismicity in the eastern portion of the Susitna region underlies the shallowest portion of the basin and are not associated with any previously identified subsurface structures.

3.6.2 Implications of minor earthquakes for active faults

From our perspective, seismic evidence for an active fault includes: (1) alignment of seismicity into a lineament (2) occurrence of moment tensors with one of its two possible fault plane parallel to the lineament (3) occurrence of large ($M \geq 6$) earthquakes. This seismic evidence should be assessed alongside geological evidence, whether in the form of slip rates inferred from dated offset units at the surface, from structural offsets inferred from seismic imaging and potential field data, and from paleoseismic evidence of past large earthquakes (Haeussler et al., 2002; Koehler et al., 2012; Saltus et al., 2016; Koehler & Carver, 2018).

Our presentation in Figure 3.11 displays these three types of seismic evidence: relocated hypocenters of modern earthquakes, source mechanisms for the largest modern earthquakes, and estimated epicenters of the largest two historical earthquakes, in 1933 and 1943. We also superimpose previously published faults, and here we discuss the possible connections between faults identified from surface and subsurface geological data with seismic activity at depth.

Most of the relocated seismicity does not exhibit seismic lineaments (Section 3.5). The only lineament we are confident about is the previously identified Talachulitna seismic zone (Figure 3.11a). It is possible that this seismic zone is an expression of a single fault, but the source mechanisms are variable, and the structure does not have definitive evidence for hosting any moderate or large earthquake. To the northeast, within the Susitna region (Figure 3.11c), the seismicity is diffuse but the mechanisms are more consistent, exhibiting thrust faulting. Deformation within the crust appears to be broadly distributed, rather than concentrating on a few discrete faults. The same pattern is true to the south, within the Upper Cook Inlet region (Figure 3.11c): diffuse seismicity with consistent thrust fault mechanisms. In both the Susitna region and the Upper Cook Inlet region, there are subsurface fault and fold structures identified from modeling seismic reflection data and potential field data (gravity, magnetics). If these shallowly-identified faults penetrate below the sedimentary basements (Figure 3.3b), then it seems reasonable to ascribe the style of faulting inferred from the earthquake mechanisms to the style of faulting occurring near the surface. Therefore we would ascribe thrust faulting to the active folds in Cook Inlet basin (Bruhn & Haeussler, 2006) and thrust faulting to the structures in Susitna basin (Lewis et al., 2015; Haeussler et al., 2017). This is in contrast to the existing catalog of earthquake mechanisms, which favors strike-slip faulting in these regions (Figure 3.12).

3.6.3 Structures responsible for 1933, 1943, and 1954 earthquakes

Large earthquakes rupture along faults with dimensions of tens of kilometers. Previous studies of large sets of earthquakes provides scaling between magnitude and fault dimensions. Assuming a circular fault (radius r , fault dimension $2r$) and a stress drop between 0.2 MPa and 20 MPa (Shearer et al., 2006), the corresponding fault dimension would be

- 10–44 km for the 1954 M_w 6.4 earthquake
- 15–70 km for the 1933 M_w 6.8 earthquake
- 27–125 km for the 1943 M_w 7.3 earthquake

The empirical relationships of Mai & Beroza (2000) are also within these ranges. These dimensions should be kept in mind when examining Figures 3.6 and 3.11.

Our probabilistic hypocentral estimations for the 1933, 1943, and 1954 earthquakes (Figure 3.6, Section 3.3.1) provide a starting point for interpreting the structures responsible (and not responsible) for these earthquakes. The 1933 earthquake (Figure 3.6) occurred within the region of the concentration of modern earthquakes in the Upper Cook Inlet region (Figure 3.11b). It seems possible that one of the northeast-striking thrust faults could have hosted the 1933 earthquake. The 1943 earthquake (Figure 3.6) maximum likelihood epicenter is on the Beluga Mountain fault (Figure 3.11c), yet the uncertainty in the epicenter also covers the north-striking faults in Susitna basin, as well as the Talachulitna seismic zone (Figure 3.11a).

Reliable source mechanisms for historical earthquakes would provide valuable constraints on the (unknown) host faults. Here we summarize results, and challenges, from Doser & Brown (2001), who estimated source mechanisms for the 1933, 1943, and 1954 earthquakes, among others. They used limited telesismic data to estimate the source mechanisms: P, PP, and S waveforms for 13 global stations, as well as first-motion polarities, where available. (By comparison, there are >100 global stations providing arrival times used in Figures 3.6 and 3.5.) They present waveform comparisons for all events in their Figure A2, offering the reader the chance to assess the reliability of the results. The numbers of stations and waveforms used for each event were as follows: 3 stations (8 waveforms) for 1933, 5 stations (9 waveforms) for 1943, 6 stations (11 waveforms) plus first-motion polarities for 1954. Surface waves were not used, though they provide stable constraints for global moment tensor inversions Dziewonski et al. (1981); Duputel et al. (2012), mainly owing to the insensitivity of their long periods to 3D structural heterogeneities in Earth.

The picture of faulting from the 1933 and 1943 mechanisms Doser & Brown (2001) is one of strike-slip faulting (Figure 3.6), either right-lateral on a northeast-striking fault or left-lateral on a northwest-striking fault. Based on the points above, and from our own experience examining

moment tensor uncertainties with modern regional earthquakes (Silwal & Tape, 2016), we would advise caution in basing any interpretation on the historical mechanisms. For example, rotation of these beachballs by 90° about their P-axes would lead to a north-striking thrust fault that would satisfy some of the historical seismic waveforms and first-motion polarities.

The Castle Mountain fault—the principal active fault within the Cook Inlet and Susitna region—was not responsible for the 1933 or 1943 earthquakes (Figure 3.6), corroborating Doser & Brown (2001). Two modern earthquakes, each well-recorded by regional stations, provide support for the Castle Mountain fault—or at least the eastern portion—as a right-lateral strike-slip fault. These earthquakes occurred just east of the Cook Inlet and Susitna region, as 1984-08-14 M_w 5.8 (depth 15 km) and 1996-11-11 M_l 4.6 (depth 17 km). A detailed study of the 1984 earthquake was presented in Lahr et al. (1986).

The 1954 earthquake likely occurred within the subducting Pacific plate, rather than on the subduction interface or within the lower overriding crust. The depth distribution of modern seismicity in this region is nearly continuous (Figure 3.7c, Figure 3.1b), making it challenging to discriminate among the three possibilities. This event has the benefit of better data than the older events, and therefore the mechanism should be more reliable. Two source mechanisms from previous studies are shown in Figure 3.6 and reveal strike-slip faulting, not low-angle thrust faulting that would be expected for the subduction interface.

3.7 Summary

We present a seismological study of the tectonically complex region of Cook Inlet and Susitna, west of Anchorage, Alaska (Figure 3.1), with emphasis on crustal earthquakes. Using arrival time data, we estimate hypocenters of all 11 historical earthquakes $M_w \geq 5.8$ that have occurred in the Cook Inlet and Susitna region. Using waveforms from modern earthquakes, we estimate source mechanisms for 53 crustal earthquakes (M_w 2.5 to 4.8). Using arrival time data, we relocate a catalog of 5726 earthquakes ($M_l \geq 1.5$). We examine these seismological results in the context of regional tectonics, regional structures (basins, faults, folds), and previously published source mechanisms of older (and larger) earthquakes.

Here we summarize our main findings:

1. Within the Cook Inlet and Susitna region, we can generalize the earthquake patterns into two time periods (Figure 3.4). In the last several decades there have been small-magnitude thrust events in the crust and larger events in the slab. Prior to 1950 or so there have been large-magnitude crustal earthquakes that were possibly strike-slip.

The existence of two crustal earthquakes (1933 M_w 6.8 and 1943 M_w 7.3) motivates our examination of modern crustal earthquakes and geological structures. The crust has not produced notable earthquakes in the recent decades of high-quality seismic data: there are zero crustal earthquakes in the GCMT catalog ((Dziewonski et al., 1981): 1976–) within our three focus regions (Figure 3.8b).

2. Our source mechanisms favor an interpretation of thrust faulting (Figure 3.12a) over strike-slip faulting (Figure 3.12b). Uncertainties in the source mechanisms are considerable, owing to the small magnitudes (which limits the inclusion of surface waves) and the extreme crustal heterogeneity (notably basins: Figure 3.3b), which was not accounted for in modeling synthetic seismograms.
3. Seismicity in the Susitna region (Figure 3.11c, Figure 3.13) is diffuse (Ratchkovsky et al., 1998) and may be related to slab dynamics (Section 3.6.1).
4. The 1933 M_w 6.8 earthquake occurred beneath Cook Inlet basin, in a region exhibiting northeast-striking thrust fault source mechanisms (Figure 3.11b) that are aligned with the strike of active fold anticlines (Bruhn & Haeussler, 2006). It is possible that the 1933 earthquake ruptured as a thrust fault, though the previously published source mechanism (using 3 stations) is a strike-slip mechanism.
5. The 1943 M_w 7.3 Susitna earthquake is the fourth largest earthquake ever to occur in mainland Alaska, following 1964 M_w 9.2 megathrust, 2002 M_w 7.9 Denali fault, and 1979 M_w 7.4 Wrangell-St. Elias. Its hypocenter was beneath the Susitna basin, possibly on a structure associated with the Beluga Mountain fault or the Talachulitna seismic zone (Figure 3.11a). Moment tensors of crustal events closest to the 1943 epicenter exhibit thrust mechanisms, consistent with inferred subsurface structures (Lewis et al., 2015; Saltus et al., 2016).
6. The 1954 M_w 6.4 earthquake beneath the Kenai peninsula was likely an intraslab earthquake. It produced the strongest shaking (MMI 8) ever documented on the western Kenai peninsula (Section 3.8). The subducting Pacific slab has produced much larger earthquakes, such as the deeper and more distant M_w 7.1 earthquake on 2016-01-24. For scenario earthquakes, it is worth considering a M_w 7.0 earthquake in the 1954 hypocentral region.
7. There appears to be a concentration of active seismicity and also large historical earthquakes (1933, 1943) beneath the deepest sedimentary basins (Cook Inlet and Susitna: Figure 3.3b). It is possible that the dynamical processes that influence basin development—over the past millions of years—are also responsible for modern earthquakes. Alternatively, modern earthquakes could arise from reactivation of ancient faults.

3.8 Summary of felt reports for 1933, 1943, and 1954 earthquakes

Here we summarize the entries for the 1933, 1943, and 1954 earthquakes within the annual earthquake volumes of the U.S. Coast and Geodetic Survey (Neumann, 1935; Bodle, 1945; Murphy & Cloud, 1956). See felt report locations on maps in Figure B.14.

1933-04-27 M_w 6.8

The complete entry in Neumann (1935):

*April 26: 16:36**. Instrumental epicenter 62° north, 151° west. Anchorage, VI. Telegraph lines were down for a distance of 50 miles from Anchorage. The shock lasted about 3 minutes. Plate glass windows in several stores were broken and stocks of good tumbled from their shelves. This earthquake was considered by residents as the worst in 30 years.

The quake was felt strongly on Kodiak Island and along the Aleutian Islands. It was felt strongly at Curry, McGrath, Seward, and Wasilla; Dillingham (Kanakanak), IV; reported light at Healy. The shock was felt at College, Fairbanks, Susitna, Valdez, and Whale Island.

Because of the difficulty in correlating the times of occurrence of the following aftershocks it has been considered best to list them all as individual shocks, even though it is evident that this is not always true.

April 26: Homer; earthquake and following tremors.

April 26: Kasllof;

April 26: Big Susitna River District, VII.

April 26: Old Tyonek, VII. Houses shaken off foundations.

1943-11-03 M_w 7.3

The complete entry in Bodle (1945):

*November 3: 04:32.3.** Anchorage. Sharp shock with abrupt heaving motion made doors swing and windows rattle. Generally felt. A light after-shock occurred at 05:40. Several slight tremors were felt at intervals until about 07:30. Pen on recording rain gage made mark about $\frac{3}{4}$ inch wide at time of main shock. Similar marks were recorded on the barograph traces. Epicenter probably near 62° north, 151° west.

Felt at McGrath 04:33. Slight shock reported by Weather Bureau Observer as continuing for about fifteen seconds. "Wall clocks in the Civil Aeronautics Administration

and Weather Bureau Offices were stopped. The baragraph trace showed no indication of the quake . . . ”

Felt at Bethel 04:37. Tremors lasting 20 seconds were felt by several. Faint rumbling underground and moderately loud cracking of ice was heard. Building swayed. “The noise moved down the river quickly and then seemed to pass under the station making the earth tremble comparable to a locomotive passing. The ice in the river made a cracking noise for about an hour after the tremors, which lasted about 20 seconds.”

Following Bodle (1945), Brockman et al. (1988) lists only three felt reports (Anchorage, McGrath, and Bethel), but we found 10 additional felt reports within the monthly weather records. Furthermore, p. 4 of the 1943-11-03 Fairbanks Daily News-Miner had an articles headlined “Big Quake Felt Here This Morn”. We speculate that the shortage of reports in Bodle (1945) was due to the national focus on WWII, which may have limited other duties such as earthquake compilations.

1954-10-03 M_w 6.4

The complete entry in Murphy & Cloud (1956):

October 3: 01:18:46*. Epicenter $60\frac{1}{2}^\circ$ north, 151° west, Kenai Peninsula, W. VIII. A sharp earthquake rocked a 1,000 square mile area of the lower Alaska mainland. Concrete walls cracked; plaster showered down; plate glass windows shattered; merchandise toppled from shelves at Anchorage, Homer, Kenai, Seward, Sterling, and Valdez. Minor landslides spilled down on the Seward-Anchorage highway. More than 140 feet of railroad tracks were knocked out of commission just north of Potter. Residents on top floors in Anchorage’s two 14-story “skyscrapers” fled into the streets when the violent rocking broke water connections. At the Denali Theater, where a midnight show was in progress, some 850 patrons rushed toward the exists [sic], climbing over seats in a frenzy to escape. Three persons were reported injured slightly in the rush. Motorists driving cars at the time of the quake said it felt “like moving along on a flat tire.” It was also felt at Cordova, Eklutna, Fairbanks, Kaslof, Kodiak, Latouche, Mantanuska [sic] Agricultural Experiment Station, Moose Pass (severe enough to shake things from the shelves), Palmer, Puntilla, and Yakutat. Five aftershocks of a few seconds duration followed the main quake at 02:43, 05:21, 05:34, 06:18, and 07:26.

The MMI VIII shaking intensity for the 1954 M_w 6.4 earthquake was the largest ever reported on the western Kenai Peninsula (Homer, Kenai, Sterling)—even exceeding the MMI VII of the 1964 M_w 9.2 earthquake (Brockman et al., 1988).

3.9 Acknowledgments

This project was supported by the Earthquakes Hazards Program of the United States Geological Survey, Award G15AP00052. We thank Domenico Di Giacomo of the International Seismological Centre for providing arrival time data for six of the historical earthquakes presented here and in Lomax et al. (2018): 1929-07-03, 1933-06-12, 1933-06-13, 1933-06-19, 1936-10-23, 1937-10-24. We thank Celso Alvizuri for code developments for data processing and moment tensor inversions.

Table 3.1: Earthquake selection for three target sub-regions and for the full region. N_e is the number of earthquakes analyzed in each region for a particular method.

Region	longitude		latitude		method	N_e	max depth (km)	min mag	date range
	min (°)	max (°)	min (°)	max (°)					
Beluga region	-151.50	-151.10	61.25	61.90	moment tensor	9	30	M_I 2.5	2007-08-15 2017-01-01
Upper Cook Inlet region	-151.50	-150.60	60.60	61.25	moment tensor	22	30	M_I 2.5	2007-08-15 2017-01-01
Susitna region	-151.10	-149.90	61.50	62.50	moment tensor	22	30	M_I 3.0	2007-08-15 2017-01-01
Cook Inlet and Susitna region	-151.75	-149.50	60.50	62.50	historical	12	200	M_W 5.8	1904-01-01 2017-01-01
	-152.00	-149.00	60.50	62.50	double difference	5726	30	M_I 1.5	1990-01-01 2017-01-01

Table 3.2: Earthquakes $M \geq 5.8$ in the Cook Inlet and Susitna region (Table 3.1) of south-central Alaska since the start of the instrumental era in 1904. The events are selected from the ISC-GEM catalog (before 1976-01-01) and GCMT catalog (after 1976-01-01). ISC-G = ISC-GEM 5.0 Storchak et al. (2013), GCMT = Global Centroid Moment Tensor catalog Dziewonski et al. (1981); Ekström et al. (2012). NA means that the earthquake was outside the time interval of a particular study.

origin time	ref.	mag. M_w	ref.	GR Gutenberg & Richter (1954) M	Abe Abe (1981) M_s, m_b	EV Engdahl & Villaseñor (2002) M_w	DB Doser & Brown (2001) M_w
1933-04-27 02:36:07	ISCG	6.78	ISCG	7.0	6.9, 7.1	6.90	7.0
1933-06-12 15:23:41	ISCG	5.82	ISCG	–	–	–	–
1933-06-13 22:19:51	ISCG	5.97	ISCG	6.25	–	–	–
1933-06-19 18:47:46	ISCG	5.85	ISCG	6.0	–	–	–
1934-06-18 09:13:52	ISCG	5.97	ISCG	6.75	–	6.60	6.1
1936-10-23 06:24:21	ISCG	6.82	ISCG	–	–	–	–
1941-07-30 01:51:29	ISCG	6.39	ISCG	6.25	–	–	6.3
1943-11-03 14:32:20	ISCG	7.34	ISCG	7.3	7.4, 7.1	7.20	7.0
1954-10-03 11:18:48	ISCG	6.36	ISCG	NA	–	–	6.6
1974-12-29 18:25:01	ISCG	5.92	ISCG	NA	–	–	NA
1975-01-01 03:55:13	ISCG	5.92	ISCG	NA	–	7.40	NA
1991-05-01 07:18:46	GCMT	6.30	GCMT	NA	NA	6.2	NA

Table 3.3: Estimated depths, with uncertainties, for the earthquakes in Table 3.2. The depths from NonLinLoc (NLL) are for the maximum likelihood; Figure 3.7 shows examples of the depth distribution of all posterior hypocenters. The right three columns list the vertical distance from the ISC-GEM epicenter to the subduction interface, for three different interface models. Events marked as * are likely slab events. For the Engdahl catalog, DEQ means that depth is a free parameter, and FEQ means that depth is fixed based on independent information.

	NLL (this study)	GR Gutenberg & Richter (1954)	DB Doser & Brown (2001)	EV Engdahl & Villaseñor (2002)	ISCG Storchak et al. (2013)	JB10 Jadamec & Billen (2010)	H12 Hayes et al. (2012)	L13 Li et al. (2013)
1933-04-27	0.33	0	9 ± 4	35 (FEQ)	15 ± 4	54	68	63
1933-06-12	0.65	0	–	–	15 ± 9	71	77	73
1933-06-13	12.71	0	–	–	15 ± 9	85	87	82
1933-06-19	16.29	0	–	–	15 ± 7	64	71	66
1934-06-18*	49.20	80	76 ± 10	50 (DEQ)	60 ± 9	63	72	66
1936-10-23	0.33	–	–	–	15 ± 14	56	68	63
1941-07-30	0.33	0	–	–	35 ± 14	49	64	59
1943-11-03	17.27	0	27 ± 4	35 (FEQ)	15 ± 4	73	75	71
1954-10-03*	55.88	N/A	60 ± 10	64	62 ± 5	40	52	45
1974-12-29*	68.10	N/A	N/A	–	65 ± 5	56	64	57
1975-01-01*	64.03	N/A	N/A	–	63 ± 5	43	57	48
		GCMT	AEC					
1991-05-01*		118	115	114 (DEQ)	113 ± 5	123	110	100

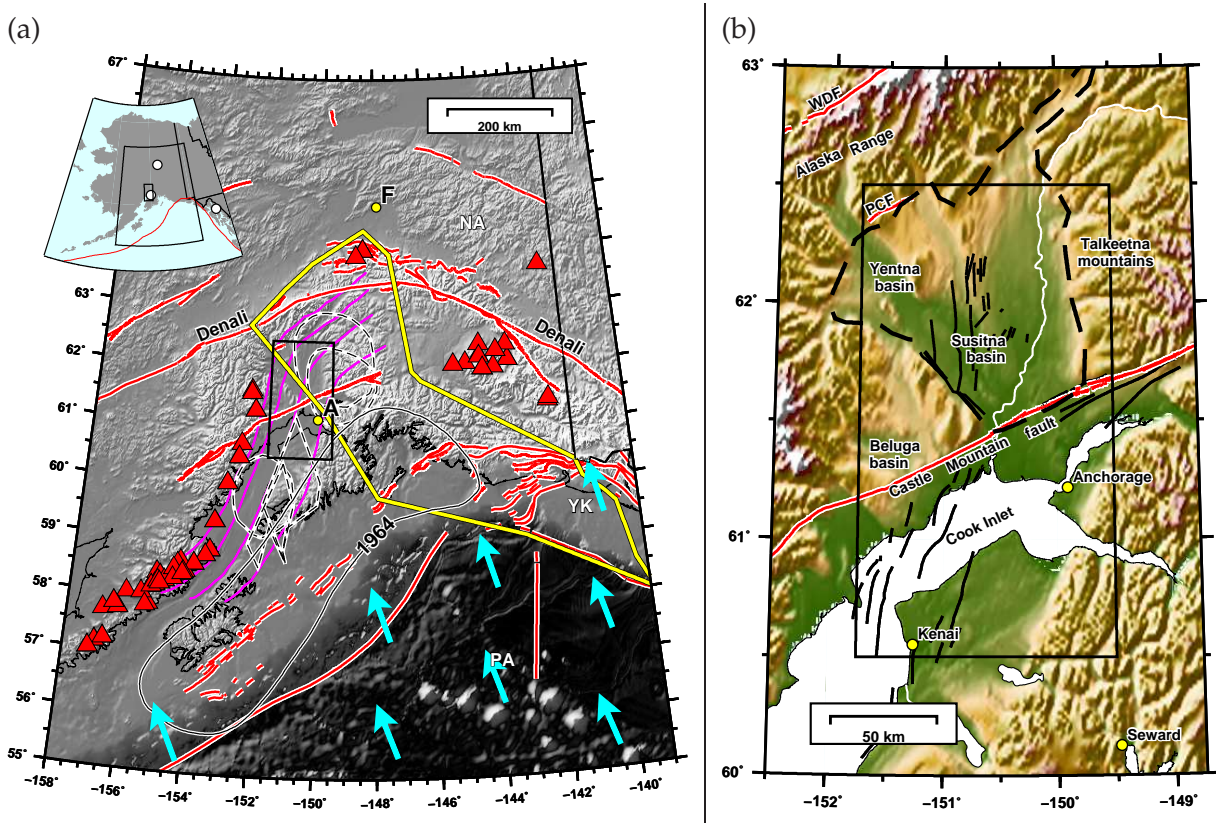


Figure 3.1: (a) Active tectonic setting of the Aleutian–Alaskan subduction zone, south-central Alaska. The rectangle in the middle shows the main study region. Cyan arrows shows the plate vectors for the subducting Pacific plate (PA) under the North American plate (NA) (Bird, 2003). Magenta curves are the 40 km, 60 km, 80 km, and 100 km contours of the top of the Pacific plate (Li et al., 2013). Yellow bounded region denotes the surface and subsurface extent of the Yakutat block (YK) (Eberhart-Phillips et al., 2006). Red triangles represent active volcanoes. Black dashed lines are inferred slow slip events from various sources (Ohta et al., 2006; Wei et al., 2012; Fu & Freymueller, 2013; Li et al., 2016). Also marked is the aftershock zone of the 1964 M_w 9.2 earthquake. Labeled cities: Anchorage (A) and Fairbanks (F). (b) Physiographic map of the Cook Inlet and Susitna region, south-central Alaska. Active faults are plotted in red and include Castle Mountain, Pass Creek (PCF) and the western Denali fault (WDF) at upper left (Koehler et al., 2012). Other active faults (Haeussler et al., 2017) and folds (Koehler et al., 2012) are marked in black. Sedimentary basins are labeled: Cook Inlet, Susitna, Yentna, and Beluga. Cook Inlet basin underlies Cook Inlet and the western Kenai peninsula (Shellenbaum et al., 2010). Black dashed lines are the boundaries of Susitna basin from Kirschner (1988).

Figure 3.2 [FOLLOWING PAGE]:

Seismicity in south-central Alaska. (a) Alaska Earthquake Center (AEC) catalog: $M_w \geq 2$, 1990-01-01 to 2017-01-01, colored by depth. The box, containing Anchorage (A), is the focus region of this study; the two profiles are shown in (b) and (c). The red lines are the active faults from Koehler et al. (2012). The blue line is the lateral extent of slab seismicity, digitized from the full AEC catalog. (b) S–N cross-section of (a) along the longitude line of -150.75° . Seismicity within 20 km of the profile is shown. Three large earthquakes of interest are projected onto the profile: 1933 $M_w 6.78$, 1943 $M_w 7.34$, and 1954 $M_w 6.36$; the hypocenters are estimated from NonLinLoc. Geometric boundaries shown are the plate interface (Li et al., 2013), the Moho (Wang & Tape, 2014), and topography (Amante & Eakins, 2009) exaggerated by a factor of 20. (c) SE–NW cross-section of (a) between Anchorage ($x = 0$ km) and the 1943 earthquake.

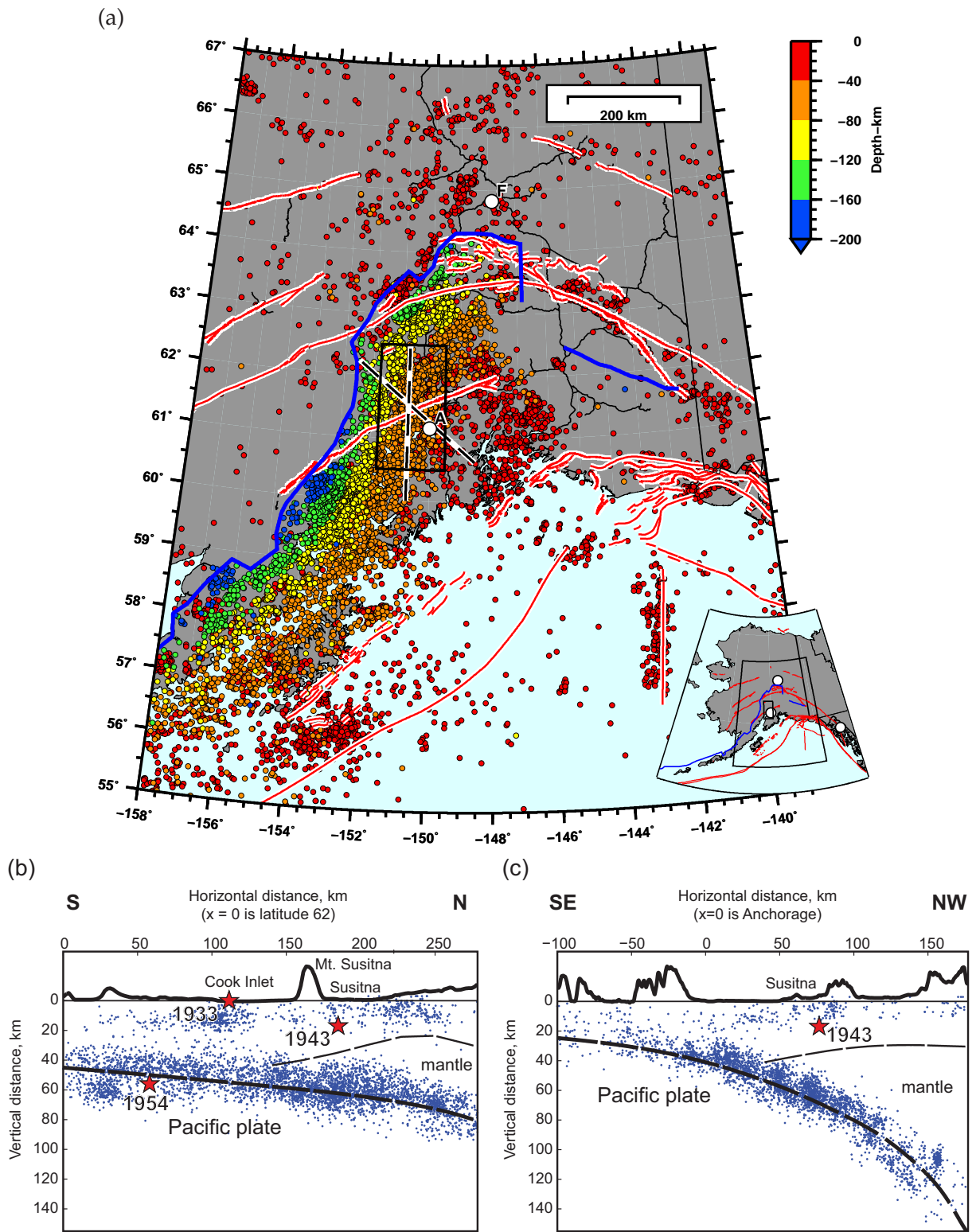


Figure 3.2:

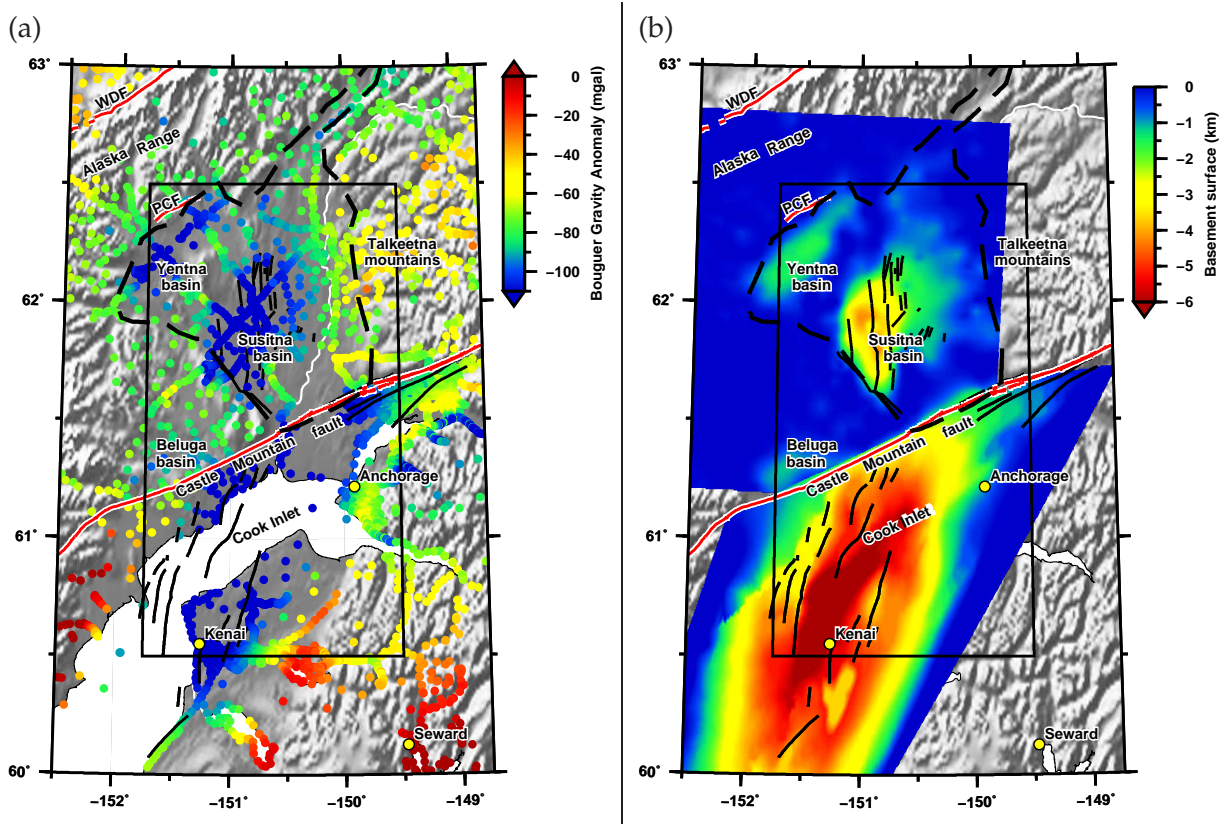


Figure 3.3: Gravity data and estimated basement depths for the Cook Inlet and Susitna region; see physiographic map in Figure 3.1b for comparison. Faults and folds plotted include active faults (Koehler et al., 2012), active folds in Cook Inlet (Bruhn & Haeussler, 2006; Koehler et al., 2012), and faults in the Susitna basin (Lewis et al., 2015; Haeussler et al., 2017). (a) Bouguer gravity data (Saltus et al., 2016). (b) Maps of depth to Tertiary basement for Cook Inlet basin (Shellenbaum et al., 2010), as well as basement surfaces for Susitna basin (Wilson et al., 2009), Yentna basin, and Beluga basin (Stanley et al., 2013). The dashed outline is the basin-bounding region of Kirschner (1988); Meyer Jr. (2005).

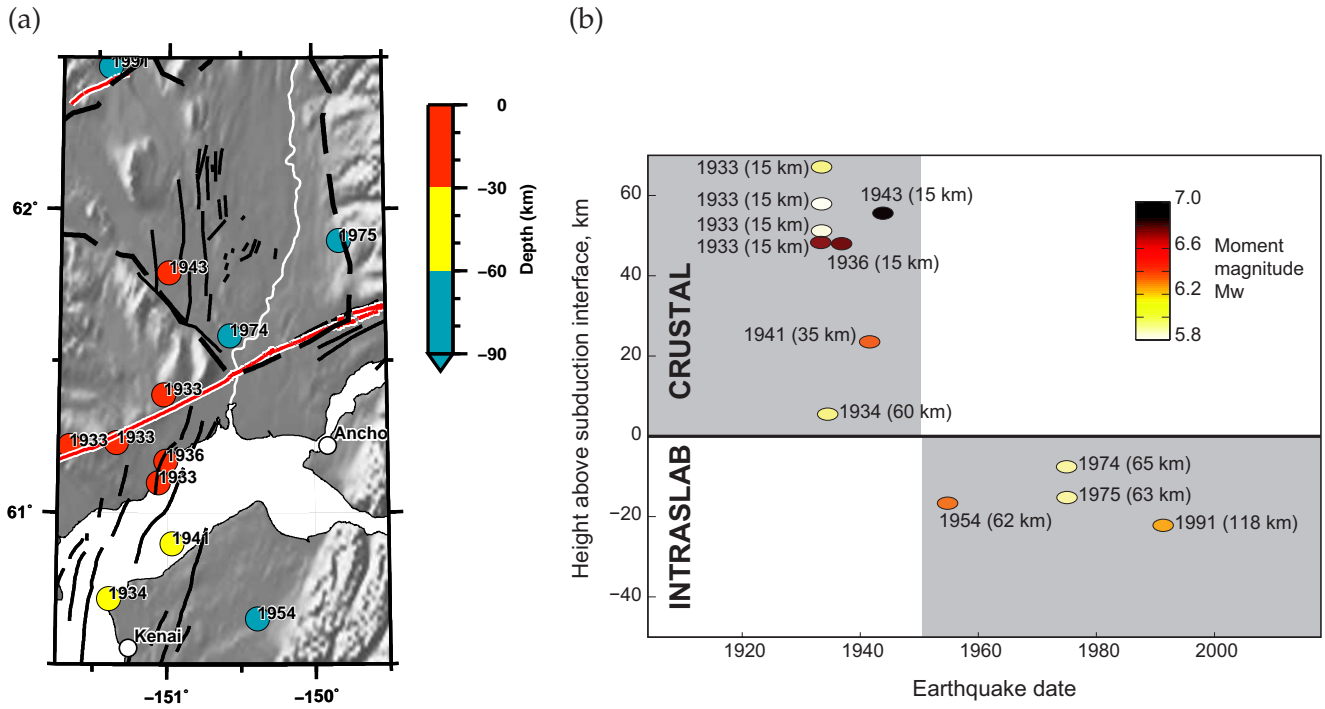


Figure 3.4: All 12 major earthquakes ($M_w \geq 5.8$) in the Cook Inlet and Susitna region (see Table 3.1). Earthquakes are selected from the ISC-GEM catalog for the time interval 1904-01-01 to 2017-01-01. (a) Map showing epicenters, colored by depth. (b) Plot of height above subduction interface (Li et al., 2013) as a function of origin time, for the 12 earthquakes in (a). The checkered shading at the year of 1950 accentuates the pattern of early crustal earthquakes and later (more recent) slab earthquakes.

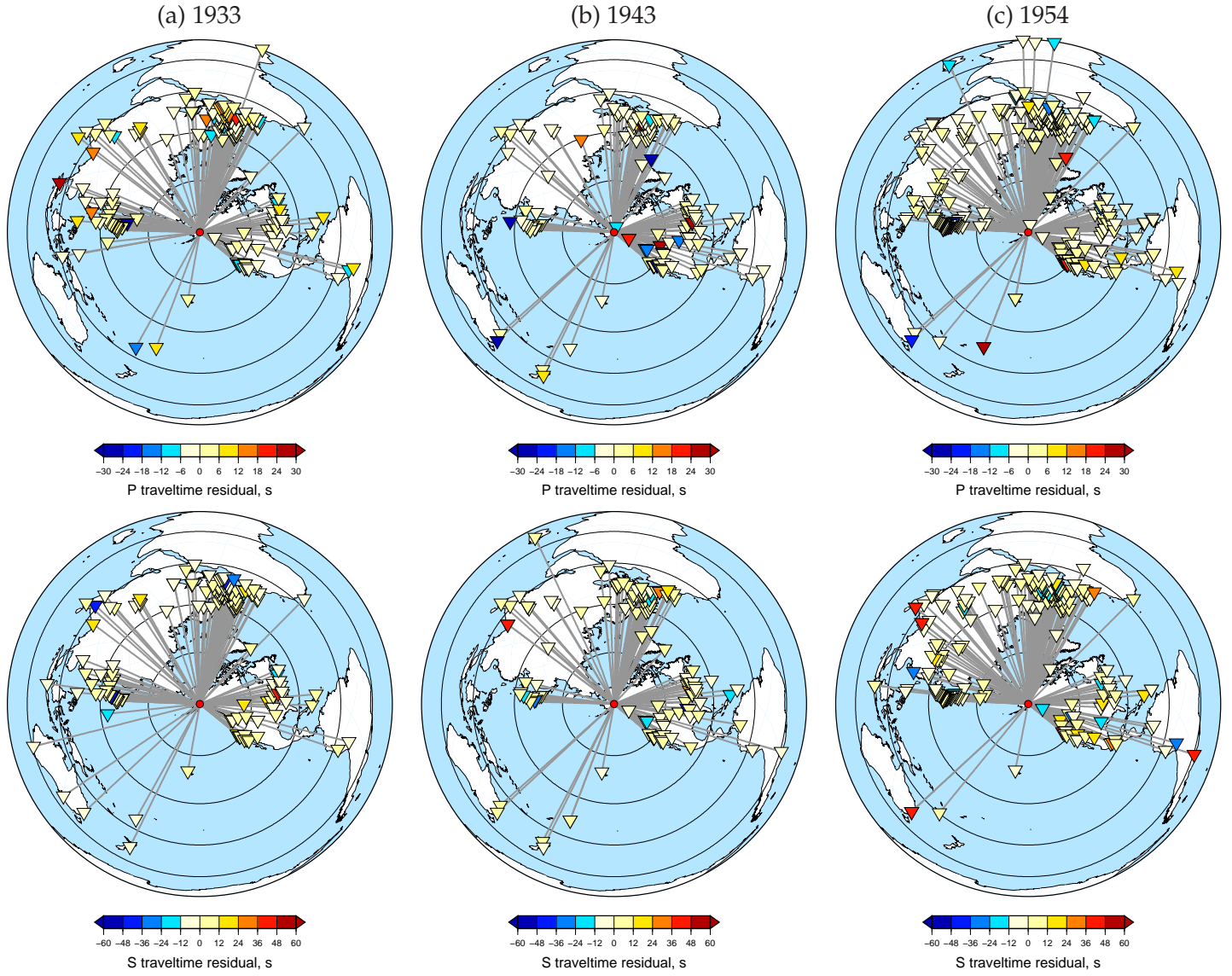


Figure 3.5: Station coverage for P arrival times (top) and S arrival times (bottom) used in estimating the epicenters for the 1933, 1943, and 1954 Alaska earthquakes. The maximum likelihood epicenter for each earthquake is marked by red circle at the center. The arrival times of the phases were obtained from ISC (International Seismological Centre, 2015). The stations are marked by inverted triangles and colored by the difference between the ISC arrival time and synthetic obtained using the ak135 velocity model (Kennett et al., 1995). Circles show epicentral distances of $\Delta = 30^\circ$, 60° , 90° , 120° , and 150° . The posterior epicenters for each earthquake are shown in Figure 3.6. For details of the results, see Lomax et al. (2018). (a) 1933 $M_w 6.78$ earthquake. There are 174 P arrival times and 158 S arrival times recorded by 179 stations. (b) 1943 $M_w 7.34$ earthquake. There are 137 P arrival times and 136 S arrival times recorded by 137 stations. (c) 1954 $M_w 6.36$ earthquake. There are 346 P arrival times and 223 S arrival times recorded by 263 stations.

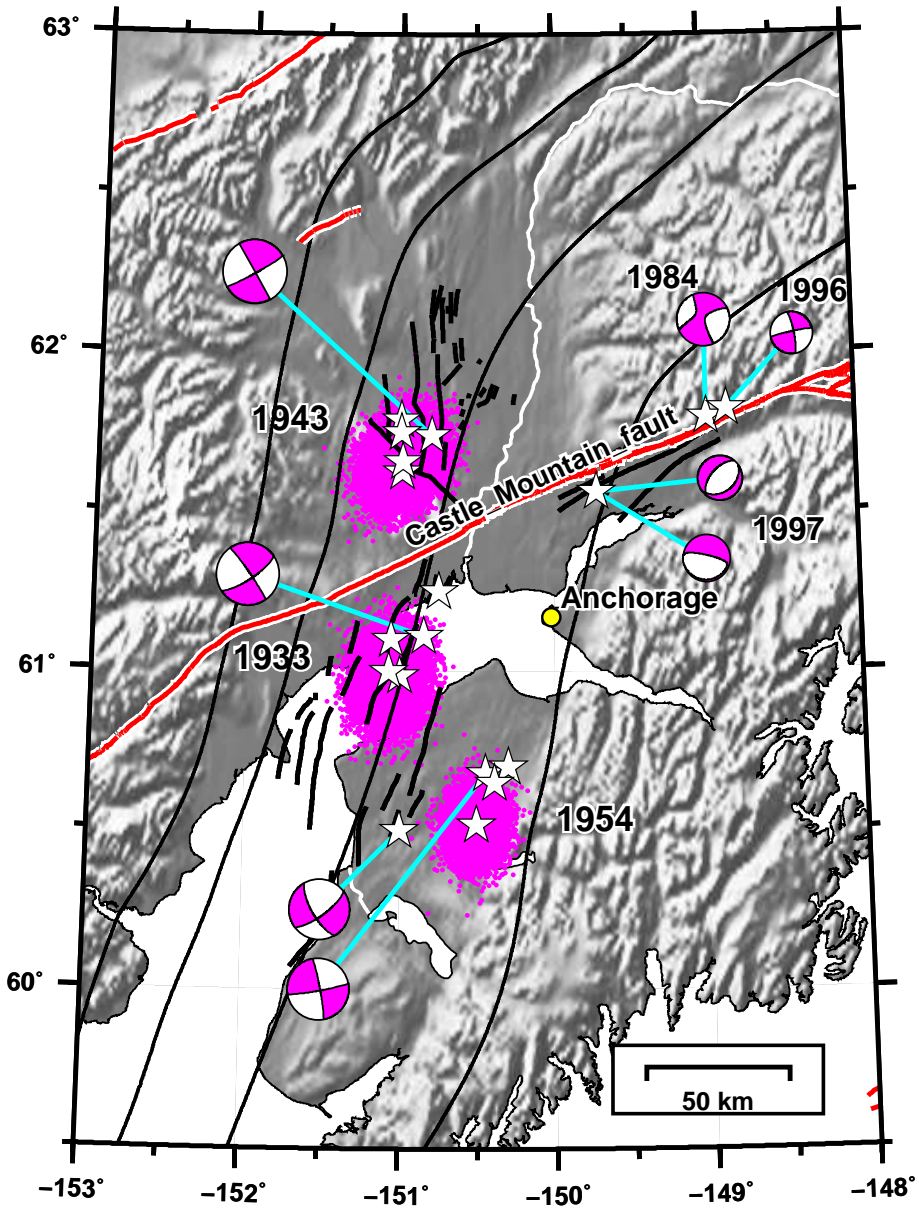


Figure 3.6: Estimated epicenters for the 1933, 1943, and 1954 earthquakes; see Lomax et al. (2018) for details. Each cloud of colored dots represents the posterior epicenters, which are centered on a maximum likelihood epicenter (star). Other stars show epicenter estimates from other studies (Table B.1: Engdahl & Villaseñor (2002); Doser & Brown (2001); Gutenberg & Richter (1954); Storchak et al. (2013)). See Figure 3.7 for information regarding the depths of the posterior samples relative to the underlying subduction interface. Also shown are active faults and folds (Koehler et al., 2012; Haeussler et al., 2017) and contours of the top of the subducting Pacific plate (40 km, 60 km, 80 km, 100 km) (Li et al., 2013). The beachballs show source mechanisms for 1933 Doser & Brown (2001), 1943 Doser & Brown (2001), 1954 Doser & Brown (2001); Wickens & Hodgson (1967), 1984 Dziewonski et al. (1981), 1996 (AEC), and 1997 (AEC, Dziewonski et al. (1981)). The 1984, 1996, and 1997 epicenters are from the AEC catalog.

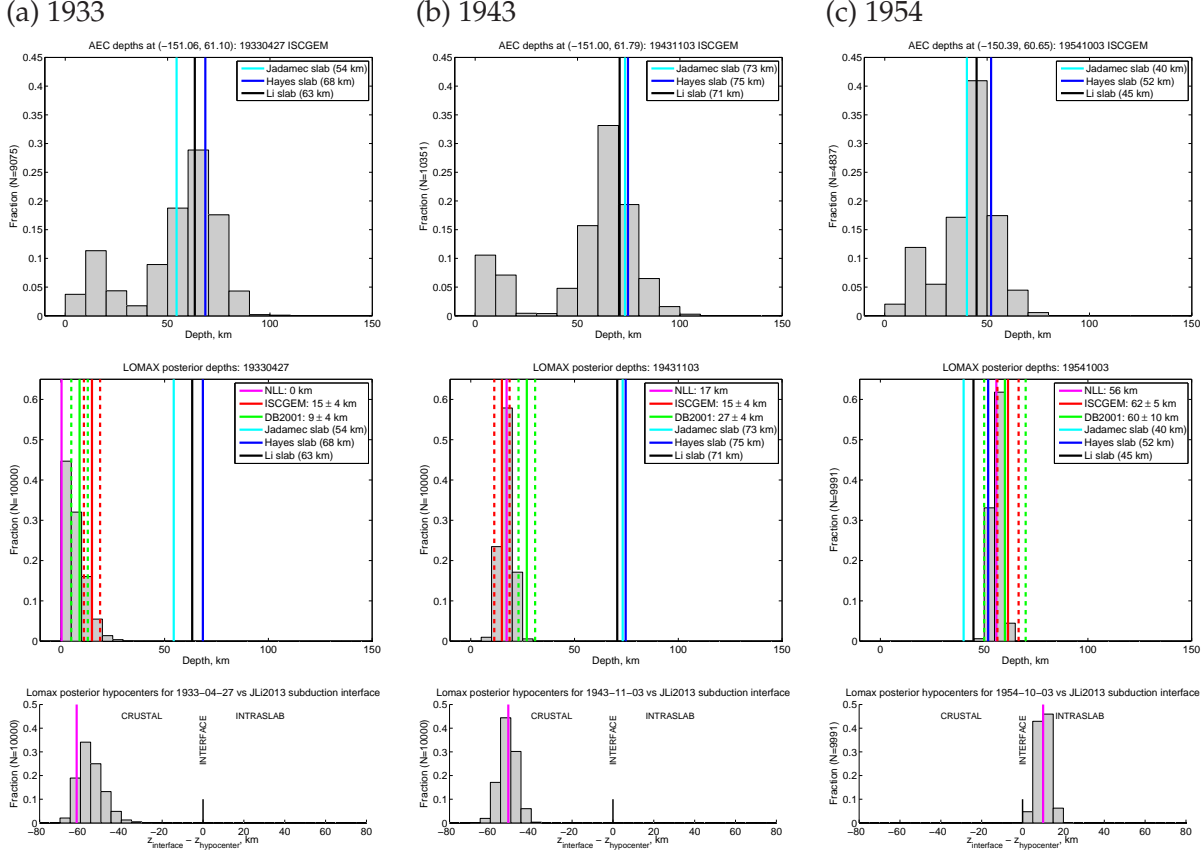


Figure 3.7: Estimated depth to slab for three historical earthquakes. Each hypocentral estimation using NonLinLoc provides a cloud of posterior hypocenters; see Figure 3.6 for a map view. For each posterior hypocenter we evaluate the vertical distance to the subduction interface models of Jadamec & Billen (2010) (cyan), Hayes et al. (2012) (blue), and Li et al. (2013) (black). (a) 1933-04-27 M_w 6.8 earthquake. (top) Distribution of depths of modern microseismicity ($M \geq 0$, 2000–2018) whose epicenters are within a 40 km of the ISC-GEM epicenter. (middle) Distribution of depths of posterior hypocenters. Also shown are our maximum-likelihood estimate from NonLinLoc (magenta) and the depth estimates, with uncertainties, from ISC-GEM (Storchak et al., 2013) (red) and DB2001 (Doser & Brown, 2001) (green). (bottom) Distribution of vertical distances between our posterior hypocenters and the underlying subduction interface from Li et al. (2013). Distributions to the left favor a crustal interpretation for the earthquake; distributions to the right favor an intraslab interpretation. (b) 1943-11-03 M_w 7.3 earthquake. (c) 1954-10-03 M_w 6.4 earthquake.

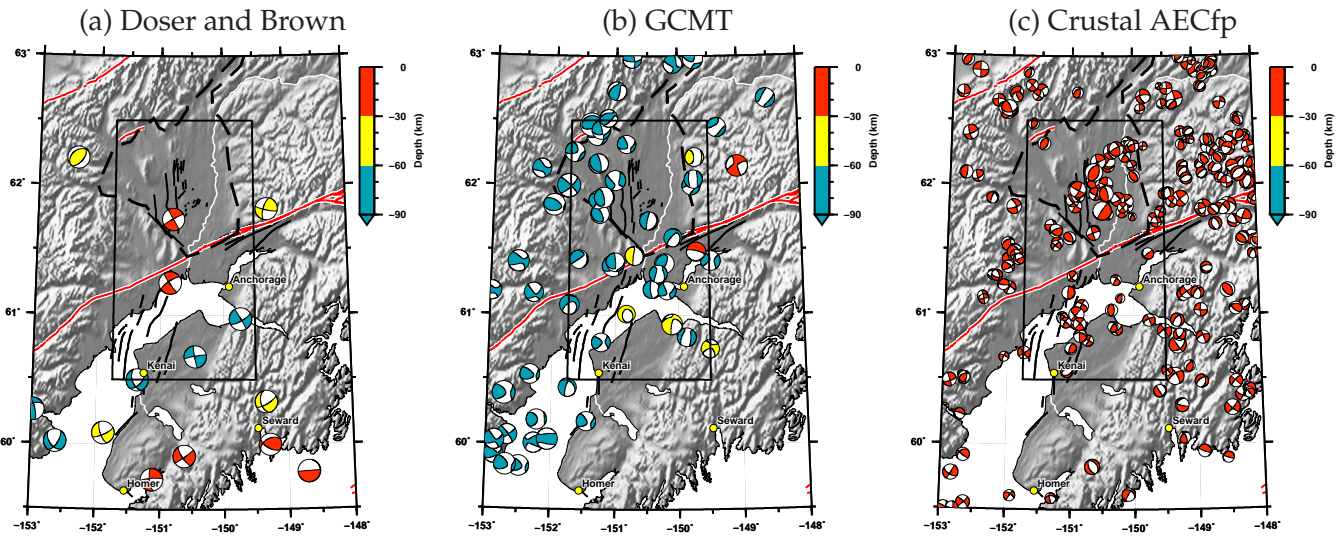


Figure 3.8: Moment tensor solutions from previous studies. (a) Major historic events (1920–1964), from Doser & Brown (2001). The three earthquakes near longitude -150° are, from north to south, the 1943, 1933, and 1954 earthquakes. (b) All events from the GCMT catalog, 1976–2017 (Dziewonski et al., 1981; Ekström et al., 2012). (c) All crustal ($\text{depth} \leq 30 \text{ km}$) events (1990-01-01 to 2017-01-01) from the Alaska Earthquake Center fault-plane catalog. These focal mechanisms are derived from P polarity observations. See Section 3.3 for more information on major historic events. See Figure 3.11 for our new moment tensor solutions.

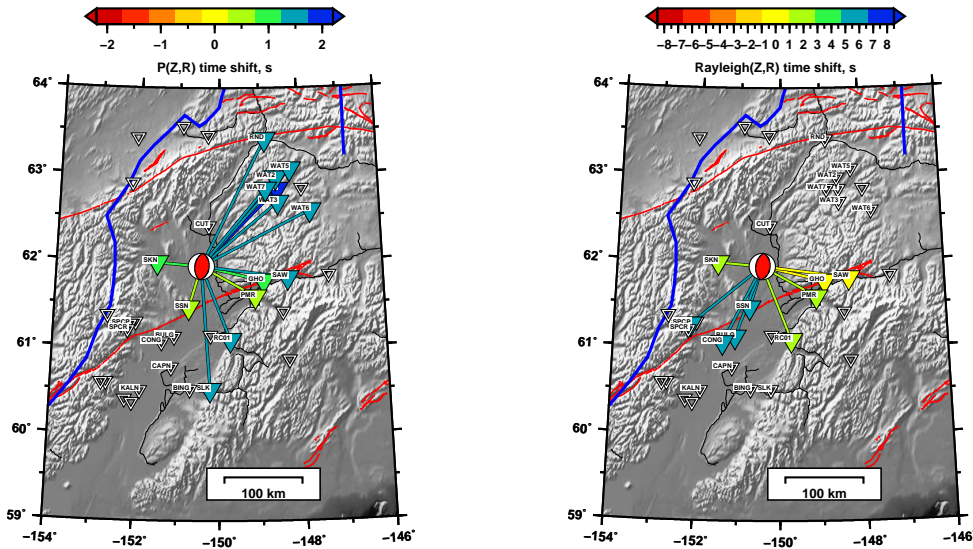
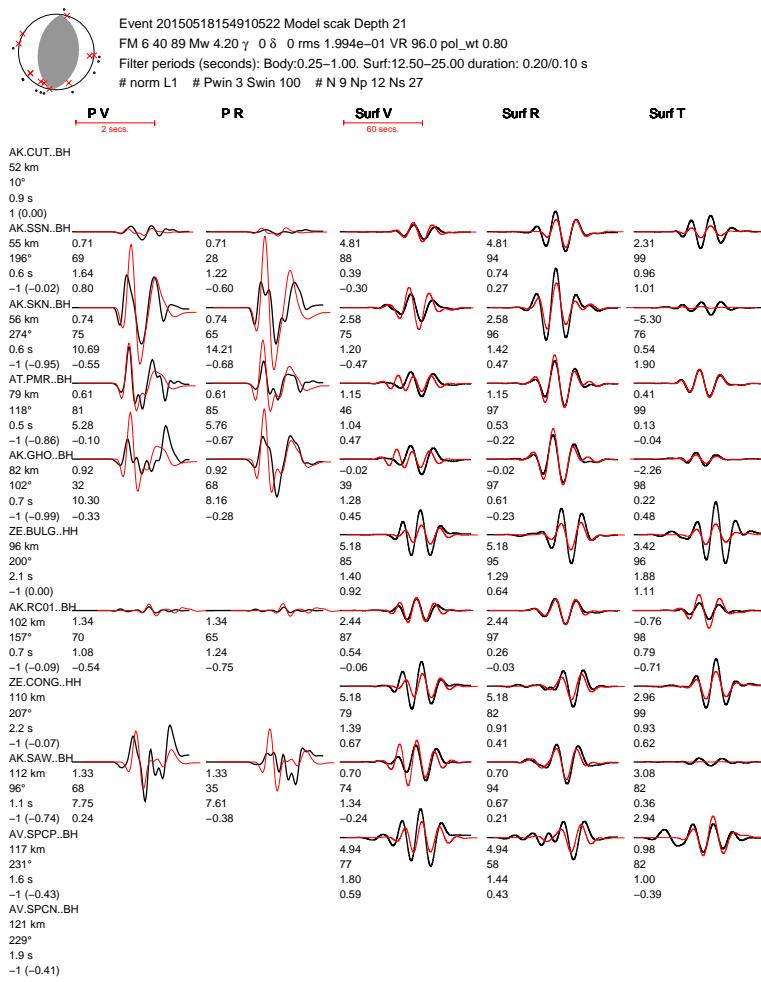


Figure 3.9: (top) Waveform fits at subset of stations used for a M_w 4.2 crustal earthquake in the Susitna region. See Table B.4 for source parameters. Waveform fits for all stations, and for all events, are available (Silwal, 2018). (bottom) Map of time shifts between observed and synthetic waveforms for the P waves (left) and Rayleigh waves (right). Open triangles denote stations with available waveforms that were not used in the inversion. Station names are listed if either the waveform or first-motion polarity was used. Note the large positive time shift for Rayleigh waves traveling to the southwest, through basins. This indicates that along these paths the assumed 1D model is too fast relative to the actual Earth structure.

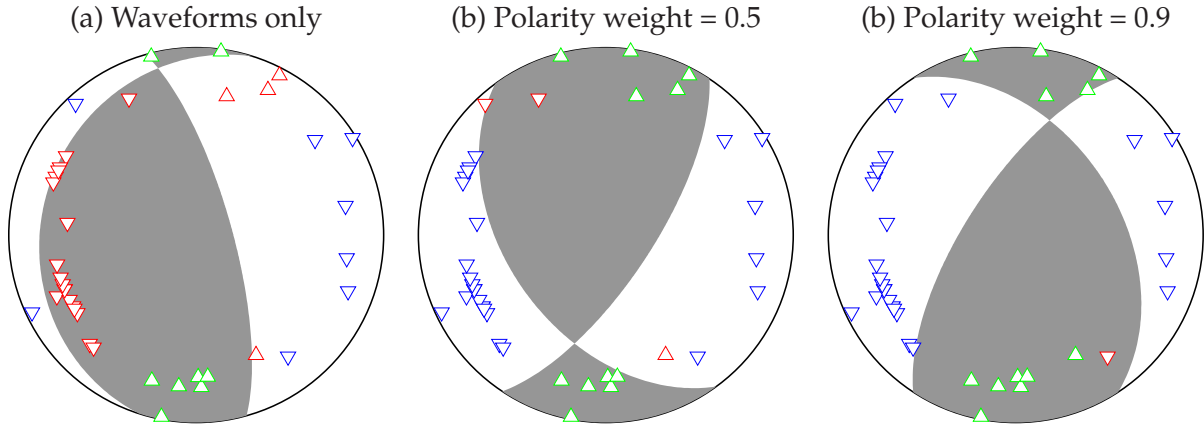


Figure 3.10: Impact of using different weights for the polarity misfit, shown for an example earthquake in Cook Inlet (eid 20150727022154395). Each beachball shows the best-fitting moment tensor for a given m in Eq. 3.3. Triangles denote lower-hemisphere piercing points for each ray path from source to station; these are calculated using an assumed 1D Earth model. Upward triangles denote upward polarity observations; downward triangles denote downward polarity observations. The color indicates agreement or not with predicted polarities: red (up or down) indicates mismatch, while green (up) and blue (down) indicate agreement. See Section 3.4.3 for details on the misfit function. (a) Waveforms only. Note that a large number of polarity mismatches occur. See Figure B.5 for waveform fits. (b) Waveforms plus polarities with weight factor 0.5. Here only three polarity measurements are mismatched. See Figure B.6 for waveform fits. (c) Waveforms plus polarities with weight factor 0.9. All observed polarities are fit, except one (in red). See Figure B.7 for waveform fits.

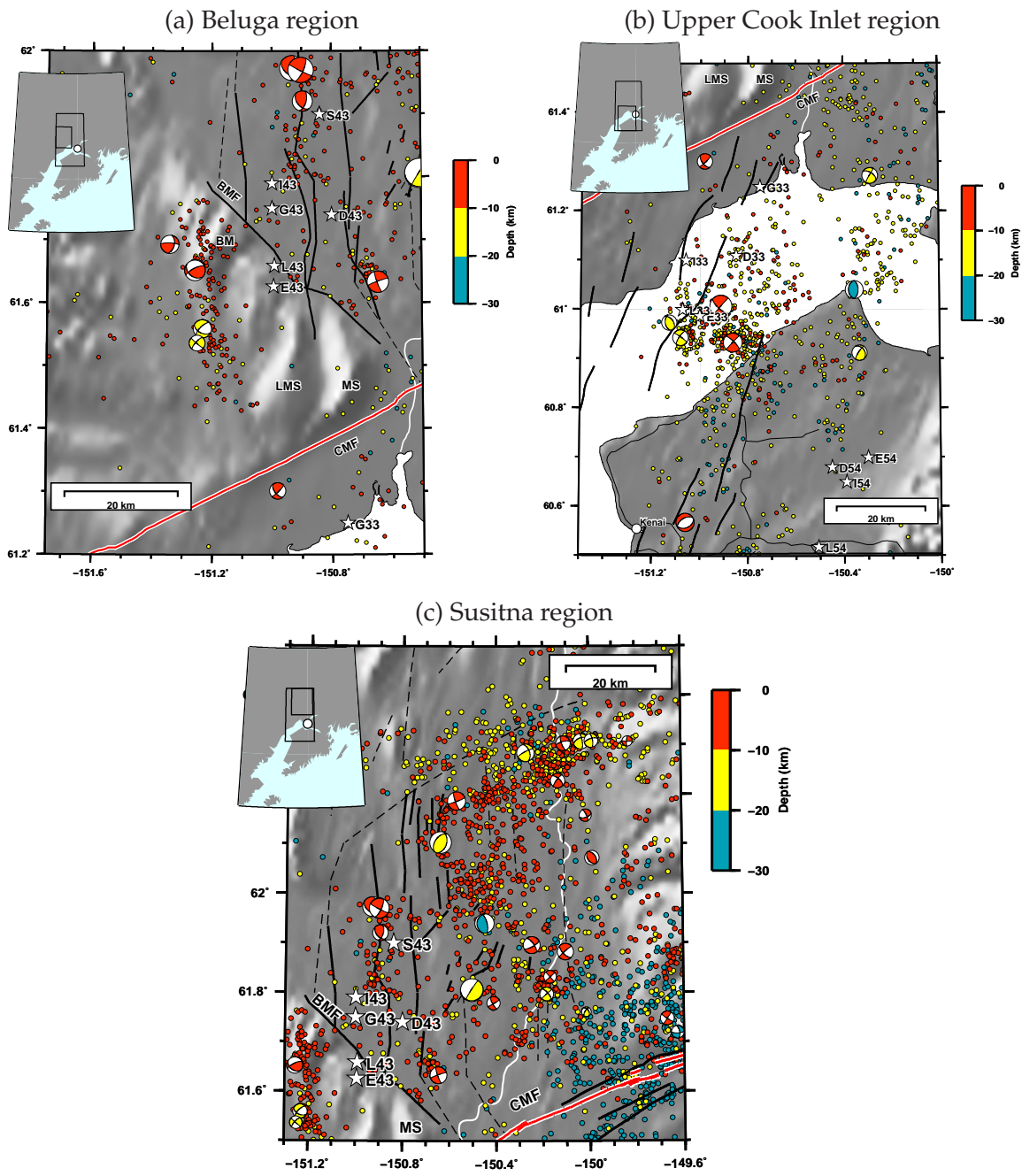


Figure 3.11: Our double couple moment tensor solutions for crustal earthquakes (depth ≤ 30 km) between 2007-08-15 and 2017-01-01 in three focus regions (Table 3.1). The displayed regions are slightly larger than the bounding regions listed in Table 3.1. Beachballs are colored by depth and sized by earthquake magnitude. Also shown are relocated seismicity (Figure 3.13) and previously published epicenters for the 1933 and 1943 earthquakes, plotted as stars (Table B.1). Text labels: CMF = Castle Mountain fault, BMF = Beluga Mountain fault, BM = Beluga Mountain, LMS = Little Mount Susitna, MS = Mount Susitna. (a) $M_w \geq 2.5$ in the Upper Cook Inlet region. (b) $M_w \geq 2.5$ in the Beluga region. (c) $M_w \geq 3.0$ in the Susitna region. See Figure B.11 for an alternative version of this figure that includes the basement surface.

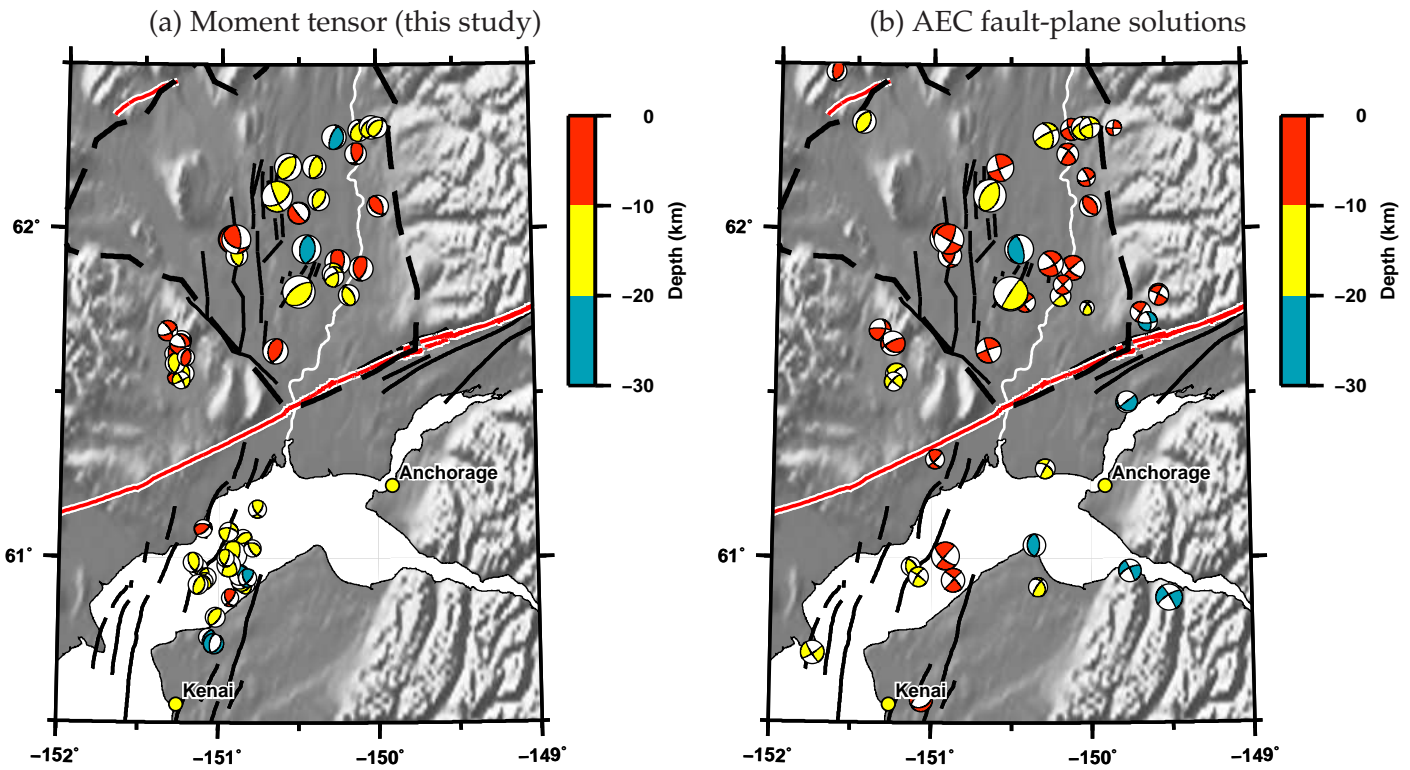


Figure 3.12: Comparison between moment tensors in this study and an existing catalog. All earthquakes shown are for depth ≤ 30 km and between 2007-08-15 to 2017-01-01. (a) Moment tensors estimated in this study: 53 total, 26 of which are in (b), 27 which are new. These mechanisms are estimated from waveforms and first-motion polarities. (b) Moment tensors in the Alaska Earthquake Center fault-plane catalog: 46 total, 26 of which are in (a), 20 of which we do not examine. These mechanisms are estimated from first-motion polarities.

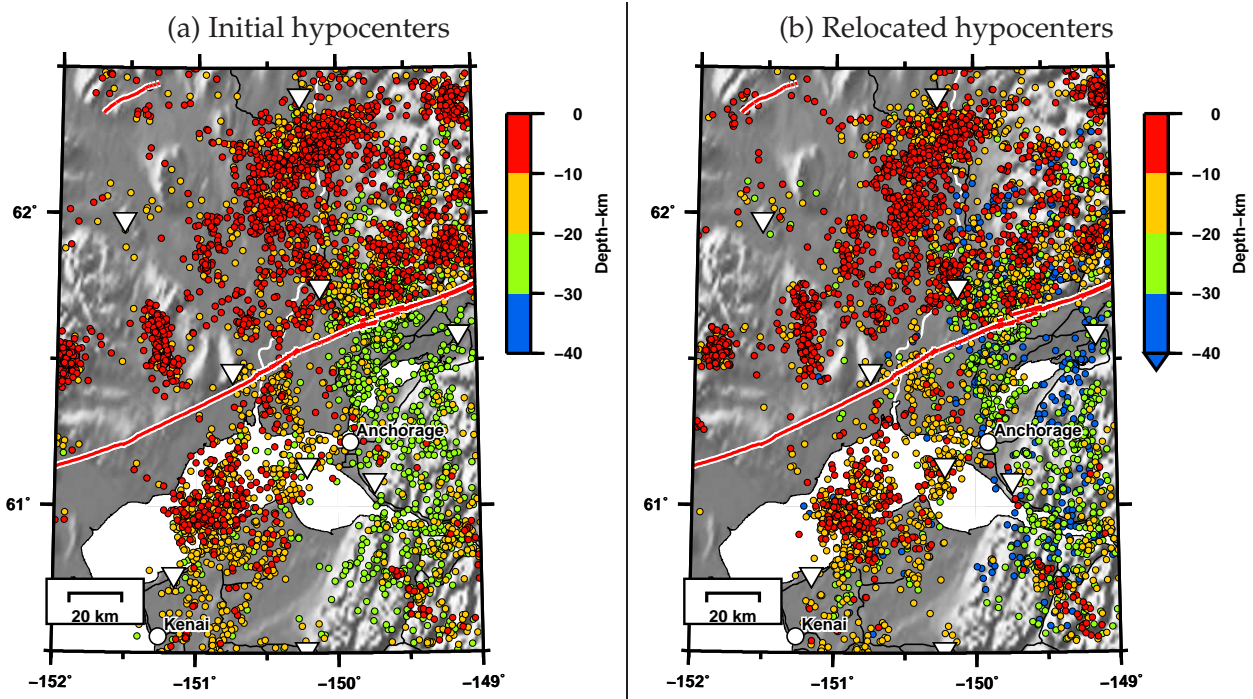


Figure 3.13: Relocation of hypocenters using a double-difference approach. The crustal earthquakes considered have depth ≤ 30 km, $M_w \geq 1.5$, and occurred between 1990-01-01 and 2017-01-01. See Section 3.5 and Figure B.13 for details.

References

- Abe, K., 1981. Magnitudes of large shallow earthquakes from 1904 to 1980, *Phys. Earth Planet. Inter.*, **27**, 72–92.
- Abers, G. & Christensen, D., 2006. Seismic and geodetic imaging of subducting terranes under North America, International Federation of Digital Seismograph Networks. Other/Seismic Network. doi:10.7914/SN/YV_2006.
- Alvizuri, C. & Tape, C., 2016. Full moment tensors for small events ($M_w < 3$) at Uturuncu volcano, Bolivia, *Geophys. J. Int.*, **206**, 1761–1783, doi:10.1093/gji/ggw247.
- Alvizuri, C. & Tape, C., 2018. Full moment tensor analysis of nuclear explosions in North Korea, *Seismol. Res. Lett.* (in review).
- Alvizuri, C., Silwal, V., Krischer, L., & Tape, C., 2018. Estimation of full moment tensors, including uncertainties, for nuclear explosions, volcanic events, and earthquakes, *J. Geophys. Res. Solid Earth*, **123**, doi:10.1029/2017JB015325.
- Amante, C. & Eakins, B. W., 2009.ETOPO1 1 Arc-Minute Global Relief Model: Procedures, Data Sources and Analysis, NOAA Technical Memorandum NESDIS NGDC-24, 19 pp.
- Bird, P., 2003. An updated digital model of plate boundaries, *Geochem. Geophys. Geosyst.*, **4**, 1027, doi:10.1029/2001GC000252.
- Bodle, R. R., 1945. *United States Earthquakes 1943*, U.S. Department of Commerce.
- Bondár, I. & Storchak, D., 2011. Improved location procedures at the International Seismological Centre, *Geophys. J. Int.*, **186**, 1220–1244, doi:10.1111/j.1365-246X.2011.05107.x.
- Brockman, S. R., Espinosa, A. F., & Michael, J. A., 1988. *Catalog of Intensities and Magnitudes for Earthquakes in Alaska and the Aleutian Islands—1786–1981*, U.S. Geol. Survey Bulletin 1840.
- Bruhn, R. L. & Haeussler, P. J., 2006. Deformation driven by subduction and microplate collision: Geodynamics of Cook Inlet basin, Alaska, *Geol. Soc. Am. Bull.*, **118**(3/4), 289–303.
- Capps, S. R., 1913. The Yentna District Alaska, Bulletin 534.
- Chiang, A., Dreger, D. S., Ford, S. R., & Walter, W. R., 2014. Source characterization of underground explosions from combined regional moment tensor and first-motion analysis, *Bull. Seismol. Soc. Am.*, **104**(4), 1587–1600, doi:10.1785/0120130228.

- Christeson, G. L., Gulick, S. P. S., van Avendonk, H. J. A., Worthington, L. L., Reece, R. S., & Pavlis, T. L., 2010. The Yakutat terrane: Dramatic change in crustal thickness across the Transition fault, Alaska, *Geology*, **38**(10), 895–898.
- Crotwell, H. P., Owens, T. J., & Ritsema, J., 1999. The TauP Toolkit: Flexible Seismic travel-time and ray-path utilities, *Seismol. Res. Lett.*, **70**(2), 154–160.
- Davies, J., Sykes, L., & Jacob, K., 1981. Shumagin seismic gap, Alaska Peninsula: History of great earthquakes, tectonic setting, and evidence for high seismic potential, *J. Geophys. Res.*, **86**(B5), 3821–3855.
- Doser, D. I., 2005. Historical Seismicity (1918–1964) of the Kodiak Island Region, *Bull. Seismol. Soc. Am.*, **95**(3), 878–895, doi:10.1785/0120040175.
- Doser, D. I., 2006. Relocations of Earthquakes (1899–1917) in South-Central Alaska, *Pure and Applied Geophysics*, **163**(8), 1461–1476, doi:10.1007/s00024-006-0085-3.
- Doser, D. I. & Brown, W. A., 2001. A study of historic earthquakes of the Prince William Sound, Alaska, Region, *Bull. Seismol. Soc. Am.*, **91**(4), 842–857.
- Douglas, A., 1967. Joint epicentre determination, *Nature*, **215**, 47–48.
- Dover, J. H., 1992. Geologic map and fold- and thrust-belt interpretation of the southeastern part of the Charley River Quadrangle, east-central Alaska, Miscellaneous Investigations Series Map 1942, 14 p., 2 sheets, scale 1:100,000.
- Duputel, Z., Rivera, L., Kanamori, H., & Hayes, G., 2012. W phase source inversion for moderate to large earthquakes, *Geophys. J. Int.*, **189**, 1125–1147.
- Dziewonski, A., Chou, T.-A., & Woodhouse, J. H., 1981. Determination of earthquake source parameters from waveform data for studies of global and regional seismicity, *J. Geophys. Res.*, **86**(B4), 2825–2852, doi:10.1029/JB086iB04p02825.
- Eberhart-Phillips, D., Christensen, D. H., Brocher, T. M., Hansen, R., Ruppert, N. A., Haeussler, P. J., & Abers, G. A., 2006. Imaging the transition from Aleutian subduction to Yakutat collision in central Alaska, with local earthquakes and active source data, *J. Geophys. Res.*, **111**, B11303, doi:10.1029/2005JB004240.
- Ekström, G., Nettles, M., & Dziewoński, A. M., 2012. The global GCMT project 2004–2010: Centroid-moment tensors for 13,017 earthquakes, *Phys. Earth Planet. Inter.*, **200–201**, 1–9, doi:10.1016/j.pepi.2012.04.002.

Engdahl, E. R. & Villaseñor, A., 2002. Global seismicity: 1900–1999, in *International Handbook of Earthquake and Engineering Seismology*, vol. 81A of **International Geophysics Series**, pp. 665–690, eds Lee, W. H. K., Kanamori, H., Jennings, P. C., & Kisslinger, C., Academic Press, London.

Engdahl, E. R., van der Hilst, R., & Buland, R., 1998. Global teleseismic earthquake relocation with improved travel times and procedures for depth determination, *Bull. Seismol. Soc. Am.*, **88**(3), 722–743.

Fisher, M. A. & Magoon, L. B., 1978. Geologic framework of lower Cook Inlet, *Am. Assoc. Petroleum Geol. Bull.*, **62**(3), 373–402.

Flores, C. & Doser, D. I., 2005. Shallow seismicity of the Anchorage, Alaska, Region (1964–1999), *Bull. Seismol. Soc. Am.*, **95**(5), 1865–1879, doi:10.1785/0120040121.

Ford, S. R., Walter, W. R., & Dreger, D. S., 2012. Event discrimination using regional moment tensors with teleseismic-*P* constraints, *Bull. Seismol. Soc. Am.*, **102**(2), 867–872, doi:10.1785/0120110227.

Fu, Y. & Freymueller, J. T., 2013. Repeated large Slow Slip Events at the south central Alaska subduction zone, *Earth Planet. Sci. Lett.*, **375**, 303–311.

Giacomo, D. D., Bondár, I., Storchak, D. A., Engdahl, E. R., Bormann, P., & Harris, J., 2015. ISC-GEM: Global instrumental earthquake catalogue (1900–2009), III. re-computed MS and mb, proxy MW, final magnitude composition and completeness assessment, *Physics of the Earth and Planetary Interiors*, **239**, 33–47, doi:10.1016/j.pepi.2014.06.005.

Gillis, R. J., Herriott, T. M., & Tsigonis, R. M., 2015. Preliminary results of reconnaissance structural studies of the western Susitna basin, south-central Alaska, Preliminary Interpretive Report 2015-3-5.

Grantz, A., 1966. *Strike-Slip Faults in Alaska*, U.S. Geol. Survey Open-File Report 66-53, Washington, D.C.

Guilhem, A., Hutchings, L., Dreger, D. S., & Johnson, L. R., 2014. Moment tensor inversions of $M \sim 3$ earthquakes in the Geysers geothermal fields, California, *J. Geophys. Res. Solid Earth*, **119**(3), 2121–2137, doi:10.1002/2013JB010271.

Gutenberg, B. & Richter, C. F., 1954. *Seismicity of the Earth and Associated Phenomena*, Princeton U. Press, Princeton, New Jersey, USA, 2nd edn.

Hackett, S. W., 1977. Gravity survey of Beluga Basin and adjacent area, Cook Inlet region, south-central Alaska.

Haeussler, P. J., 2008. An overview of the neotectonics of interior Alaska: Far-field deformation from the Yakutat microplate collision, in *Active Tectonics and Seismic Potential of Alaska*, vol. 179 of **Geophysical Monograph**, pp. 83–108, eds Freymueller, J. T., Haeussler, P. J., Wesson, R., & Ekström, G., Am. Geophys. Un., Washington, D.C.

Haeussler, P. J. & Saltus, R. W., 2011. Location and extent of Tertiary structures in Cook Inlet basin, Alaska, and mantle dynamics that focus deformation and subsidence, in *Studies by the U.S. Geological Survey in Alaska 2008–2009*, pp. 1–26, eds Dumoulin, J. A. & Galloway, J. P., U.S. Geol. Survey, Washington, D.C., Professional Paper 1776-D.

Haeussler, P. J., Bruhn, R. L., & Pratt, T. L., 2000. Potential seismic hazards and tectonics of the upper Cook Inlet basin, Alaska, based on analysis of Pliocene and younger deformation, *Geol. Soc. Am. Bull.*, **112**(9), 1414–1429.

Haeussler, P. J., Best, T. C., & Waythomas, C. F., 2002. Paleoseismology at high latitudes: Seismic disturbance of upper Quaternary deposits along the Castle Mountain fault near Houston, Alaska, *Geol. Soc. Am.*, **114**(10), 1296–1310.

Haeussler, P. J., Saltus, R. W., Stanley, R. G., Ruppert, N., Lewis, K., Karl, S. M., & Bender, A., 2017. The Peters Hills basin, a Neogene wedge-top basin on the Broad Pass thrust fault, south-central Alaska, *Geosphere*, **13**(5), 1464–1488, doi:10.1130/GES01487.1.

Hauksson, E. & Shearer, P., 2005. Southern California hypocenter relocation with waveform cross-correlation, Part 1: Results using the double-difference method, *Bull. Seismol. Soc. Am.*, **95**(3), 896–903.

Hayes, G. P., Wald, D. J., & Johnson, R. L., 2012. Slab1.0: A three-dimensional model of global subduction zone geometries, *J. Geophys. Res.*, **117**, B01302, doi:10.1029/2011JB008524.

Ichinose, G., Somerville, P., Thio, H. K., Graves, R., & O'Connell, D., 2007. Rupture process of the 1964 Prince William Sound, Alaska, earthquake from the combined inversion of seismic, tsunami, and geodetic data, *J. Geophys. Res.*, **112**, B07306, doi:10.1029/2006JB004728.

International Seismological Centre, 2015. On-line Bulletin, <http://www.isc.ac.uk>, Internatl. Seis. Cent., Thatcham, United Kingdom (accessed 2017-05-03).

International Seismological Centre, 2018. ISC-GEM Global Instrumental Earthquake Catalogue, Version 5.0, released on 2018-02-27.

Jadamec, M. A. & Billen, M. I., 2010. Reconciling surface plate motions with rapid three-dimensional mantle flow around a slab edge, *Nature*, **465**, 338–342, doi:10.1038/nature09053.

Kennett, B. L. N., Engdahl, E. R., & Buland, R., 1995. Constraints on seismic velocities in the Earth from traveltimes, *Geophys. J. Int.*, **122**, 108–124.

Kirschner, C. E., 1988. Map Showing Sedimentary Basins of Onshore and Continental Shelf Areas, Alaska, U.S. Geol. Survey Miscellaneous Investigation Series I-1873.

Koehler, R. D. & Carver, G. A., 2018. Active faults and seismic hazards in Alaska, Alaska Div. Geol. Geophys. Surv., Miscellaneous Publication 160, <http://doi.org/10.14509/29705>.

Koehler, R. D., Farrell, R.-E., Burns, P. A. C., & Combellick, R. A., 2012. Quaternary faults and folds in Alaska: A digital database, Alaska Div. Geol. Geophys. Surv. Miscellaneous Publication 141, 31 p., 1 sheet, scale 1:3,700,000.

Lahr, J. C., Page, P. A., Stephens, C. D., & Fogelman, K. A., 1986. Sutton, Alaska, earthquake of 1984: Evidence for activity on the Talkeetna segment of the Castle Mountain fault system, *Bull. Seismol. Soc. Am.*, **76**(4), 967–983.

LePain, D. L., Stanley, R. G., Helmold, K. P., & Shellenbaum, D. P., 2013. *Geologic Framework and Petroleum Systems of Cook Inlet Basin, South-Central Alaska*, vol. 104, American Association of Petroleum Geologists.

LePain, D. L., Stanley, R. G., Harun, N. T., Helmold, K. P., & Tsigonis, R. M., 2015. Reconnaissance stratigraphic studies in the Susitna basin, Alaska, during the 2014 field season, Preliminary Interpretive Report 2015-3-2.

Lewis, K. A., Potter, C. J., Shah, A. K., Stanley, R. G., Haeussler, P. J., & Saltus, R. W., 2015. Preliminary Interpretation of Industry Two-Dimensional Seismic Data from Susitna Basin, South-Central Alaska, U.S. Geol. Survey open-file report 2015-1138.

Li, J., Abers, G. A., Kim, Y., & Christensen, D., 2013. Alaska megathrust 1: Seismicity 43 years after the great 1964 Alaska megathrust earthquake, *J. Geophys. Res.*, **118**, 4861–4871, doi:10.1002/jgrb.50358.

Li, S., Freymueller, J., & McCaffrey, R., 2016. Slow slip events and time-dependent variations in locking beneath Lower Cook Inlet of the Alaska-Aleutian subduction zone, *J. Geophys. Res. Solid Earth*, **121**, 1060–1079, doi:10.1002/2015JB012491.

Lomax, A., Virieux, J., Volant, P., & Berge, C., 2000. Probabilistic earthquake location in 3D and layered models: Introduction of a Metropolis-Gibbs method and comparison with linear locations, in *Advances in Seismic Event Location*, pp. 101–134, eds Thurber, C. H. & Rabinowitz, N., Kluwer, Amsterdam.

Lomax, A., Silwal, V., & Tape, C., 2018. Hypocenter estimation for 14 earthquakes in south-central Alaska (1929–1975), ScholarWorks@UA at <http://hdl.handle.net/11122/8380>: descriptor file and zipped set of text files for each earthquake.

Mai, P. M. & Beroza, G. C., 2000. Source scaling properties from finite-fault-rupture models, *Bull. Seismol. Soc. Am.*, **90**(3), 604–615.

Meyer Jr., J. G., 2005. Principal facts for gravity data collected in the northern Susitna Basin area, southcentral Alaska, Alaska Alaska Div. Geol. Geophys. Surv. Preliminary Interpretive Report 2005-5.

Murphy, L. M. & Cloud, W. K., 1956. *United States Earthquakes 1954*, U.S. Department of Commerce.

Mustać, M. & Tkalcic, H., 2016. Point source moment tensor inversion through a Bayesian hierarchical model, *Geophys. J. Int.*, **204**, 311–323, doi:10.1093/gji/ggv458.

Mustać, M. & Tkalcic, H., 2017. On the use of data noise as a site-specific weight parameter in a hierarchical Bayesian moment tensor inversion: The case study of The Geysers and Long Valley caldera earthquakes, *Bull. Seismol. Soc. Am.*, **107**(4), 1914–1922, doi:10.1785/0120160379.

Neumann, F., 1935. *United States Earthquakes 1933*, U.S. Department of Commerce.

Ohta, Y., Freymueller, J. T., Hreinsdóttir, S., & Suito, H., 2006. A large slow slip event and the depth of the seismogenic zone in the south central Alaska subduction zone, *Earth Planet. Sci. Lett.*, **247**, 108–116.

Page, R. A., Biswas, N. N., Lahr, J. C., & Pulpan, H., 1991. Seismicity of continental Alaska, in *Neotectonics of North America*, The Geology of North America, chap. 4, pp. 47–68, eds Slemmons, D. B., Engdahl, E. R., Zoback, M. D., & Blackwell, D. D., Geol. Soc. Am., Boulder, Colo., USA, Decade Map Volume 1.

- Plafker, G., Hudson, T. L., Bruns, T., & Rubin, M., 1978. Late Quaternary offsets along the Fairweather fault and crustal plate interactions in southern Alaska, *Can. J. Earth Sci.*, **15**(5), 805–816.
- Ratchkovski, N. A. & Hansen, R. A., 2002. New evidence for segmentation of the Alaska subduction zone, *Bull. Seismol. Soc. Am.*, **92**(5), 1754–1765.
- Ratchkovsky, N. A., Pujol, J., & Biswas, N. N., 1998. Relocation of shallow earthquakes in southern Alaska using Joint Hypocenter Determination method, *J. Seis.*, **2**, 87–102.
- Reasenberg, P. & Oppenheimer, D., 1985. FPFIT, FPPLLOT and FPPAGE: Fortran computer programs for calculating and displaying earthquake fault-plane solutions, Open-File Report 85-739.
- Ridgway, K. D., Trop, J. M., & Finzel, E. S., 2012. Modification of continental forearc basins by flat-slab subduction processes: A case study from southern Alaska, in *Tectonics of Sedimentary Basins: Recent Advances*, pp. 327–346, eds Busby, C. & Perez, A. A., Wiley-Blackwell.
- Rondenay, S., Montési, L. G. J., & Abers, G. A., 2010. New geophysical insight into the origin of the Denali volcanic gap, *Geophys. J. Int.*, **182**, 613–630.
- Saltus, R. W., Stanley, R. G., Haeussler, P. J., Jones III, J. V., Potter, C. J., & Lewis, K. A., 2016. Late Oligocene to present contractional structure in and around the Susitna basin, Alaska—Geophysical evidence and geological implications, *Geosphere*, **12**(5), 1–13, doi:10.1130/GES01279.1.
- Shearer, P., Hauksson, E., & Lin, G., 2005. Southern California hypocenter relocation with waveform cross-correlation, Part 2: Results using source-specific station terms and cluster analysis, *Bull. Seismol. Soc. Am.*, **95**(3), 904–915, doi:10.1785/0120040168.
- Shearer, P. M., Prieto, G. A., & Hauksson, E., 2006. Comprehensive analysis of earthquake source spectra in southern California, *J. Geophys. Res.*, **111**, B06303, doi:10.1029/2005JB003979.
- Shellenbaum, D. P., Gregersen, L. S., & Delaney, P. R., 2010. Top Mesozoic unconformity depth map of the Cook Inlet Basin, Alaska, Alaska Div. Geol. Geophys. Surv. Report of Investigation 2010-2, 1 sheet, scale 1:500,000, available at <http://www.dggs.alaska.gov/pubs/id/21961> (last accessed 2016-10-30).
- Silwal, V., 2018. Seismic moment tensor catalog for crustal earthquakes in the Cook Inlet and Susitna region of southern Alaska, ScholarWorks@UA at <http://hdl.handle.net/11122/8383>: descriptor file, text file of catalog, figures with waveform fits, and input weight files.
- Silwal, V. & Tape, C., 2016. Seismic moment tensors and estimated uncertainties in southern Alaska, *J. Geophys. Res. Solid Earth*, **121**, 2772–2797, doi:10.1002/2015JB012588.

Stähler, S. C. & Sigloch, K., 2016. Fully probabilistic seismic source inversion – Part 2: Modelling errors and station covariances, *Solid Earth*, **7**, 1521–1536, doi:10.5194/se-2016-87.

Stanley, R. G., Haeussler, P. J., Benowitz, J. A., Goodman, D. K., Ravn, R. L., Shellenbaum, D. P., Saltus, R. W., Lewis, K. A., & Potter, C. J., 2013. New stratigraphic revelations in the subsurface Susitna basin, south-central Alaska, from geochronology and biostratigraphy [poster]: GSA Cordilleran Section Meeting, Fresno, CA, May 22, 2013, Tech. rep., Alaska Division of Geological & Geophysical Surveys.

Storchak, D. A., Di Giacomo, D., Bondár, I., Engdahl, E. R., Harris, J., Lee, W. H. K., Villaseñor, A., & Bormann, P., 2013. Public release of the ISC–GEM Global Instrumental Earthquake Catalogue (1900–2009), *Seismol. Res. Lett.*, **84**(5), 810–815, doi:10.1785/0220130034.

Tape, C., Christensen, D. H., & Driskell, M. M., 2015. Southern Alaska Lithosphere and Mantle Observation Network, International Federation of Digital Seismograph Networks. Other/Seismic Network. doi:10.7914/SN/ZE_2015.

Tape, C., Christensen, D., Moore-Driskell, M. M., Sweet, J., & Smith, K., 2017. Southern Alaska Lithosphere and Mantle Observation Network (SALMON): a seismic experiment covering the active arc by road, boat, plane, and helicopter, *Seismol. Res. Lett.*, **88**(4), 1185–1202, doi:10.1785/0220160229.

Veenstra, E., Christensen, D. H., Abers, G. A., & Ferris, A., 2006. Crustal thickness variation in south-central Alaska, *Geology*, **34**(9), 781–784.

Waldhauser, F. & Ellsworth, W. L., 2000. A double-difference earthquake location algorithm: Method and application to the Northern Hayward fault, California, *Bull. Seismol. Soc. Am.*, **90**(6), 1353–1368, doi:10.1785/0120000006.

Wang, Y. & Tape, C., 2014. Seismic velocity structure and anisotropy of the Alaska subduction zone derived from surface wave tomography, *J. Geophys. Res. Solid Earth*, **119**, 8845–8865, doi:10.1002/2014JB011438.

Wéber, Z., 2018. Probabilistic joint inversion of waveforms and polarity data for double-couple focal mechanisms of local earthquakes, *Geophys. J. Int.*, **213**, 1586–1598, doi:10.1093/gji/ggy096.

Wei, M., McGuire, J. J., & Richardson, E., 2012. A slow slip event in the south central Alaska Subduction Zone and related seismicity anomaly, *Geophys. Res. Lett.*, **39**, L15309, doi:10.1029/2012GL052351.

Wickens, A. J. & Hodgson, J. H., 1967. Computer Re-Evaluation of Earthquake Mechanism Solutions, Publications of the Dominion Observatory, Vol. 33, No. 1, Ottawa, Canada Department of Energy, Mines, and Resources, Contribution 103 to the International Upper Mantle Project.

Willis, J. B., Haeussler, P. J., Bruhn, R. L., & Willis, G. C., 2007. Holocene Slip Rate for the Western Segment of the Castle Mountain Fault, Alaska, *Bulletin of the Seismological Society of America*, **97**(3), 1019–1024, doi:10.1785/0120060109.

Wilson, F. H., Hults, C. P., Schmoll, H. R., Haeussler, P. J., M.Schmidt, J., Yehle, L. A., & Labay, K. A., 2009. Preliminary Geologic Map of the Cook Inlet Region, Alaska, Open-File Report 2009-1108.

Zhang, H. & Thurber, C. H., 2003. Double-difference tomography: the method and its application to the Hayward fault, California, *Bull. Seismol. Soc. Am.*, **93**(5), 1875–1889, doi:10.1785/0120020190.

Zhao, L.-S. & Helmberger, D. V., 1994. Source estimation from broadband regional seismograms, *Bull. Seismol. Soc. Am.*, **84**(1), 91–104.

Zhu, L. & Helmberger, D., 1996. Advancement in source estimation techniques using broadband regional seismograms, *Bull. Seismol. Soc. Am.*, **86**(5), 1634–1641.

Zhu, L. & Rivera, L. A., 2002. A note on the dynamic and static displacements from a point source in multilayered media, *Geophys. J. Int.*, **148**, 619–627, doi:10.1046/j.1365-246X.2002.01610.x.

Chapter 4

Seismic wavefield simulations within a three-dimensional seismic velocity model for Alaska¹

4.1 Abstract

We present a three-dimensional seismic velocity model for mainland Alaska, in preparation for an iterative tomographic inversion using spectral-element and adjoint methods. The crustal and upper mantle tomographic model is from the body-wave model of Eberhart-Phillips et al. (2006), but modified by including topography and bathymetry, by removing the uppermost slow layer, and then embedding sedimentary basin models for Cook Inlet basin, Susitna basin, and Nenana basin. We select a set of 60 earthquakes ($M_w = 4.0\text{--}7.1$, 2000–2017) to investigate the accuracy of the tomographic model. We first estimate a moment tensor for each earthquake by comparing observed waveforms (body and surface waves) with synthetic waveforms computed in a layered model. We then use the moment tensors within wavefield simulations to generate full-length, three-component synthetic seismograms for comparison with observed seismograms. To maximize the fraction of usable stations per earthquake, we establish three regions for simulations—south-central Alaska, central Alaska, and eastern Alaska—with 20 earthquakes in each region. The depth of each simulation region is 400 km in order to accommodate the deepest earthquakes, which occur within the subducting Pacific plate. Each simulation region has a tomographic model defined on a hexahedral finite-element mesh. We perform simulations on two different resolution meshes in order to quantify the minimum resolvable period for each simulation region. An automated window selection tool is used to quantify the misfit between observed and synthetics seismograms over two period ranges: 3–10 s and 10–30 s. Sufficient agreement between waveforms provides a basis for initiating an iterative tomographic inversion using a larger set of earthquakes.

4.2 Introduction

Alaska is a prime target for seismic imaging, due to its pervasive slab and crustal seismicity, as well as its complex subsurface structure, which provides a partial record of its complex tectonic evolution. The structural complexity warrants application of sophisticated techniques for seismic imaging, such as the application of three-dimensional seismic wavefield simulations (Liu et al., 2004; Tape et al., 2009), which require minimal approximations and also allow for the inclusion of full-length seismic waveforms. In this study we perform wavefield simulations to investigate a three-dimensional velocity model covering mainland Alaska (Figure 4.1).

The southern Alaska margin has experienced convergence in the form of subduction, collision, and accretion for the past 160 Ma (Jarrard, 1986). The most recent perturbation to oceanic

¹Prepared for submission to *Geophys. J. Int.*: Silwal, V., Tape, C., and Casarotti, E., 2018. Seismic wavefield simulations within a three-dimensional seismic velocity model for Alaska.

subduction began with the arrival of the Yakutat block approximately 30 Ma. This wedge of over-thickened crust, presumably an oceanic plateau, is considered to be responsible for the uplift of the Alaska Range, the rapid uplift and remarkable relief of the coastal St. Elias mountains, the propagation of intraplate deformation several hundred km from the trench, the broad flattening of the subducting slab, the formation of the Northern Foothills fold-and-thrust belt, the extinguishing of the eastern Aleutian arc, the activity of the Wrangell volcanic arc, the lateral flow at the edge of the Pacific/Yakutat slab, and rupturing of the oceanward Pacific crust ($M_w \geq 7.8$ events in 1987–1992) (Plafker et al., 1978; Hwang & Kanamori, 1992; Eberhart-Phillips et al., 2006; Bemis & Wallace, 2007; Ridgway et al., 2002, 2007; Fuis et al., 2008; Haeussler, 2008; Jadamec & Billen, 2010; Christensen & Abbers, 2010; Christeson et al., 2010).

The tectonic evolution of Alaska is partly recorded within surface geology and subsurface structures. The subsurface structure of Alaska is inferred from six major data sets: (1) land-based and air-based gravity and magnetic surveys covering most of the state (Saltus et al., 1999, 2001, 2007, 2008); (2) the Trans-Alaska Crustal Transect (TACT: Fuis et al., 1991, 2008); (3) numerous marine seismic surveys in southern Alaska (e.g., Moore et al., 1991; Wolf et al., 1991; Ye et al., 1997; Gulick et al., 2007; Christeson et al., 2010); (4) P and S body-wave traveltimes, either from local or global events (Kissling & Lahr, 1991; Zhao et al., 1995; Eberhart-Phillips et al., 2006; Qi et al., 2007a,b); (5) surface waves, derived from earthquakes (Wang & Tape, 2014) or ambient noise (Ward, 2015); and (6) crustal reverberations from teleseismic body waves (Ferris et al., 2003; Veenstra et al., 2006; Rondenay et al., 2010). TACT provided a detailed 2D crustal model spanning the entire state. However, it is difficult to extrapolate a 2D model into a 3D model. Eberhart-Phillips et al. (2006) used traveltimes recorded from shots of the TACT experiment, in addition to earthquake traveltimes from both the permanent network and the 1999–2000 BEAAR PASSCAL array (Ferris et al., 2003). They derived a V_p and V_s model using local-earthquake tomography.

Our study establishes a first step toward an iterative tomographic inversion in Alaska using seismic wavefield simulations. Our target region is southern and central Alaska, where station coverage is maximal, on account of the road system and previous temporary deployments. We establish three simulation regions in order to maximize the amount of well-recorded data within the region (Section 4.3): (1) Cook Inlet in southern Alaska, (2) Interior in central Alaska, and (3) Wrangell in south-eastern Alaska. Using body waves and surface waves, we estimate moment tensors for 20 earthquakes within each region (Section 4.4). In Section 4.5 we describe the construction of the three-dimensional (3D) seismic velocity model, which is based on Eberhart-Phillips et al. (2006), but with topography and embedded sedimentary basins.

For each simulation region, we generate different hexahedral finite-element meshes and different velocity models (Section 4.6), in order to perform a series of tests (Section 4.7): (1) quantifi-

cation of the minimum resolvable period; (2) computational effect of smoothing the topography; (3) influence of the minimum shear wave velocity; and (4) influence of embedded sedimentary basins. Finally in Section 4.8 we compare observed waveforms with synthetics generated using our preferred model and mesh.

Seismic wavefield simulations have been widely used to model seismic wave propagation in complex tectonic settings, such as those with basins. Our study presents the first simulations for earthquakes in Alaska. In comparison to previous work in California (Liu et al., 2004; Rodgers et al., 2008), Alaska offers the advantage of more earthquakes and also deeper earthquakes due to the underlying subducting slab. These earthquakes allow us to better sample the 3D tomographic models with a wide range of frequencies, offering a promising foundation for a future tomographic inversion.

4.3 Three target regions of mainland Alaska

We partition our target region of mainland Alaska into three regions. Because the computational cost of our technique scales with the number of events, it is in our interest to maximize the number of measured waveforms for each simulation. For a smaller region, the most distant stations will have a better signal-to-noise ratios than the most distant stations in a larger region. Thus we are able to maximize the number of time steps in the simulation during which the synthetic wavefield is in good enough agreement with the observed wavefield (at discrete station points) to make measurements. We select three regions on the basis of: (1) availability of broadband stations; (2) availability of local earthquakes; (3) signal-to-noise ratios for moderate ($M_w = 3.5 - 5.5$) events; and (4) presence of tectonically interesting targets. Earthquakes and broadband stations are well distributed among the three regions. Each region is structurally and tectonically different (Table 4.2). This is appealing from a scientific standpoint, as well as from a computational standpoint, since we will be testing the tomographic inversion in different settings.

The first simulation region is the subduction setting of southern Alaska (Figure 4.2). Here the Cook Inlet forearc basin is a dominant feature, with dimensions 200 km by 50 km by 7.5 km deep. The basin directly overlies an extremely seismically active slab; several moment tensors of these events are shown in Figure 4.2. The region contains Anchorage, with 300,000 people, as well as several recently active volcanoes (Spurr, Redoubt, Augustine). The MOOS (Li et al., 2013) and SALMON (Tape et al., 2017) networks provide enhanced data coverage in this region (Table C.1).

The second simulation region is for interior Alaska, whose crust is broadly deforming within several scales of strike-slip fault systems (Page et al., 1995), in response to forces of collision and subduction. The profile in Figure 4.1 reveals seismicity throughout much of the crust, both laterally and vertically. Figure 4.2 shows the source and station distribution, in addition to Nenana

basin (Van Kooten et al., 2012; Tape et al., 2015), Denali fault, Kaltag–Tintina fault, and the Minto Flats fault zone. The BEAAR (Ferris et al., 2003) and FLATS (Tape et al., 2018) networks provide enhanced data coverage in this region.

The third region is the collisional setting of the Yakutat block in southeastern Alaska (Figure 4.2). We refer to this region as Wrangell in this study. The seismicity is predominantly crustal and dominated by aftershocks of the M_w 7.9 Denali fault earthquake. A weakly defined Wrangell Benioff zone exists but does not seem to produce moderate ($M_w > 4$) earthquakes (Stephens et al., 1984).

4.4 Earthquake sources for simulation

We select 20 events in each region for estimating moment tensors and performing wavefield simulations. Our selection criteria are motivated by our future application of a simulation-based inversion (e.g., Tape et al., 2009), in which the computational cost scales with the number of earthquakes and is unrelated to the number of stations. Therefore we seek events that are well-recorded at the largest number of stations and that provide the most complete coverage (laterally and with depth) of the simulation regions.

4.4.1 Event selection

Our event selection for moment tensors starts with the Alaska Earthquake Center (AEC) catalog, which provides hypocenters, origin times, and local magnitudes (M_l). We compare the earthquake catalog with the number of seismic stations active within the simulation region, which varies as a function of time on account of numerous temporary seismic deployments (Table C.1).

Our event selection for each region takes the following steps:

1. Select all events $M_w \geq 3.5$ recorded by at least 30 stations. The minimum magnitude is specified since we require sufficient signal-to-noise levels for in the period range 2–30 s (in particular the longer periods), which is needed for estimating moment tensors and for wavefield simulations.
2. Exclude events within 20 km from the simulation boundary. Events near the boundary require longer propagation distances to stations within the region; furthermore the events are more influenced by imperfect absorbing boundary conditions in simulations.
3. Perform declustering in order to achieve a more uniform distribution of events. This involves dividing the simulation region into “bricks,” and within each brick we keep a fixed number of events. The parameters controlling the brick size and the number of events kept

per brick can be adjusted such that the resultant number of events is close to some desired number (in our case, 20).

Our selection parameters, and resultant events, are summarized in Table 4.1 and illustrated in Figures C.1–C.3.

4.4.2 Moment tensor inversion

We use all broadband (channels HH* and BH*) seismic waveforms available at the IRIS Data Management Center. Using ObsPy (Beyreuther et al., 2010; Krischer et al., 2015), we extract and process waveforms from IRIS for all 60 earthquakes. We perform moment tensor inversion using the ‘cut-and-paste’ approach (Zhu & Helmberger, 1996; Silwal & Tape, 2016) for the events selected above. In this approach, each three-component seismogram is cut into two body wave windows and three surface wave windows. Different bandpass filters are applied to the body waves and surface waves. The same procedures are applied to synthetic seismograms, which are then quantitatively compared with the recorded seismograms, via a misfit function.

Synthetic seismograms are computed using the same 1D velocity model (`scaik`) as is used by the Alaska Earthquake Center for locating earthquakes. See Figure 4.2 and Tables C.2–C.4 for moment tensor inversion solutions for events in each region.

4.5 Construction of seismic velocity model

A 3D seismic wavefield simulation is performed within a 3D seismic model that defines V_P , V_S , and density at all points within the domain. Next we describe how our 3D seismic velocity model is constructed from existing components.

Each simulation region extends from 400 km depth to the topographic surface. We fill the simulation volumes with values derived from Eberhart-Phillips et al. (2006) (`E2006`), which is derived from body waves from local earthquakes and active sources. This model is described by $20 \times 23 \times 14$ nodes of V_P and V_S values (Figure 4.3). The coarse sampling of this model requires a procedure for interpolation and extrapolation, the result of which is illustrated in Figure 4.3. Density is obtained from V_P by using the empirical scaling relationship of Brocher (2005). Inside `SPECFEM3D`, there will be a further interpolation to compute the velocity and density values at the Gauss–Lobatto–Legendre (GLL) points.

Within the interpolated model of Eberhart-Phillips et al. (2006), we embed several sedimentary basin models. From inspection of recorded seismic waveforms—in Alaska and elsewhere—we know that these basins have a strong influence on the seismic wavefield within our target period range of interest (3–30 s). The Cook Inlet basin of southern Alaska has a maximal depth of 7.5 km,

and the basement geometry is provided by Shellenbaum et al. (2010). The largest basin in central Alaska is the Nenana basin, which has a maximal depth of 6 km (Van Kooten et al., 2012; Tape et al., 2015). We use the empirical relationships of Brocher (2005, 2008) to construct depth-dependent velocity and density models for the Nenana and Cook Inlet basins. These relationships allow us to “produce” a basin model that had the best-known geometry and low-enough wave speeds to produce amplification and resonance within the wavefield simulations. The offshore sedimentary sequence on the Yakutat block is up to 9 km thick (Christeson et al., 2010; Worthington et al., 2010); we have not yet implemented this unit into the model in Figure 4.2.

The top-most layer in the E2006 model is at 1 km above sea level, and the second layer is at 2 km below the sea level. We remove the top-most layer and extrapolate the model upwards. We also test the effect of applying a velocity threshold of $vs = 1000$ m/s (Section 4.7).

4.6 Meshing

Topography can have a significant effect on the seismic wavefield, as demonstrated with prior wavefield simulations (Ma et al., 2007; Lee et al., 2008). We use 1 arc-minute (1.8 km) topography and bathymetry model, ETOPO1 (Amante & Eakins, 2009), for building the mesh. We interpolate the ETOPO1 data to 1 km grid spacing using bilinear interpolation (`interp2` function of MATLAB). All three meshes use the same UTM zone 6V. We use GEOCUBIT (Casarotti et al., 2008; Peter et al., 2011) to prepare unstructured hexahedral meshes for three target regions in Alaska.

The three meshes are constructed with input parameters similar to the ones used for hundreds of simulations in southern California (Tape et al., 2011). All three meshes are of the same dimensions: 400 km by 500 km. The meshes have ~ 1.25 km element sizes at the surface and ~ 18 km sizes below the Moho, with two refinement layers in between; these are visible in Figure 4.4 and Figure 4.5. Table 4.2 lists comparisons between the southern California simulation regions and the three Alaska regions. Each of the three Alaska regions is comparable in size to the southern California region. Both Alaska and California have strong topographic gradients, which pose challenges for meshing. Figure 4.4 shows a comparison of a mesh with topography and a mesh with smoothed topography in the vicinity of Denali. It is essential to accurately model wave propagation through such topography.

Each mesh is unique in its tectonic settings. Cook Inlet is the most diverse mesh in terms of the geophysical features. It is in subduction setting with the Cook Inlet forearc basin and volcanoes of the Aleutian arc. We also include two other smaller basins, Susitna and Yentna basin into our 3D model. It also has two major mountain ranges: the western Alaska range and the Talkeetna mountains. Silwal et al. (2018) showed the strong effect of Sustina basin on waveforms when performing moment tensor inversion. Wrangell has accreting Yakutat plate and the crust under

Peninsular and Wrangell terrane is about 50–60 km thick (Fuis et al., 2008). Slab-tears prevent the subducting Pacific plate from reaching the Wrangell mesh, which makes it difficult to get deep events for testing our 3D model (Section 4.4.1). The Interior mesh has the central Denali fault and Denali. Most of the Interior lies in a strike-slip system between the central Alaska range and the Tintina fault. Interior also has a transtensional Nenana basin in the strike-slip Minto Flats fault zone. Also, the subducting Pacific plate extends all the way to the Interior Alaska.

4.6.1 Topography smoothing

We also test the effect of topographic smoothing on wavefield simulation. For this we apply a symmetric 2D median filter (`median2` function of MATLAB). See Figure C.14 and Figure C.15 for difference due to smoothing the topography.

4.7 Wavefield simulations and minimum resolvable period

We use the latest version of SPECFEM3D for seismic wave propagation (Komatitsch et al., 2004; Peter et al., 2011). We visualize the propagating waves on the topographic surface at different time-stamps, which provides insight into the model, mesh, and source. For example, in Figure 4.6 we can see the effect of the Cook Inlet basin on the propagating waves.

Before running the simulations for the selected events we need to decide what mesh (including the choice of topography) and velocity model we are going to use for our final run. This includes deciding whether to use smoothed or unsmoothed topography for the mesh. For the velocity model, we use E2006 model with or without basin, and also analyzing the effect of velocity thresholding. The results of the following tests are summarized in Table C.5 and Table C.6.

- **Maximum allowable time-step** Theoretical maximum allowable time-step, dt , estimated by SPECFEM is computed using CFL (Courant–Friedrichs–Lewy) condition.

$$C = \frac{u\Delta t}{\Delta x} \leq C_{max} \quad (4.1)$$

This takes into account only the mesh dimensions and not the model used.

The ‘actual’ usable time-step (dt) is generally smaller than the theoretical estimate. This is opposite to the mesh used in southern California (Tape et al., 2010) for which the usable was larger than the theoretical dt . The usable time-step also seems to depend only on the mesh discretization, and not on the velocity model. Note that smoothing the topography changes the mesh discretization.

Allowable time-steps were tested using 0.001 s discretization. Same allowable time-step for smoothed and unsmoothed topography mesh, as in the case of Cook Inlet and Interior, does

not imply that there would be no differences had the smaller time discretization been used for testing (lower order differences). This could be seen by comparing the corresponding theoretical dt values that differ at order of 1e-5 s. Using NGLL7 gives a better estimate of theoretical allowable time-step that is closer to the actual value, as compared to the NGLL5 results.

- **Minimum resolvable period**

Here we try to estimate the ‘acceptable’ minimum resolvable period, above which data and synthetics can be compared, and window selection for adjoint source estimation can be deformed. This requires running simulations with coarse (NGLL5 = five GLL interpolation points) and fine (NGLL7 = seven GLL interpolation points) meshes, and estimating the period below which the synthetics do not match (see Figure 4.7). Since we are only interested in body and surface waves, our acceptable measure of minimum resolvable period is based on waveform fit for ~200 seconds from the P arrival.

Theoretical estimates of minimum resolvable period depend only on the mesh discretization, and is given by the cumulative estimate of the minimum resolvable period of individual mesh elements Figure 4.4. Actually minimum resolvable is much lower than the theoretical value.

We use the root-mean-square as the measure of misfit between the waveforms:

$$\Phi = \sqrt{\frac{||\mathbf{u} - \mathbf{v}||}{||\mathbf{u}||}} \quad (4.2)$$

where \mathbf{u} and \mathbf{v} represents the waveforms generated using the coarse and fine meshes, respectively.

The minimum resolvable period is estimated manually by comparing the NGLL5 and NGLL7 synthetics at varying lowpass period for the worst fitting station. Only the first 100 seconds of the synthetics were used for estimating the minimum resolvable period, in order to avoid the differences in the coda. Also, this window has the major arrivals, which will be used in tomographic inversion. See Figure 4.8 for variation of minimum resolvable period across all stations in Cook Inlet mesh.

- **Effect of using smoothed topography**

Use of smoothed topography is justified if it reduces the simulation time, and the synthetics generated using unsmoothed and smoothed topography must match below the minimum resolvable period for the unsmoothed mesh. We expect the topography effect to be severe for the Interior and Wrangell meshes due to the high relief of the Alaska range, St. Elias range,

and the Wrangell volcanoes. See Figure 4.4 for effect of smoothing near Denali. Figure 4.5 shows the effect of topography smoothing on the Interior mesh. We can see that the effect is more visible in the Alaska range and at periods lower than 4 seconds. See Figure C.16 and Figure C.17 for effect of topography smoothing on the Wrangell mesh.

- **Embedding basin and velocity threshold**

Grid sampling in the E2006 model is very sparse and it fails to represent basins and other smaller scale features (Figure 4.3). Therefore, the basins also do not appear in the interpolated-extrapolated E2006 model. We embed the velocity models for major basins into the E2006 model to investigate the effect of basin on propagating wavefield (Figure 4.9). See Section 4.5 for more information.

Also, when adding the topography the shallow low-velocity layer gets extended upwards. This can create non-real seismic phases since the topographic features (mountains) are composed of rocks having higher seismic velocity than basins and shallow soil layer. In order to avoid such ringing signals we apply a minimum shear wave velocity threshold of 1000 m/s. Applying velocity thresholding is not required when not including a basin because the minimum vs is above 1000 m/s.

See Figure C.20 and Figure C.21, respectively, for effects of velocity thresholding on waveforms in the absence and presence of major basins in Cook Inlet mesh. The map in Figure C.22 shows the difference across all stations. See Figure C.18 and Figure C.19 for the effects of velocity thresholding in absence and presence of basin in Interior mesh.

4.8 Wavefield simulations and comparison with data

From this point onwards we use mesh with non-smoothed topography, and the 3D model with basin and velocity thresholding.

4.8.1 1D–3D comparison

We start by performing the data-synthetic comparisons for 1D and 3D velocity models. The 1D model, `scak`, is the same that was used for moment tensor inversion (Section 4.4.2). Silwal & Tape (2016); Silwal et al. (2018) also used the same model for estimating moment tensors in southern Alaska and reported that the synthetic 1D model was faster by ~ 10 s for 16–40 seconds surface waves. However, for moment tensor inversion the synthetics were computed using the frequency-wavenumber integration method (Zhu & Rivera, 2002). The synthetics computed using SPECFEM3D confirm their findings (Figure 4.10). And as anticipated, the data-synthetic fits were considerably better when using the 3D velocity model.

4.9 Discussion

4.9.1 Minimum resolvable period test

Table C.5 and Table C.6 summarize the results from different simulations. We use quantities such as minimum resolvable period, simulation time, and required time-step, to compare the effects of topography and velocity model on different simulations.

1. Adding a low-velocity basin increases the minimum resolvable period. The acceptable minimum resolvable period increases from 3.5 sec to 4 sec after adding the Cook Inlet basin, however, the theoretical min resolvable period stays same at 6.4 sec. When estimating the minimum resolvable period, we only consider the first ~100 sec of the waveforms that will be used for time-window selection for computing adjoint source.
2. We also found that the actual usable time-step is systematically lower than the theoretical time-step for all test runs.
3. One way to increase the time-step is by smoothing the topography. For the Wrangell mesh smoothing the topography increased the dt from 0.014 s to 0.015 s.
4. We don't see any systematic effect on simulation time from topography smoothing and varying the model. For the Cook Inlet mesh, applying velocity thresholding tends to increase the simulation time, for both the smoothed and unsmoothed topography case. However, for the Interior mesh, velocity thresholding tends to reduce the simulation time. The major difference in these two meshes are: the presence of slab and a larger deeper basin in the Cook Inlet mesh, whereas the Interior mesh has higher topographic relief because of Denali. We also noted that for all simulations in the Cook Inlet and Wrangell meshes topography smoothing took more time than the unsmoothed mesh. Also, adding the basin and not applying velocity thresholding increased the simulation time.
5. Since topography smoothing does not significantly reduce the simulation time, we use non-smoothed topography for the rest of the tests when comparing data with synthetics for 20 events in each mesh.

4.9.2 Effect of 3D structure on seismic waveforms

Our final set of simulations for all events was performed on non-smoothed topography, with basins present and velocity thresholding. Figure 4.11 shows the effect of basins on seismic waveforms. We can see that even a slight change in azimuth can significantly perturb the recorded

waveforms. This effect due to the basin is less pronounced for slab events since most of the ray-paths coming from below do not transect through the basin.

We also found out that our synthetic 3D model does not accurately represent the Wrangell mountains region (Figure 4.12). The effects of topography are also most prominent in the Wrangell mesh.

Among all three meshes, the 3D velocity model for the Interior is closest to the actual velocity model (Figure 4.13). The effect of Denali could not be seen because it lies close to the boundary of the mesh.

4.10 Summary

1. We perform seismic wavefield simulations in three different regions: Cook Inlet, Interior, and Wrangell. For each simulation region we use the real topographic surface, which is part of an unstructured hexahedral mesh of finite elements. Each simulation region—namely the 3D seismic velocity model defined on the mesh—produces synthetic seismograms that are numerically accurate to a minimum period of about 3 seconds, and this minimum period varies throughout each region.
2. We estimate moment tensors for 20 earthquakes in each region. These moment tensors are used to assess the accuracy of the tomographic model for each region by comparing observed seismograms with synthetic seismograms. We find that the Interior model provides the best fit, while the Wrangell model provides the worst fit.
3. For the periods of interest (3–30 s), sedimentary basins have a strong influence on the seismic wavefield and are necessary to fit arrival times and amplitudes of surface waves at stations within and adjacent to these basins.

Table 4.1: Parameters for selecting earthquakes within the three subregions.

region	minimum # of stations	time range		minimum magnitude M_w	declustering nx ny zcut (km)	boundary buffer (km)
Cook Inlet	30	2007-01-01	2018-05-02	4.5	9 8 30	20
Interior	30	1999-01-01	2018-05-02	4.0	10 10 30	20
Wrangell	30	2002-12-01	2018-05-02	4.1	10 10 30	20

Table 4.2: Comparison among the three simulation regions of Alaska and the simulation region of southern California (Tape et al., 2009, 2010). The minimum period is the minimum resolvable period for the surface layers of the hexahedral mesh. The number of moment tensors for the Alaska regions is from the AEC catalog (Ratchkovski & Hansen, 2002); for southern California it is the catalog of Tape et al. (2009); Liu et al. (2009). The min/max values of topography are extracted from ETOPO1, which has a sampling interval of approximately 1.8 km (Amante & Eakins, 2009). The max number of stations lists the number of total broadband stations over the time interval 1999–2011; the permanent number of active stations is listed in parentheses.

	Cook Inlet	Interior	Wrangell	southern California
width (east-west), km	500	400	400	640
length (north-south), km	400	500	500	505
depth, km	400	400	400	60
minimum period, s	4.0	2.0	1.5	2.0
tectonic setting	subduction	strike-slip	collision	strike-slip
deepest seismicity	144	144	42	36
major basins	Cook Inlet, Susitna, Yentna	Nenana	Copper River, offshore	Los Angeles, Ventura, Santa Maria, Salton trough
major mountains	Talkeetna, east- ern Alaska Range	Denali, central Alaska Range	Wrangell Mountains, western Alaska Range	San Gabriel, southern Sierra Nevada, Coast Ranges
major faults	Castle moun- tain, western Denali fault	Minto Flats fault zone, central Denali fault	eastern De- nali fault, Totschunda	San Andreas, San Jacinto, Garlock
major volcanoes	Aleutian Arc volcanoes	none	Wrangell volca- noes	none
highest topography, km	3.6	5.64	5.43	4.0
lowest topography, km	-0.3	0.04	-0.46	-4.2
highest moho, km	-16.2	-19.3	-11.8	-9.8
lowest moho, km	-48.2	-43.6	-48.2	-39.7
number of moment tensors	20	20	20	234
max number of stations	140	127	128	210

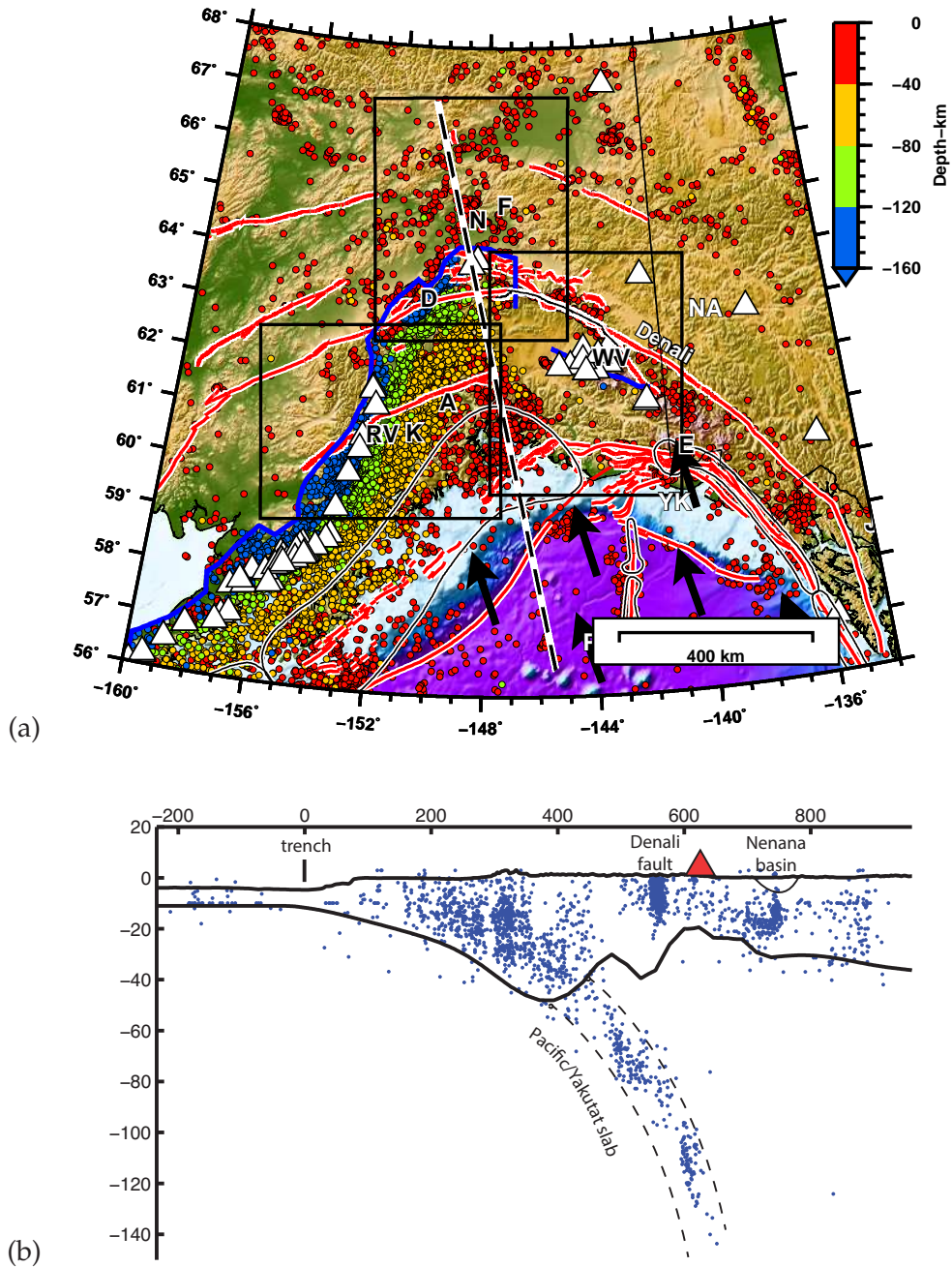


Figure 4.1: Active tectonic setting of the Aleutian–Alaskan subduction zone. (a) Seismicity ($M > 3$, 1990–2010), major active faults, active volcanoes, and aftershock zones of major ($M = 7.5$ – 9.2) earthquakes of the past 100 years. Location labels: F = Fairbanks, N = Nenana, D = Denali, A = Anchorage, K = Kenai, RV = Redoubt volcano, WV = Wrangell volcano, E = Mt. St. Elias. Plate labels: NA = North America, PA = Pacific, YK = Yakutat block; arrows indicate PA motion relative to NA (Bird, 2003). Each block denotes a simulation region: Cook Inlet, Interior, and Wrangell, which are expanded in Figure 4.2. (b) Seismicity profile along the dashed line in (a), with vertical exaggeration of 4:1. Upright triangle denotes Jumbo Dome and Buzzard Creek volcanic centers.

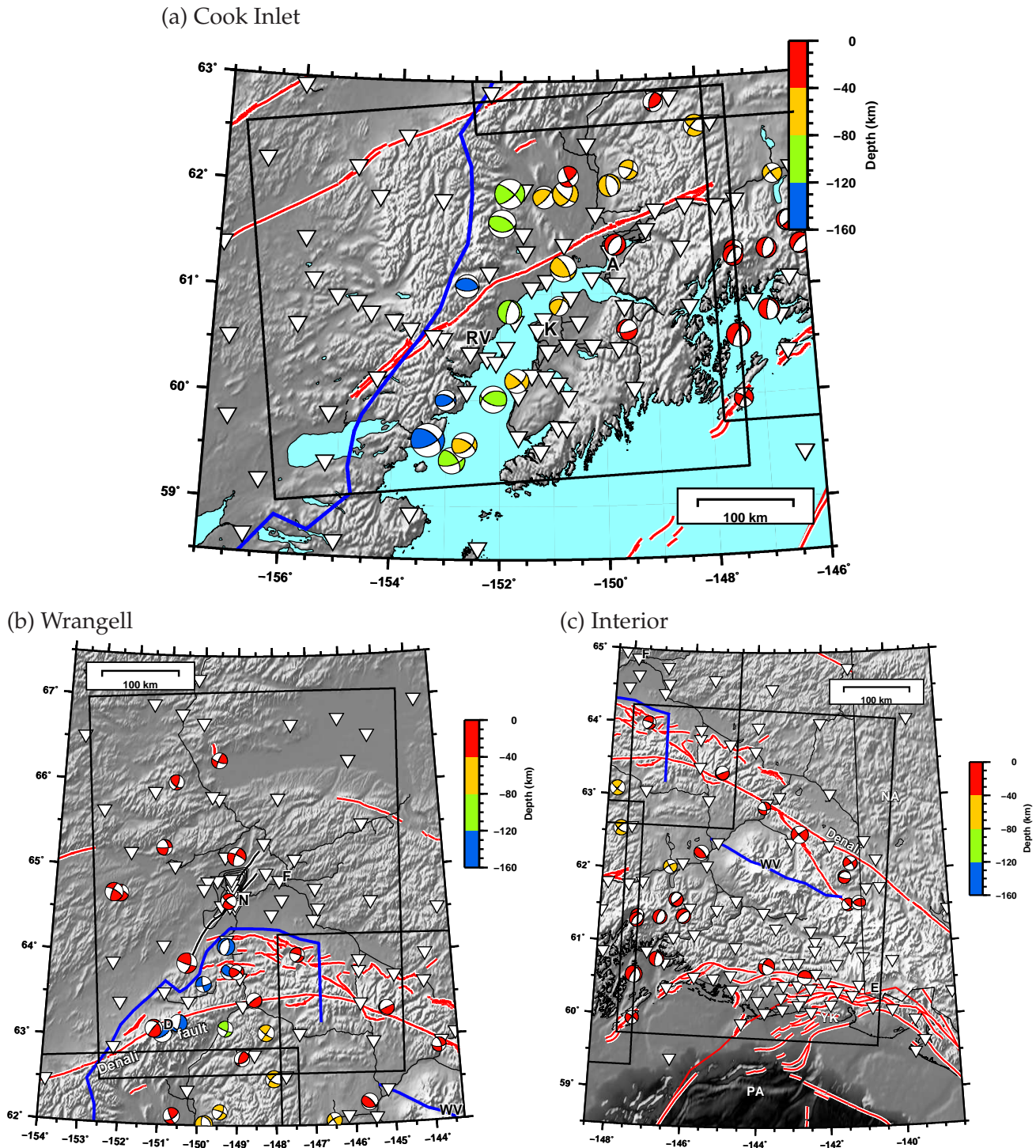


Figure 4.2: Three simulation regions, plus moment tensor solutions for 20 earthquakes in each region. See Section 4.4.1 for event selection criteria and Section 4.4.2 for the inversion methodology. (a) Cook Inlet region. See also Table C.2. (b) Wrangell region. See also Table C.4. (c) Interior region. See also Table C.3.

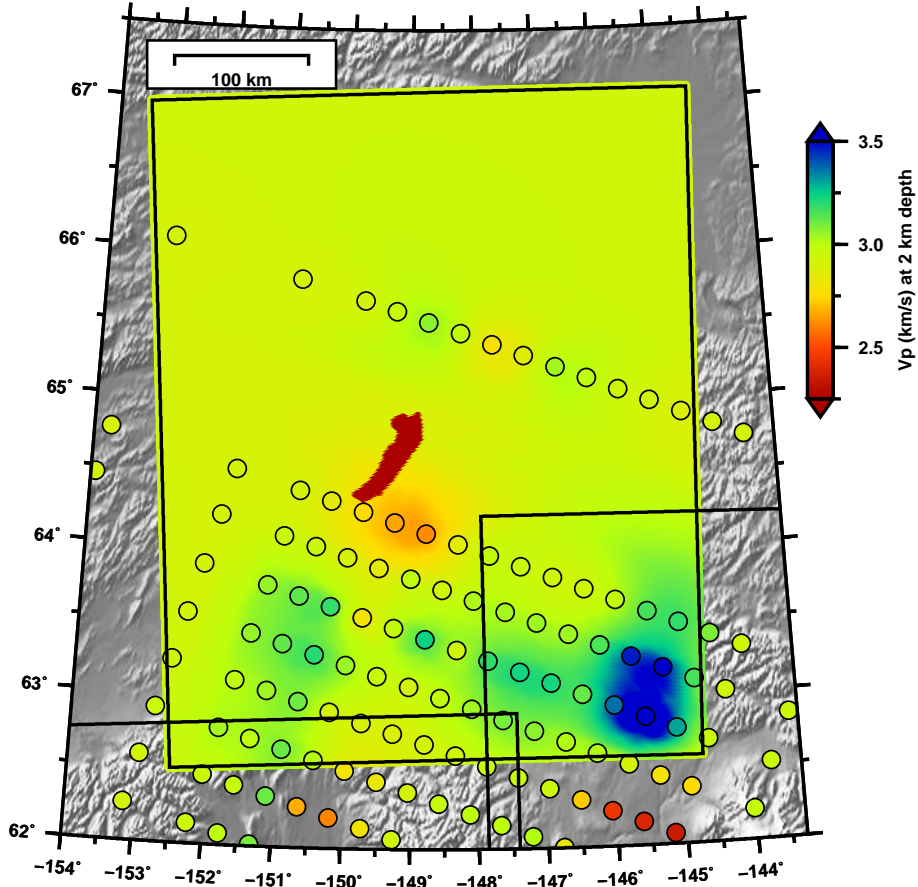
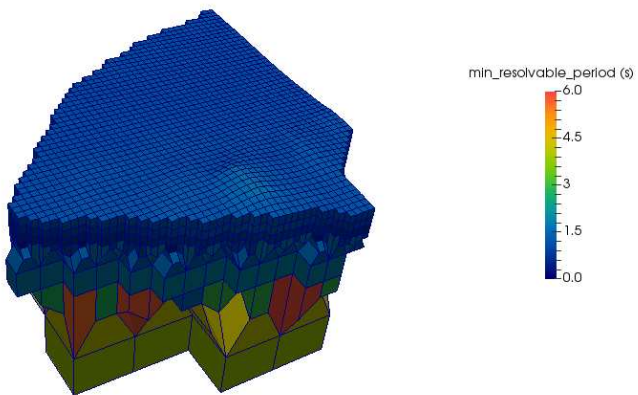


Figure 4.3: Horizontal cross section of V_P at 2 km depth, from the tomographic model of Eberhart-Phillips et al. (2006). The circles show the nodes in the original model; the rectangle shows the interpolated and extrapolated version used in the simulation region. The red feature at the center denotes the (slow) Nenana basin, which we embedded into the interpolated tomographic model. See Figures C.6–C.12 for V_P and V_S at the nodes, for a range of depths.

(a)



(b)

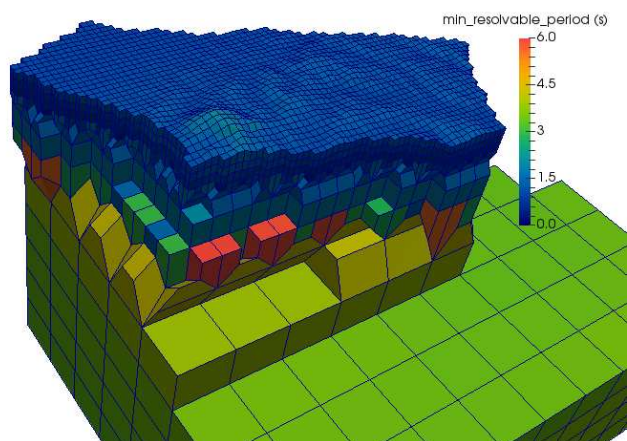


Figure 4.4: Effect of topographic smoothing near Denali and colored by theoretical minimum resolvable period (in seconds) for each mesh element. We can also see that minimum resolvable period roughly scales with the size of the elements and is higher for larger mesh elements, and is worst for tripling elements.

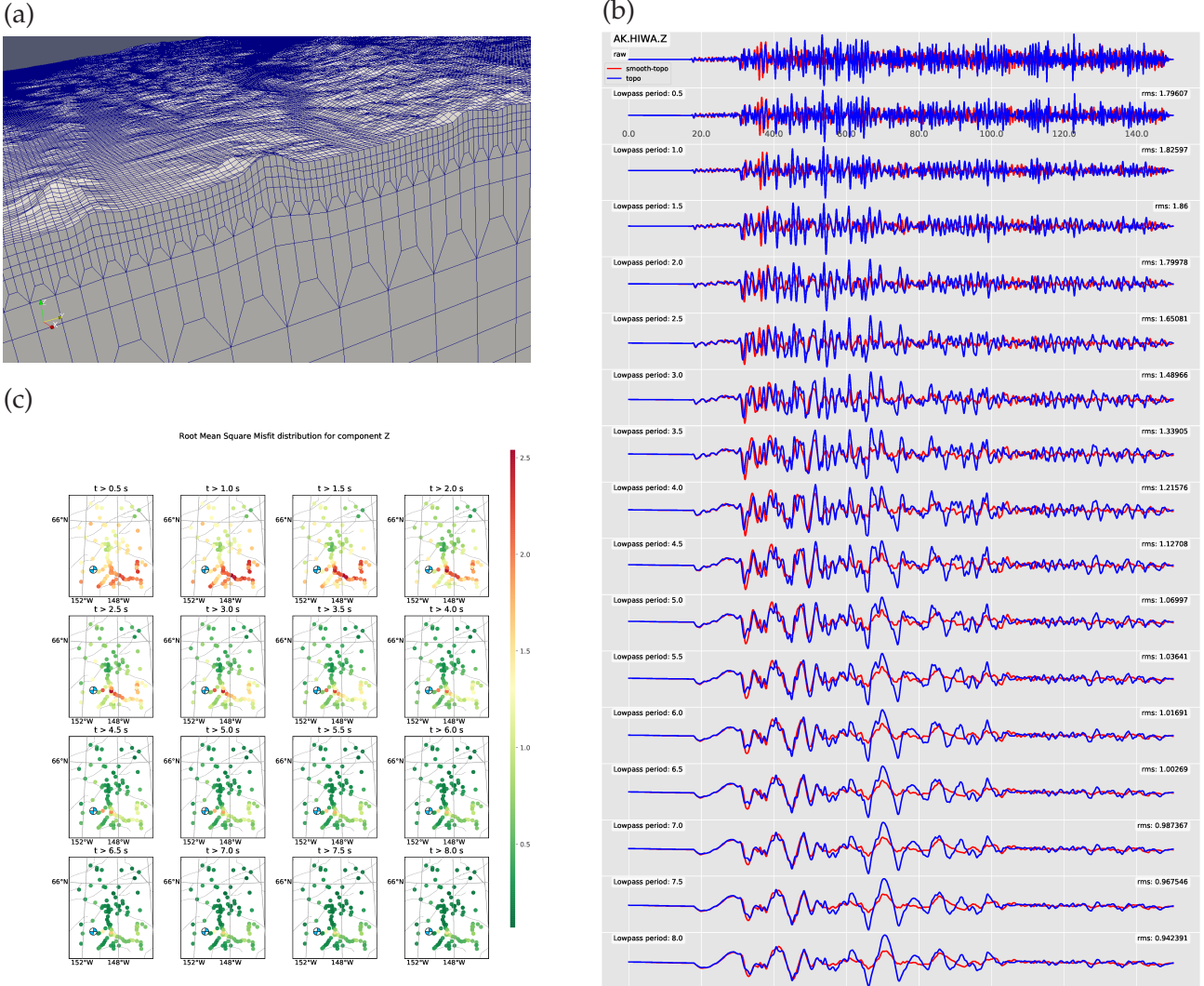


Figure 4.5: Effect of topographic smoothing on the Interior mesh. (c) Map subplots shows that the rms misfit is significantly larger (in red) for the stations on the Alaska range. (b) Comparisons between waveforms generated using smoothed (red) and unsmoothed topography (blue). Waveforms are shown for an example station (AK.HIWA.Z) and filtered at varying low-pass periods. The simulation time for both the runs is comparable (Table C.6). See Figure C.16 and Figure C.17 effects of topographic smoothing on Wrangell mesh.

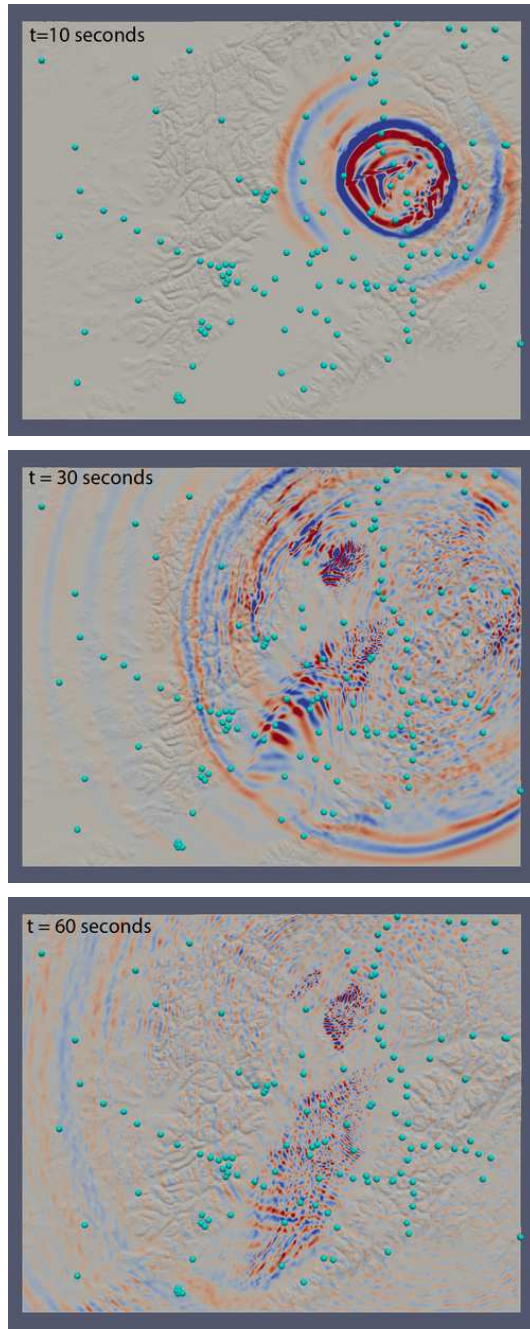


Figure 4.6: Snapshots of a 3D wavefield simulation showing the influence of the Cook Inlet and Susitna basins on the seismic wavefield. The simulation is performed for the 2009-04-07 Anchorage event for which the source was obtained from (Silwal & Tape, 2016). Colors represent the vertical component of simulated ground velocity. Cyan circles denote broadband stations.

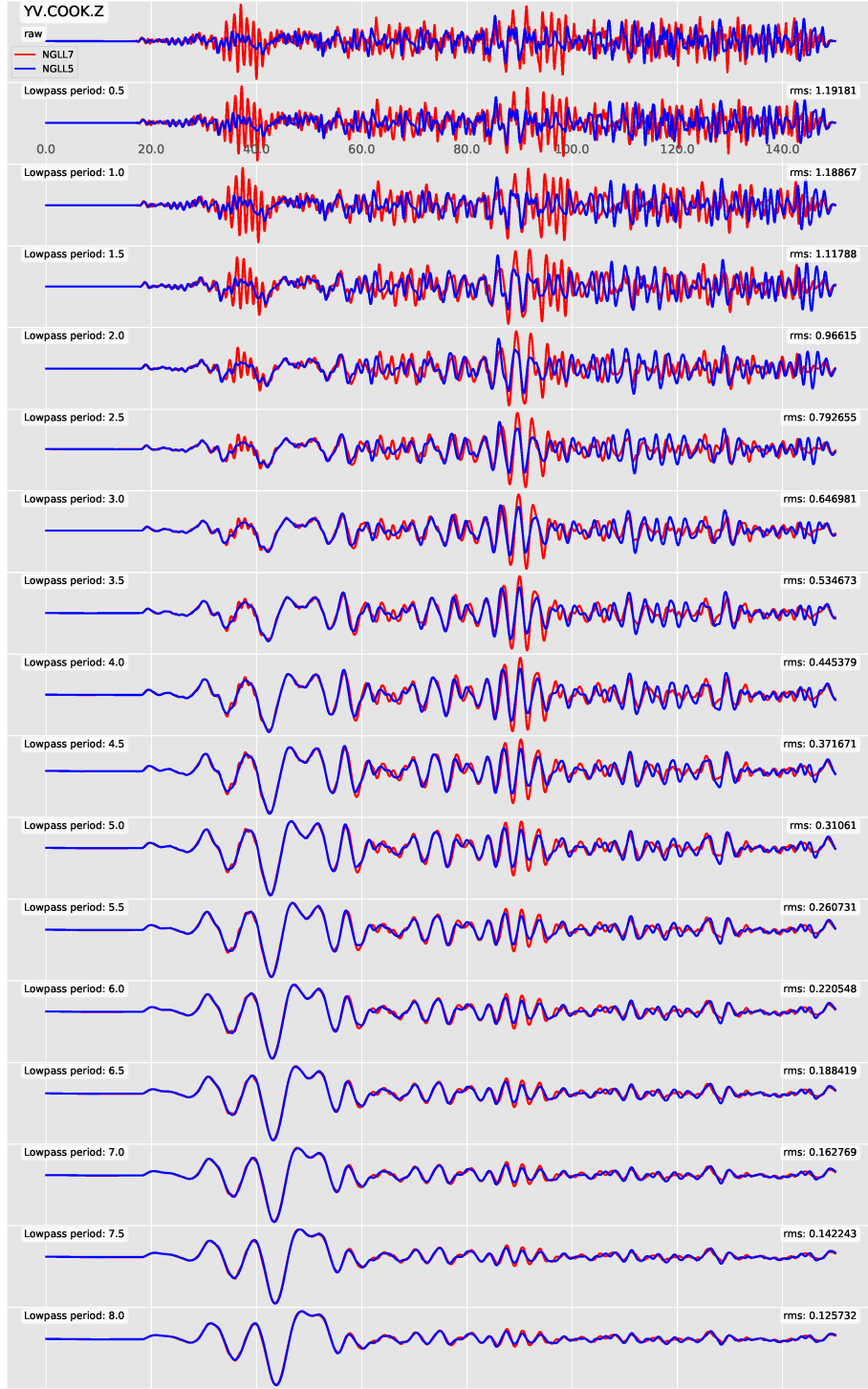


Figure 4.7: Estimating minimum resolvable period for single synthetic seismogram in the Cook Inlet mesh. Synthetics are generated using a coarse mesh (NGLL5) and a fine mesh (NGLL7), and then filtered at varying low-pass periods. Both sets of synthetics are generated using E2006 with embedded basins: Cook Inlet, Susitna, and Yentna. NGLL5 (blue) and NGLL7 (red) waveforms for an example station (YV.COOK.Z) shows that the differences are significantly large at higher frequencies. See Figure 4.8 for the waveform difference across all stations.

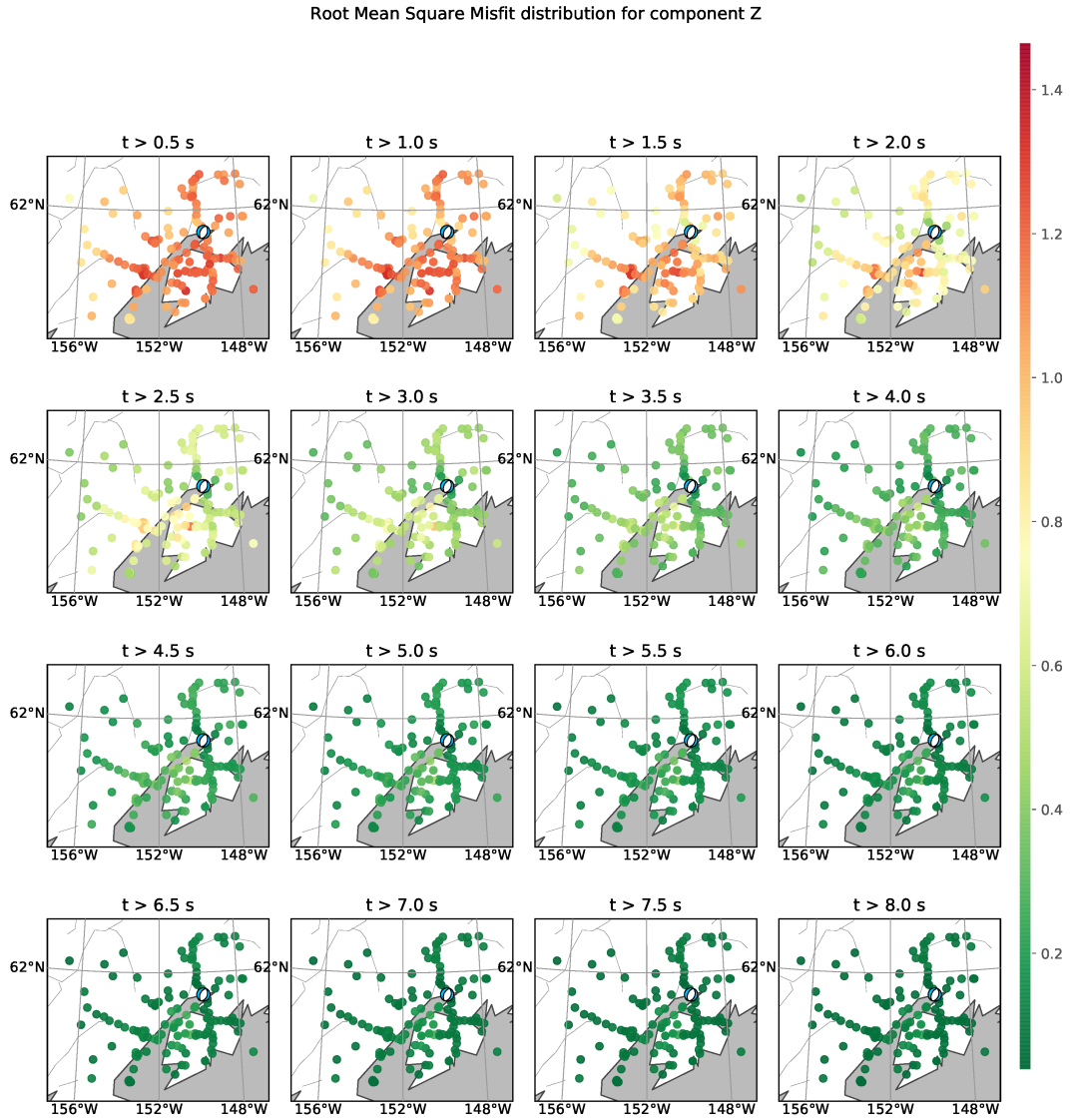


Figure 4.8: Estimating minimum resolvable period for a simulation in Cook Inlet mesh. Stations are colored by the root mean-square (rms) difference between waveforms generated using coarse mesh (NGLL5) and fine mesh (NGLL7). Each subplot shows the rms difference for waveforms filtered at different low-pass periods. See Figure 4.7 for an example set of waveforms at one of the stations (YV.COOK.Z). For this run our preferred minimum resolvable period is 4.0 s, whereas the theoretical estimate is 6.4 s. See Table C.5 for minimum resolvable period for all simulations. Our goal is to find the approximate period above which difference between coarse and fine mesh waveforms is negligible, i.e., all stations are colored green.

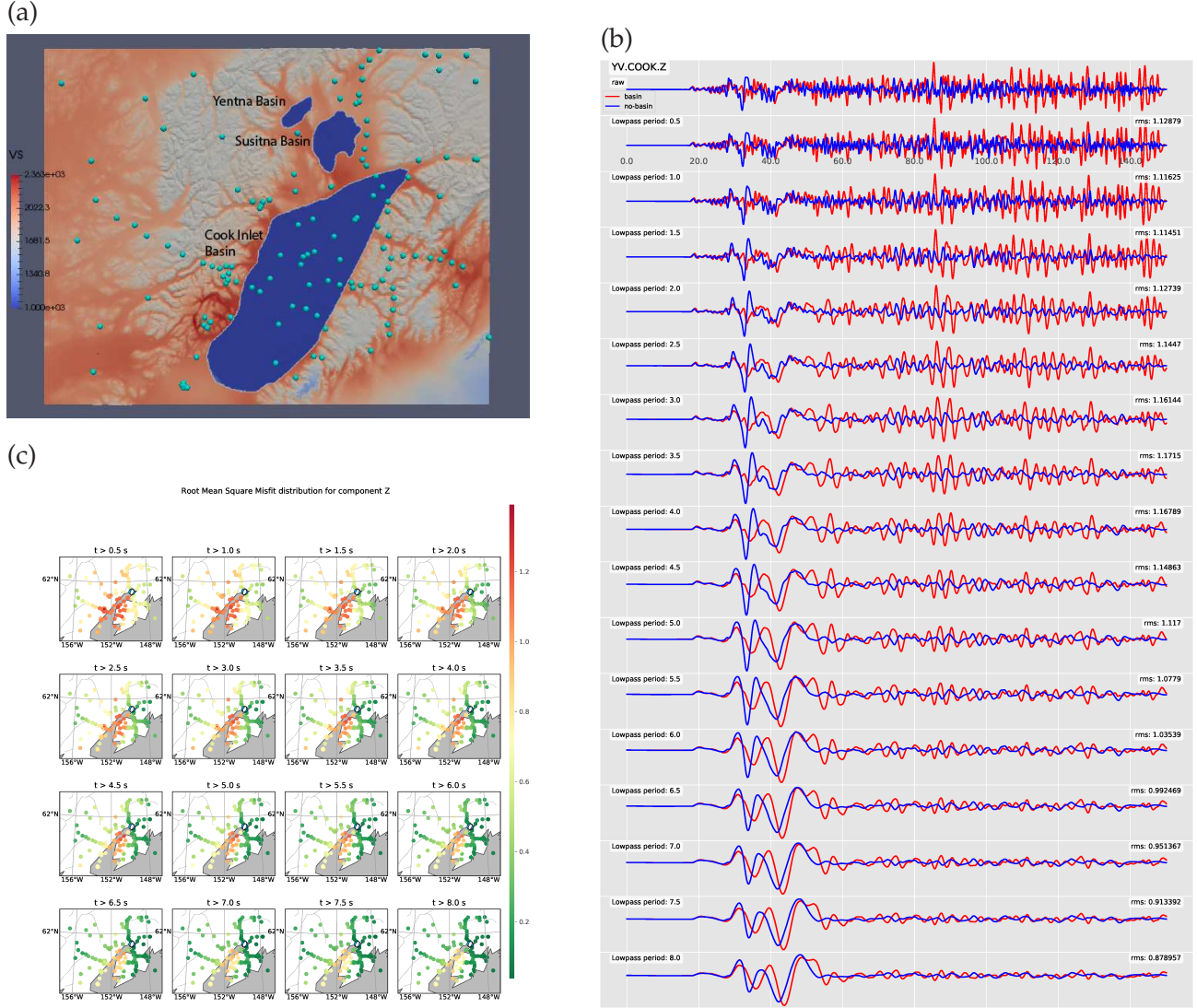


Figure 4.9: Effect of including basin on seismic waveforms. 1D velocity models for three basins are embedded into the 3D velocity model: Cook Inlet, Susitna and Yentna basin. (a) Surface view of velocity model with low velocity basins (blue). Blue circles denote broadband stations in the region. (b) Comparisons between waveforms generated with basin (red) and without basin (blue), and filtered at varying low-pass periods. (c) Map subplots shows that the rms misfit between waveforms is significantly large at the basin station even at ~ 8 seconds.

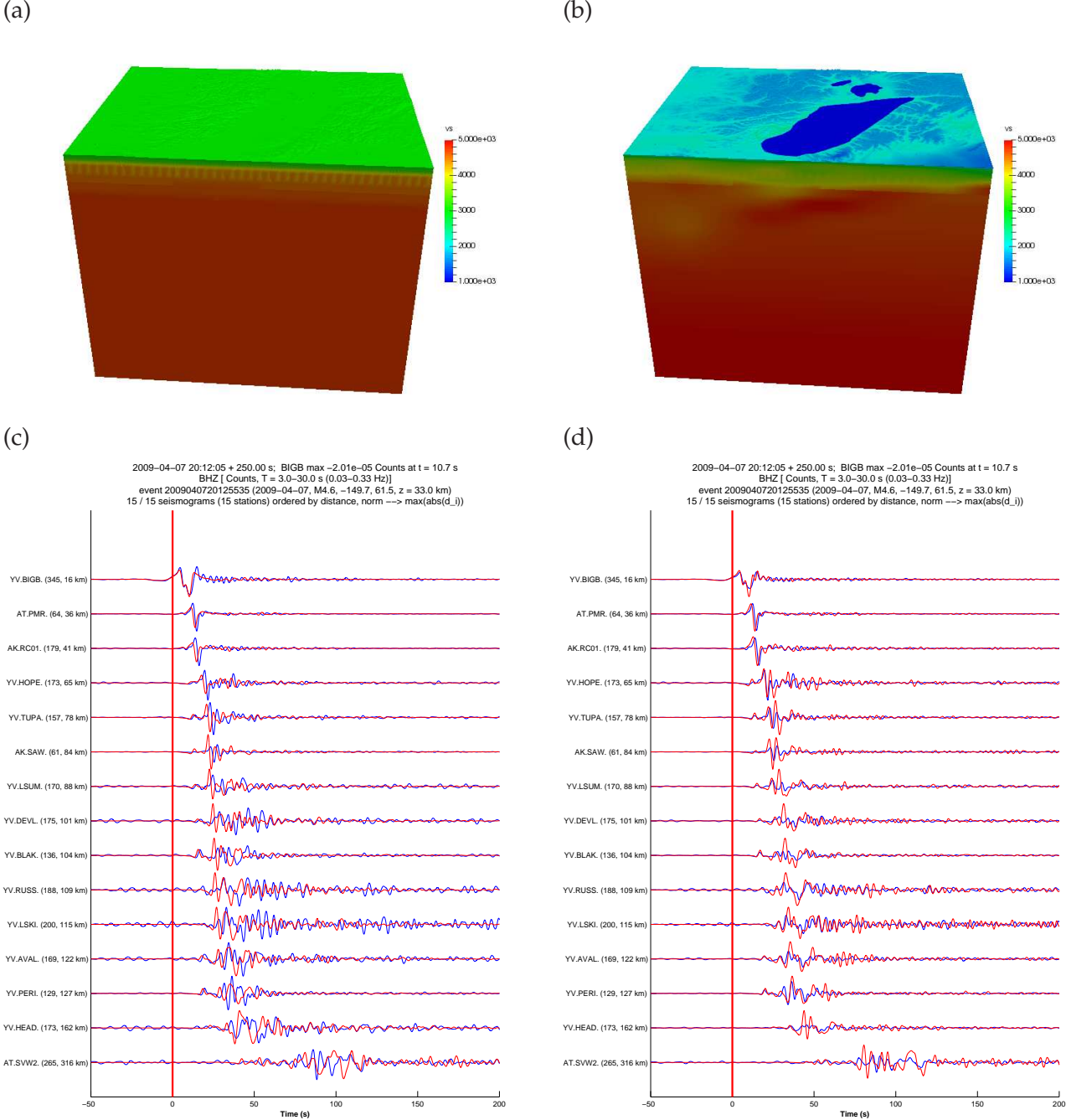


Figure 4.10: Comparison between waveforms generated using 1D and 3D velocity model. The same 1D model (a), scak, was also used for moment tensor inversion; (b) the 3D model is the interpolated E2006 model with 1D basin and velocity thresholding ($vs_{min} = 1000$ m/s). (c-d) Data (blue) and synthetics (red) comparisons at multiple stations. Stations are sorted by distance and waveforms are normalized by the maximum amplitude of synthetics. We can see that the 1D model is relatively faster than the data and the 3D model. Also, the data-synthetics fit at farther stations is much worse for 1D model, compared to the 3D model.

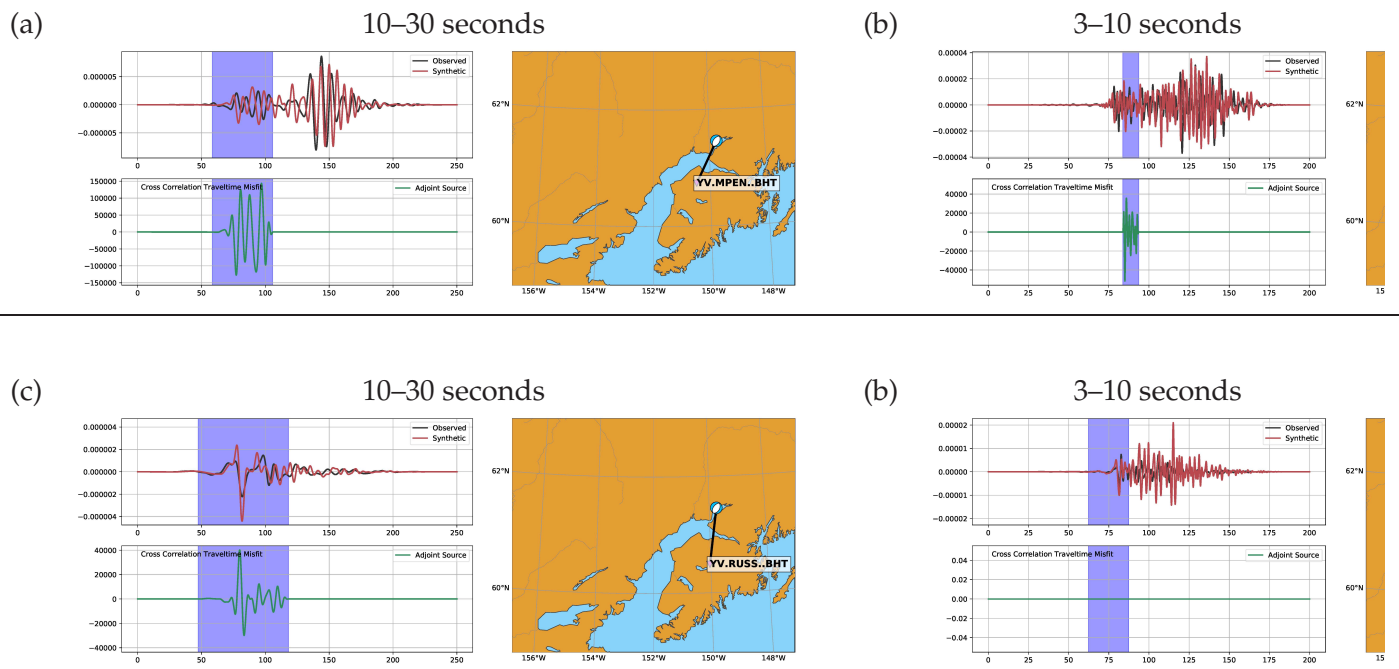


Figure 4.11: Effect of a basin on waves traversing through the basin. Observed (black) and synthetics (red) waveforms are shown at basin (YV.MPEN.T) and non-basin (YV.RUSS.T) sites. Also shown is the cross-correlation misfit measure between the observed and synthetics at (a) 10–30 s, and (b) 3–10 s.

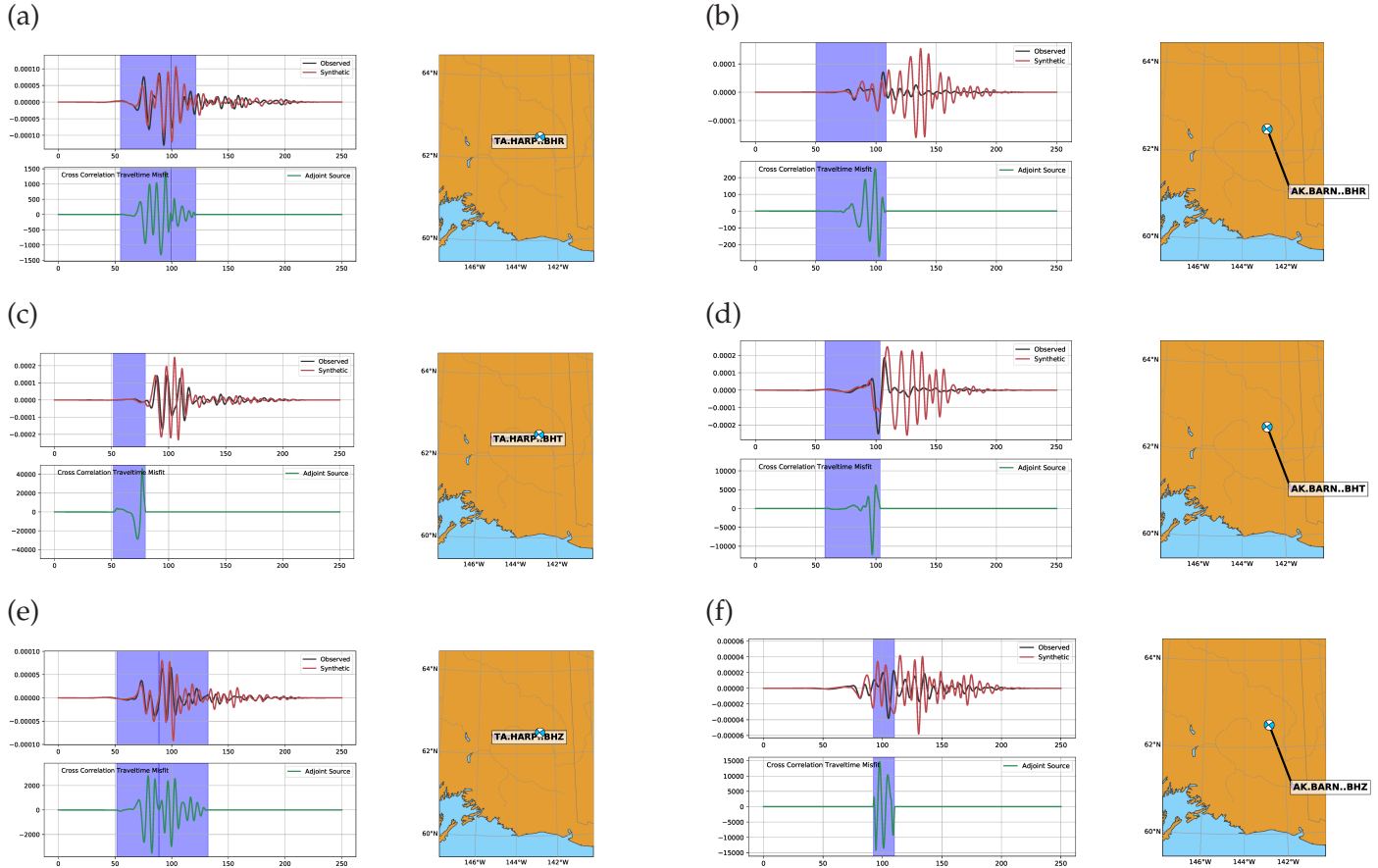
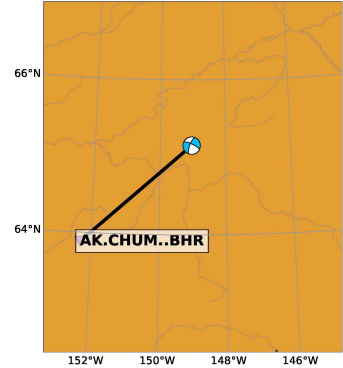
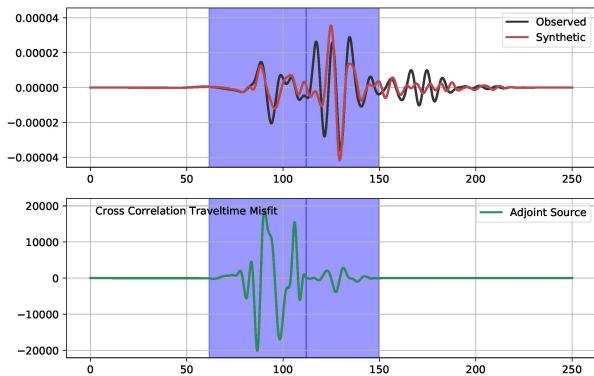


Figure 4.12: Radial, transverse, and vertical components for two stations in the Wrangell mesh. The data-synthetic fits for waves going to the east and getting recorded at the TA.HARP station are much better than the waveforms recorded at AK.BARN. A similar pattern was observed at other sites to south. This perhaps is due to the thick crust (upto 50 km) beneath Wrangells.

(a)



(b)

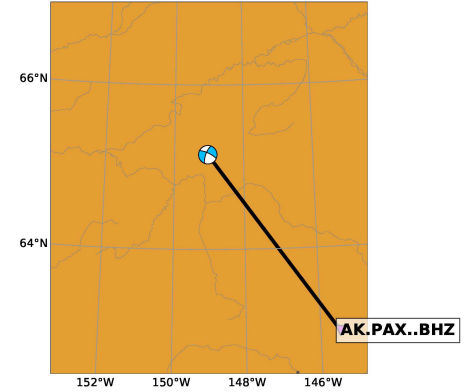
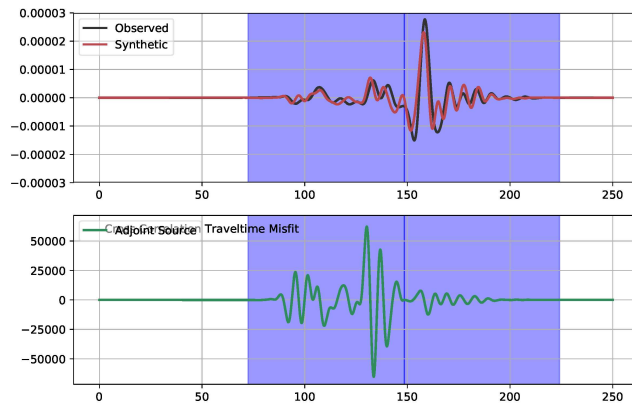


Figure 4.13: The data-synthetics fits are best for the Interior mesh. This perhaps is due to the lack of any large basin. Also the topography effects are minimal, compared to the Wrangell mesh, since the central Alaska range is at the edge of mesh.

References

- Amante, C. & Eakins, B. W., 2009. ETOPO1 1 Arc-Minute Global Relief Model: Procedures, Data Sources and Analysis, NOAA Technical Memorandum NESDIS NGDC-24, 19 pp.
- Bemis, S. P. & Wallace, W. K., 2007. Neotectonic framework of the north-central Alaska Range foothills, in *Tectonic Growth of a Collisional Continental Margin: Crustal Evolution of Southern Alaska*, pp. 549–572, eds Ridgway, K. D., Trop, J. M., Glen, J. M. G., & O'Neill, J. M., Geol. Soc. Am., Boulder, Colo., USA, Special Paper 431.
- Beyreuther, M., Barsch, R., Krischer, L., Megies, T., Behr, Y., & Wassermann, J., 2010. ObsPy: A Python toolbox for seismology, *Seismol. Res. Lett.*, **81**(3), 530–533, doi:10.1785/gssrl.81.3.530.
- Bird, P., 2003. An updated digital model of plate boundaries, *Geochem. Geophys. Geosyst.*, **4**, 1027, doi:10.1029/2001GC000252.
- Brocher, T. M., 2005. Empirical relations between elastic wavespeeds and density in the Earth's crust, *Bull. Seismol. Soc. Am.*, **95**(6), 2081–2092.
- Brocher, T. M., 2008. Compressional and shear-wave velocity versus depth relations for common rock types in northern California, *Bull. Seismol. Soc. Am.*, **98**(2), 950–968.
- Casarotti, E., Stupazzini, M., Lee, S. J., Komatitsch, D., Piersanti, A., & Tromp, J., 2008. CUBIT and seismic wave propagation based upon the spectral-element method: An advanced unstructured mesher for complex 3D geological media, in *Proceedings of the 16th International Meshing Roundtable*, pp. 579–597, Springer, Berlin.
- Christensen, D. H. & Abers, G. A., 2010. Seismic anisotropy under central Alaska from SKS splitting observations, *J. Geophys. Res.*, **115**, B04315, doi:10.1029/2009JB006712.
- Christeson, G. L., Gulick, S. P. S., van Avendonk, H. J. A., Worthington, L. L., Reece, R. S., & Pavlis, T. L., 2010. The Yakutat terrane: Dramatic change in crustal thickness across the Transition fault, Alaska, *Geology*, **38**(10), 895–898.
- Eberhart-Phillips, D., Christensen, D. H., Brocher, T. M., Hansen, R., Ruppert, N. A., Haeussler, P. J., & Abers, G. A., 2006. Imaging the transition from Aleutian subduction to Yakutat collision in central Alaska, with local earthquakes and active source data, *J. Geophys. Res.*, **111**, B11303, doi:10.1029/2005JB004240.

Ferris, A., Abers, G. A., Christensen, D. H., & Veenstra, E., 2003. High resolution image of the subducted Pacific (?) plate beneath central Alaska, 50–150 km depth, *Earth Planet. Sci. Lett.*, **214**, 575–588.

Fuis, G. S., Ambos, E. L., Mooney, W. D., Christensen, N. I., & Geist, E., 1991. Crustal structure of accreted terranes in southern Alaska, Chugach Mountains and Copper River basin, from seismic refraction results, *J. Geophys. Res.*, **96**(B3), 4187–4227.

Fuis, G. S., Moore, T. E., Plafker, G., Brocher, T. M., Fisher, M. A., Mooney, W. D., Nokleberg, W. J., Page, R. A., Beaudoin, B. C., Christensen, N. I., Levander, A. R., Lutter, W. J., Saltus, R. W., & Ruppert, N. A., 2008. Trans-Alaska Crustal Transect and continental evolution involving subduction underplating and synchronous foreland thrusting, *Geology*, **36**(3), 267–270.

Gulick, S. P. S., Lowe, L. A., Pavlis, T. L., Gardner, J. V., & Mayer, L. A., 2007. Geophysical insights into the Transition fault debate: Propagating strike slip in response to stalling Yakutat block subduction in the Gulf of Alaska, *Geology*, **35**(8), 763–766.

Haeussler, P. J., 2008. An overview of the neotectonics of interior Alaska: Far-field deformation from the Yakutat microplate collision, in *Active Tectonics and Seismic Potential of Alaska*, vol. 179 of **Geophysical Monograph**, pp. 83–108, eds Freymueller, J. T., Haeussler, P. J., Wesson, R., & Ekström, G., Am. Geophys. Un., Washington, D.C.

Hwang, L. J. & Kanamori, H., 1992. Rupture process of the 1987–1988 Gulf of Alaska earthquake sequence, *J. Geophys. Res.*, **97**(B13), 19,881–19,908.

Jadamec, M. A. & Billen, M. I., 2010. Reconciling surface plate motions with rapid three-dimensional mantle flow around a slab edge, *Nature*, **465**, 338–342, doi:10.1038/nature09053.

Jarrard, R. D., 1986. Relations among subduction parameters, *Rev. Geophys.*, **24**(2), 217–284.

Kissling, E. & Lahr, J. C., 1991. Tomographic image of the Pacific Slab under southern Alaska, *Eclogae geol. Helv.*, **84**(2), 297–315.

Komatitsch, D., Liu, Q., Tromp, J., Süss, P., Stidham, C., & Shaw, J. H., 2004. Simulations of ground motion in the Los Angeles basin based upon the spectral-element method, *Bull. Seismol. Soc. Am.*, **94**(1), 187–206, doi:10.1785/0120030077.

Krischer, L., Mengies, T., Barsch, R., Beyreuther, M., Lecocq, T., Caudron, C., & Wassermann, J., 2015. ObsPy: a bridge for seismology into the scientific Python ecosystem, *Computational Science & Discovery*, **8**(1), 014003, doi:10.1088/1749-4699/8/1/014003.

Lee, S.-J., Chen, H.-W., Liu, Q., Komatitsch, D., Huang, B.-S., & Tromp, J., 2008. Three-dimensional simulations of seismic-wave propagation in the Taipei basin with realistic topography based upon the spectral-element method, *Bull. Seismol. Soc. Am.*, **98**(1), 253–264.

Li, J., Abers, G. A., Kim, Y., & Christensen, D., 2013. Alaska megathrust 1: Seismicity 43 years after the great 1964 Alaska megathrust earthquake, *J. Geophys. Res.*, **118**, 4861–4871, doi:10.1002/jgrb.50358.

Liu, Q., Polet, J., Komatitsch, D., & Tromp, J., 2004. Spectral-element moment tensor inversions for earthquakes in southern California, *Bull. Seismol. Soc. Am.*, **94**(5), 1748–1761, doi: 10.1785/012004038.

Liu, Q., Tape, C., Maggi, A., & Tromp, J., 2009. Moment tensor inversions for adjoint tomography of southern California, in *2009 Southern California Earthquake Center Annual Meeting, Proceedings and Abstracts*, vol. 19, p. 260.

Ma, S., Archuleta, R. J., & Page, M. T., 2007. Effects of large-scale surface topography on ground motions, as demonstrated by a study of the San Gabriel Mountains, Los Angeles, California, *Bull. Seismol. Soc. Am.*, **97**(6), 2066–2079.

Moore, J. C., Diebold, J., Fisher, M. A., Sample, J., Brocher, T., Talwani, M., Ewing, J., von Huene, R., Rowe, C., Stone, D., Stevens, C., & Sawyer, D., 1991. EDGE deep seismic reflection transect of the eastern Aleutian arc-trench layered lower crust reveals underplating and continental growth, *Geology*, **19**, 420–424.

Page, R. A., Plafker, G., & Pulpan, H., 1995. Block rotation in east-central Alaska: A framework for evaluating earthquake potential?, *Geology*, **23**(7), 629–632.

Peter, D., Komatitsch, D., Luo, Y., Martin, R., Le Goff, N., Casarotti, E., Le Loher, P., Magnoni, F., Liu, Q., Blitz, C., Nissen-Meyer, T., Basini, P., & Tromp, J., 2011. Forward and adjoint simulations of seismic wave propagation on fully unstructured hexahedral meshes, *Geophys. J. Int.*, **186**, 721–739.

Plafker, G., Hudson, T. L., Bruns, T., & Rubin, M., 1978. Late Quaternary offsets along the Fairweather fault and crustal plate interactions in southern Alaska, *Can. J. Earth Sci.*, **15**(5), 805–816.

Qi, C., Zhao, D., & Chen, Y., 2007a. Search for deep slab segments under Alaska, *Phys. Earth Planet. Inter.*, **165**, 68–82.

Qi, C., Zhao, D., Chen, Y., & Ruppert, N. A., 2007b. New insight into the crust and upper mantle structure under Alaska, *Polar Science*, **1**, 85–100.

Ratchkovski, N. A. & Hansen, R. A., 2002. New constraints on tectonics of interior Alaska: Earthquake locations, source mechanisms, and stress regime, *Bull. Seismol. Soc. Am.*, **92**(3), 998–1014, doi:10.1785/0120010182.

Ridgway, K. D., Trop, J. M., Nokleberg, W. J., Davidson, C. M., & Eastham, K. R., 2002. Mesozoic and Cenozoic tectonics of the eastern and central Alaska Range: Progressive basin development and deformation in a suture zone, *Geol. Soc. Am. Bull.*, **114**(12), 1480–1504.

Ridgway, K. D., Thoms, E. E., Layer, P. W., Lesh, M. E., White, J. M., & Smith, S. V., 2007. Neogene transpressional foreland basin development on the north side of the central Alaska Range, Usibelli Group and Nenana Gravel, Tanana basin, in *Tectonic Growth of a Collisional Continental Margin: Crustal Evolution of Southern Alaska*, pp. 507–547, eds Ridgway, K. D., Trop, J. M., Glen, J. M. G., & O'Neill, J. M., Geol. Soc. Am., Boulder, Colo., USA, Special Paper 431.

Rodgers, A., Petersson, A., Nilsson, S., Sjögren, B., & McCandless, K., 2008. Broadband waveform modeling of moderate earthquakes in the San Francisco Bay area and preliminary assessment of the USGS 3D seismic velocity model, *Bull. Seismol. Soc. Am.*, **98**(2), 969–988.

Rondenay, S., Montési, L. G. J., & Abers, G. A., 2010. New geophysical insight into the origin of the Denali volcanic gap, *Geophys. J. Int.*, **182**, 613–630.

Saltus, R. W., Hudson, T. L., & Connard, G. G., 1999. A new magnetic view of Alaska, *GSA Today*, **9**(3), 1–6.

Saltus, R. W., Haeussler, P. J., Bracken, R. E., Doucette, J. P., & Jachens, R. C., 2001. Anchorage Urban Region Aeromagnetics (AURA) Project – Preliminary Geophysical Results, Open-File Report 01-0085.

Saltus, R. W., Hudson, T. L., & Wilson, F. H., 2007. The geophysical character of southern Alaska—Implications for crustal evolution, in *Tectonic Growth of a Collisional Continental Margin: Crustal Evolution of Southern Alaska*, pp. 1–20, eds Ridgway, K. D., Trop, J. M., Glen, J. M. G., & O'Neill, J. M., Geol. Soc. Am., Boulder, Colo., USA, Special Paper 431.

Saltus, R. W., Brown II, P. J., Morin, R. L., & Hill, P. L., 2008. 2006 Compilation of Alaska Gravity Data and Historical Reports, U.S. Geol. Survey Digital Series 264, CD-ROM.

Shellenbaum, D. P., Gregersen, L. S., & Delaney, P. R., 2010. Top Mesozoic unconformity depth map of the Cook Inlet Basin, Alaska, Alaska Div. Geol. Geophys. Surv. Report of Investigation 2010-2, 1 sheet, scale 1:500,000, available at <http://www.dggs.alaska.gov/pubs/id/21961> (last accessed 2016-10-30).

Silwal, V. & Tape, C., 2016. Seismic moment tensors and estimated uncertainties in southern Alaska, *J. Geophys. Res. Solid Earth*, **121**, 2772–2797, doi:10.1002/2015JB012588.

Silwal, V., Tape, C., & Lomax, A., 2018. Crustal earthquakes in the Cook Inlet and Susitna region of southern Alaska, *Tectonophysics* (submitted).

Stephens, C. D., Fogelman, K. A., Lahr, J. C., & Page, R. A., 1984. Wrangell Benioff zone, southern Alaska, *Geology*, **12**, 373–376.

Tape, C., Liu, Q., Maggi, A., & Tromp, J., 2009. Adjoint tomography of the southern California crust, *Science*, **325**, 988–992, doi:10.1126/science.1175298.

Tape, C., Liu, Q., Maggi, A., & Tromp, J., 2010. Seismic tomography of the southern California crust based on spectral-element and adjoint methods, *Geophys. J. Int.*, **180**, 433–462.

Tape, C., Casarotti, E., Plesch, A., & Shaw, J. H., 2011. Seismogram-based assessment of the southern California seismic velocity model CVM-H 11.9 with 234 reference earthquakes, in *2011 Southern California Earthquake Center Annual Meeting, Proceedings and Abstracts*, vol. 21, p. 235.

Tape, C., Silwal, V., Ji, C., Keyson, L., West, M. E., & Ruppert, N., 2015. Transtensional tectonics of the Minto Flats fault zone and Nenana basin, central Alaska, *Bull. Seismol. Soc. Am.*, **105**(4), 2081–2100, doi:10.1785/0120150055.

Tape, C., Christensen, D., Moore-Driskell, M. M., Sweet, J., & Smith, K., 2017. Southern Alaska Lithosphere and Mantle Observation Network (SALMON): a seismic experiment covering the active arc by road, boat, plane, and helicopter, *Seismol. Res. Lett.*, **88**(4), 1185–1202, doi:10.1785/0220160229.

Tape, C., Holtkamp, S., Silwal, V., Hawthorne, J., Kaneko, Y., Ampuero, J. P., Ji, C., Ruppert, N., Smith, K., & West, M. E., 2018. Earthquake nucleation and fault slip complexity in the lower crust of central Alaska, *Nature Geoscience*, **11**, 536–541, doi:10.1038/s41561-018-0144-2.

Van Kooten, G. K., Richter, M., & Zippi, P. A., 2012. Alaska's Interior rift basins: a new frontier for discovery, *Oil & Gas J.*, **110**(1a), 48–57.

Veenstra, E., Christensen, D. H., Abbers, G. A., & Ferris, A., 2006. Crustal thickness variation in south-central Alaska, *Geology*, **34**(9), 781–784.

Wang, Y. & Tape, C., 2014. Seismic velocity structure and anisotropy of the Alaska subduction zone derived from surface wave tomography, *J. Geophys. Res. Solid Earth*, **119**, 8845–8865, doi:10.1002/2014JB011438.

Ward, K. M., 2015. Ambient noise tomography across the southern Alaskan Cordillera, *Geophys. Res. Lett.*, **42**, 3218–3227, doi:10.1002/2015GL063613.

Wolf, L. W., Stone, D. B., & Davies, J. N., 1991. Crustal structure of the active margin, south central Alaska: An interpretation of seismic refraction data from the Trans-Alaska Crustal Transect, *J. Geophys. Res.*, **96**(B10), 16,455–16,469.

Worthington, L. L., Gulick, S. P. S., & Pavlis, T. L., 2010. Coupled stratigraphic and structural evolution of a glaciated orogenic wedge, offshore St. Elias orogen, Alaska, *Tectonics*, **29**, TC6013, doi:10.1029/2010TC002723.

Ye, S., Flueh, E. R., Klaeschen, D., & von Huene, R., 1997. Crustal structure along the EDGE transect beneath the Kodiak shelf off Alaska derived from OBH seismic refraction data, *Geophys. J. Int.*, **130**, 283–302.

Zhao, D., Christensen, D., & Pulpan, H., 1995. Tomographic imaging of the Alaska subduction zone, *J. Geophys. Res.*, **100**(B4), 6487–6504.

Zhu, L. & Helmberger, D., 1996. Advancement in source estimation techniques using broadband regional seismograms, *Bull. Seismol. Soc. Am.*, **86**(5), 1634–1641.

Zhu, L. & Rivera, L. A., 2002. A note on the dynamic and static displacements from a point source in multilayered media, *Geophys. J. Int.*, **148**, 619–627, doi:10.1046/j.1365-246X.2002.01610.x.

Chapter 5

Conclusion

We perform moment tensor inversions in Alaska using body waves and surface waves. In Chapter 2 we showed that using more stations and using body waves in addition to surface waves can improve the moment tensor solution. Further improvement in the inversion technique included:

- Implementing an L1-norm misfit function and demonstrating that it results in a more stable solution (Chapter 2). This was applied and tested in a range of tectonic settings: subduction (Silwal & Tape, 2016; Silwal et al., 2018), strike-slip (Tape et al., 2015, 2018), volcanic (Alvizuri & Tape, 2016), and nuclear events (Alvizuri et al., 2018).
- A new probabilistic approach for quantifying the uncertainty in moment tensor inversion (Chapter 2). This was applied to double couple moment tensor solutions (Silwal & Tape, 2016) and later applied to full moment tensors (Alvizuri et al., 2018). The theoretical description of uncertainty estimation is provided in Tape & Tape (2016).
- Introducing a generalized misfit function that combines waveform misfit and first-motion polarity misfit (Chapter 3). The misfit function also takes into account number of stations, bandpass used for filtering, and length of time window to be used for data-synthetics comparison, such that the final misfit measurement rewards the use of more of the recorded seismic wavefield. This was applied and tested on crustal earthquakes (Silwal et al., 2018) and full moment tensor solutions in range of tectonic settings (Alvizuri et al., 2018).

The improvement in the moment tensor inversion technique is an ever-evolving process, and the improvements depend on the sources under investigation. The improvements in Chapter 3 arose from the need to determine stable solutions for small-to-intermediate magnitude crustal earthquakes.

Chapter 3 is a focused study on crustal earthquakes in the Cook Inlet and Susitna region of south-central Alaska (see Figure 5.1 for comparison with Chapter 2 sources). We performed moment tensor inversion for 53 modern crustal earthquakes using high-frequency body waves (1–10 Hz) and first-motion polarities, and the predominance of thrust faulting solutions suggest a compressive regime in the region. Since there were no crustal earthquake in the GCMT catalog (1976–), we looked in other historical catalogs and found 11 major earthquakes ($M_w \geq 5.8$) since 1904 in Cook Inlet and Susitna region. Probabilistic hypocenter estimation using P-arrival times at numerous teleseismic stations for these 11 earthquakes showed that several were indeed crustal. The absence of large crustal earthquakes after the 1950's could perhaps be due to the extensional stress perturbation in southern Alaska after the 1964 earthquake, as suggested by Doser & Brown

(2001). We also performed hypocenter relocation using the double-difference algorithm and re-confirmed seismicity is diffuse under Susitna basin. However, the seismicity under the Cook Inlet basin is clustered under the deepest part of the basin, and the source mechanisms align with previously identified anticlines.

Chapter 3 can also be seen as a connecting link between Chapter 2 and Chapter 4. Chapter 2 presents a misfit function to obtain a reliable solution for intermediate-magnitude earthquakes. In Chapter 3 we modified the misfit function by including polarity misfit to obtain reliable solutions for crustal earthquakes in the presence of basins. In Chapter 4 we use a 3D velocity model and investigate the effect of structure (basin, topography, heterogeneity), using the moment tensors determined in Chapter 2.

For moment tensor inversions of smaller earthquakes using the 1D velocity model in Chapter 3, we mostly used high-frequency body waves, since there was poor signal-to-noise for surface waves. We were able to do this by only allowing the first pulse of data and synthetics to match. The effects of basin, topography, subducting pacific plate, and other local heterogeneties were so severe, that reliable fits between data and synthetics—even at longer periods—could not be achieved. Chapter 4 tries to investigate these factors. We interpolated a published 3D velocity model of Alaska Eberhart-Phillips et al. (2006) and added the basin and topography to it. After testing different variations in topography and the velocity model, we present a 3D reference velocity model that will be used as a starting model for adjoint tomography in Alaska. This reference model is the interpolated Eberhart-Phillips et al. (2006) model, embedded with major basins, and including topography.

5.1 Code Development

Code development and creating reproducible workflows have been a focus of our efforts. Most of the codes used are publicly available (or available upon request), and are used by multiple users that helps in faster bug detection and resolution. The following list contains the primary codes that were developed as part of the thesis:

1. **pysep**

<https://github.com/uafseismo/pysep>

A python based package for extracting waveforms from IRIS and processing them using obspy to get them ready for moment tensor inversion capuaf or adjoint seismogram extraction and processing package.

Contributors (alphabetical): Celso Alvizuri, Lion Krischer, Vipul Silwal, Kyle Smith, Carl Tape.

2. **capuaf**

<https://github.com/uafseismo/capuaf>

Seismic moment tensor inversion code using "cut-and-paste" approach developed at UAF. The official version of CAP is available for download from the website of Lupei Zhu <http://www.eas.slu.edu/People/LZhu/home.html>.

Contributors (alphabetical): Celso Alvizuri, Vipul Silwal, Carl Tape.

3. **wfdiff**

<https://github.com/vsilwal/wfdiff>

A python based waveform difference package for synthetic-synthetic waveform difference. Typically this is used for estimating minimum-resolvable period, however, it can also be used for visualizing the effect of topography or basin (Section 4.7), and for data-synthetics comparisons.

Contributors (alphabetical): Lion Krischer, Vipul Silwal, Carl Tape.

5.2 Future work

1. Throughout this study we used a 1D velocity model for moment tensor estimation. Previous authors have examined the role of 3D vs 1D structure on estimating moment tensors (e.g., Liu et al., 2004; Zhao et al., 2006; Covellone & Savage, 2012; Nayak & Dreger, 2018). Our future efforts are guided towards building a python based package that allows use of 3D synthetics for full moment tensor and uncertainty estimation.
2. It is common to use a time shift when performing waveform based moment tensor inversion to account for structures not present in the velocity model used to generate the synthetics. In Chapter 2 and Chapter 3 we note the time shifts between the data and synthetics. We believe that the source of this time shift was the use of the 1D velocity model that is faster than the actual earth structure. The time shifts were reduced for synthetics generated using the 3D velocity model (Figure 4.10). More work needs to be done for analyzing the impact of 1D model on moment tensor solution and the time shifts.
3. In Chapter 2 we showed that one should be cautious in using the time shifts since this could lead to a solution that is a local minimum. This local minimum is in fact the completely opposite moment tensor ($-M_0$) to the global solution (M_0). Recent work by Alvizuri et al. (2018) also documented the same feature for full moment tensor inversions. The inclusion of first-motion polarities helps resolve this issue.

4. I performed moment tensor inversions for 240 earthquakes in this thesis. This involved manually selecting waveforms for which the data-synthetics fits are good. A total of 74,775 unique waveforms were used for this purpose. A future approach should try to adopt a machine-learning algorithm for automating this process so that it can be applied on a larger set of earthquakes.
5. Adjoint tomography in Alaska is in progress. The moment tensor catalog from Chapter 2 will form part of the sources to be used in southern Alaska. More sources will be computed for recent earthquakes in each region, to benefit from increased station coverage due to the temporary arrays of TA, SALMON, and FLATS.

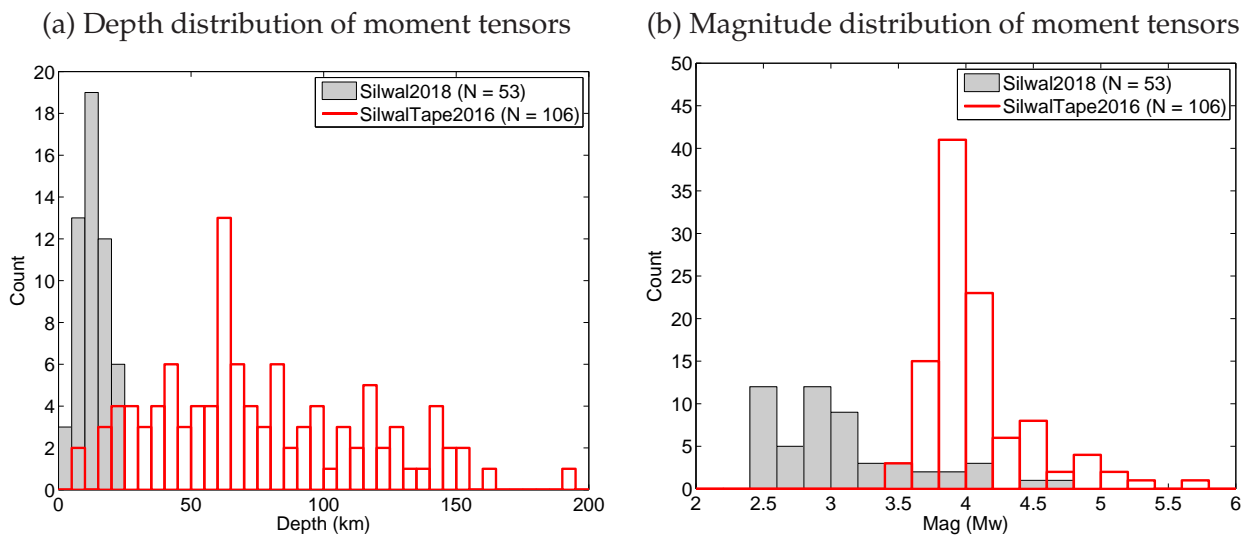


Figure 5.1: Comparison of depth and magnitude distribution of moment tensors estimated in Silwal et al. (2018) (gray) and those in Silwal & Tape (2016) (red).

References

- Alvizuri, C. & Tape, C., 2016. Full moment tensors for small events ($M_w < 3$) at Uturuncu volcano, Bolivia, *Geophys. J. Int.*, **206**, 1761–1783, doi:10.1093/gji/ggw247.
- Alvizuri, C., Silwal, V., Krischer, L., & Tape, C., 2018. Estimation of full moment tensors, including uncertainties, for nuclear explosions, volcanic events, and earthquakes, *J. Geophys. Res. Solid Earth*, **123**, doi:10.1029/2017JB015325.
- Covellone, B. M. & Savage, B., 2012. A quantitative comparison between 1D and 3D source inversion methodologies: Application to the Middle East, *Bull. Seismol. Soc. Am.*, **102**(5), 2189–2199, doi:10.1785/0120110278.
- Doser, D. I. & Brown, W. A., 2001. A study of historic earthquakes of the Prince William Sound, Alaska, Region, *Bull. Seismol. Soc. Am.*, **91**(4), 842–857.
- Eberhart-Phillips, D., Christensen, D. H., Brocher, T. M., Hansen, R., Ruppert, N. A., Haeussler, P. J., & Abers, G. A., 2006. Imaging the transition from Aleutian subduction to Yakutat collision in central Alaska, with local earthquakes and active source data, *J. Geophys. Res.*, **111**, B11303, doi:10.1029/2005JB004240.
- Liu, Q., Polet, J., Komatitsch, D., & Tromp, J., 2004. Spectral-element moment tensor inversions for earthquakes in southern California, *Bull. Seismol. Soc. Am.*, **94**(5), 1748–1761, doi:10.1785/012004038.
- Nayak, A. & Dreger, D. S., 2018. Source inversion of seismic events associated with the sinkhole at napoleonville salt dome, louisiana using a 3d velocity model, *Geophysical Journal International*, doi:10.1093/gji/ggy202.
- Silwal, V. & Tape, C., 2016. Seismic moment tensors and estimated uncertainties in southern Alaska, *J. Geophys. Res. Solid Earth*, **121**, 2772–2797, doi:10.1002/2015JB012588.
- Silwal, V., Tape, C., & Lomax, A., 2018. Crustal earthquakes in the Cook Inlet and Susitna region of southern Alaska, *Tectonophysics* (submitted).
- Tape, C., Silwal, V., Ji, C., Keyson, L., West, M. E., & Ruppert, N., 2015. Transtensional tectonics of the Minto Flats fault zone and Nenana basin, central Alaska, *Bull. Seismol. Soc. Am.*, **105**(4), 2081–2100, doi:10.1785/0120150055.

Tape, C., Holtkamp, S., Silwal, V., Hawthorne, J., Kaneko, Y., Ampuero, J. P., Ji, C., Ruppert, N., Smith, K., & West, M. E., 2018. Earthquake nucleation and fault slip complexity in the lower crust of central Alaska, *Nature Geoscience*, **11**, 536–541, doi:10.1038/s41561-018-0144-2.

Tape, W. & Tape, C., 2016. A confidence parameter for seismic moment tensors, *Geophys. J. Int.*, **205**, 938–953, doi:10.1093/gji/ggw057.

Zhao, L., Chen, P., & Jordan, T. H., 2006. Strain Green's tensors, reciprocity, and their applications to seismic source and structure studies, *Bull. Seismol. Soc. Am.*, **96**(5), 1753–1763, doi: 10.1785/0120050253.

Appendix A

Supplemental Information for Chapter 2 (Seismic moment tensors and estimated uncertainties in southern Alaska)

A.1 ScholarWorks@UA collection

Our moment tensor catalog of 106 events is available in the text file in Table A.5. We provide the complete results of our analysis in Silwal (2015), which includes the following files:

- `scholarworks.pdf` Description of the figures in the collection.
- `PartI_inv.pdf` Waveform fits for 21 Part I catalog events (Table 2.4). The waveform match is shown for moment tensor M_{111} obtained when using body waves and surface waves at the good stations. (See Section A.2.1 for waveform selection criteria and Table 2.1 for description of moment tensor notations.)
- `PartI_dep.pdf` Depth grid search results for the M_{111} moment tensor inversion for Part I events.
- `PartI_unc.pdf` Uncertainty analysis for the M_{111} moment tensor inversion for Part I events.
- `PartII_inv.pdf` Waveform fits for all 85 events in Part II catalog.
- `input_weight_files.zip` Input weight files for all 21 Part I catalog events.

A.2 Methods

A.2.1 Waveform selection criteria

As we demonstrated in Section 2.3.4 and Figure 2.12, the use of the L1 norm in the misfit function greatly reduces the need to exclude bad waveforms. (By “bad,” we mean that there are errors associated with data gaps or station metadata. Waveforms that are complex due to 3D structure are not considered bad.) For all inversions (except for case M_{110} , for which all waveforms were used) we use waveform selection criteria based on amplitude anomalies, $\ln(A_{\text{obs}}/A_{\text{syn}})$, where A is the maximum value of the waveform within the time window, either for data or synthetics. The five time windows are vertical P (PV), radial P (PR), vertical Rayleigh (SurfZ), radial Rayleigh (SurfR), and transverse Love (SurfT). Our criteria were:

1. Turn off PV and PR if the amplitude ratio of either one exceeds 2.5.

Both PV and PR need to be either ON (weight=1) or OFF (weight=0) together. In other words, we prefer not to use any P waveform if we can only fit it on a single component.

2. Turn off SurfV and SurfR if the amplitude ratio of either one exceeds 1.5.

Both SurfV and SurfR need to be either ON (weight=1) or OFF (weight=0) together. In other words, we prefer not to use any Rayleigh waveform if we can only fit it on a single component.

3. Turn off SurfT if the amplitude ratio exceeds 1.5.

Figure A.2 shows how we established the threshold amplitude ratio values. Our motivation was to remove the largest amplitude outliers, since it is possible that these could influence the outcome of the inversions, which use a waveform difference (i.e., based on amplitudes) for the misfit function.

A.2.2 Time shifts

Time shifts between data and synthetics are useful in assessing the quality of the 1D velocity model. The maximum allowable time shift is ± 2 s for body waves and ± 10 s for surface waves; we assume that any measured time shift outside these limits is an artifact due to cycle skipping between data and synthetics. The measured time shifts can be represented on a spatial map, with each source-station path colored according to the time shift (Figure A.3). In Figure A.3 we see a systematic variation in time shifts as a function of station azimuth. Similar plots of time shifts for other time windows (PV, PR, SurfT) and cross-correlation values for all time windows are useful in assessing the quality of the waveform fits between data and synthetics.

A.2.3 Variance Reduction

In our study we use probability density $p(M)$ (Eq. 2.10) as part of our assessment of the quality of our moment tensor solutions. In the published literature, moment tensor solutions are often assessed in terms of their variance reduction. The CAP code of Zhu & Helmberger (1996) uses a misfit function based on an L2 norm (Eq. 2.5). In our study we use an L1 norm (Eq. 2.4). For each of these norms we calculate variance reduction as:

$$VR_{L1}(M) = 100 \times \left(1 - \left(\frac{\Phi_{L1}(M)}{u_{L1}} \right)^2 \right) \quad (\text{A.1})$$

$$VR_{L2}(M) = 100 \times \left(1 - \frac{\Phi_{L2}(M)}{u_{L2}} \right) \quad (\text{A.2})$$

where

$$u_{L1} = \sum_{j=1}^{N_s} \sum_{i=1}^5 \left[\mathbf{u}_{ij}^T \mathbf{W}_{ij} \mathbf{u}_{ij} \right]^{1/2} \quad (\text{A.3})$$

$$u_{L2} = \sum_{j=1}^{N_s} \sum_{i=1}^5 \mathbf{u}_{ij}^T \mathbf{W}_{ij} \mathbf{u}_{ij} \quad (\text{A.4})$$

VR is represented as a percentage and varies from $-\infty$ to 100%, with 100% being a perfect fit between data and synthetics. A negative variance reduction can occur when the misfit norm in the numerator is larger than the data norm in the denominator.

A.3 Results

A.3.1 Extended analysis for the example event

For the example event 20090407201255351 we performed a suite of inversions for different subsets of data ($(M_{111}, M_{110}, M_{011}, M_{101}, M_{112}, M_{012})$; see Table 2.1 for description). The uncertainty analysis for M_{111} (obtained using body and surface waves at selected stations) is shown in Figure 2.5; for the rest see Figures A.11–A.15. These figures show how the confidence measure \mathcal{P}_{AV} changes with the choice of data used.

See Tables A.3 and A.4 for the summarized results of a similar analysis of all 21 Part I catalog events.

A.3.2 Two small events

Among the 85 Part II events, 20081118195651180 had the largest difference ($\omega = 70^\circ$) from the solution in the AEC first-motion catalog (see Figures A.5–A.7). For the identical misfit function (same set of waveforms), the variance reduction is higher for the CAP solution than for the AEC solution (60 vs 29). This shows that either the body waves or the MOOS stations—neither of which were used in the AEC first-motion solution—are probably very important in estimating this moment tensor. Our magnitude estimate of $M_w 4.0$ is much higher than the magnitude from the AEC catalog ($M_w 3.5$).

Figures A.8–A.10 provides a second example of a small event. The difference between our preferred CAP solution and the AEC first-motion solution is $\omega = \angle(M_{111}, M_{\text{fm}}) = 68^\circ$. The variance reduction is better for the CAP solution (38 vs 31), and the body waves fit better. However the comparison shows the challenges associated with moment tensor inversions for events with lower signal-to-noise ratios (like smaller events): the waveform fits for two very different moment tensors appear to be qualitatively comparably good. An uncertainty analysis would benefit these events, as would a detailed investigation of the inclusion of first-motion polarities along with the waveforms.

A.3.3 Comparison between moment tensor catalogs

Figure A.19 shows maps of different moment tensor catalogs. Figure A.20 compares our moment tensors M_{CAP} with those from the AEC moment tensor catalog M_{AEC} . The x -axis shows the

decrease in variance reduction for M_{AEC} relative to M_{CAP} . To make the comparison as fair as possible, we allowed the magnitude m_{AEC} to vary when calculating VR ; these are the blue points in Figure A.20. The plot shows a correlation between the decrease in variance reduction and the angular difference $\omega = \angle(M_{CAP}, M_{AEC})$, with one event having $\omega = 55^\circ$ and $\Delta VR = 25$ (see Figures 2.10 and 2.11).

References

- Ekström, G., Nettles, M., & Dziewoński, A. M., 2012. The global GCMT project 2004–2010: Centroid-moment tensors for 13,017 earthquakes, *Phys. Earth Planet. Inter.*, **200-201**, 1–9, doi: 10.1016/j.pepi.2012.04.002.
- Kanamori, H., 1977. The energy release in great earthquakes, *J. Geophys. Res.*, **82**, 2981–2987.
- Lahr, J. C., 1975. Detailed seismic investigation of Pacific-North American plate interaction in southern Alaska, *Ph. D. Thesis, Columbia University*, p. 88.
- Matumoto, T. & Page, R. A., 1964. Microaftershocks following the alaska earthquake of 28 march 1964: Determination of hypocenters and crustal velocities in the kenai peninsula-prince william sound area, the prince william sound, alaska, earthquake of 1964 and aftershocks, *U.S. Govt. Printing Office, Washington*, **10**(3), 157–173.
- Ratchkovski, N. A. & Hansen, R. A., 2002. New constraints on tectonics of interior Alaska: Earthquake locations, source mechanisms, and stress regime, *Bull. Seismol. Soc. Am.*, **92**(3), 998–1014, doi:10.1785/0120010182.
- Silver, P. G. & Jordan, T. H., 1982. Optimal estimation of scalar seismic moment, *Geophys. J. R. Astron. Soc.*, **70**, 755–787.
- Silwal, V., 2015. Seismic moment tensor catalog for southern Alaska, ScholarWorks@UA at <http://hdl.handle.net/11122/6025> (last accessed 2016-01-22): descriptor file, text file of catalog, figures with waveform fits, depth searches, and uncertainty analyses.
- Tape, W. & Tape, C., 2012. A geometric setting for moment tensors, *Geophys. J. Int.*, **190**, 476–498, doi:10.1111/j.1365-246X.2012.05491.x.
- Zhu, L. & Helmberger, D., 1996. Advancement in source estimation techniques using broadband regional seismograms, *Bull. Seismol. Soc. Am.*, **86**(5), 1634–1641.

Table A.1: 1D structural model `scak` used for generating Green's functions for the moment tensor inversions (Matumoto & Page, 1964; Lahr, 1975).

top of layer, km	bottom of layer, km	thickness km	V_S m/s	V_P m/s	density kg/m ³	Q_S	Q_P
0	4	4	3010	5300	2520	300	600
4	9	5	3180	5600	2610	300	600
9	14	5	3520	6200	2780	300	600
14	19	5	3920	6900	2970	300	600
19	24	5	4200	7400	3120	300	600
24	33	9	4370	7700	3200	300	600
33	49	16	4490	7900	3260	300	600
49	66	17	4600	8100	3320	300	600
66	–	–	4720	8300	3370	300	600

Table A.2: Discretized grid for moment tensor grid search. NPTS is the number of search points for each interval. m_{AEC} is the magnitude listed in the AEC seismicity catalog. By using the cosine of dip θ we achieve uniform orientations. The depth range listed is representative; when needed, we used a wider search range and a finer (1 km) increment (see Silwal, 2015).

parameter	min	max	interval		NPTS	
			(m varies)	(m fixed)	(m varies)	(m fixed)
depth z	$z_{AEC} - 20$	$z_{AEC} + 20$	2 km	–	21	0
magnitude m	$m_{AEC} - 0.5$	$m_{AEC} + 0.5$	0.1	–	11	0
strike κ	0°	360°	10	5	36	72
rake σ	-90°	90°	10	5	19	37
cos(dip) $h = \cos \theta$	0	1	0.1	0.05	9	18
total number of points (magnitude and depth fixed)					1,422,036	47,952

Table A.3: Summary of inversions for 21 high-quality events when the inversion is performed using the L1 norm. The subtable for 20090407201255351 is in Table 2.3. The number ω is the angular distance of the corresponding moment tensor from M_{111} . Since M_{AEC} and M_{fm} are obtained from the AEC catalog, neither a waveform match (VR) nor an uncertainty analysis (\mathcal{P}_{AV}) was performed.

Misfit (see Table 2.1)	depth km	M_w	ω deg	$p(M_0)$	\mathcal{P}_{AV}		Misfit (see Table 2.1)	depth km	M_w	ω deg	$p(M_0)$	\mathcal{P}_{AV}	
Event 20070911234634153 (1)													
L1	M_{111}	94	4.4	–	3.19	0.89	L1	M_{111}	69	4.9	–	7.65	0.97
L1	M_{110}	94	4.4	0	0.12	0.56	L1	M_{110}	83	4.9	29	1.02	0.80
L1	M_{011}	90	4.4	16	10.85	0.99	L1	M_{011}	73	4.9	0	19.03	0.98
L1	M_{101}	94	4.4	0	1.31	0.80	L1	M_{101}	61	4.9	12	3.53	0.84
L1	M_{112}	122	4.5	37	2.80	0.85	L1	M_{112}	71	4.9	16	9.76	0.98
L1	M_{012}	100	4.4	15	10.04	0.98	L1	M_{012}	77	4.9	0	37.40	0.99
L1	M_{AEC}	100	4.4	21	–	–	L1	M_{AEC}	75	4.8	4	–	–
L1	M_{fm}	101	4.4	12	–	–	L1	M_{fm}	70	5.0	77	–	–
Event 20070919112226549 (2)													
L1	M_{111}	47	4.5	–	2.35	0.92	L1	M_{111}	139	5.1	–	8.28	0.94
L1	M_{110}	39	4.4	22	0.12	0.61	L1	M_{110}	143	5.0	10	1.66	0.84
L1	M_{011}	45	4.5	18	5.72	0.97	L1	M_{011}	141	5.0	50	23.07	0.99
L1	M_{101}	39	4.6	23	0.93	0.87	L1	M_{101}	139	5.1	0	6.93	0.94
L1	M_{112}	57	4.6	20	3.67	0.92	L1	M_{112}	137	5.1	53	3.38	0.91
L1	M_{012}	51	4.5	31	4.52	0.97	L1	M_{012}	145	5.1	43	14.12	0.95
L1	M_{AEC}	35	4.4	34	–	–	L1	M_{AEC}	165	5.0	32	–	–
L1	M_{fm}	31	4.4	21	–	–	L1	M_{fm}	144	4.9	67	–	–
Event 20071003140612444 (3)													
L1	M_{111}	32	5.0	–	4.38	0.88	L1	M_{111}	65	5.1	–	1.66	0.90
L1	M_{110}	32	5.0	13	2.57	0.83	L1	M_{110}	67	5.1	0	0.82	0.81
L1	M_{011}	38	5.0	62	4.46	0.95	L1	M_{011}	75	5.2	8	9.15	0.98
L1	M_{101}	36	5.1	119	3.16	0.68	L1	M_{101}	65	5.5	68	0.51	0.58
L1	M_{112}	26	4.9	55	5.52	0.95	L1	M_{112}	63	5.0	19	1.98	0.90
L1	M_{012}	46	5.1	61	10.43	0.98	L1	M_{012}	71	5.1	8	9.69	0.98
L1	M_{AEC}	40	5.2	54	–	–	L1	M_{AEC}	75	5.3	11	–	–
L1	M_{fm}	45	5.0	67	–	–	L1	M_{fm}	69	5.3	19	–	–
Event 20080327230745201 (7)													
L1	M_{111}	65	5.1	–	1.66	0.90							
L1	M_{110}	67	5.1	0	0.82	0.81							
L1	M_{011}	75	5.2	8	9.15	0.98							
L1	M_{101}	65	5.5	68	0.51	0.58							
L1	M_{112}	63	5.0	19	1.98	0.90							
L1	M_{012}	71	5.1	8	9.69	0.98							
L1	M_{AEC}	75	5.3	11	–	–							
L1	M_{fm}	69	5.3	19	–	–							

Table A.3[CONTINUED]:

Misfit (see Table 2.1)	depth km	M_w	ω deg	$p(M_0)$	\mathcal{P}_{AV}	Misfit (see Table 2.1)	depth km	M_w	ω deg	$p(M_0)$	\mathcal{P}_{AV}		
Event 20071010180326301 (4)													
L1	M_{111}	27	4.2	0	1.56	0.90	L1	M_{111}	54	4.2	—	4.36	0.95
L1	M_{110}	25	4.2	10	0.23	0.63	L1	M_{110}	48	4.1	0	0.08	0.56
L1	M_{011}	37	4.3	7	8.07	0.99	L1	M_{011}	56	4.2	10	16.03	0.99
L1	M_{101}	29	4.4	53	2.85	0.77	L1	M_{101}	40	4.3	14	5.82	0.92
L1	M_{112}	45	4.3	41	4.80	0.95	L1	M_{112}	56	4.2	19	13.52	0.96
L1	M_{012}	45	4.3	41	11.53	0.99	L1	M_{012}	56	4.2	19	28.88	0.99
L1	M_{AEC}	15	4.1	19	—	—	L1	M_{AEC}	50	4.1	14	—	—
L1	M_{fm}	12	4.0	20	—	—	L1	M_{fm}	43	4.1	13	—	—
Event 20080918194353069 (9)													
L1	M_{111}	81	4.6	—	0.88	0.78	L1	M_{111}	81	4.9	—	11.76	0.94
L1	M_{110}	89	4.6	19	0.08	0.54	L1	M_{110}	83	4.9	10	13.38	0.95
L1	M_{011}	93	4.6	11	2.67	0.92	L1	M_{011}	85	5.0	0	28.26	0.99
L1	M_{101}	79	4.7	56	0.88	0.71	L1	M_{101}	103	5.3	110	130.61	0.89
L1	M_{112}	85	4.6	151	0.93	0.51	L1	M_{112}	83	4.9	0	21.56	0.99
L1	M_{012}	77	4.6	10	13.55	0.96	L1	M_{012}	95	5.0	10	41.25	0.99
L1	M_{AEC}	85	4.5	8	—	—	L1	M_{AEC}	85	4.9	26	—	—
L1	M_{fm}	90	4.7	27	—	—	L1	M_{fm}	88	4.8	25	—	—
Event 20081228071310738 (10)													
L1	M_{111}	82	4.6	—	4.28	0.95	L1	M_{111}	96	4.3	—	0.75	0.78
L1	M_{110}	76	4.5	18	0.16	0.60	L1	M_{110}	96	4.3	31	0.04	0.52
L1	M_{011}	84	4.5	26	24.92	0.99	L1	M_{011}	98	4.3	0	9.41	0.98
L1	M_{101}	90	4.7	17	3.59	0.91	L1	M_{101}	120	4.5	59	0.72	0.59
L1	M_{112}	92	4.6	21	4.42	0.97	L1	M_{112}	120	4.3	55	0.23	0.57
L1	M_{012}	88	4.5	26	32.69	0.99	L1	M_{012}	92	4.3	13	6.17	0.96
L1	M_{AEC}	80	4.4	25	—	—	L1	M_{AEC}	90	4.2	17	—	—
L1	M_{fm}	89	4.5	27	—	—	L1	M_{fm}	90	4.0	19	—	—
Event 20090124180950811 (11)													
L1	M_{111}	105	5.8	—	1.33	0.85	L1	M_{111}	111	4.3	—	0.89	0.83
L1	M_{110}	117	5.7	10	0.71	0.72	L1	M_{110}	101	4.2	10	0.06	0.56
L1	M_{011}	103	5.7	10	14.86	0.98	L1	M_{011}	107	4.3	27	2.56	0.96
L1	M_{101}	109	6.0	52	0.31	0.68	L1	M_{101}	115	4.6	125	6.43	0.67
L1	M_{112}	97	5.7	20	2.14	0.93	L1	M_{112}	121	4.2	50	0.24	0.60
L1	M_{012}	97	5.7	10	9.56	0.98	L1	M_{012}	113	4.3	20	31.20	0.99
L1	M_{AEC}	95	5.7	30	—	—	L1	M_{AEC}	105	4.3	24	—	—
L1	M_{fm}	98	5.9	29	—	—	L1	M_{fm}	118	4.1	21	—	—
Event 20090317011333066 (14)													
L1	M_{111}	96	4.3	—	0.75	0.78	L1	M_{111}	96	4.3	31	0.04	0.52
L1	M_{110}	98	4.3	0	9.41	0.98	L1	M_{110}	98	4.3	59	0.72	0.59
L1	M_{011}	120	4.5	55	0.23	0.57	L1	M_{011}	120	4.3	13	6.17	0.96
L1	M_{101}	92	4.3	17	—	—	L1	M_{101}	90	4.2	19	—	—
L1	M_{112}	92	4.3	13	6.17	0.96	L1	M_{112}	90	4.0	19	—	—
L1	M_{012}	90	4.2	17	—	—	L1	M_{012}	90	4.0	19	—	—
L1	M_{AEC}	90	4.2	17	—	—	L1	M_{AEC}	90	4.0	19	—	—
L1	M_{fm}	90	4.0	19	—	—	L1	M_{fm}	90	4.0	19	—	—
Event 20090414171427415 (16)													
L1	M_{111}	111	4.3	—	0.89	0.83	L1	M_{111}	101	4.2	10	0.06	0.56
L1	M_{110}	107	4.3	27	2.56	0.96	L1	M_{110}	107	4.3	27	2.56	0.96
L1	M_{011}	115	4.6	125	6.43	0.67	L1	M_{011}	115	4.6	125	6.43	0.67
L1	M_{101}	121	4.2	50	0.24	0.60	L1	M_{101}	121	4.2	50	0.24	0.60
L1	M_{112}	113	4.3	20	31.20	0.99	L1	M_{112}	113	4.3	20	31.20	0.99
L1	M_{012}	105	4.3	24	—	—	L1	M_{012}	105	4.3	24	—	—
L1	M_{AEC}	118	4.1	21	—	—	L1	M_{AEC}	118	4.1	21	—	—
L1	M_{fm}	118	4.1	21	—	—	L1	M_{fm}	118	4.1	21	—	—

Table A.3[CONTINUED]:

Misfit (see Table 2.1)	depth km	M_w	ω deg	$p(M_0)$	\mathcal{P}_{AV}
---------------------------	-------------	-------	-----------------	----------	--------------------

Event 20090215193500098 (12)

L1	M_{111}	43	4.5	–	1.80	0.93
L1	M_{110}	43	4.5	0	0.86	0.84
L1	M_{011}	45	4.5	12	4.14	0.97
L1	M_{101}	55	4.5	36	1.09	0.77
L1	M_{112}	51	4.6	17	2.61	0.95
L1	M_{012}	43	4.5	17	7.26	0.98
L1	M_{AEC}	35	4.5	25	–	–
L1	M_{fm}	37	4.3	27	–	–

Event 20090524094004552 (18)

L1	M_{111}	109	4.6	–	2.02	0.89
L1	M_{110}	123	4.6	13	0.13	0.58
L1	M_{011}	125	4.7	24	9.84	0.98
L1	M_{101}	107	4.6	0	1.12	0.82
L1	M_{112}	125	4.7	43	2.88	0.84
L1	M_{012}	129	4.7	24	5.47	0.90
L1	M_{AEC}	125	4.6	29	–	–
L1	M_{fm}	125	4.7	27	–	–

Event 20090622192805162 (19)

L1	M_{111}	62	5.4	–	4.30	0.94
L1	M_{110}	64	5.4	0	2.45	0.89
L1	M_{011}	62	5.4	10	14.97	0.99
L1	M_{101}	52	5.6	24	3.04	0.66
L1	M_{112}	60	5.4	10	6.61	0.96
L1	M_{012}	60	5.4	10	16.27	0.99
L1	M_{AEC}	80	5.5	13	–	–
L1	M_{fm}	65	5.5	13	–	–

Misfit (see Table 2.1)	depth km	M_w	ω deg	$p(M_0)$	\mathcal{P}_{AV}
---------------------------	-------------	-------	-----------------	----------	--------------------

Event 20090430045457938 (17)

L1	M_{111}	40	4.8	–	5.52	0.89
L1	M_{110}	40	4.8	0	3.88	0.85
L1	M_{011}	48	4.9	10	5.18	0.96
L1	M_{101}	62	4.6	118	0.59	0.63
L1	M_{112}	44	4.8	28	8.80	0.91
L1	M_{012}	50	4.9	16	4.48	0.92
L1	M_{AEC}	40	4.9	25	–	–
L1	M_{fm}	53	4.9	65	–	–

Event 20090626164820729 (20)

L1	M_{111}	56	4.2	–	7.72	0.95
L1	M_{110}	50	4.1	13	0.05	0.53
L1	M_{011}	54	4.2	19	11.65	0.98
L1	M_{101}	50	4.2	10	6.74	0.75
L1	M_{112}	58	4.3	14	10.03	0.97
L1	M_{012}	56	4.2	30	25.28	0.98
L1	M_{AEC}	60	4.2	25	–	–
L1	M_{fm}	59	4.2	20	–	–

Event 20090730223910267 (21)

L1	M_{111}	60	4.6	–	3.62	0.94
L1	M_{110}	54	4.5	28	0.04	0.52
L1	M_{011}	60	4.6	10	7.35	0.97
L1	M_{101}	60	4.7	29	4.33	0.89
L1	M_{112}	58	4.5	36	4.56	0.97
L1	M_{012}	58	4.5	30	2.52	0.96
L1	M_{AEC}	30	4.4	17	–	–
L1	M_{fm}	44	4.6	28	–	–

Table A.4: An abridged version of the information in Table A.3 (and Table 2.3). Here we exclude the depths and magnitudes and also the values for the AEC moment tensors. We take M_{111} to be the best solution, in the sense that it fits the most waveforms; ω is measured with respect to the M_{111} moment tensor. The column labels are described in Table 2.1. The data in this table were used in making Figure 2.14.

	$p(M_0)$						ω						\mathcal{P}_{AV}					
	111	110	011	101	112	012	111	110	011	101	112	012	111	110	011	101	112	012
1	3.19	0.12	10.85	1.31	2.80	10.04	-	0	16	0	37	15	0.89	0.56	0.99	0.80	0.85	0.98
2	2.35	0.12	5.72	0.93	3.67	4.52	-	22	18	23	20	31	0.92	0.61	0.97	0.87	0.92	0.97
3	4.38	2.57	4.46	3.16	5.52	10.43	-	13	62	119	55	61	0.88	0.83	0.95	0.68	0.95	0.98
4	1.56	0.23	8.07	2.85	4.80	11.53	-	10	7	53	41	41	0.90	0.63	0.99	0.77	0.95	0.99
5	7.65	1.02	19.03	3.53	9.76	37.40	-	29	0	12	16	0	0.97	0.80	0.98	0.84	0.98	0.99
6	8.28	1.66	23.07	6.93	3.38	14.12	-	10	50	0	53	43	0.94	0.84	0.99	0.94	0.91	0.95
7	1.66	0.82	9.15	0.51	1.98	9.69	-	0	8	68	19	8	0.90	0.81	0.98	0.58	0.90	0.98
8	4.36	0.08	16.03	5.82	13.52	28.88	-	0	10	14	19	19	0.95	0.56	0.99	0.92	0.96	0.99
9	0.88	0.08	2.67	0.88	0.93	13.55	-	19	11	56	151	10	0.78	0.54	0.92	0.71	0.51	0.96
10	4.28	0.16	24.92	3.59	4.42	32.69	-	18	26	17	21	26	0.95	0.60	0.99	0.91	0.97	0.99
11	1.33	0.71	14.86	0.31	2.14	9.56	-	10	10	52	20	10	0.85	0.72	0.98	0.68	0.93	0.98
12	1.80	0.86	4.14	1.09	2.61	7.26	-	0	12	36	17	17	0.93	0.84	0.97	0.77	0.95	0.98
13	11.76	13.38	28.26	130.61	21.56	41.25	-	10	0	110	0	10	0.94	0.95	0.99	0.89	0.99	0.99
14	0.75	0.04	9.41	0.72	0.23	6.17	-	31	0	59	55	13	0.78	0.52	0.98	0.59	0.57	0.96
15	3.30	0.04	9.26	2.26	2.27	10.44	-	26	9	21	10	10	0.95	0.52	0.98	0.77	0.95	0.98
16	0.89	0.06	2.56	6.43	0.24	31.20	-	10	27	125	50	20	0.83	0.56	0.96	0.67	0.60	0.99
17	5.52	3.88	5.18	0.59	8.80	4.48	-	0	10	118	28	16	0.89	0.85	0.96	0.63	0.91	0.92
18	2.02	0.13	9.84	1.12	2.88	5.47	-	13	24	0	43	24	0.89	0.58	0.98	0.82	0.84	0.90
19	4.30	2.45	14.97	3.04	6.61	16.27	-	0	10	24	10	10	0.94	0.89	0.99	0.66	0.96	0.99
20	7.72	0.05	11.65	6.74	10.03	25.28	-	13	19	10	14	30	0.95	0.53	0.98	0.75	0.97	0.98
21	3.62	0.04	7.35	4.33	4.56	2.52	-	28	10	29	36	30	0.94	0.52	0.97	0.89	0.97	0.96

Table A.5: [AVAILABLE ONLINE] <https://scholarworks.alaska.edu/handle/11122/6025>. Text file version of our moment tensor catalog of 106 events, including Part I (Table 2.4) and Part II. Details can be found within the header lines, which also refer to Kanamori (1977); Silver & Jordan (1982); Tape & Tape (2012).

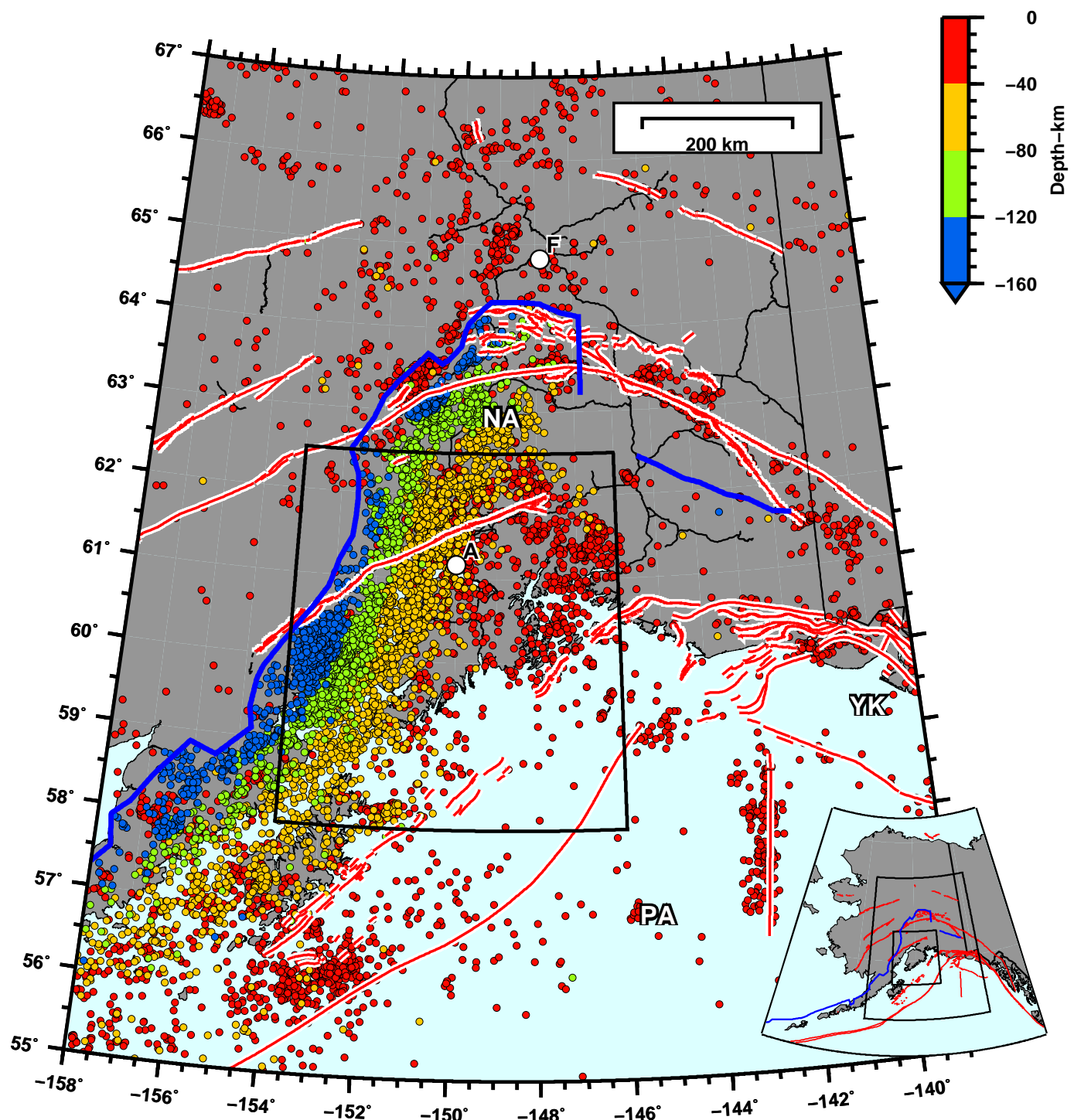


Figure A.1: Seismicity in southern Alaska for $M_w \geq 3.0$ between 1990–2014 (source: Alaska Earthquake Center catalog). For caption details, see Figure 3.5, which also shows the Cook Inlet basement surface (but no seismicity).

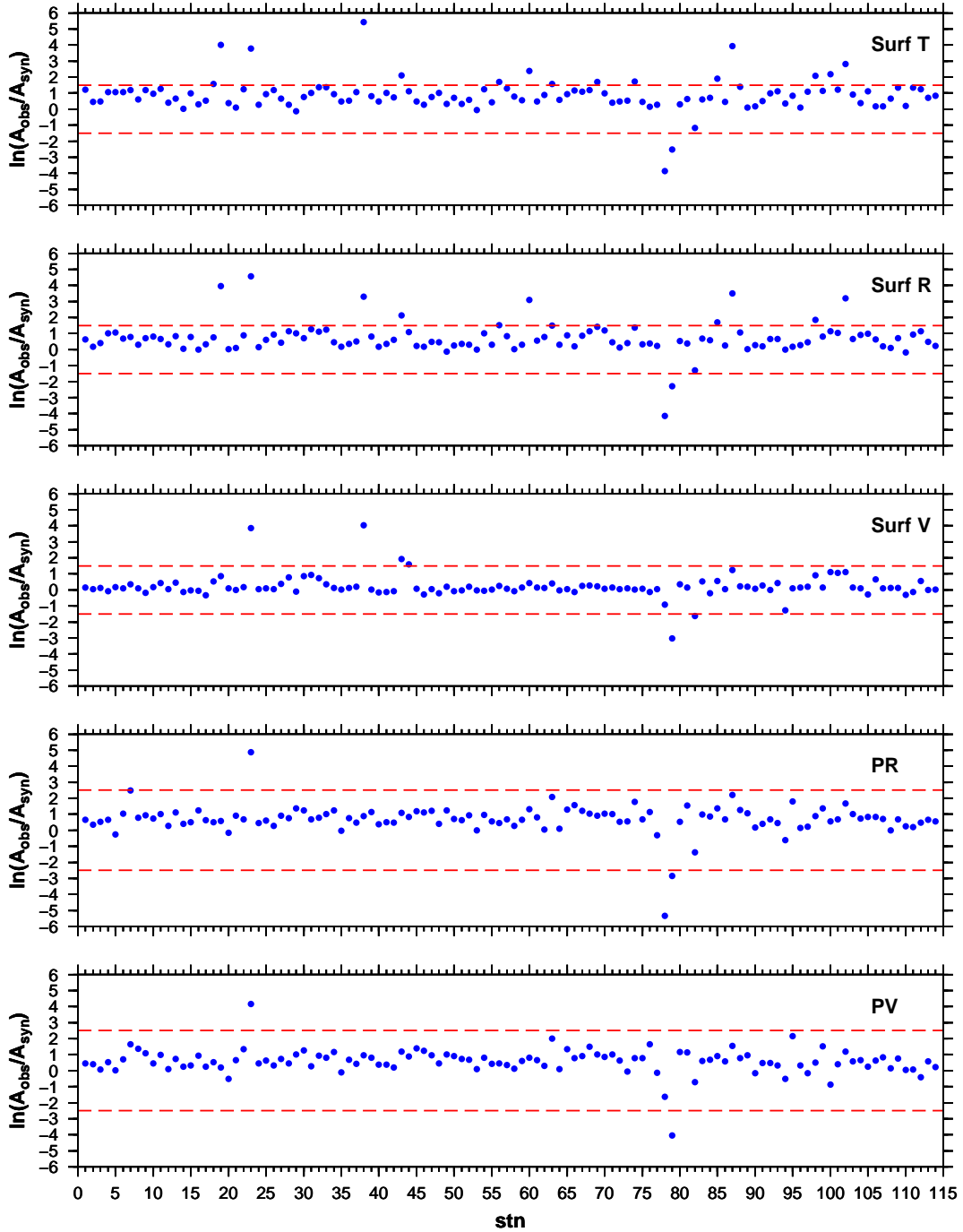


Figure A.2: Waveform amplitude ratios between observed data and synthetics, $\ln(A_{\text{obs}}/A_{\text{syn}})$, where A is the max value of the waveform within the time window. Each row represents a different time window used in the moment tensor inversions: P wave vertical component (PV), P wave radial component (PR), Rayleigh wave vertical component (SurfV), Rayleigh wave horizontal component (SurfR), and Love wave transverse component (SurfT). The y -value is the amplitude ratio for a given time window for a given station, averaged over all 21 events (Part I catalog). The x -value is a station index; for the purposes here, what matters is that certain stations are consistent outliers. We use these amplitude ratios to determine threshold levels (red dashed lines) for waveform selection, which are chosen as 2.5 for body waves and 1.5 for surface waves. Waveform selection criteria are listed in Section A.2.1.

CAP results for eid 20090407201255351, depth 39 km (catalog 33.0 km)

model scak_039 (strike 200, dip 52.011387, rake -90) Mw 4.50 VR 54.5

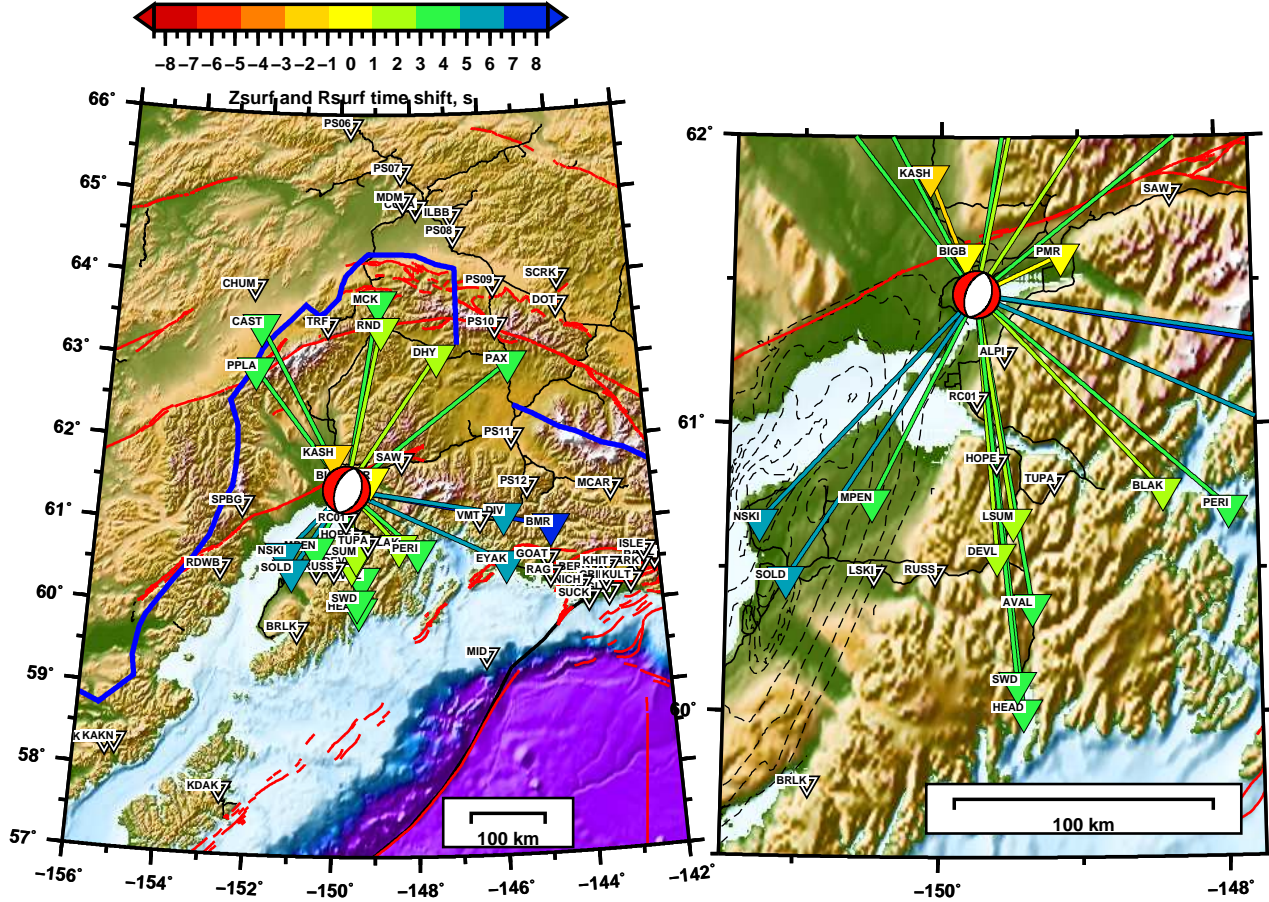


Figure A.3: Source-station paths used for event 20090407201255351. The ray paths are colored by the cross correlation time-shift values for the Rayleigh waves (SurfV and SurfR). Notice the large systematic time-shifts (up to +8 seconds) at large distances. Positive time-shifts mean that the synthetic is arriving before the data, i.e., the assumed 1D velocity model is faster than the true Earth model. Notice that the time-shifts to stations toward the southwest, in Cook Inlet basin, are larger than paths in other directions having comparable distances.

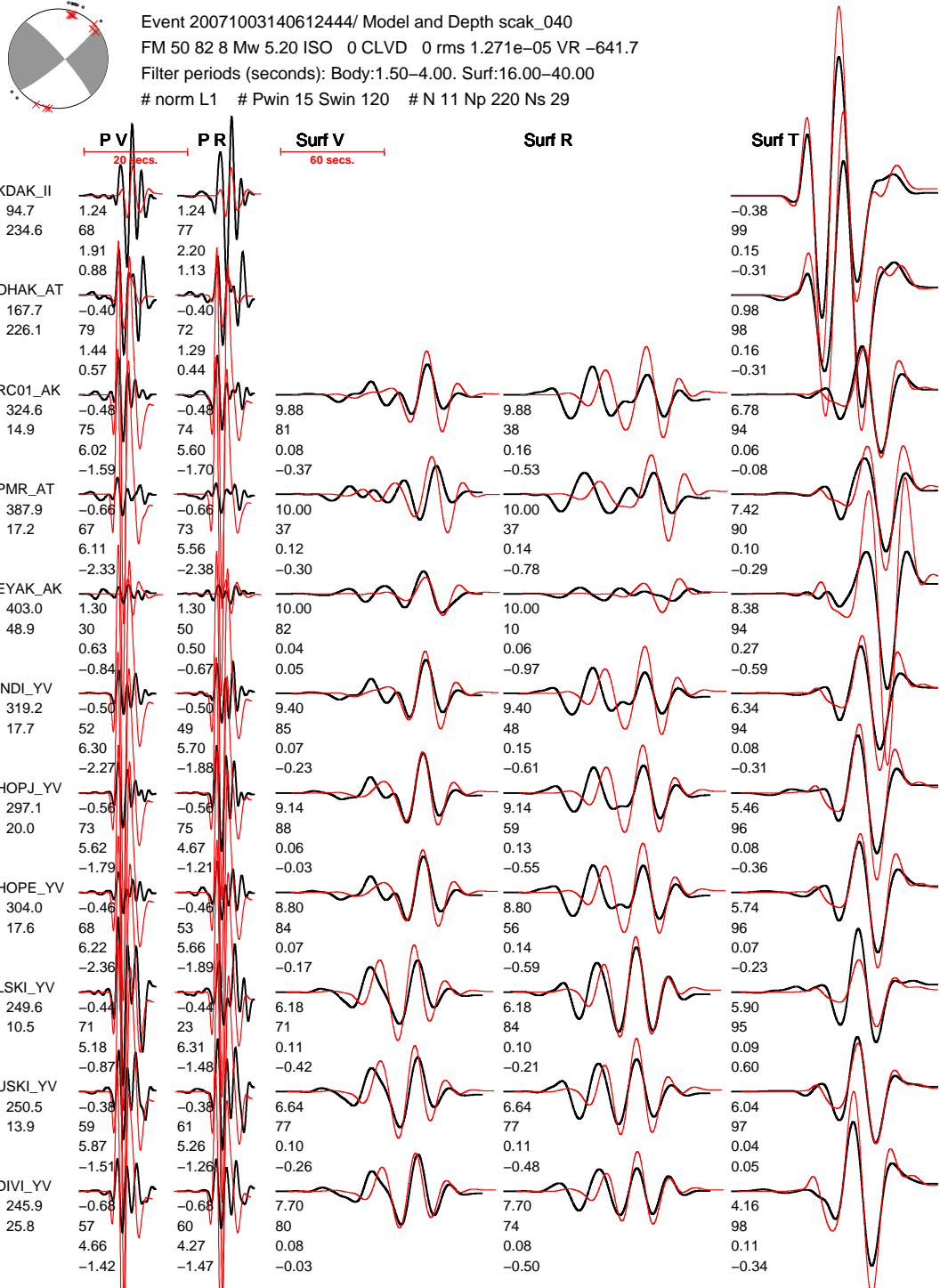


Figure A.4: Waveform fits for event 20071003140612444 using the AEC moment tensor solution (fixed orientation, depth, and magnitude M_w 5.2). It is not too surprising that there are poor fits to the body waves, since only long period surface waves were used by AEC for finding their solution. See Figure 2.10 for our solution obtained using both the body and surface waves, and Figure 2.11 for waveform fits when we allow the AEC solution to search over magnitude.

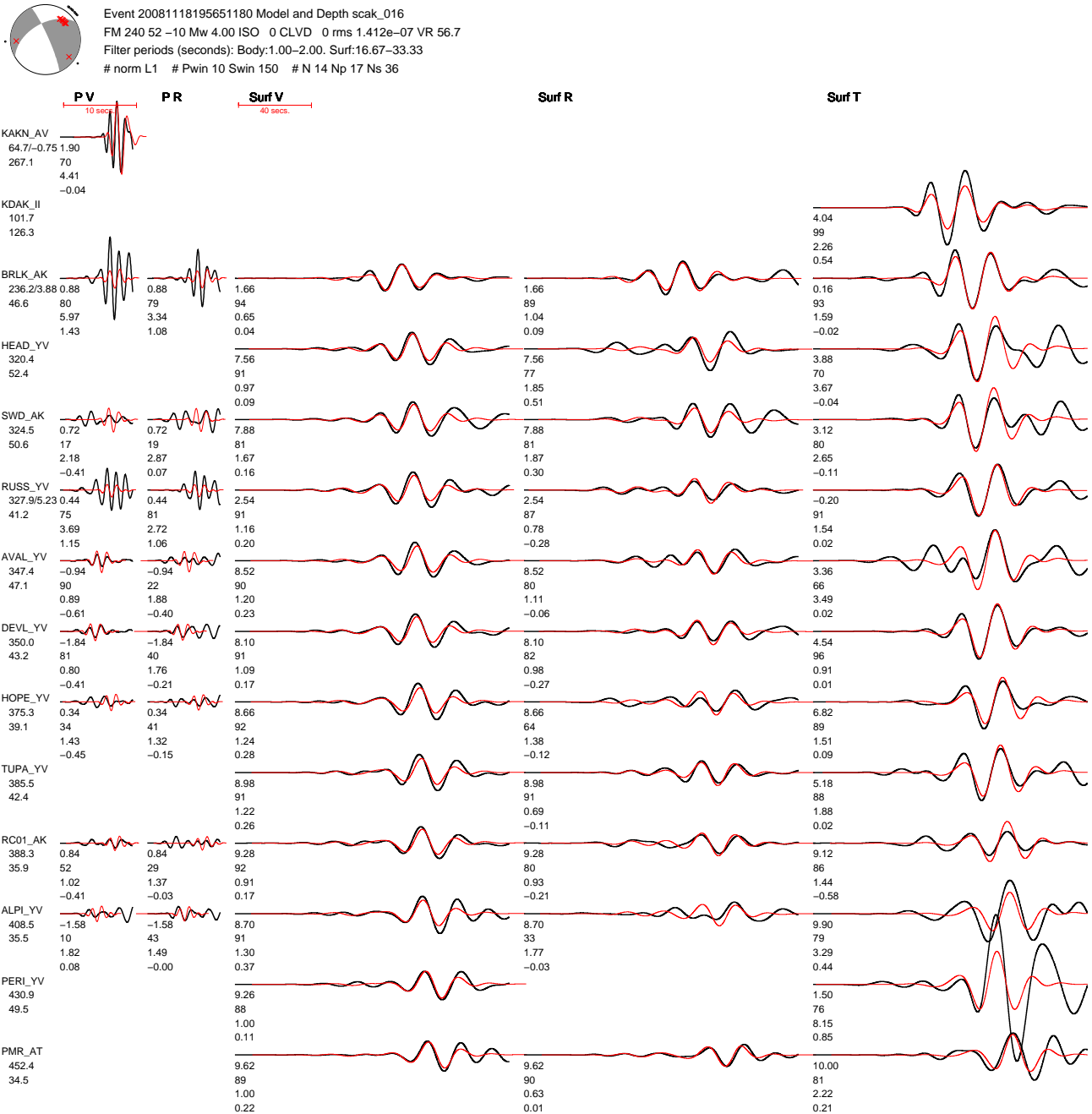


Figure A.5: Moment tensor solution and waveform fits for a small magnitude event 20081118195651180 (Table A.5). Our magnitude estimate (M_w 4.0) is significantly higher than the AEC catalog (M_w 3.5). See Figure A.6 for the waveform fits for the AEC first-motion solution.

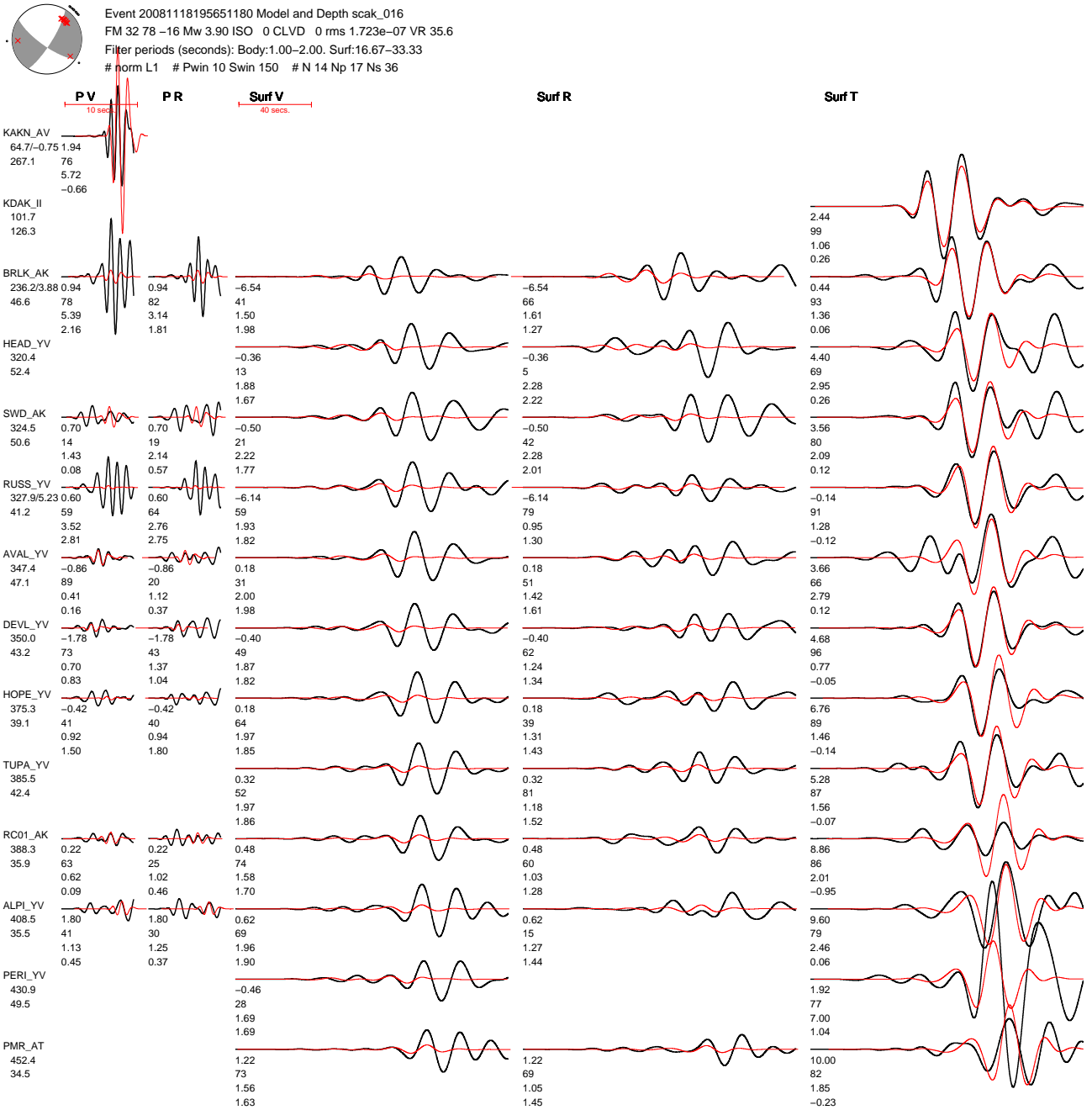


Figure A.6: Waveform fits for event 20081118195651180 using the solution from the AEC first-motion catalog. Here we allow the magnitude to vary in order to achieve the best possible waveform fits for this fixed hypocenter and orientation. The magnitude obtained (M_w 3.9) is significantly higher than the AEC catalog magnitude (M_w 3.5). Figure A.7 shows the waveform fits when the magnitude is fixed to be the magnitude in the AEC catalog. See Figure A.5 for comparison with our solution.

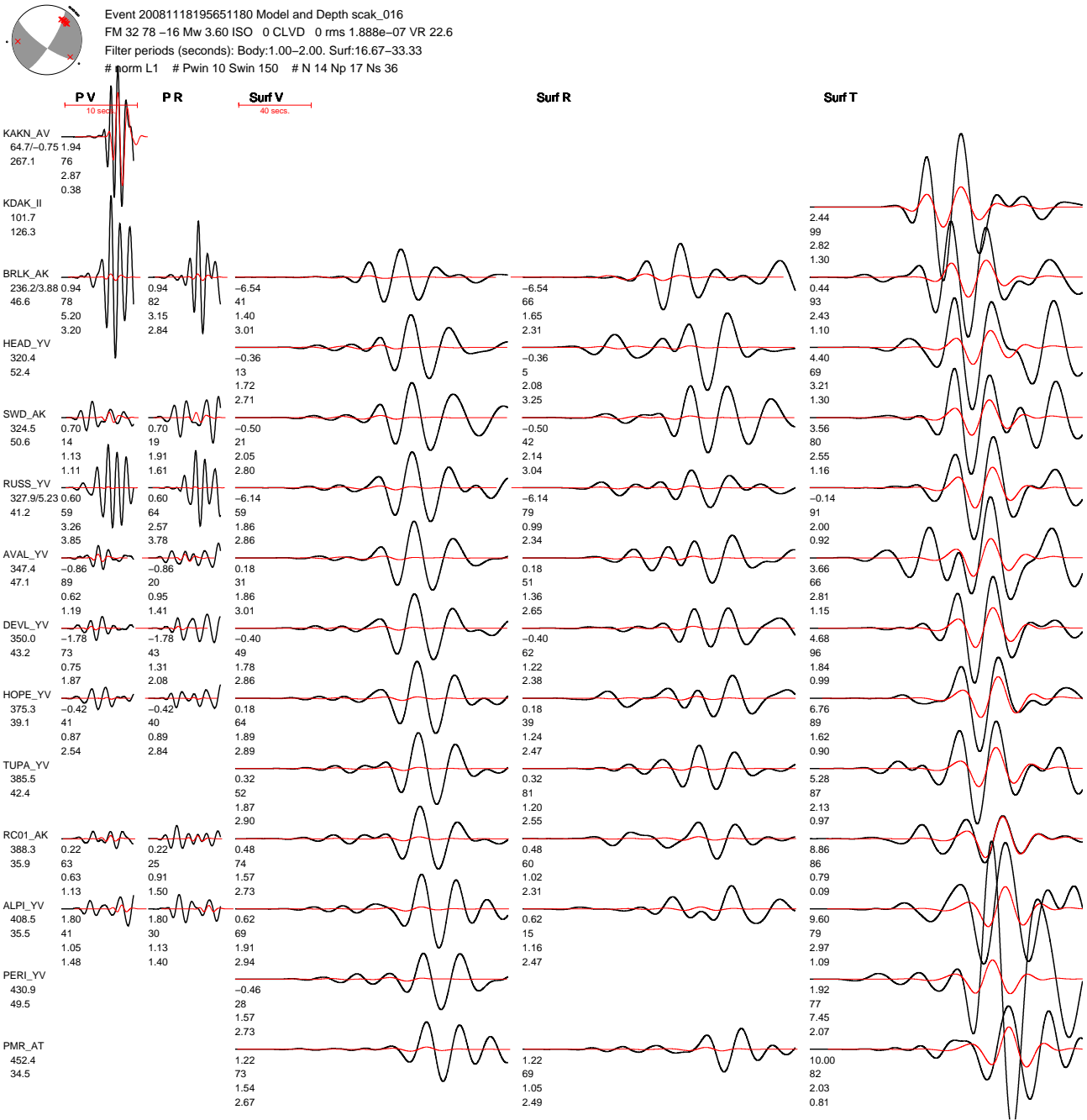


Figure A.7: Waveform fits for 20081118195651180 at AEC first-motion solution and at their magnitude estimate (see Figure A.6 for waveform fits when allowed to search over magnitude). Smaller amplitude of synthetics shows that the magnitude have been underestimated. The use of long period surface waves for more accurate estimate of magnitude have been known for quite some time now. Magnitude used in this case is M_w 3.6 which is obtained using the first-motion polarity match only, which is much smaller than our estimate of M_w 4 obtained using both the body and surface waves match (see Figure A.5).

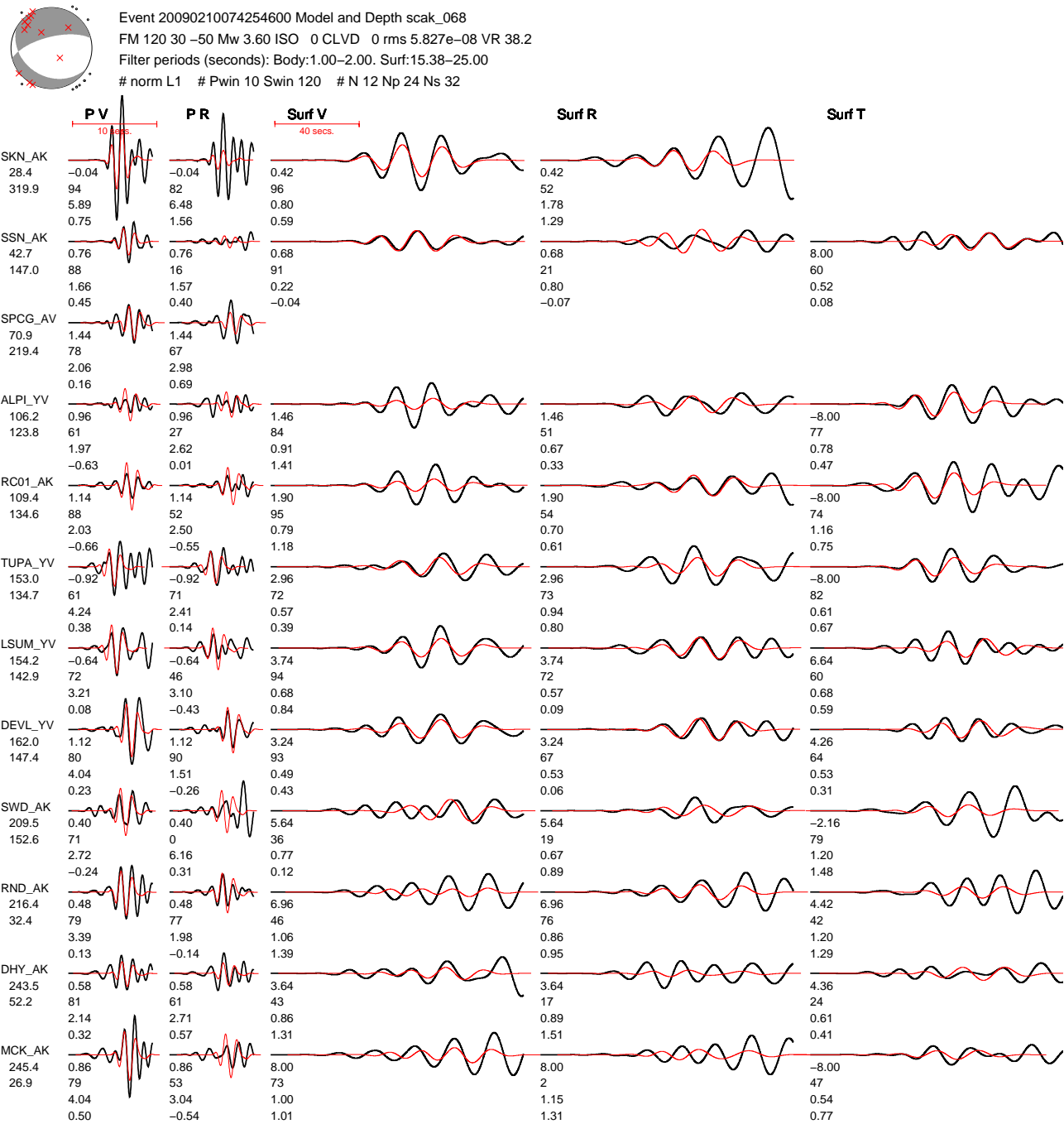


Figure A.8: Waveform fits for subset of stations for a small magnitude event (20090210074254600, depth 68 km, M_w 3.6) when inversion is performed using body and surface wave fitting (CAP). Omega difference from AEC first-motion solution (Figure A.9) is 68°. See figure header for details about the moment tensor inversion.

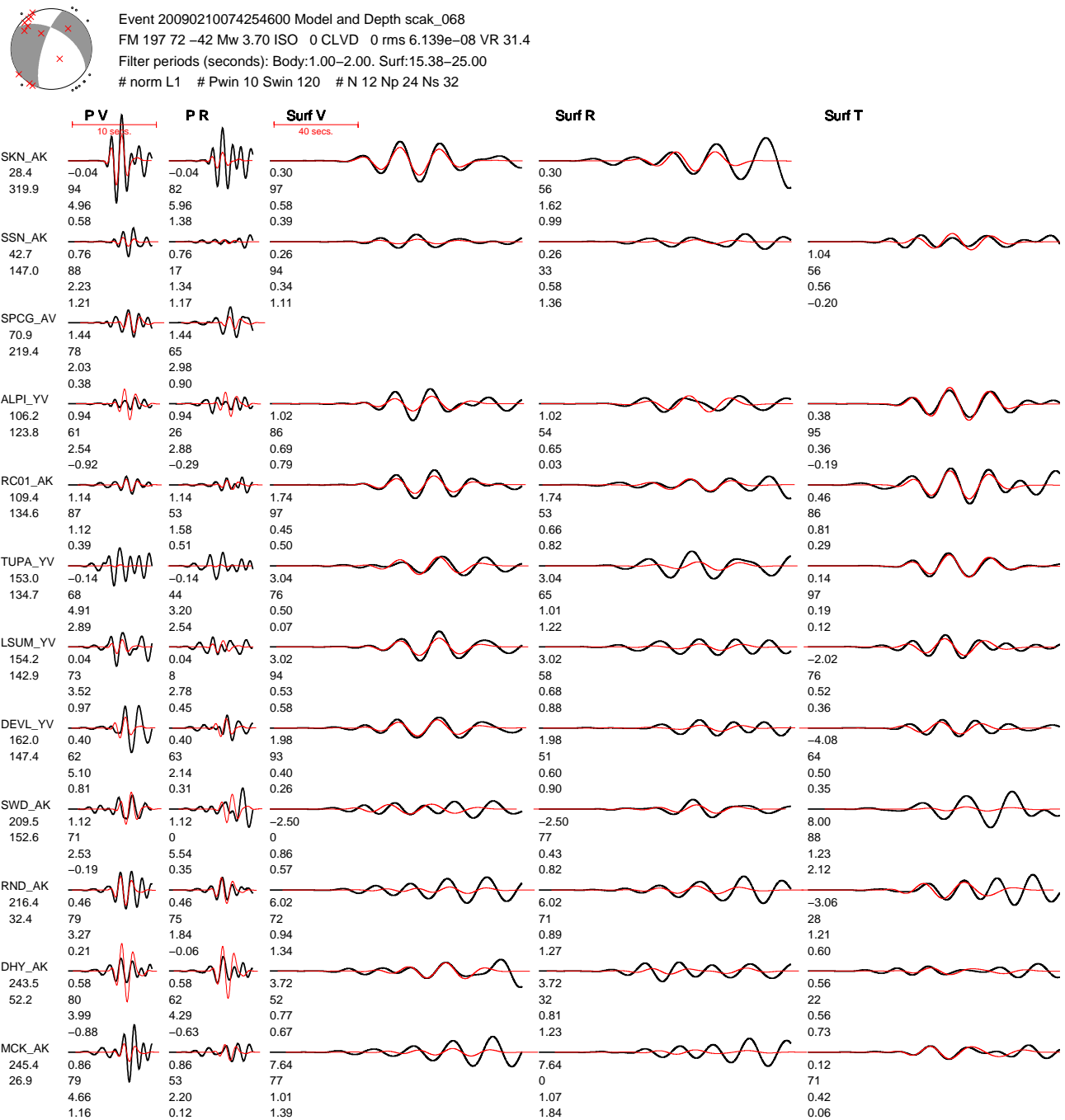


Figure A.9: Waveform fits for subset of stations for a small magnitude event 20090210074254600, at AEC first-motion solution and variable magnitude search. The solution used here is obtained using first-motion polarity information only. See Figure A.10 for waveform fits when fixed at AEC magnitude, and Figure A.8 for our solution obtained from CAP (obtained using body and surface waves). Magnitude obtained in this case is M_w 3.7. See figure header for details about the moment tensor inversion.

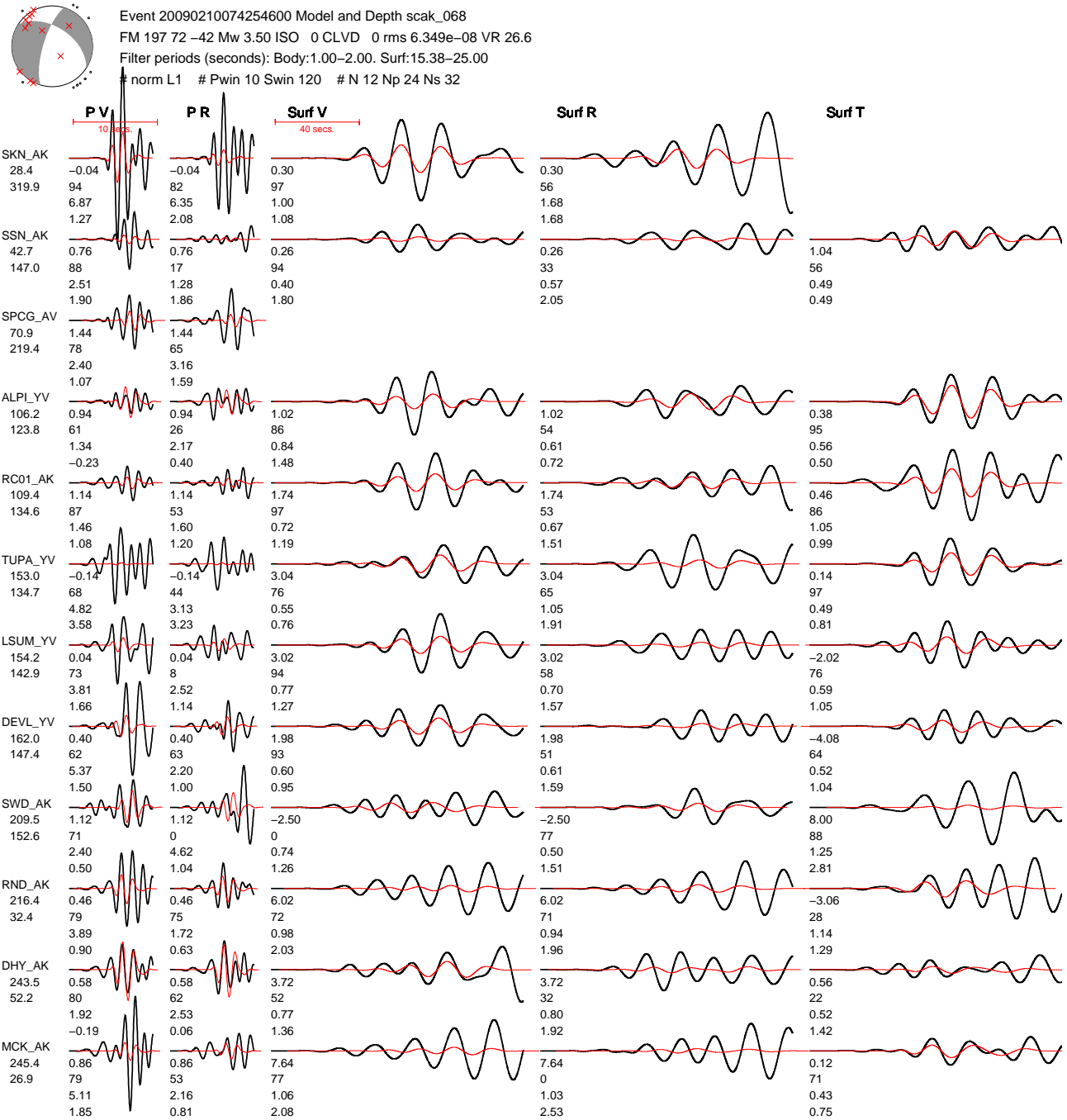


Figure A.10: Waveform fits for subset of stations for a small magnitude event 20090210074254600, at AEC first-motion solution and fixed magnitude. See Figure A.9 for waveform fits when searching over magnitude, and Figure A.8 for our solution obtained from CAP. Magnitude used in this case is M_w 3.5. See figure header for details about the moment tensor inversion.

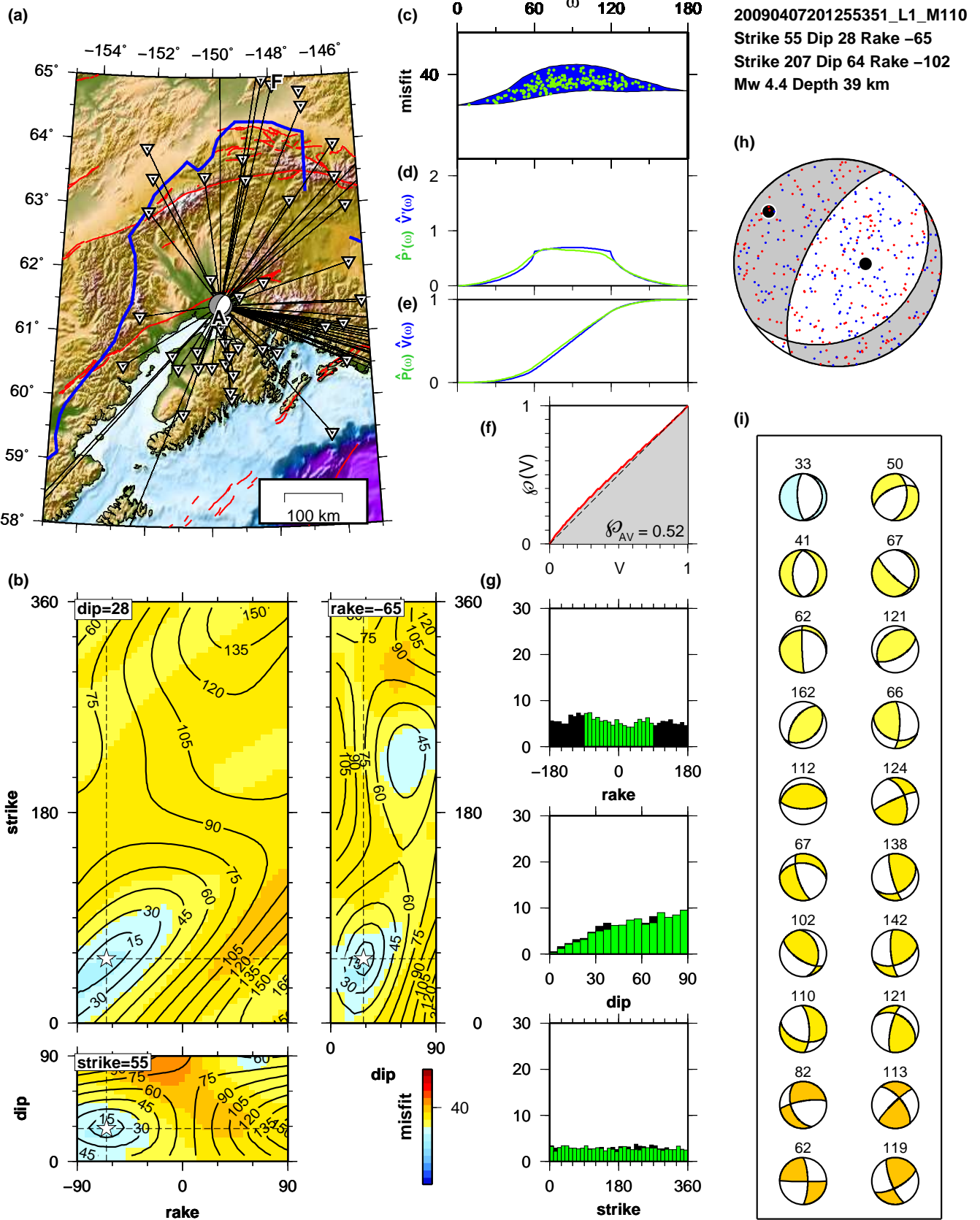


Figure A.11: Same as Figure 2.7, but for a different subset of data (M_{110} ; see Table 2.1). Each of the six data subset choices is used in Figure 2.7 (M_{111}) and Figures A.11–A.15 ($M_{110}, M_{011}, M_{101}, M_{112}, M_{012}$), respectively.

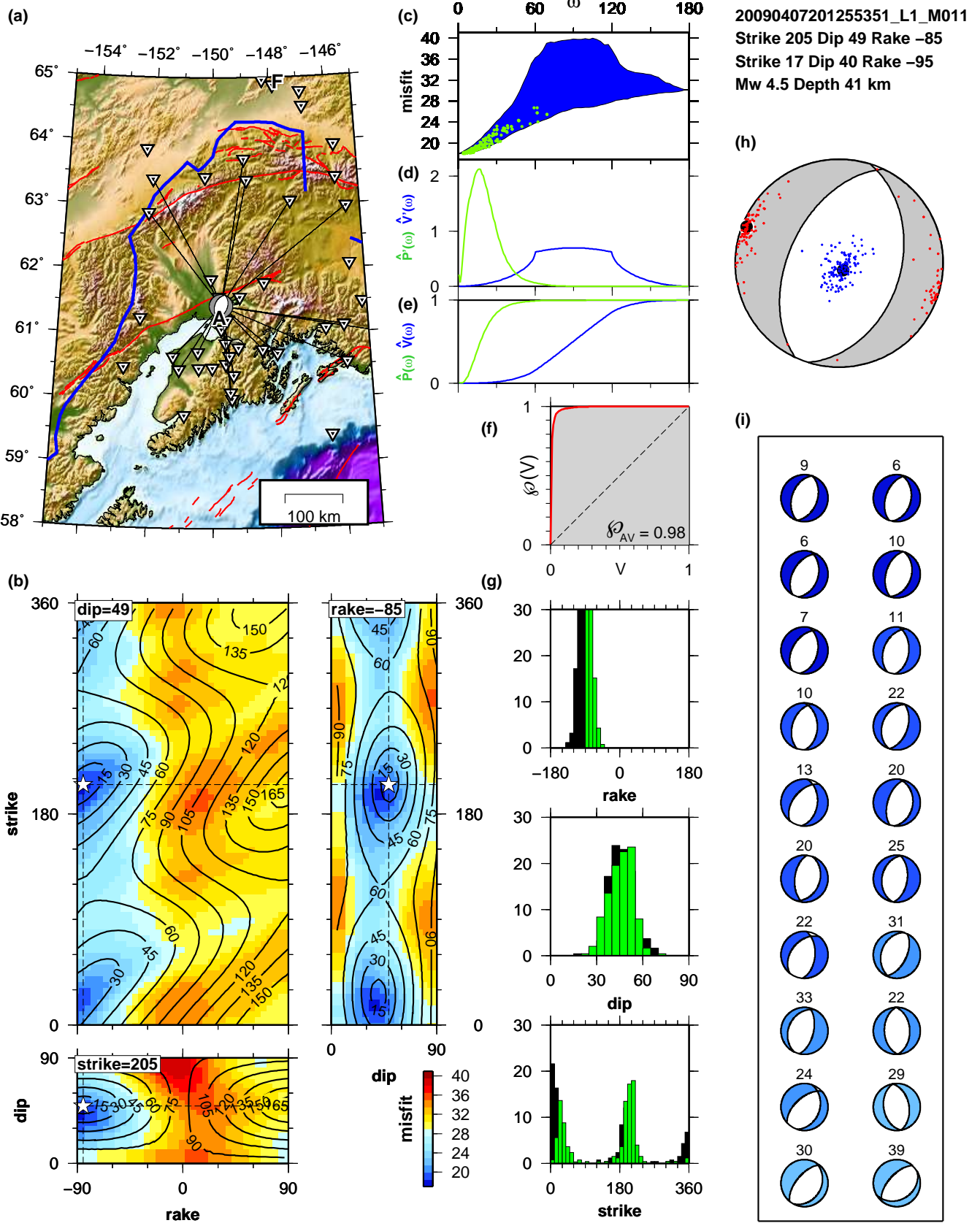


Figure A.12: Same as Figure 2.7, but for a different subset of data (M_{011} ; see Table 2.1). Each of the six data subset choices is used in Figure 2.7 (M_{111}) and Figures A.11–A.15 ($M_{110}, M_{011}, M_{101}, M_{112}, M_{012}$), respectively.

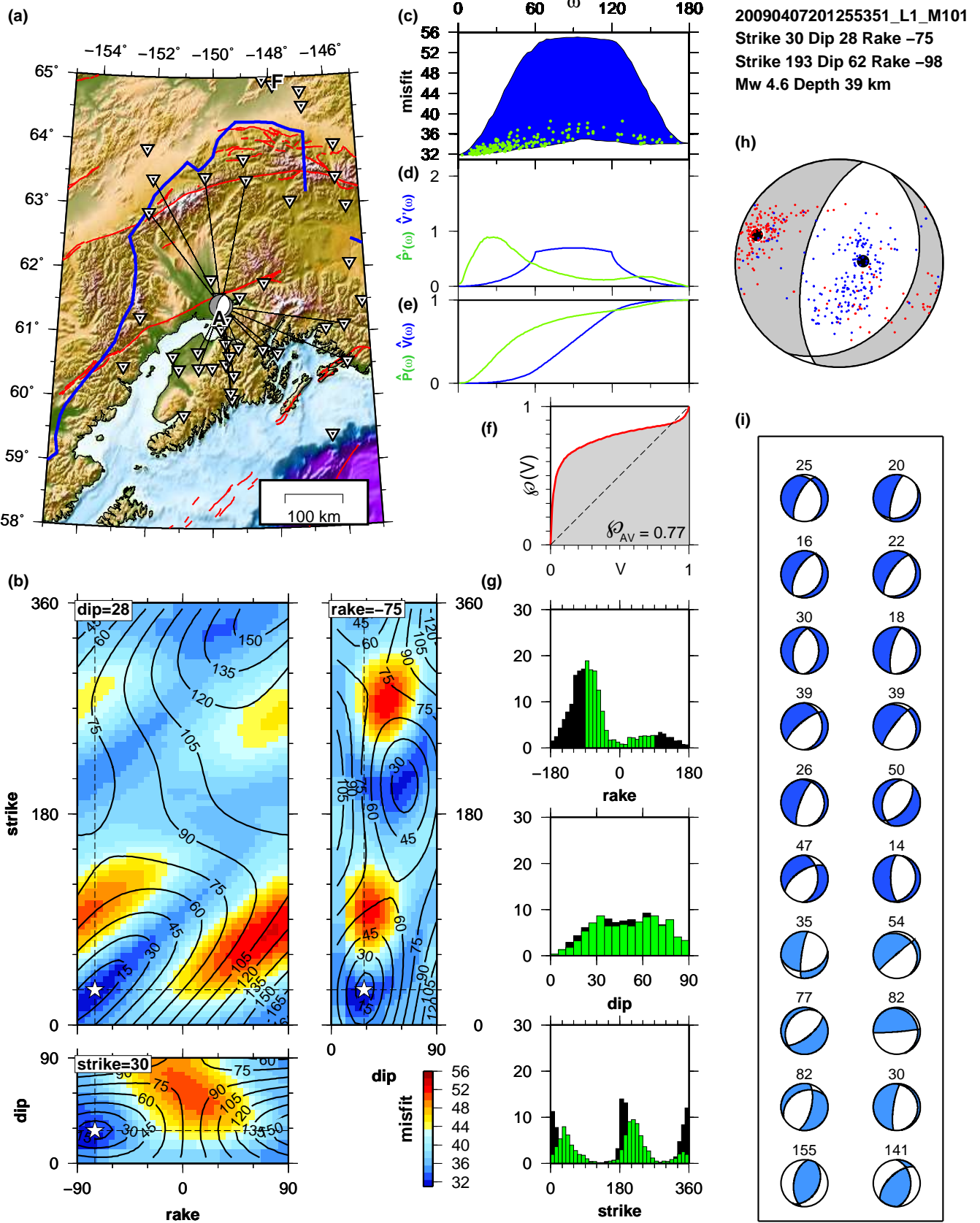


Figure A.13: Same as Figure 2.7, but for a different subset of data (M_{101} ; see Table 2.1). Each of the six data subset choices is used in Figure 2.7 (M_{111}) and Figures A.11–A.15 (M_{110} , M_{011} , M_{101} , M_{112} , M_{012}), respectively.

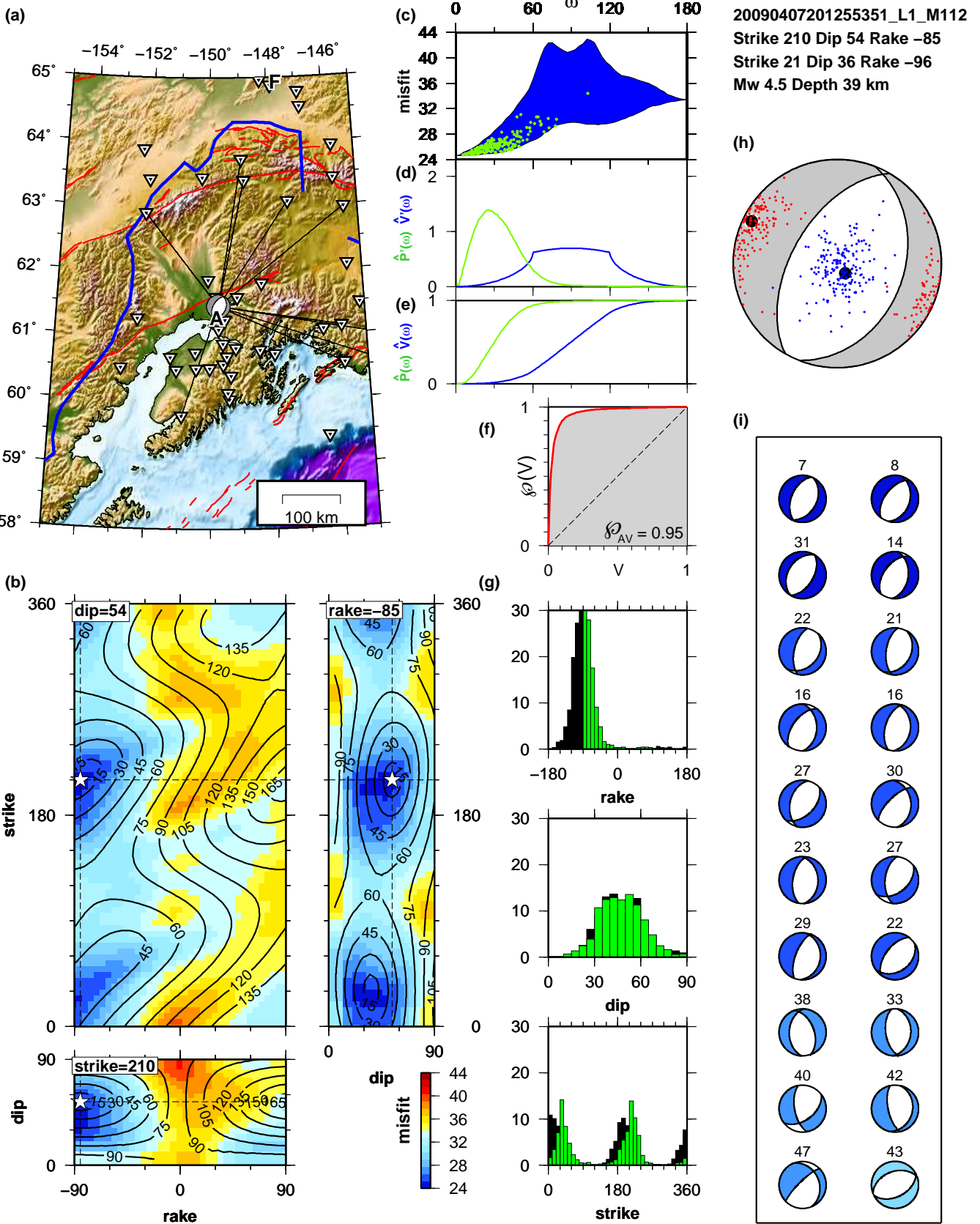


Figure A.14: Same as Figure 2.7, but for a different subset of data (M_{112} ; see Table 2.1). Each of the six data subset choices is used in Figure 2.7 (M_{111}) and Figures A.11–A.15 ($M_{110}, M_{011}, M_{101}, M_{112}, M_{012}$), respectively.

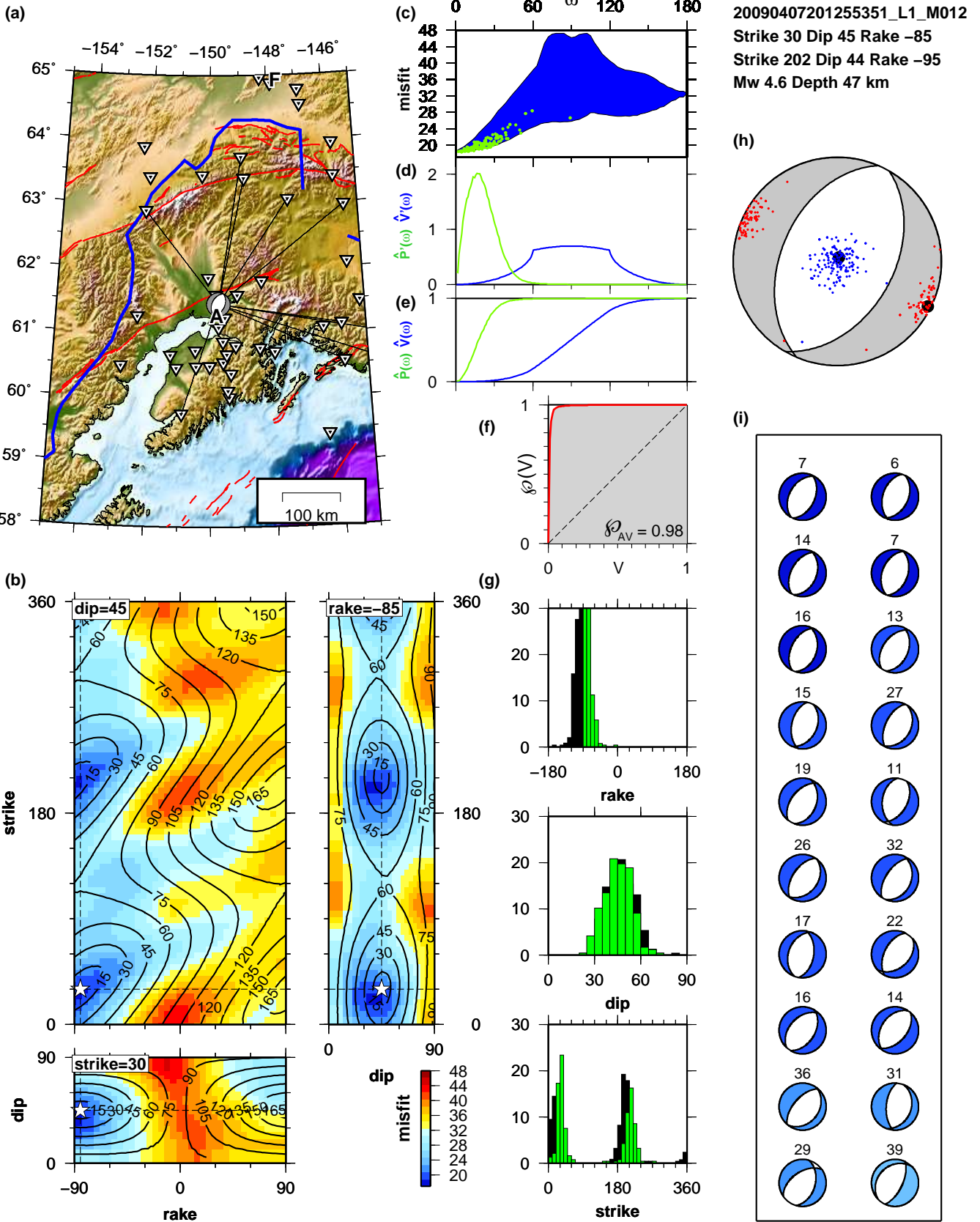


Figure A.15: Same as Figure 2.7, but for a different subset of data (M_{012} ; see Table 2.1). Each of the six data subset choices is used in Figure 2.7 (M_{111}) and Figures A.11–A.15 ($M_{110}, M_{011}, M_{101}, M_{112}, M_{169}, M_{012}$), respectively.

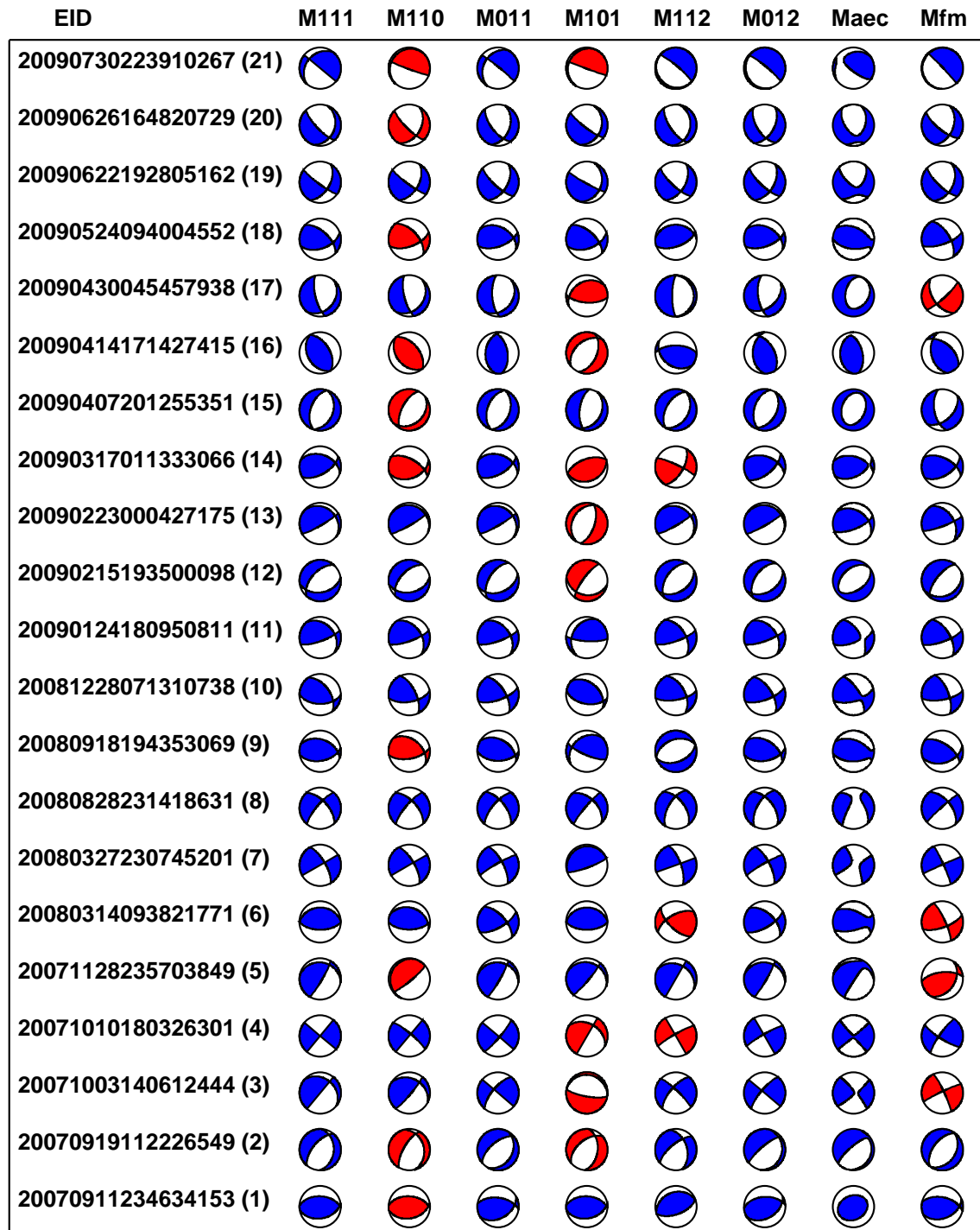


Figure A.16: Same as Figure 2.13 but using the L2 norm instead of the L1 norm. Solutions in the first column should be close to solutions in the first column of Figure 2.13 since only good stations are used in both cases. A comparison between L1 and L2 results for four cases is shown in Figure 2.12.

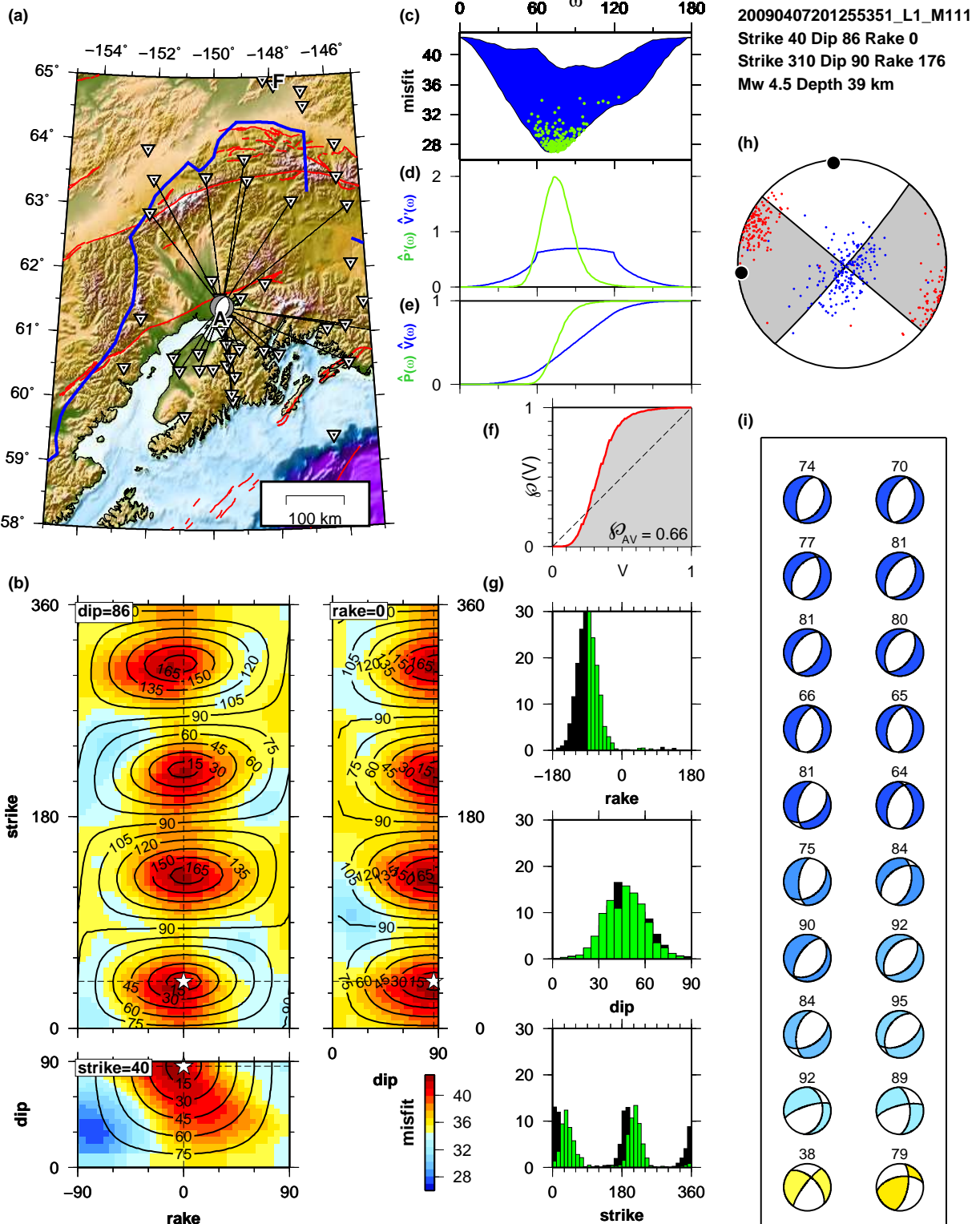


Figure A.17: Same as Figure 2.7, except here we have chosen the reference moment tensor to be the maximum misfit solution M_x rather than the minimum. (a) Beachball for M_x (strike 40° , dip 86° , rake 0°) and $\omega = \angle(M_0, M_x) = 74^\circ$. See Figure 2.7 for analysis when global minimum M_0 is chosen as M_{ref} , and see Section 2.8.1 for discussion.

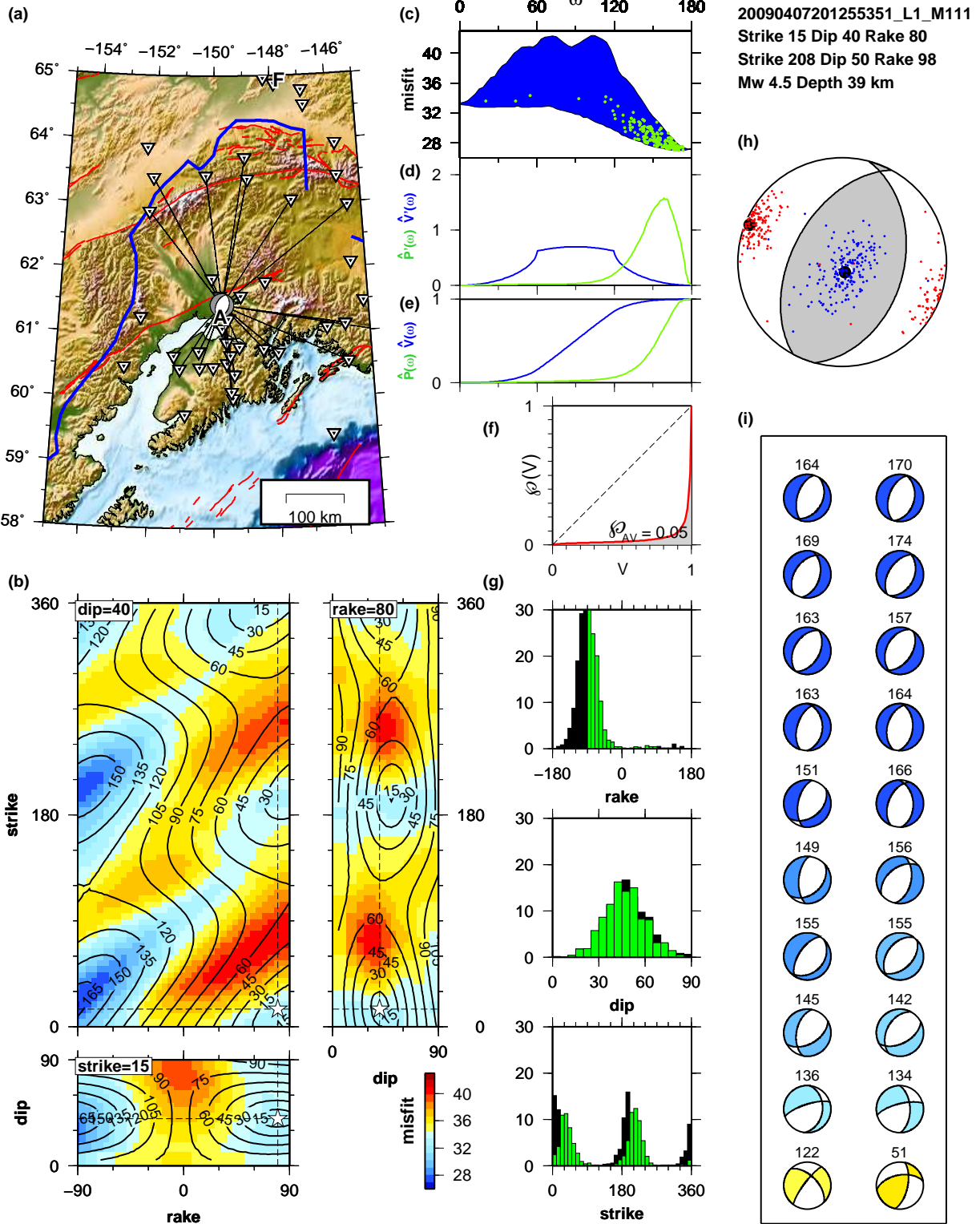
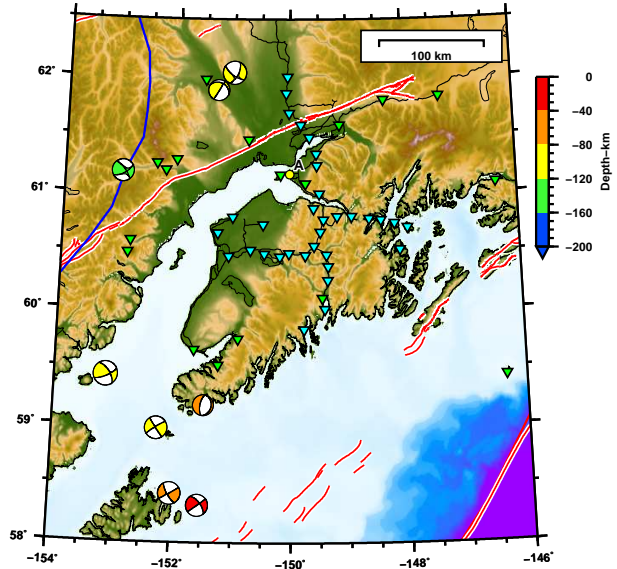
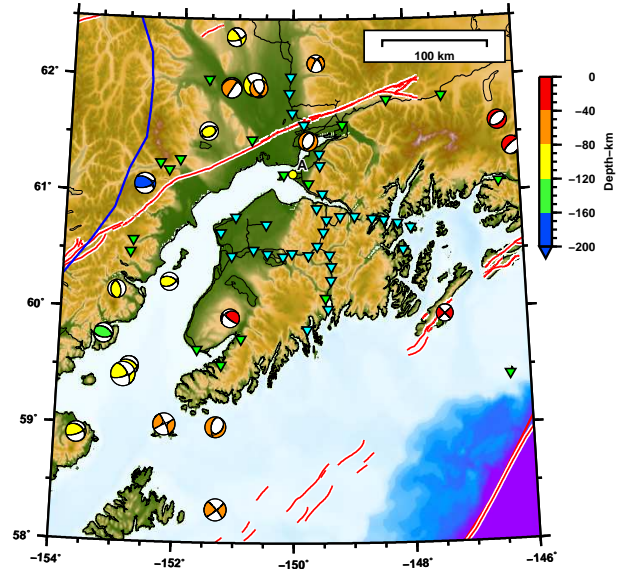


Figure A.18: Same as Figure 2.7, except here we choose the reference moment tensor to be $-M_0$, where M_0 is the best-fitting solution.

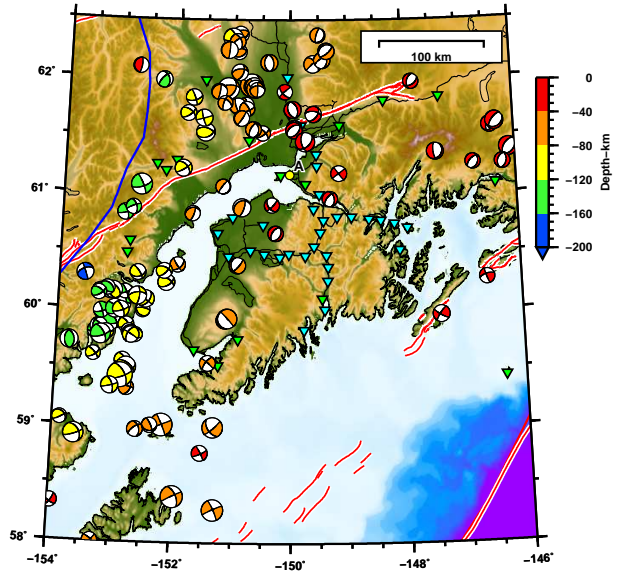
(a) GCMT catalog



(b) AEC moment tensor



(c) AEC first-motion (same events as in Figure 2.2)



(d) CAP Part I (same events as in (b))

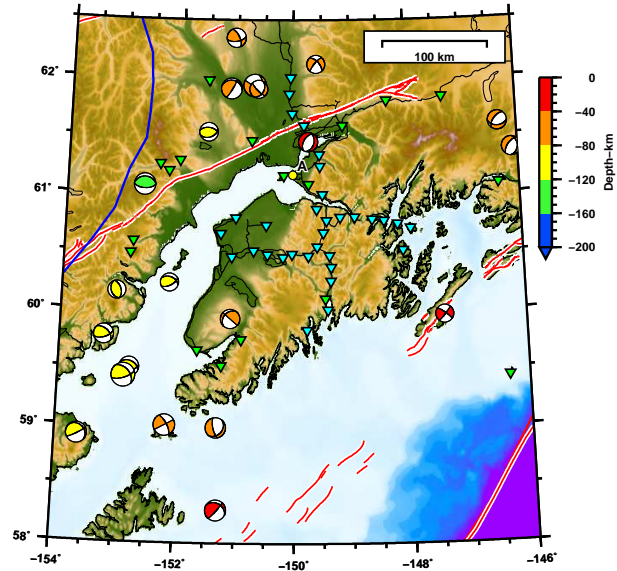


Figure A.19: Moment tensor catalogs for the time period of the MOOS deployment (2007-08-15 to 2009-08-15). (a) GCMT catalog (Ekström et al., 2012). (b) AEC moment tensor catalog (21 events: same as Part I catalog) (Ratchkovski & Hansen, 2002). (c) Subset of Figure 2.2 events in the AEC first-motion catalog. Figure 2.2 shows our moment tensors for the same events. (d) Our moment tensor solutions for the events shown in (b) (Part I catalog).

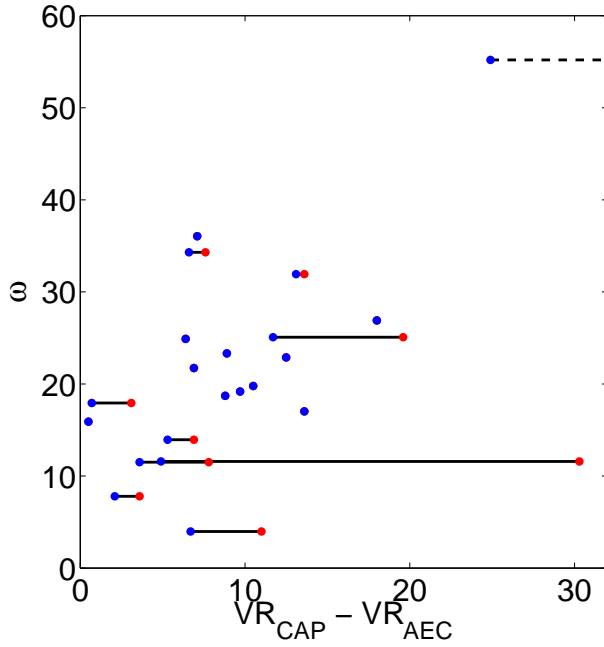


Figure A.20: Improvement in waveform fits between our solutions (M_{CAP}) and AEC moment tensor solution (M_{AEC}) for the 21 Part I events, measured in terms of $VR_{\text{CAP}} - VR_{\text{AEC}}$ and $\omega = \angle(M_{\text{CAP}}, M'_{\text{AEC}})$, where the prime notation indicates the closest double couple to M_{AEC} . The improvement in VR for CAP is measured for two separate cases: (red) AEC moment tensor with the AEC magnitude; (blue) AEC moment tensor free to search over magnitude. The blue points are necessarily to the left of (or on top of) the red points. For the highest ω event, 20071003140612444 (uppermost blue point), VR worsens severely when magnitude is fixed; the red point for that event is off the plotting scale at $\Delta VR = 207$.

Appendix B

Supporting Information for Chapter 3 (Crustal earthquakes in the Cook Inlet and Susitna region of southern Alaska)

B.1 Misfit reward factors

This section supports Section 3.4.3.

As summarized in Section 7.3 of Silwal & Tape (2016), while fitting observed and synthetic waveforms, we frequently encounter cases where the total normalized misfit when using more data (larger time-windows, wider bandpass, and more stations) is larger than the one obtained when using fewer data. In essence, overfitting can occur when using fewer waveforms: the synthetic waveforms may result in a low misfit, yet the moment tensor solution may be incorrect.

This happens because it is much easier to fit a single waveform (or waveforms for fewer stations) and could result in a lower misfit for a wrong solution (Figure B.2). We address this by modifying our misfit function to include scale factors that reward the use of:

1. a longer time window for Pnl and surface waves
2. a broader bandpass for Pnl and surface waves
3. more stations

This weighting has been used for full moment tensor inversions in Alvizuri et al. (2018) and Alvizuri & Tape (2018).

B.1.1 Waveform reward factor for longer time windows and a broader bandpass

For each station j and each time window i , we consider a weighting matrix in Equation (3.1). Our choice is a constant-valued diagonal matrix

$$\mathbf{W}_{ij} = \frac{w_{ij}}{d_{ij}b_{ij}} \mathbf{I} \quad (\text{B.1})$$

where w_{ij} is the user-specified weight for the ij th time window, d_{ij} is the length of window in seconds, and b_{ij} is the length of bandpass in Hertz. In our study, $w_{ij} = 1$ always, but there may be reason to test weighting body waves and surface waves differently (Alvizuri & Tape, 2016) or to emphasize or demphasize a particular time window. The longer time windows and wider bandpass will lead to smaller values of the diagonal of \mathbf{W}_{ij} , resulting in lower misfit values (Eq. 3.1) and larger VR values.

B.1.2 Station reward factor for using more stations

The final scaled misfit function (Eq. 3.3)

$$\Phi(M, N_s) = h(N_s) \times \Phi(M), \quad (\text{B.2})$$

is scaled by a weighting function $h(N_s)$ so that the total misfit $\Phi(M)$ is rewarded for using more stations. We define this weighting function as

$$h(N_s) = 0.5 + 1.5e^{-N_s/C} \quad (\text{B.3})$$

where N_s is the number of stations and C represents a reference number of stations and governs the shape of the weighting function (see Figure B.1). When $N_s = C$, $h(N_s) = 0.5 + 1.5e^{-1} \approx 1$. As N_s increases, $h(N_s)$ decreases, leading to a lower misfit function (i.e., reward). As N_s decreases, $h(N_s)$ increases, leading to a higher misfit function (i.e., penalty). The constant 0.5 is included to prevent the misfit from going to zero for the cases where large number of stations are used.

We show an example of the impact of Equation (B.3) for an example event. With $N_s = 3$ and $C = 7$, we have $h(N_s) \approx 1.5$, which increases the misfit function and leads to a very low VR value, in spite of the appearance of well-fitting waveforms (Figure B.2a). With $N_s = 5$, we have a different $h(N_s)$ and also a different best-fitting moment tensor (Figure B.2b). Our preferred solution uses $N_s = 9$ and is shown in Figure B.3. Figure B.4 demonstrates that using more stations will not always result in lower misfit (and higher VR). Here we had a 10th station that is a clear outlier. Thanks to the use of an L1-norm in the misfit function, we are able to still obtain the same best-fitting moment tensor (Figure B.3), but the VR value is now much lower (26.2 vs 51.8), despite having a lower penalty factor for using more stations. If the 10th station had comparable or better waveform fits than the other stations, then we would expect the lower penalty factor to result in lower misfit and higher VR .

References

- Alvizuri, C. & Tape, C., 2016. Full moment tensors for small events ($M_w < 3$) at Uturuncu volcano, Bolivia, *Geophys. J. Int.*, **206**, 1761–1783, doi:10.1093/gji/ggw247.
- Alvizuri, C. & Tape, C., 2018. Full moment tensor analysis of nuclear explosions in North Korea, *Seismol. Res. Lett.* (in review).
- Alvizuri, C., Silwal, V., Krischer, L., & Tape, C., 2018. Estimation of full moment tensors, including uncertainties, for nuclear explosions, volcanic events, and earthquakes, *J. Geophys. Res. Solid Earth*, **123**, doi:10.1029/2017JB015325.
- Brockman, S. R., Espinosa, A. F., & Michael, J. A., 1988. *Catalog of Intensities and Magnitudes for Earthquakes in Alaska and the Aleutian Islands—1786–1981*, U.S. Geol. Survey Bulletin 1840.
- Doser, D. I. & Brown, W. A., 2001. A study of historic earthquakes of the Prince William Sound, Alaska, Region, *Bull. Seismol. Soc. Am.*, **91**(4), 842–857.
- Engdahl, E. R. & Villaseñor, A., 2002. Global seismicity: 1900–1999, in *International Handbook of Earthquake and Engineering Seismology*, vol. 81A of **International Geophysics Series**, pp. 665–690, eds Lee, W. H. K., Kanamori, H., Jennings, P. C., & Kisslinger, C., Academic Press, London.
- Gutenberg, B. & Richter, C. F., 1954. *Seismicity of the Earth and Associated Phenomena*, Princeton U. Press, Princeton, New Jersey, USA, 2nd edn.
- Kirschner, C. E., 1988. Map Showing Sedimentary Basins of Onshore and Continental Shelf Areas, Alaska, U.S. Geol. Survey Miscellaneous Investigation Series I-1873.
- Li, J., Abers, G. A., Kim, Y., & Christensen, D., 2013. Alaska megathrust 1: Seismicity 43 years after the great 1964 Alaska megathrust earthquake, *J. Geophys. Res.*, **118**, 4861–4871, doi:10.1002/jgrb.50358.
- Lomax, A., Virieux, J., Volant, P., & Berge, C., 2000. Probabilistic earthquake location in 3D and layered models: Introduction of a Metropolis-Gibbs method and comparison with linear locations, in *Advances in Seismic Event Location*, pp. 101–134, eds Thurber, C. H. & Rabinowitz, N., Kluwer, Amsterdam.
- Lomax, A., Silwal, V., & Tape, C., 2018. Hypocenter estimation for 14 earthquakes in south-central Alaska (1929–1975), ScholarWorks@UA at <http://hdl.handle.net/11122/8380>: descriptor file and zipped set of text files for each earthquake.

Silwal, V. & Tape, C., 2016. Seismic moment tensors and estimated uncertainties in southern Alaska, *J. Geophys. Res. Solid Earth*, **121**, 2772–2797, doi:10.1002/2015JB012588.

Storchak, D. A., Di Giacomo, D., Bondár, I., Engdahl, E. R., Harris, J., Lee, W. H. K., Villaseñor, A., & Bormann, P., 2013. Public release of the ISC–GEM Global Instrumental Earthquake Catalogue (1900–2009), *Seismol. Res. Lett.*, **84**(5), 810–815, doi:10.1785/0220130034.

Table B.1: Source location and origin time for 1933, 1943 and 1954 earthquakes from various sources. See Figures 3.6 and 3.11 for locations on a map.

label	origin time	lat	lon	depth	reference
L33	1933-04-27 02:36:07.115	61.00	-151.07	0	this study
I33	1933-04-27 02:36:07.770	61.10	-151.06	15 ± 4	Storchak et al. (2013)
G33	1933-04-27 02:36:04	61.25	-150.75	0	Gutenberg & Richter (1954)
E33	1933-04-27 02:36:11.510	60.99	-151.00	35	Engdahl & Villasenor (2002)
D33	1933-04-27 02:36	61.11	-150.85	9 ± 4	Doser & Brown (2001)
L43	1943-11-03 14:32:22.982	61.66	-151.00	17	This study
I43	1943-11-03 14:32:20.840	61.79	-151.00	15 ± 9	Storchak et al. (2013)
G43	1943-11-03 14:32:17	61.75	-151.00	0	Gutenberg & Richter (1954)
E43	1943-11-03 14:32:24.120	61.63	-151.00	35	Engdahl & Villasenor (2002)
D43	1943-11-03 14:32	61.74	-150.80	27 ± 4	Doser & Brown (2001)
L54	1954-10-03 11:18:49.136	60.52	-150.51	56	This study
I54	1954-10-03 11:18:48.530	60.65	-150.39	62 ± 5	Storchak et al. (2013)
E54	1954-10-03 11:18:47	60.70	-150.30	64	Engdahl & Villasenor (2002)
D54	1954-10-03 11:18	60.68	-150.45	60 ± 10	Doser & Brown (2001)

Table B.2: Double couple moment tensor solutions for 9 crustal earthquakes in the Beluga region (Table 3.1).

label	eid	lat	lon	strike	dip	rake	M_w	depth	Nstn
1	2008-01-26 04:29:42	61.56	-151.23	141	50	67	3.0	11.0	19
2	2008-02-05 03:51:42	61.55	-151.28	46	54	58	2.6	2.0	14
3	2009-05-16 01:51:04	61.66	-151.25	61	49	68	2.9	7.0	10
4	2010-03-28 16:05:36	61.69	-151.34	326	70	-29	3.0	5.0	6
5	2012-03-06 06:12:58	61.54	-151.25	63	84	9	2.6	12.0	12
6	2012-06-29 11:07:39	61.62	-151.30	168	38	85	2.5	8.0	7
7	2014-01-24 12:07:03	61.65	-151.26	342	50	-33	3.0	8.0	9
8	2014-07-14 06:04:10	61.59	-151.29	165	37	70	3.0	11.0	14
9	2016-04-18 18:02:12	61.61	-151.22	8	44	82	2.6	7.0	10

Table B.3: Double couple moment tensor solutions for 22 crustal earthquakes in the Upper Cook Inlet region (Table 3.1).

label	origin time	latitude	longitude	strike	dip	rake	M_w	depth	stations
1	2008-04-08 17:16:30	61.06	-150.85	229	48	71	2.6	16.0	32
2	2008-04-15 08:42:17	60.97	-151.13	135	41	70	2.8	13.0	30
3	2008-10-06 18:24:38	61.15	-150.76	147	60	38	2.6	13.0	16
4	2008-11-22 05:30:47	60.99	-151.16	156	54	72	2.9	10.0	15
5	2009-05-02 09:50:52	60.88	-150.93	152	46	33	2.6	5.0	16
6	2009-09-05 01:52:36	60.94	-151.08	6	65	90	2.9	15.0	9
7	2010-06-18 08:10:34	61.09	-151.10	49	58	58	2.6	7.0	6
8	2010-10-13 14:45:37	61.08	-150.94	14	83	35	2.8	11.0	11
9	2010-12-28 23:08:30	61.00	-150.94	21	34	60	2.8	13.0	7
10	2012-02-13 17:40:33	60.93	-151.09	311	42	29	2.5	10.0	8
11	2012-03-08 10:57:43	61.01	-150.91	154	44	54	4.0	10.0	11
12	2012-08-02 06:11:38	60.82	-151.02	208	31	84	2.9	18.0	12
13	2013-03-24 15:24:30	60.92	-150.83	348	40	46	2.7	12.0	12
14	2013-03-26 04:30:06	60.93	-150.86	253	62	-81	2.9	10.0	13
15	2014-02-03 00:03:07	60.92	-151.13	11	32	79	2.9	15.0	17
16	2014-11-15 03:01:00	60.76	-151.07	214	58	85	2.5	20.0	23
17	2014-12-11 00:48:39	60.74	-151.03	33	35	-70	3.0	20.0	22
18	2014-12-28 17:00:32	60.95	-150.87	320	16	58	3.1	20.0	23
19	2015-03-15 08:56:11	61.03	-150.79	284	34	50	2.5	15.0	21
20	2015-07-27 02:21:54	60.98	-150.94	319	50	24	3.5	16.0	42
21	2015-08-30 21:27:12	61.00	-150.96	151	37	48	2.6	15.0	31
22	2015-11-24 21:25:57	60.94	-150.82	152	53	35	2.7	20.0	32

Table B.4: Double couple moment tensor solutions for 22 crustal earthquakes in the Susitna region (Table 3.1).

label	eid	lat	lon	strike	dip	rake	M_w	depth	Nstn
1	2007-12-19 21:58:56	62.23	-150.13	166	58	62	3.2	8.0	16
2	2008-04-18 04:14:58	62.05	-150.50	331	8	-81	3.2	3.0	10
3	2008-06-02 17:27:40	61.88	-150.10	172	37	65	3.6	6.0	23
4	2010-07-08 03:15:49	61.81	-150.50	41	30	77	4.8	15.0	9
5	2010-12-01 23:19:44	62.30	-150.11	355	59	61	3.2	10.0	9
6	2010-12-14 02:22:37	62.28	-150.27	3	24	73	3.6	21.0	8
7	2011-04-05 18:30:24	62.31	-150.03	24	54	68	3.4	12.0	9
8	2011-04-16 06:01:41	62.31	-149.99	24	54	68	3.1	11.0	12
9	2011-10-21 17:09:40	61.90	-150.25	162	47	66	3.7	3.0	12
10	2011-12-03 09:33:58	61.97	-150.93	17	82	88	4.1	6.0	17
11	2012-01-27 17:10:28	61.80	-150.18	327	54	76	3.1	10.0	15
12	2012-04-29 10:57:57	62.07	-149.99	131	42	67	3.2	6.0	16
13	2013-01-20 21:56:58	62.19	-150.40	12	31	86	3.4	15.0	12
14	2013-09-23 09:21:18	61.63	-150.65	186	42	74	3.7	6.0	17
15	2013-09-30 06:32:02	61.92	-150.90	163	48	84	3.2	10.0	17
16	2014-01-21 14:29:20	62.09	-150.37	192	38	72	3.1	16.0	17
17	2015-01-19 10:36:11	62.19	-150.57	25	50	76	4.0	10.0	23
18	2015-05-18 15:49:10	61.94	-150.45	6	40	89	4.2	21.0	17
19	2016-01-18 04:05:56	62.10	-150.64	156	80	39	4.5	10.0	28
20	2016-05-29 23:49:37	61.87	-150.28	168	71	30	3.1	16.0	24
21	2016-12-01 23:55:55	61.86	-150.27	354	53	31	3.0	18.0	27
22	2016-12-04 13:15:44	61.97	-150.90	117	42	38	4.2	8.0	27

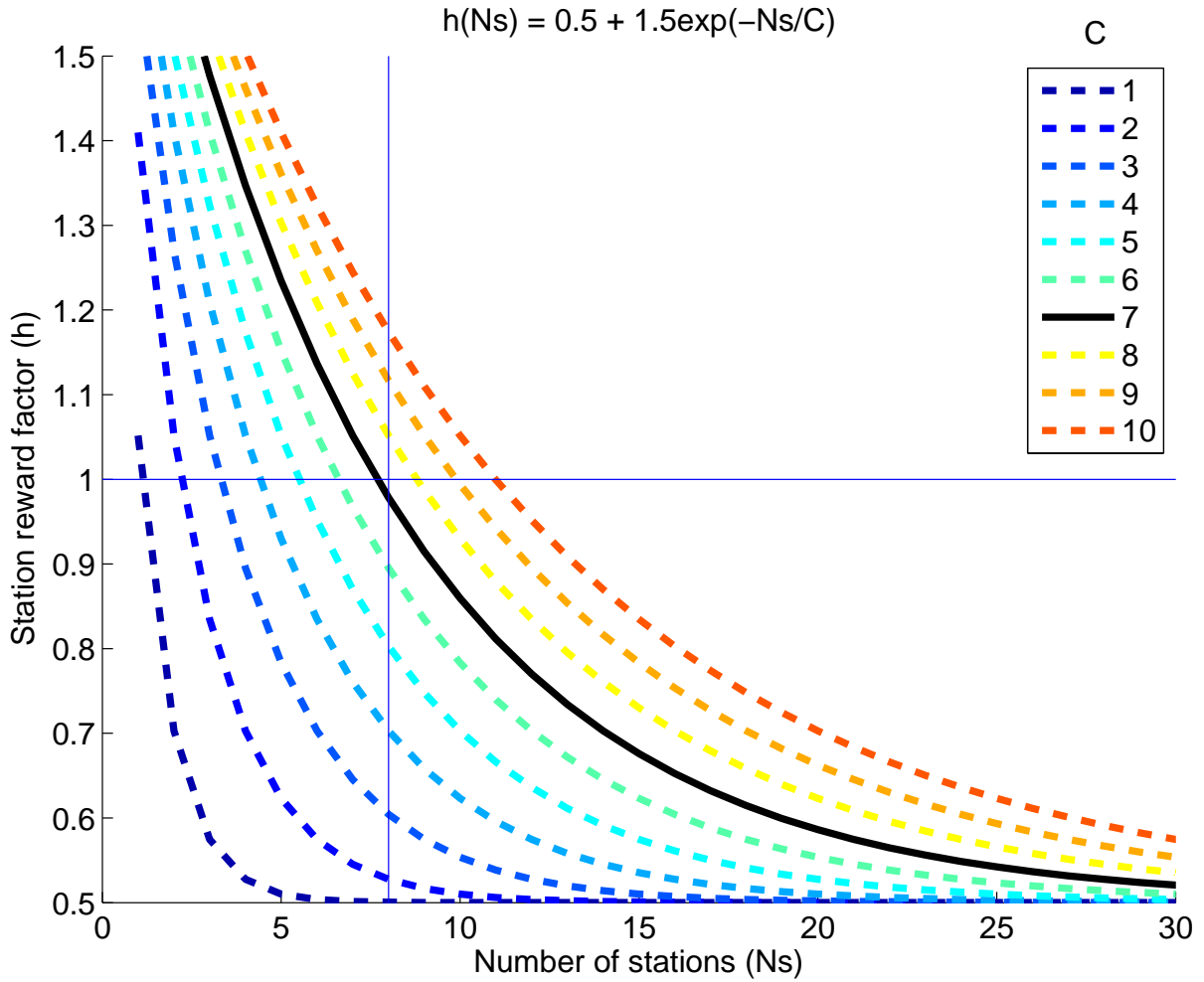
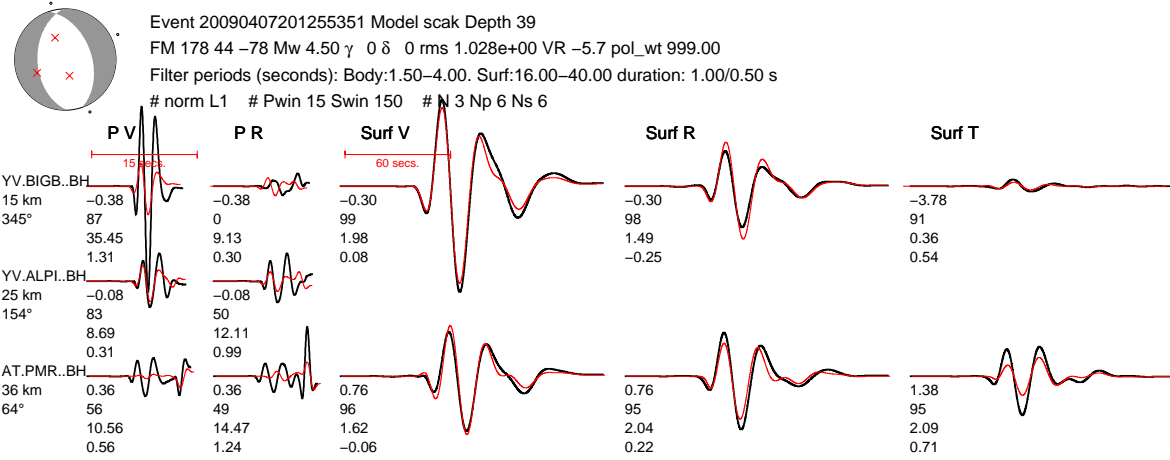


Figure B.1: Plotting the station reward factor $h(N_s)$ (Eq. B.3), which is used in the misfit function (Eq. 3.3). Our chosen function is for $C = 7$ (thick black line). The function $h(N_s)$ is approximately the same for $N_s = C$, and it will increase (penalty) for fewer stations and decrease (reward) for more stations.

(a)



(b)

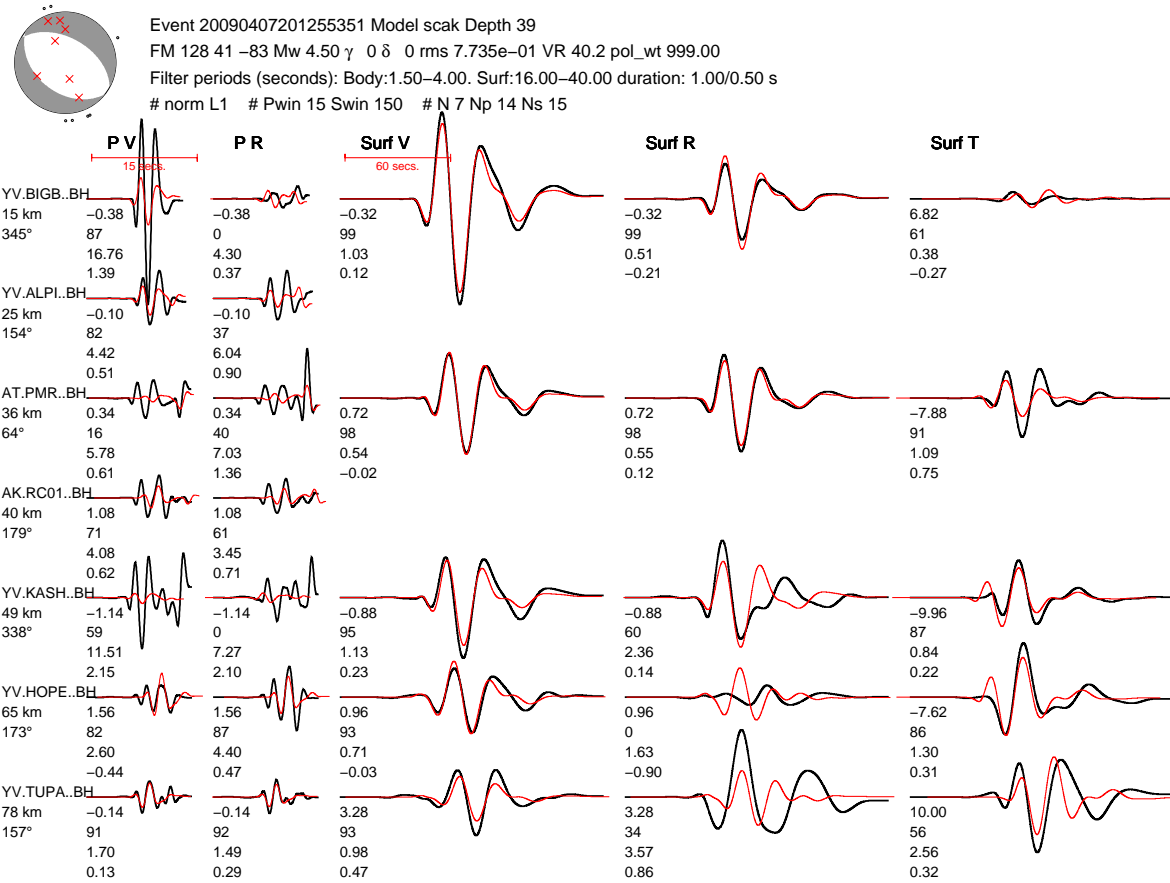


Figure B.2: The effect of the number of stations on moment tensor solutions. Best-fitting moment tensor and waveform fits when using (a) 3 stations and (b) 7 stations. Notice the increase in VR (and the decrease in the RMS misfit) as we increase the number of stations; this is due to the station reward factor (Eq. B.3). Also compare the beachballs with the preferred solution in Figure B.3.

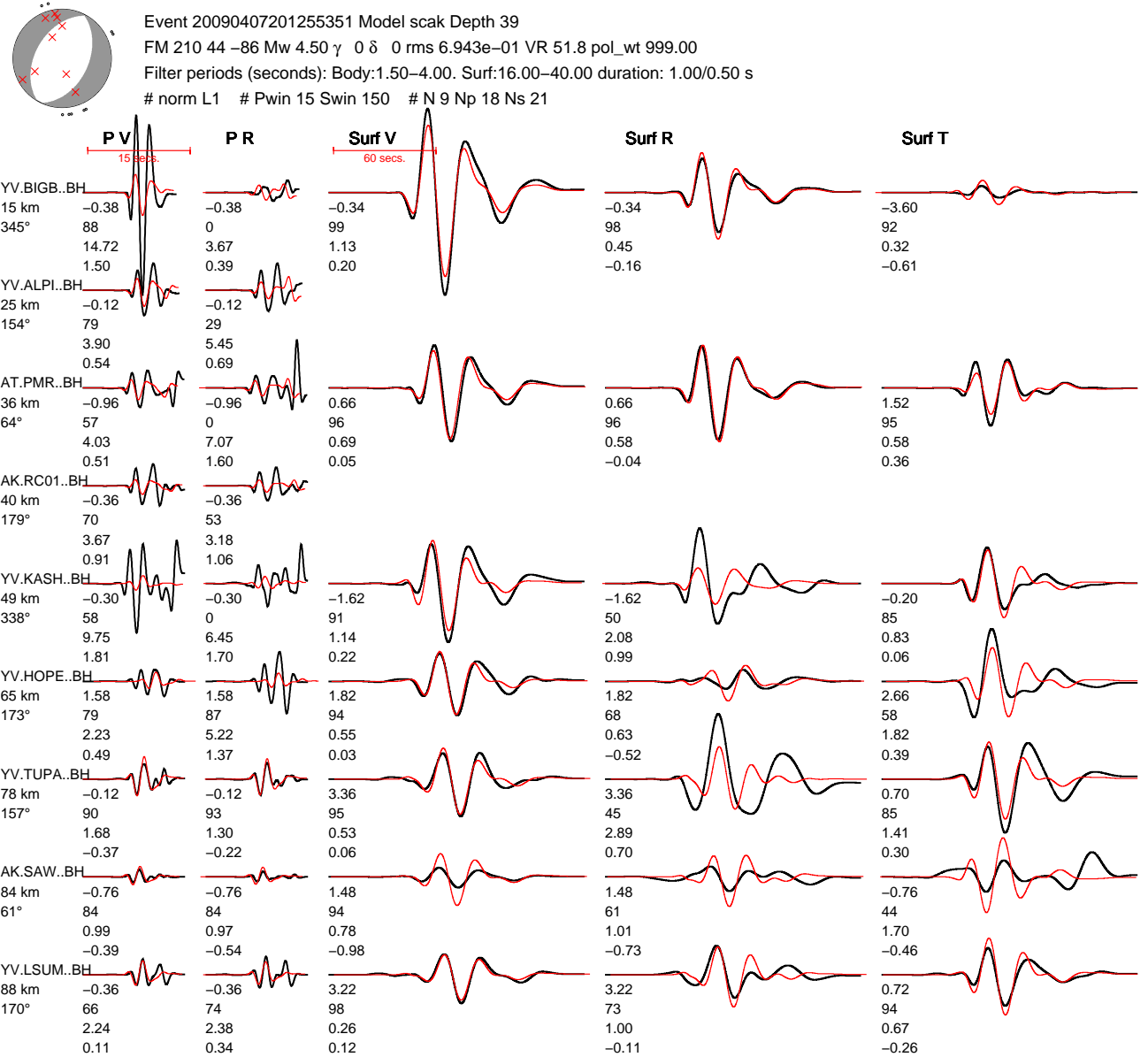


Figure B.3: Waveform fits when using 9 stations instead of fewer stations (Figure B.2). Here the VR is higher due to the station reward factor (Eq. B.3).

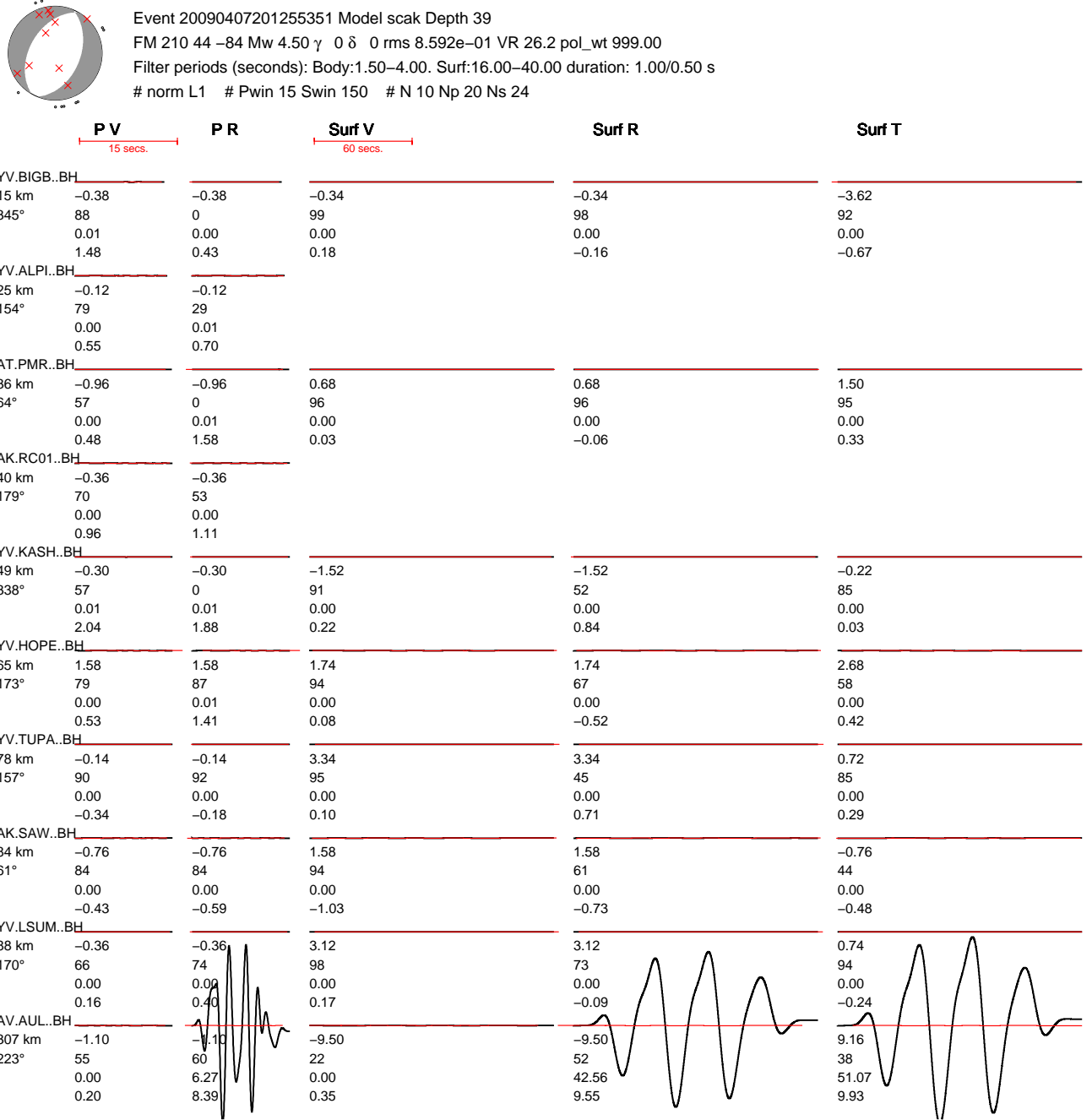


Figure B.4: Waveform fits when using 10 stations. There are more stations than in Figure B.3, which will lead to a lower value of $h(N_s)$ (greater reward). However, waveforms from the newly added station, AV.AUL, are clearly bad, which results in a VR that is lower than in Figure B.3, despite having more stations. The anomalous amplitude of AV.AUL causes the other waveforms not to be visible on this plotting scale; however, they are expected to be very similar to those in Figure B.3. Note that the best-fitting moment tensor is similar to what is obtained in Figure B.3; this is due to the use of an L1 misfit function that is insensitive to outliers.

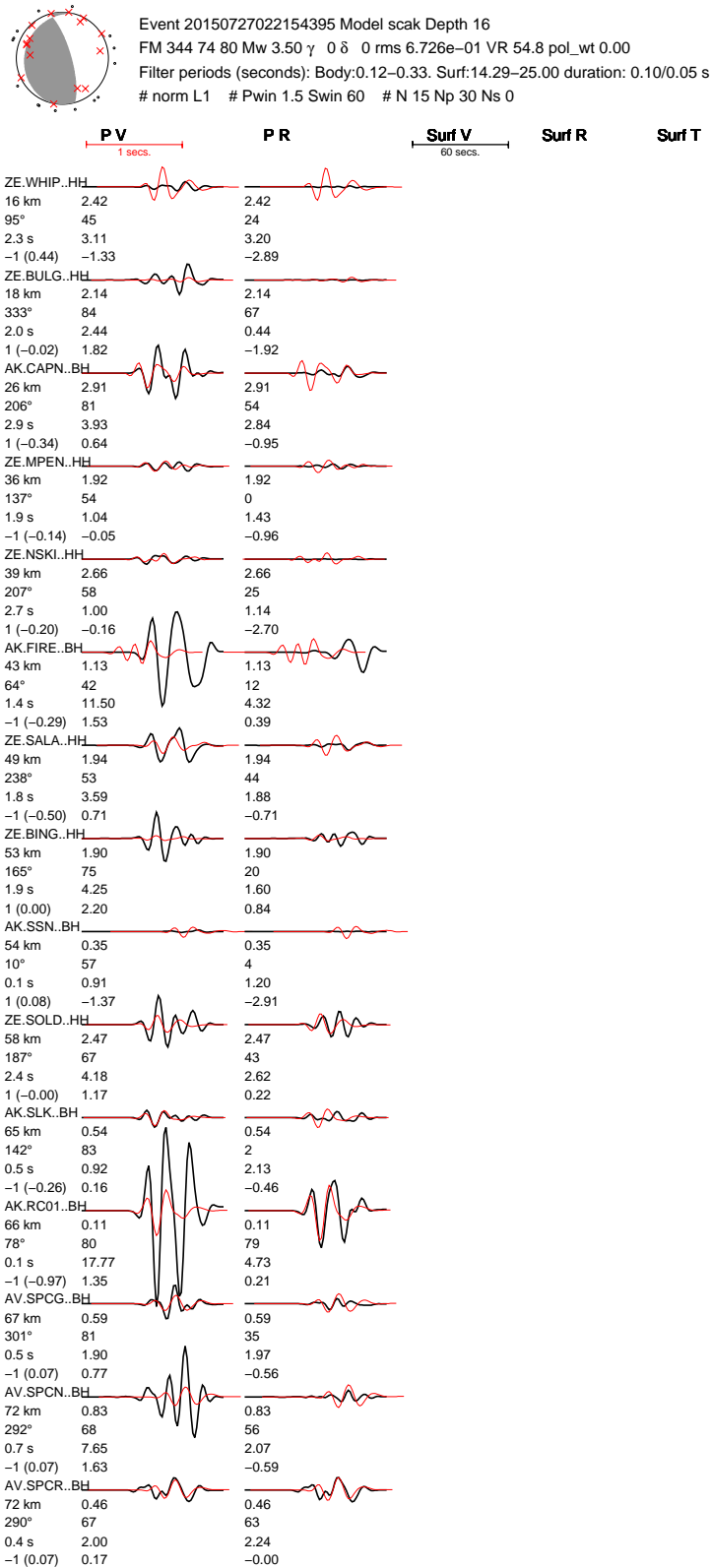


Figure B.5: Waveform fits using polarity weight $m = 0.0$. See Figure 3.10.

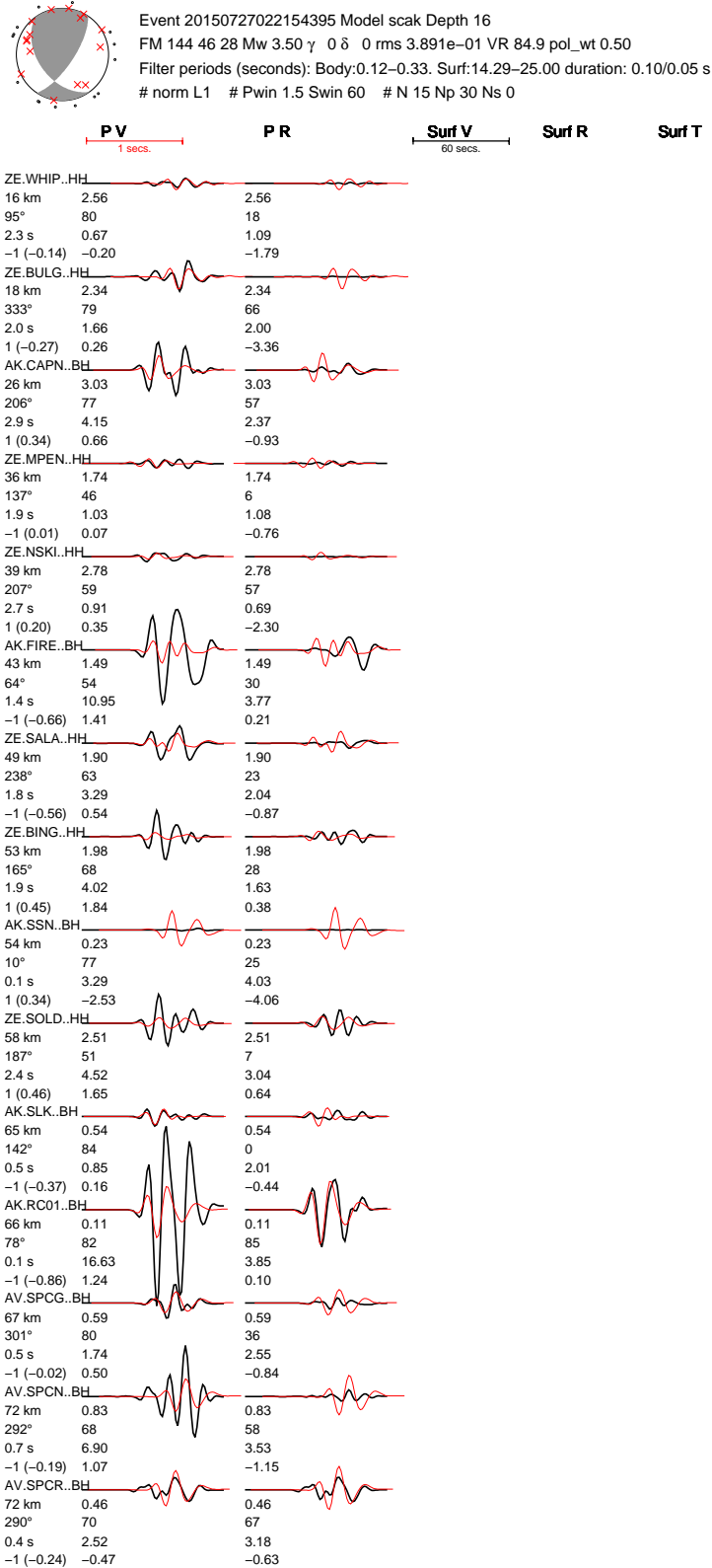


Figure B.6: Waveform fits using polarity weight $m = 0.5$. See Figure 3.10.

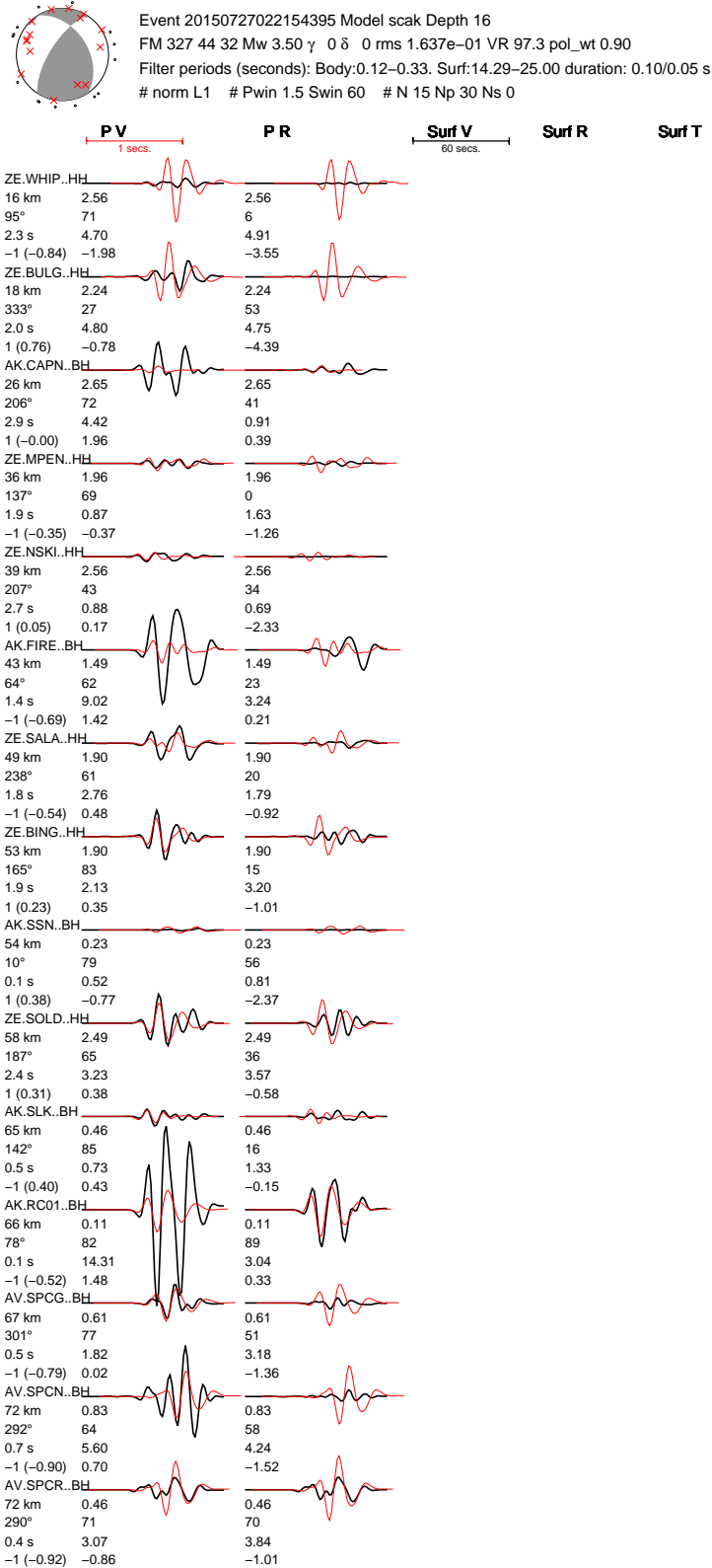


Figure B.7: Waveform fits using polarity weight $m = 0.9$. See Figure 3.10.

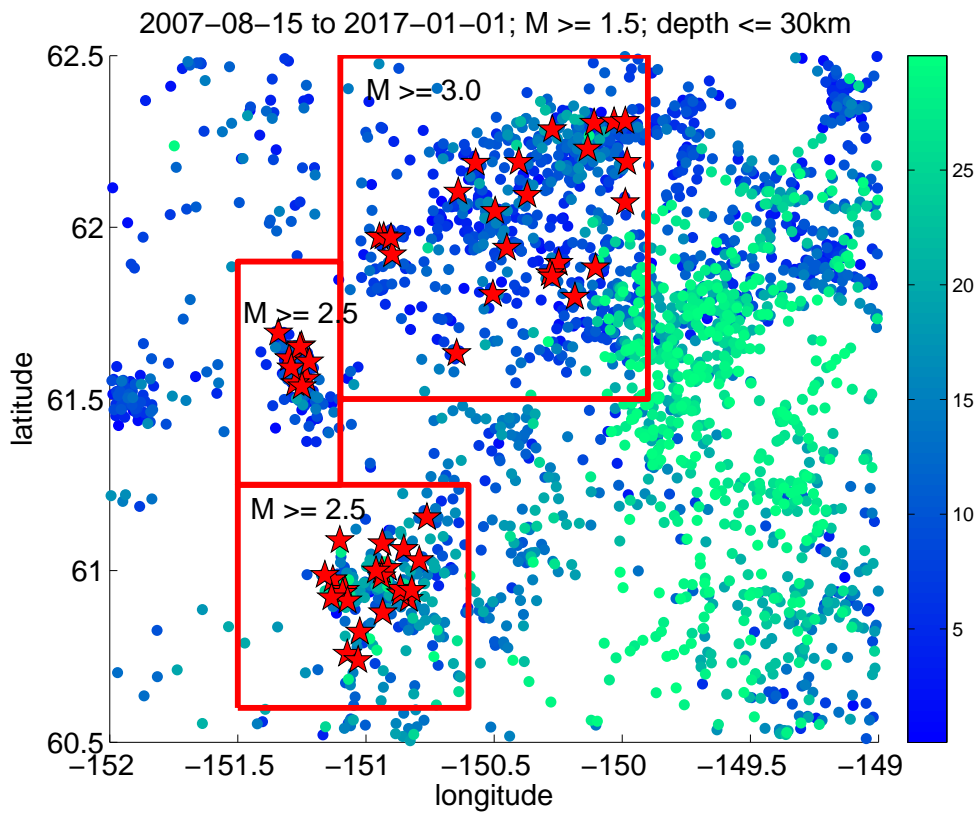
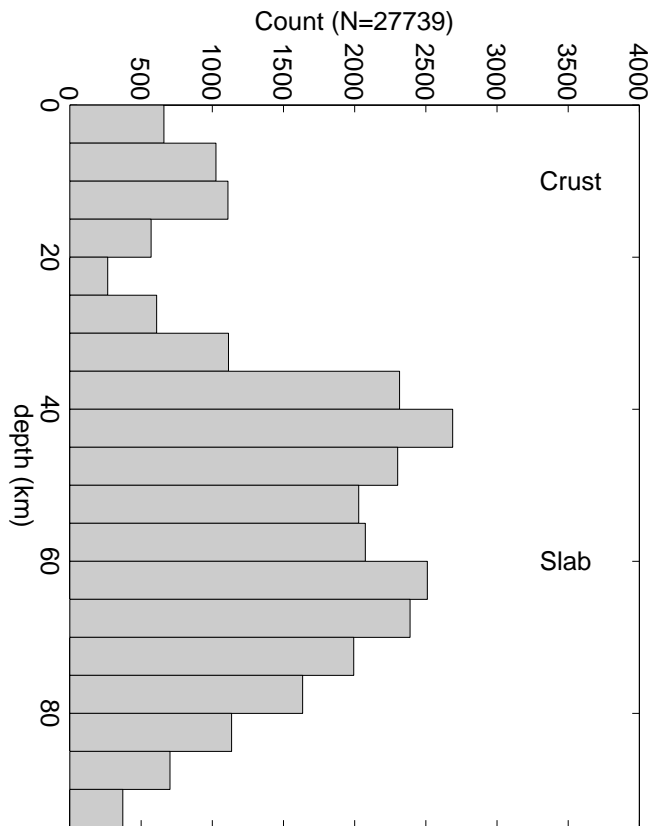


Figure B.8: Event selection for moment tensor inversion. AEC catalog with $M_l \geq 1.5$, depth ≤ 30 km, from 2007-08-15 to 2017-01-01. Events are colored by depth, with deeper events (green) plotted on top. Red stars are events that were selected for moment tensor inversion. See Table 3.1 for region-specific selection criteria.



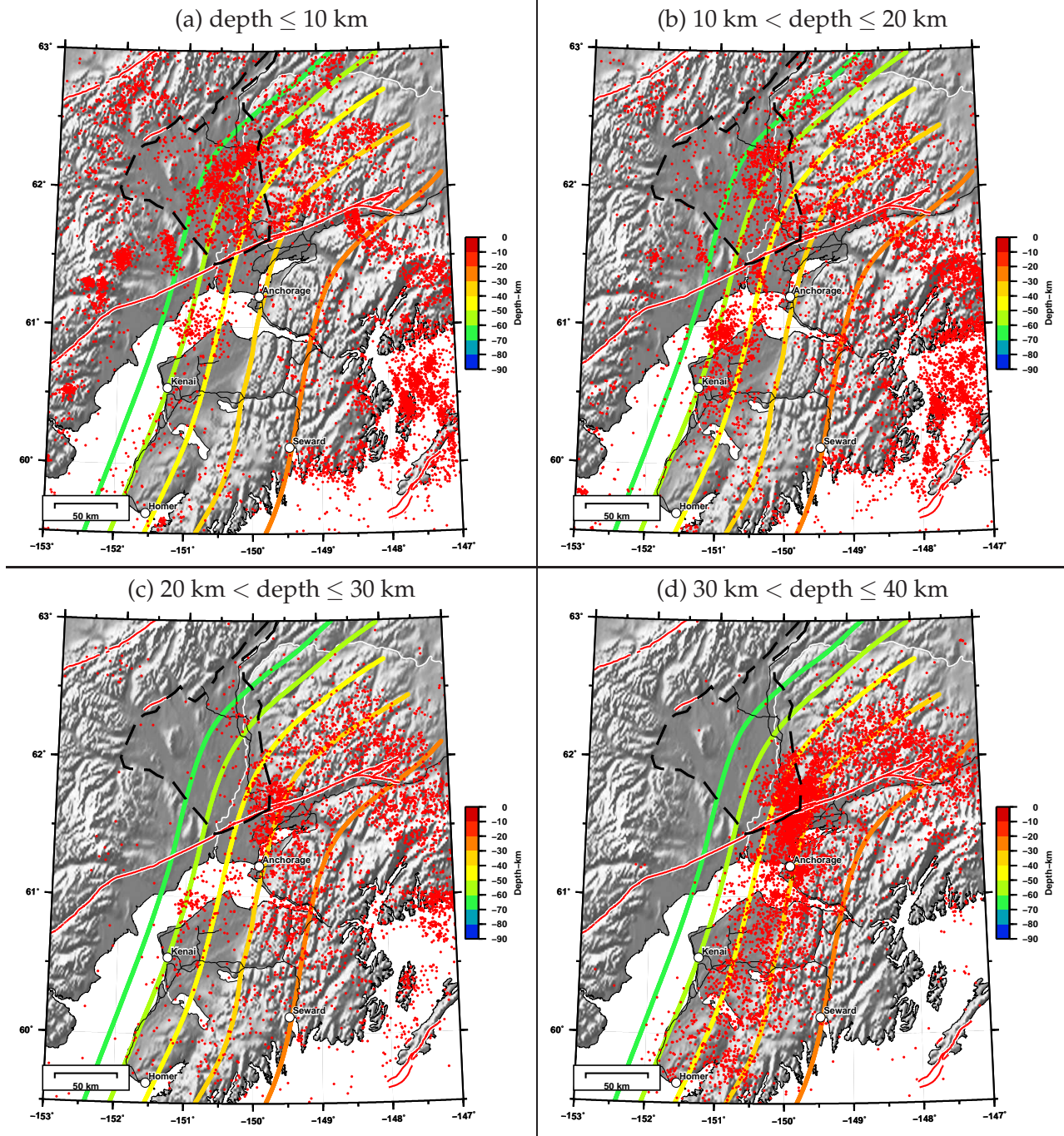


Figure B.10: Variation in seismicity with depth for events from 1990-01-01 to 2017-01-01 with magnitude $M_l \geq 1.5$. Earthquakes (in red) are for depth ranges (a) $\leq 10 \text{ km}$, (b) $10\text{--}20 \text{ km}$, (c) $20\text{--}30 \text{ km}$, and (d) $30\text{--}40 \text{ km}$. The colored contours are for the subduction interface (Li et al., 2013) at depths 30, 40, 50, 60, and 70 km. The black dashed line represents the boundary of Susitna basin (Kirschner, 1988).

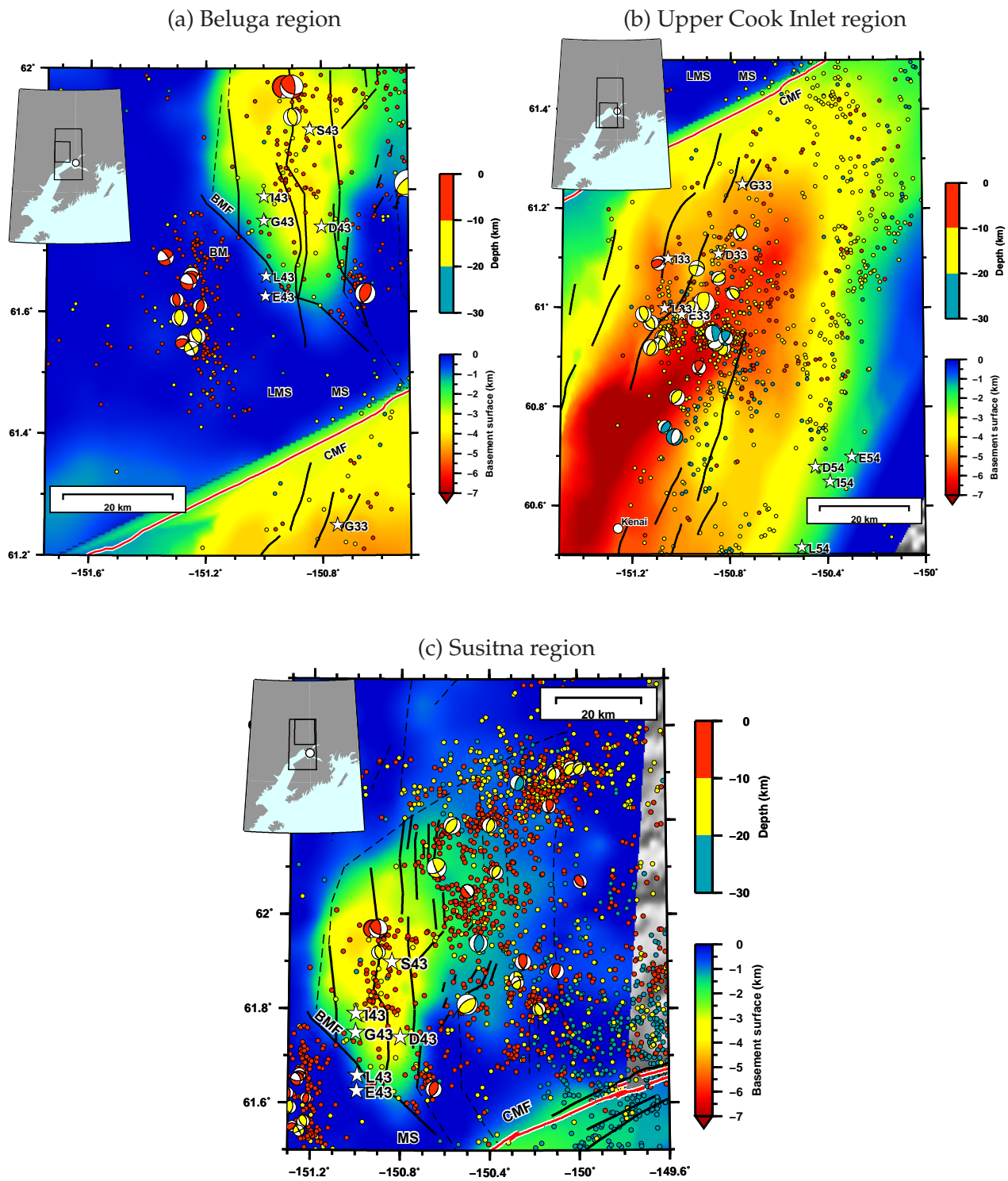


Figure B.11: Same as Figure 3.11, but plotted with an underlying basement surface instead of gray-shaded topography.

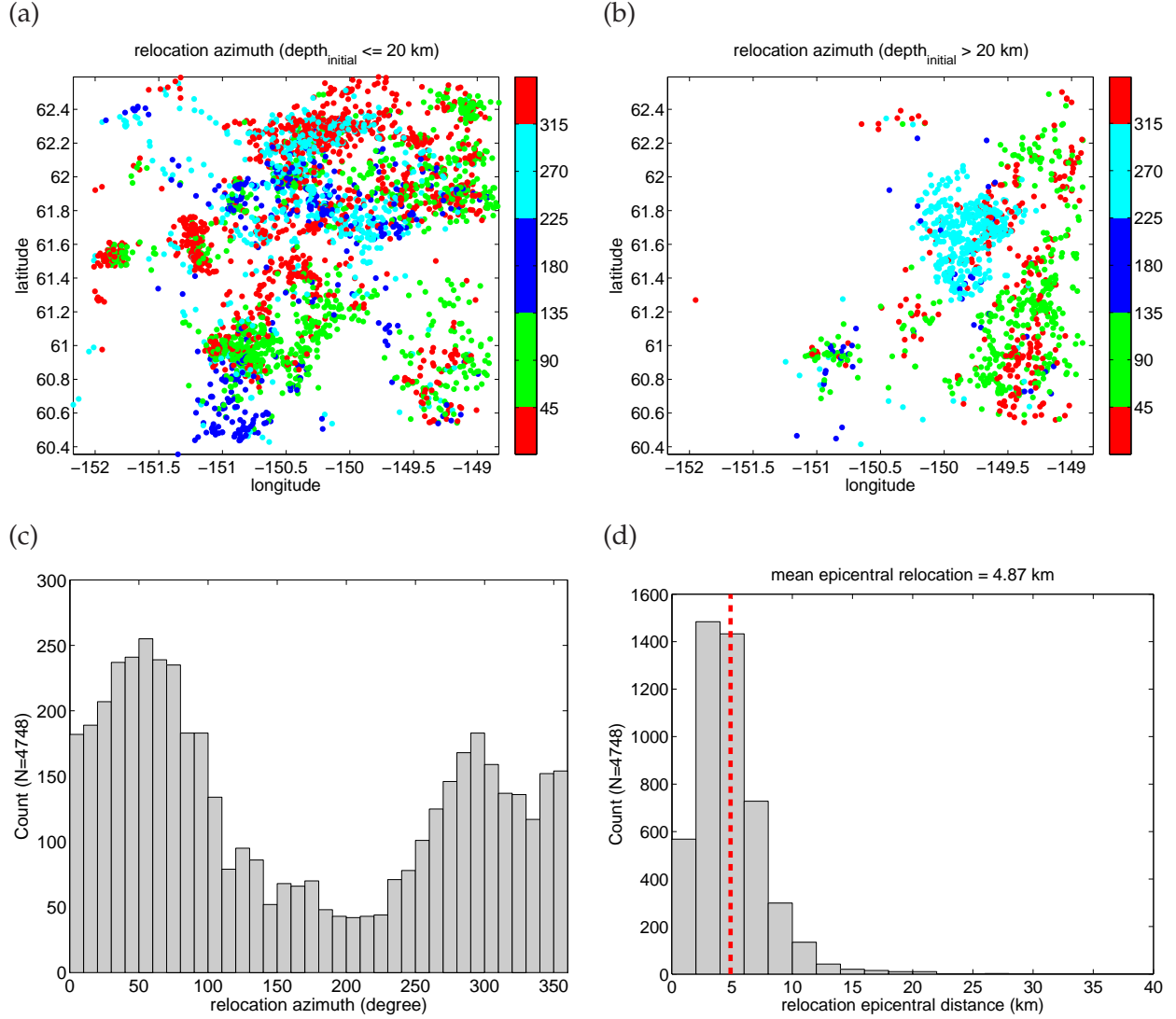


Figure B.12: Changes in epicenters due to relocation. (a) Map view representing the azimuth from the initial epicenters to the relocated epicenter for earthquakes $\leq 20 \text{ km}$. Red dots indicate relocations toward the north, dark blue toward the south, cyan toward the west, and green toward the east. (b) Same as (a) but for earthquakes $> 20 \text{ km}$. (c) Distribution of the azimuths from the initial epicenters to the relocated epicenters for all 4748 crustal earthquakes. (d) Distribution of horizontal distances between original and relocated epicenters; the mean difference is 4.87 km.

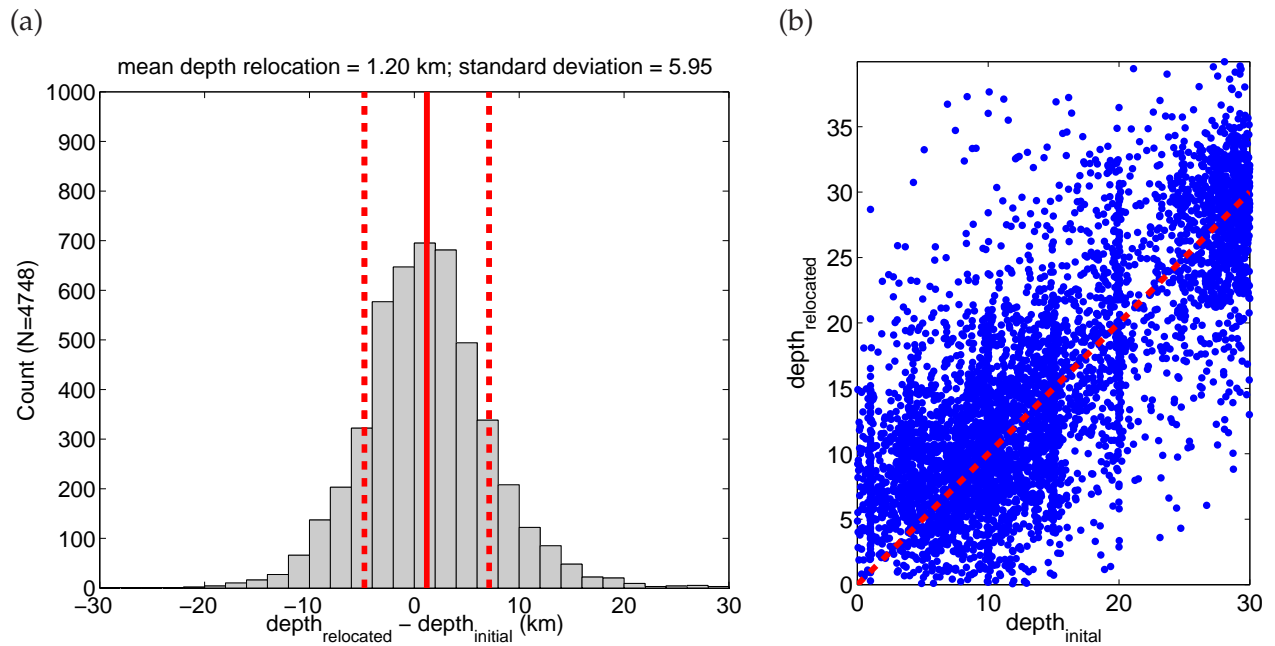


Figure B.13: Changes in depths due to relocation. (a) Distribution of changes in depth; the mean and standard deviation are 1.20 km and 5.95 km respectively. (b) Initial depth vs relocated depth. Red dashed line indicates that the relocated depth is same as the final depth. Points above the red dashed line represent events that are relocated to a deeper depth, whereas, for points below the line the events are relocated to a shallower depth.

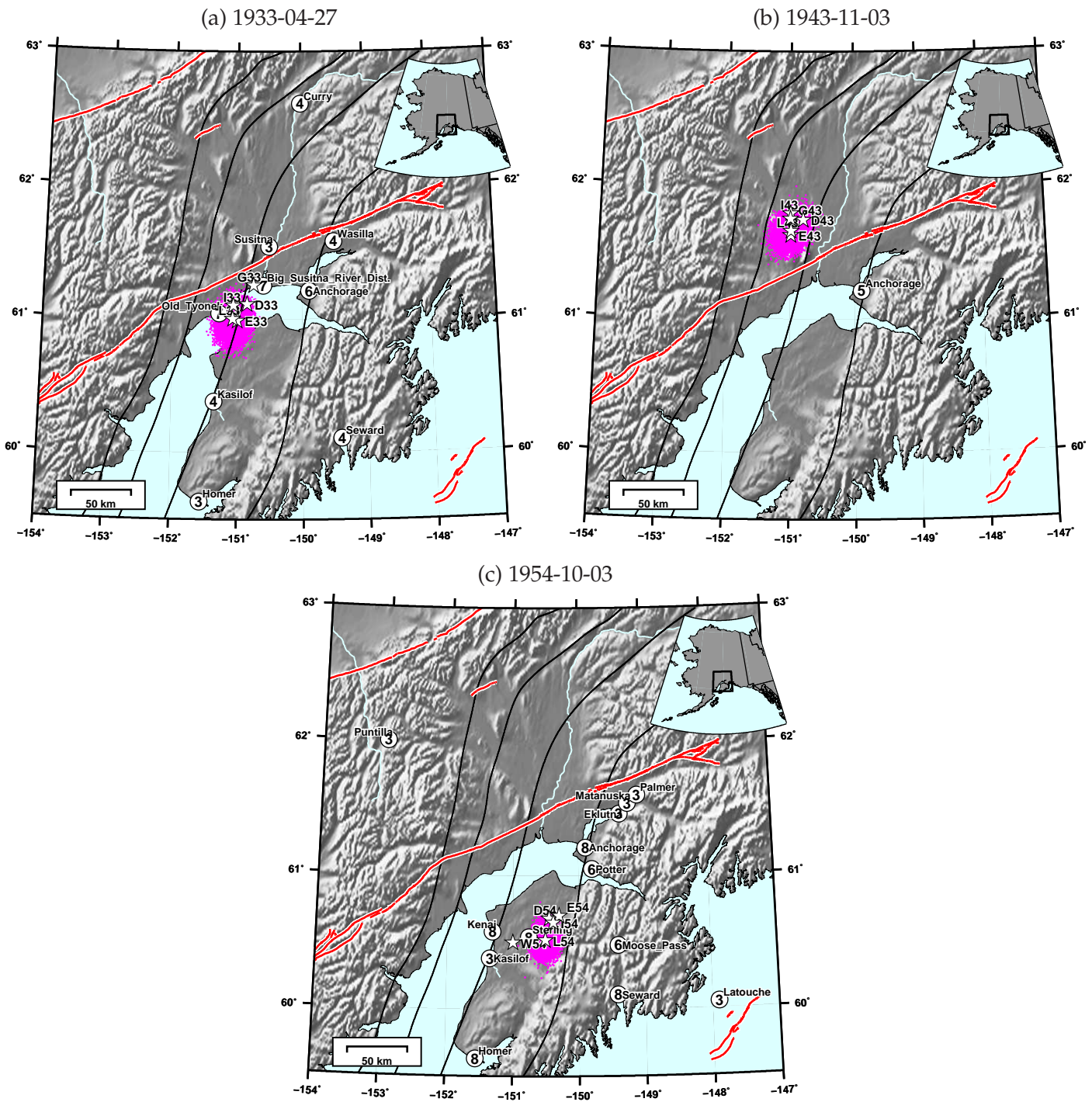


Figure B.14: Felt reports from Brockman et al. (1988) for the 1933, 1943, and 1954 earthquakes. Note that there are felt reports outside the plotted region for all three earthquakes, and there are felt reports that are not listed in Brockman et al. (1988) (e.g., Appendix 3.8). Also shown for each earthquake is the maximum likelihood epicenter (star) and epicenters of the posterior distribution obtained from NonLinLoc (Lomax et al., 2000). See Lomax et al. (2018) for results from other events in Table 3.2.

Appendix C

Supporting Information for Chapter 4 (Seismic wavefield simulations within a three-dimensional seismic velocity model for Alaska)

Overview

This supplement contains:

1. Table of the seismic networks used in this study
2. Tables of moment tensors for each of the three regions
3. Tables comparing resolvable period, time-step, and simulation time for different meshes and models
4. Figures illustrating event selection
5. Figures of the tomographic model of Eberhart-Phillips et al. (2006)
6. Figures related to topographic smoothing
7. Figures related to testing the presence of basin and the implementation of a minimum shear wavespeed
8. Figures showing the effect of smoothing the topography

Table C.1: Permanent (top) and temporary (bottom) seismic networks for which seismograms were extracted.

code	Networks	active period
AK	Alaska Regional network	
AT	National Tsunami Warning Center Alaska Seismic Network	
CN	Canadian National Seismic Network	
II	IRIS/IDA	
IU	IRIS/USGS	
US	US National Seismic Network	
TA	UArray Transportable Array	2016–2019
XE	BEAAR - Broadband Experiment Across Alaska Range	1999–2001
XR	ARCTIC - Alaska Receiving Cross Transect of the Inner Core	2004–2007
XZ	STEEP - St. Elias Erosion/Tectonics Project	2005–2012
YV	MOOS - Multidisiplinary Observations of Subduction	2007–2009
XV	FLATS	2014–2019
ZE	SALMON	2015–2017

Table C.2: Double couple moment tensor solutions for 20 earthquakes in the Cook Inlet mesh region.

	origin time	latitude	longitude	strike	dip	rake	M_w	depth (km)	# of stations
1	2007-11-28 23:57:03	61.91	-151.13	44	75	65	4.8	70.0	67
2	2008-03-14 09:38:21	61.07	-152.64	89	58	81	5.0	144.0	55
3	2008-09-12 19:50:39	62.15	-149.43	290	77	-30	4.1	44.0	39
4	2008-11-09 23:36:57	60.00	-153.02	63	53	56	4.4	127.0	30
5	2008-12-13 19:55:44	60.89	-150.86	26	80	63	4.1	46.0	47
6	2009-01-24 18:09:50	59.43	-152.89	71	64	38	5.6	98.0	27
7	2009-04-07 20:12:55	61.45	-149.74	218	49	-81	4.5	34.0	20
8	2009-06-22 19:28:05	61.94	-150.70	25	51	-23	5.4	65.0	50
9	2012-12-04 01:42:48	61.24	-150.77	92	36	38	5.6	64.0	69
10	2014-05-05 04:59:44	60.65	-149.56	80	71	-61	4.4	38.0	79
11	2014-05-10 14:16:10	60.01	-152.13	247	40	54	5.7	89.0	47
12	2014-09-25 17:51:17	61.94	-151.82	47	68	17	6.3	109.0	74
13	2014-09-27 03:53:11	62.01	-149.82	173	66	-77	4.7	47.0	97
14	2014-11-29 21:06:48	62.54	-148.06	123	62	-21	4.6	62.0	105
15	2015-06-24 22:32:21	61.66	-151.96	90	40	68	5.8	114.0	82
16	2016-01-18 04:05:56	62.10	-150.64	154	77	28	4.4	10.0	137
17	2016-01-24 10:30:29	59.62	-153.34	63	64	44	7.1	126.0	47
18	2017-03-02 02:11:30	59.58	-152.65	52	54	37	5.3	78.0	65
19	2017-05-07 04:25:19	60.18	-151.68	50	63	16	5.1	67.0	75
20	2017-05-30 02:18:45	60.83	-151.82	194	72	-81	5.1	81.0	115

Table C.3: Double couple moment tensor solutions for 20 earthquakes in the Interior mesh region.

	origin time	latitude	longitude	strike	dip	rake	M_w	depth (km)	# of stations
1	2000-09-01 05:04:40	63.19	-150.53	13	78	-62	4.8	137.0	32
2	2000-11-09 16:25:15	64.69	-152.23	288	64	9	4.5	34.0	20
3	2000-11-29 10:35:47	63.90	-150.35	107	82	31	5.5	16.0	17
4	2001-03-25 11:34:50	64.63	-149.25	130	75	-33	4.3	22.0	15
5	2001-06-04 18:42:36	64.70	-152.40	295	72	17	5.0	23.0	16
6	2001-06-07 06:28:32	66.01	-150.79	127	51	28	4.1	10.0	20
7	2001-06-19 12:42:09	64.00	-147.41	288	82	-41	4.0	5.0	17
8	2009-09-20 11:57:39	63.65	-149.90	75	76	-12	4.2	144.0	40
9	2013-02-26 09:32:18	64.10	-149.31	210	32	-72	4.7	139.0	53
10	2013-05-25 08:29:29	66.28	-149.56	202	81	17	4.3	12.0	32
11	2014-06-20 01:06:22	63.13	-149.31	112	74	30	4.3	82.0	78
12	2014-06-29 06:58:43	63.46	-148.56	233	78	81	4.2	7.0	39
13	2014-08-31 03:06:57	65.15	-149.04	200	73	-16	5.0	17.0	51
14	2015-05-11 09:25:42	63.08	-148.25	126	78	5	4.5	67.0	95
15	2016-05-15 05:51:00	63.08	-150.95	55	59	70	5.3	132.0	103
16	2016-05-18 03:25:48	65.25	-151.07	352	51	-7	4.2	15.0	75
17	2016-07-11 20:05:57	63.81	-149.23	103	43	51	4.2	123.0	138
18	2017-04-29 11:15:48	63.12	-151.17	319	31	13	4.8	12.0	139
19	2017-09-21 22:15:20	62.78	-148.88	194	57	56	4.1	20.0	67
20	2017-12-30 11:43:16	63.80	-149.02	47	62	28	4.0	7.0	140

Table C.4: Double couple moment tensor solutions for 20 earthquakes in the Wrangell mesh region.

	origin time	latitude	longitude	strike	dip	rake	M_w	depth (km)	# of stations
1	2007-09-19 11:22:26	61.38	-146.11	227	63	-85	4.4	31.0	67
2	2007-10-10 18:03:26	59.96	-147.41	213	86	-13	4.0	12.0	71
3	2008-08-05 19:48:07	61.54	-141.37	139	84	50	3.8	11.0	42
4	2008-10-08 09:53:01	60.71	-143.72	191	50	-17	4.9	8.0	54
5	2009-02-15 19:35:00	61.60	-146.33	85	40	-54	4.4	37.0	52
6	2009-02-24 16:20:23	62.88	-143.80	346	67	-29	3.9	6.0	55
7	2009-07-25 07:46:07	61.36	-147.42	66	37	-42	4.0	23.0	54
8	2010-02-25 14:01:18	61.92	-141.47	103	73	-75	3.9	8.0	36
9	2010-06-20 17:28:08	60.78	-146.81	188	73	-77	4.5	11.0	51
10	2010-09-05 10:41:26	63.35	-145.09	248	88	76	4.2	3.0	44
11	2011-08-03 06:08:37	62.11	-141.28	58	86	15	4.2	13.0	44
12	2011-12-09 01:25:42	62.25	-145.65	100	28	57	4.5	16.0	62
13	2012-10-31 02:57:43	62.05	-146.55	240	73	7	4.1	42.0	61
14	2012-12-25 03:43:32	61.30	-147.44	59	37	-73	4.3	37.0	70
15	2013-07-14 08:15:15	61.57	-141.08	250	49	58	4.3	8.0	52
16	2014-09-24 07:30:57	61.35	-146.78	26	30	-81	4.3	27.0	102
17	2016-08-19 17:36:28	61.60	-146.34	48	74	-67	4.2	23.0	161
18	2017-02-13 07:17:12	62.51	-142.75	231	81	5	5.2	8.0	121
19	2017-11-13 16:00:37	60.56	-142.66	264	8	78	4.3	20.0	104
20	2017-11-27 22:18:30	60.56	-147.43	211	73	-70	5.1	17.0	138

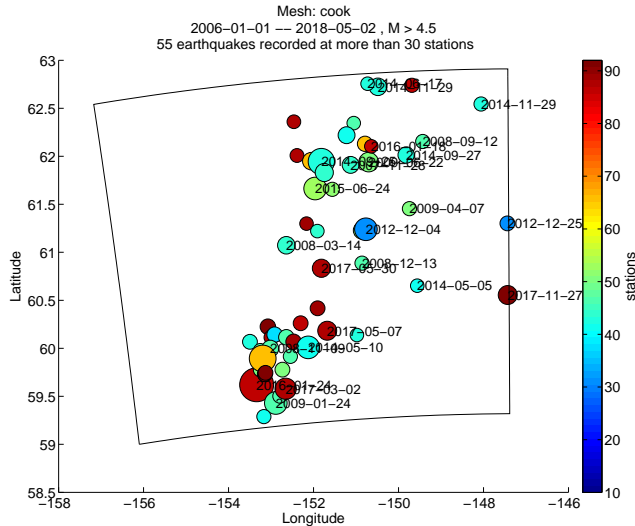
Table C.5: Expected and actual minimum resolvable periods for various mesh and model combinations. The effect of model is documented in two ways: (1) embedding a low-velocity basin into the 3D model, and (2) applying a velocity threshold ($vsmin = 1000$ m/s). Also shown is the actual usable time step that is systematically lower than the theoretically expected time step.

region	basin	smoothed topo	vsmin (m/s)	minimum res. period (s)		time-step, dt (s)			
						NGLL5		NGLL7	
				expected	actual	actual	expected	actual	expected
cook	No	No	822.5	6.4	3.5	0.015	0.0164	0.007	0.0080
cook	Yes	No	778.9	6.4	4.0	0.015	0.0164	0.007	0.0080
cook	Yes	No	1000.0	6.4	4.0	0.015	0.0164	0.007	0.0080
cook	No	Yes	822.5	6.4	4.0	0.015	0.0164	0.007	0.0081
cook	No	Yes	1000.0	6.4	4.0	0.015	0.0164	0.007	0.0081
cook	Yes	Yes	778.9	6.4	4.0	0.015	0.0164	0.007	0.0081
cook	Yes	Yes	1000.0	6.4	4.0	0.015	0.0164	0.007	0.0081
interior	No	No	1620.0	5.9	2.0	0.015	0.0168	0.007	0.0083
interior	No	No	1000.0	5.9	2.0	0.015	0.0168	0.007	0.0083
interior	Yes	No	655.4	5.9	2.0	0.015	0.0168	0.007	0.0083
interior	Yes	No	1000.0	5.9	2.0	0.015	0.0168	0.007	0.0083
interior	No	Yes	1620.0	5.9	2.0	0.015	0.0168	0.007	0.0083
interior	No	Yes	1000.0	5.9	2.0	0.015	0.0168	0.007	0.0083
interior	Yes	Yes	655.4	5.9	2.0	0.015	0.0168	0.007	0.0083
interior	Yes	Yes	1000.0	5.9	2.0	0.015	0.0168	0.007	0.0083
wrangell	No	No	822.8	6.3	2.0	0.014	0.0162	0.006	0.0080
wrangell	No	No	1000.0	6.3	1.5	0.014	0.0162	0.006	0.0080
wrangell	No	Yes	822.8	6.0	2.5	0.015	0.0164	0.007	0.0081
wrangell	No	Yes	1000.0	6.0	2.0	0.015	0.0164	0.007	0.0081

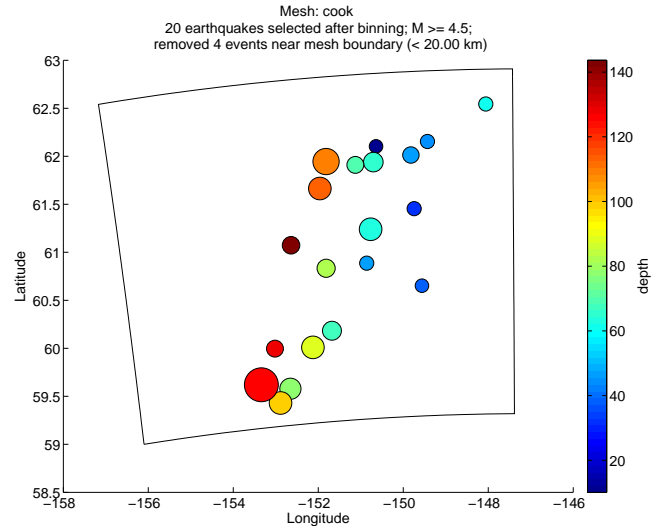
Table C.6: Comparison of computational costs for various meshes and models.

region	basin	smoothed topo	vsmin (m/s)	cores	NGLL5			NGLL7		
					DT (s)	NSTEP	simulation time hh:mm:ss	DT (s)	NSTEP	simulation time hh:mm:ss
cook	No	No	822.5	72	0.015	20000	00:32:54	0.007	43000	04:28:15
cook	No	No	1000	72	0.015	20000	00:38:42	0.007	43000	04:20:58
cook	Yes	No	778.9	72	0.015	20000	00:33:14	0.007	43000	04:19:49
cook	Yes	No	1000	72	0.015	20000	00:38:35	0.007	43000	04:19:26
cook	No	Yes	822.5	72	0.015	20000	00:33:29	0.007	43000	04:26:49
cook	No	Yes	1000	72	0.015	20000	00:39:05	0.007	43000	04:28:40
cook	Yes	Yes	778.9	72	0.015	20000	00:34:52	0.007	43000	04:24:21
cook	Yes	Yes	1000	72	0.015	20000	00:39:05	0.007	43000	04:03:11
interior	No	No	1620	72	0.015	20000	00:33:21	0.007	43000	04:22:32
interior	No	No	1000	72	0.015	20000	00:33:19	0.007	43000	04:00:56
interior	Yes	No	655.4	72	0.015	20000	00:33:32	0.007	43000	04:24:44
interior	Yes	No	1000	72	0.015	20000	00:33:19	0.007	43000	04:24:34
interior	No	Yes	1620	72	0.015	20000	00:33:45	0.007	43000	04:26:13
interior	No	Yes	1000	72	0.015	20000	00:33:14	0.007	43000	04:24:35
interior	Yes	Yes	655.4	72	0.015	20000	00:38:58	0.007	43000	03:51:04
interior	Yes	Yes	1000	72	0.015	20000	00:32:55	0.007	43000	04:25:54
wrangell	No	No	822.8	72	0.014	20000	00:38:44	0.006	50000	05:05:49
wrangell	No	No	1000	72	0.014	20000	00:38:10	0.006	43000	04:22:37
wrangell	No	Yes	822.8	72	0.015	20000	00:39:26	0.007	43000	04:02:07
wrangell	No	Yes	1000	72	0.015	20000	00:39:30	0.007	43000	04:26:25

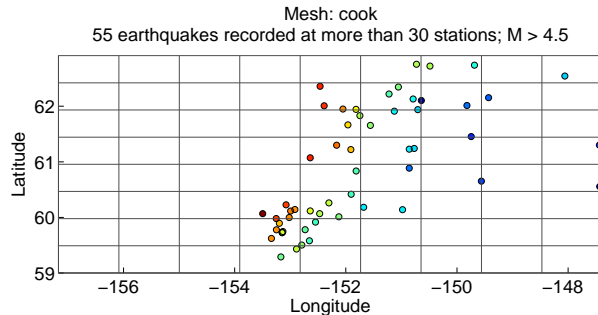
(a)



(b)



(c)



(d)

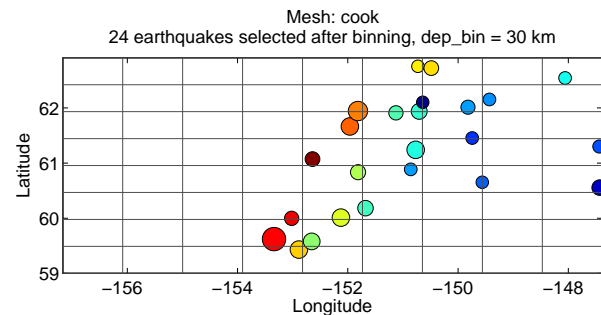


Figure C.1: Event selection for simulation in Cook Inlet mesh. The selection workflow goes from (a)→(c)→(d)→(b). (a) All significant events ($M_w > 4.5$), 2007-01-01–2018-05-02, that are recorded are more than 30 stations. The circle are scaled by the size of the earthquake, and color represents the number of stations at which it is recorded. (c) Same as figure (a) but plotted in bins ($nx=9$, $ny=8$) for declustering. Only one event from each bin is selected. The depth cut of the bins is at 30 km ($nz=2$), so that we can select both the crustal and deep events. In this and all other subplots, the color represents the depth of the earthquake. (d) Selected earthquakes after declustering. (b) Final set of events selected after removing events that are closer than 20 km from the mesh boundary. See Figure C.3 and Figure C.2 for events selection in Wrangell and Interior mesh.

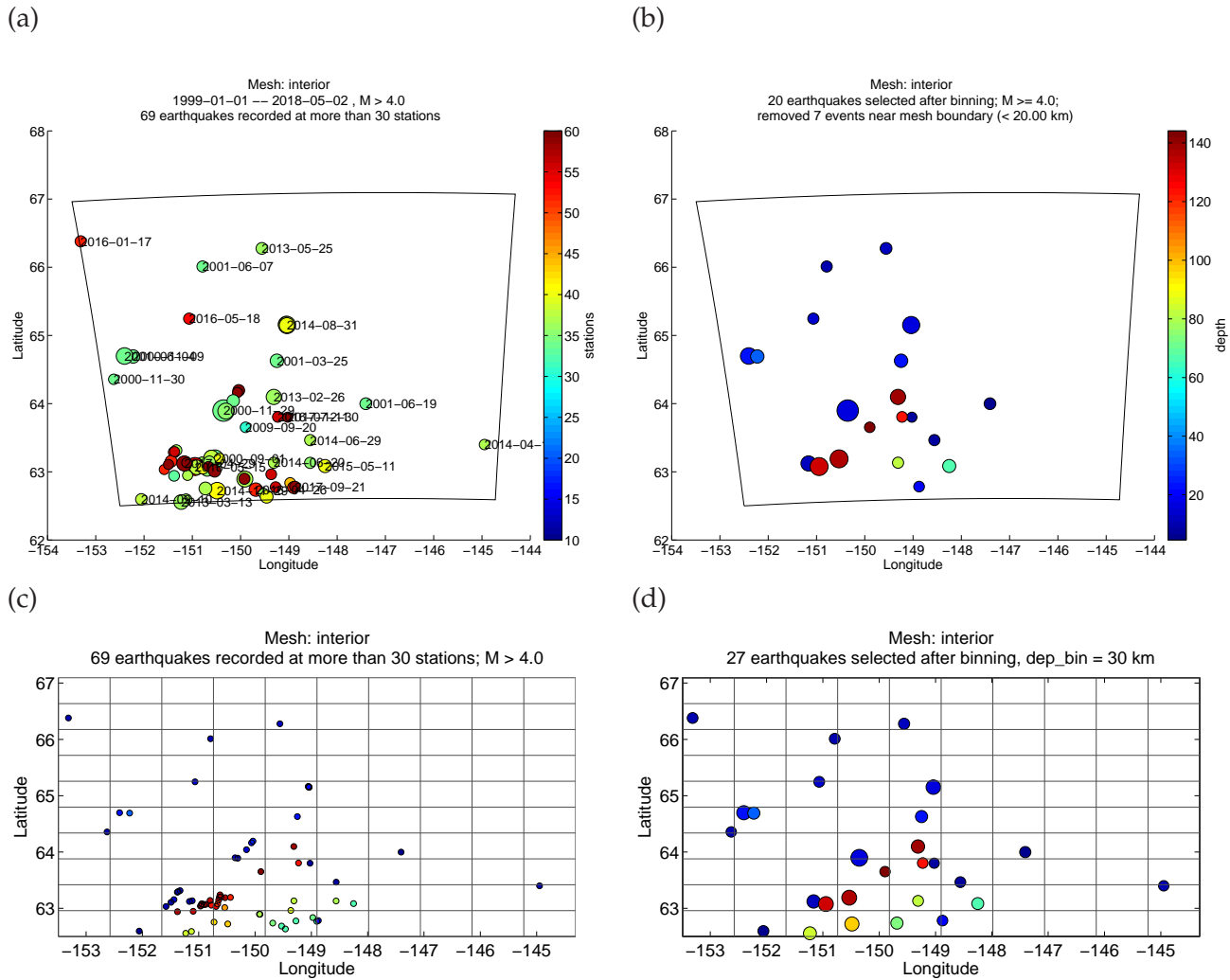
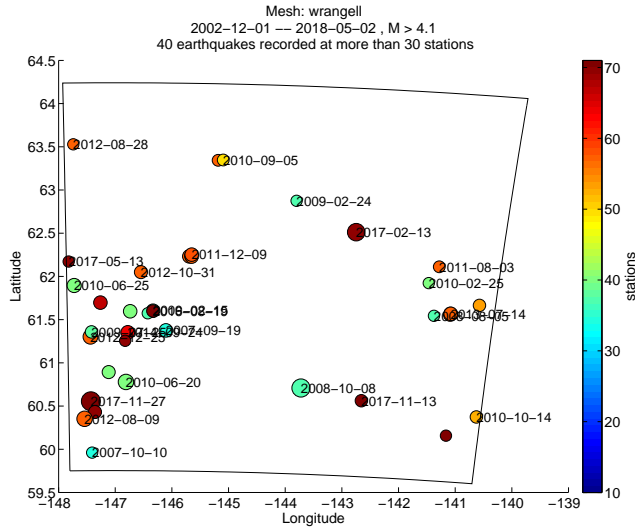
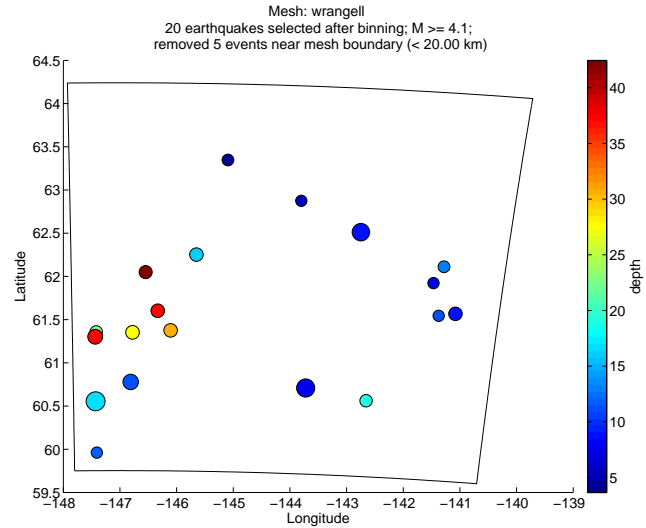


Figure C.2: Event selection for simulation in the Interior mesh. See Figure C.1 caption for details.

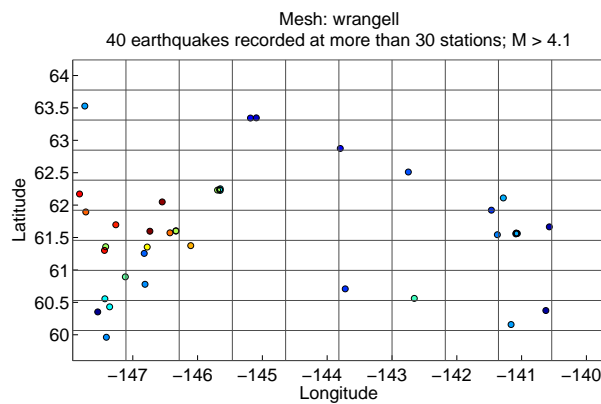
(a)



(b)



(c)



(d)

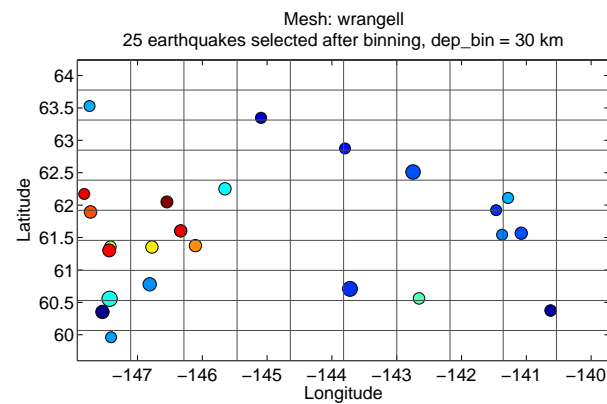


Figure C.3: Event selection for simulation in Wrangell mesh. See Figure C.1 caption for details.

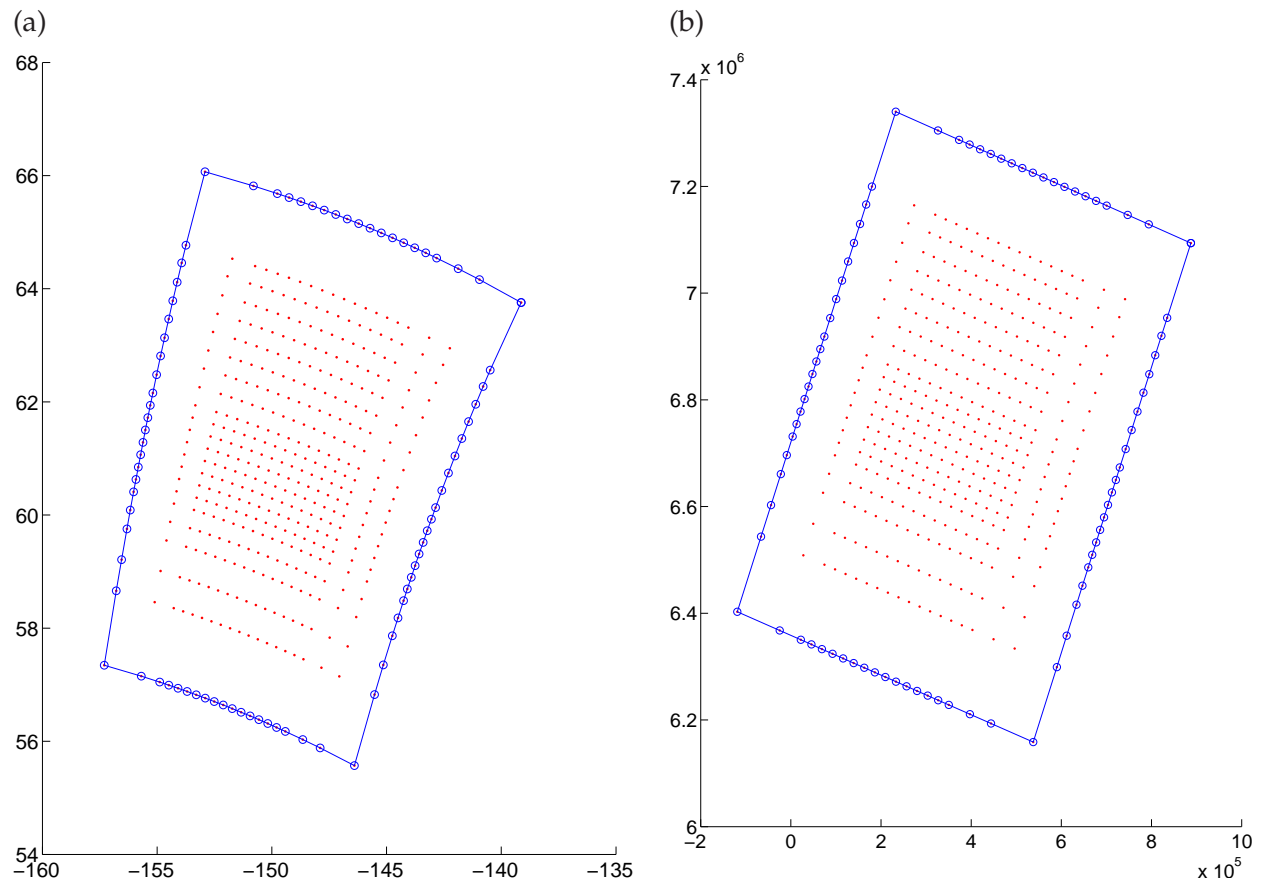


Figure C.4: Gridpoint nodes used for the tomographic inversion by Eberhart-Phillips et al. (2006).
 (a) Nodes plotted in longitude-latitude coordinates. (b) Nodes plotted in Alaska State Plane Coordinates. See Figure C.6 to Figure C.12 for Vp and Vs velocity at the nodes.

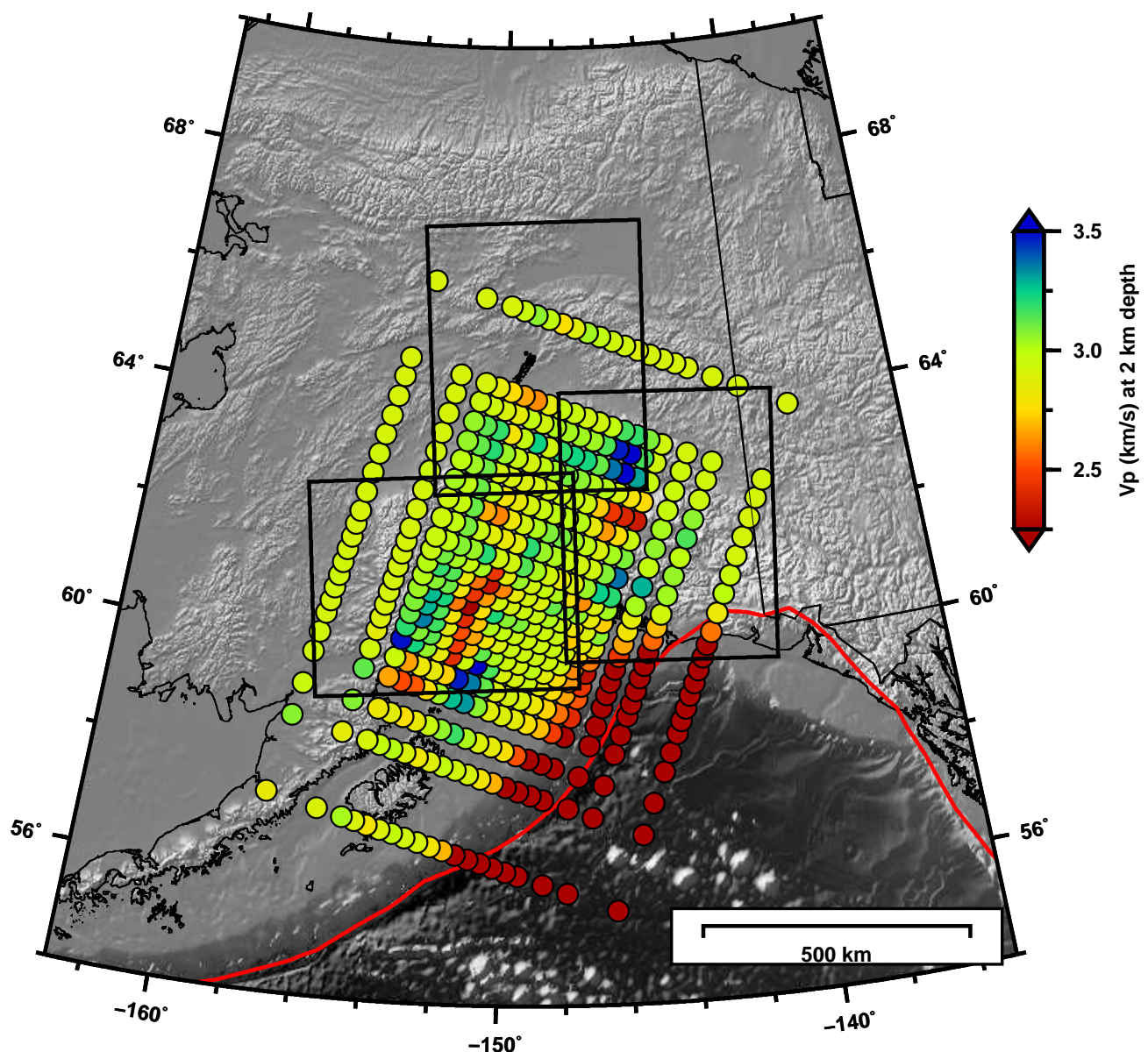


Figure C.5: V_p velocity at E2006 nodes (Eberhart-Phillips et al., 2006) at depth = 2 km below the sea level. Black boxes represent the three simulation regions.

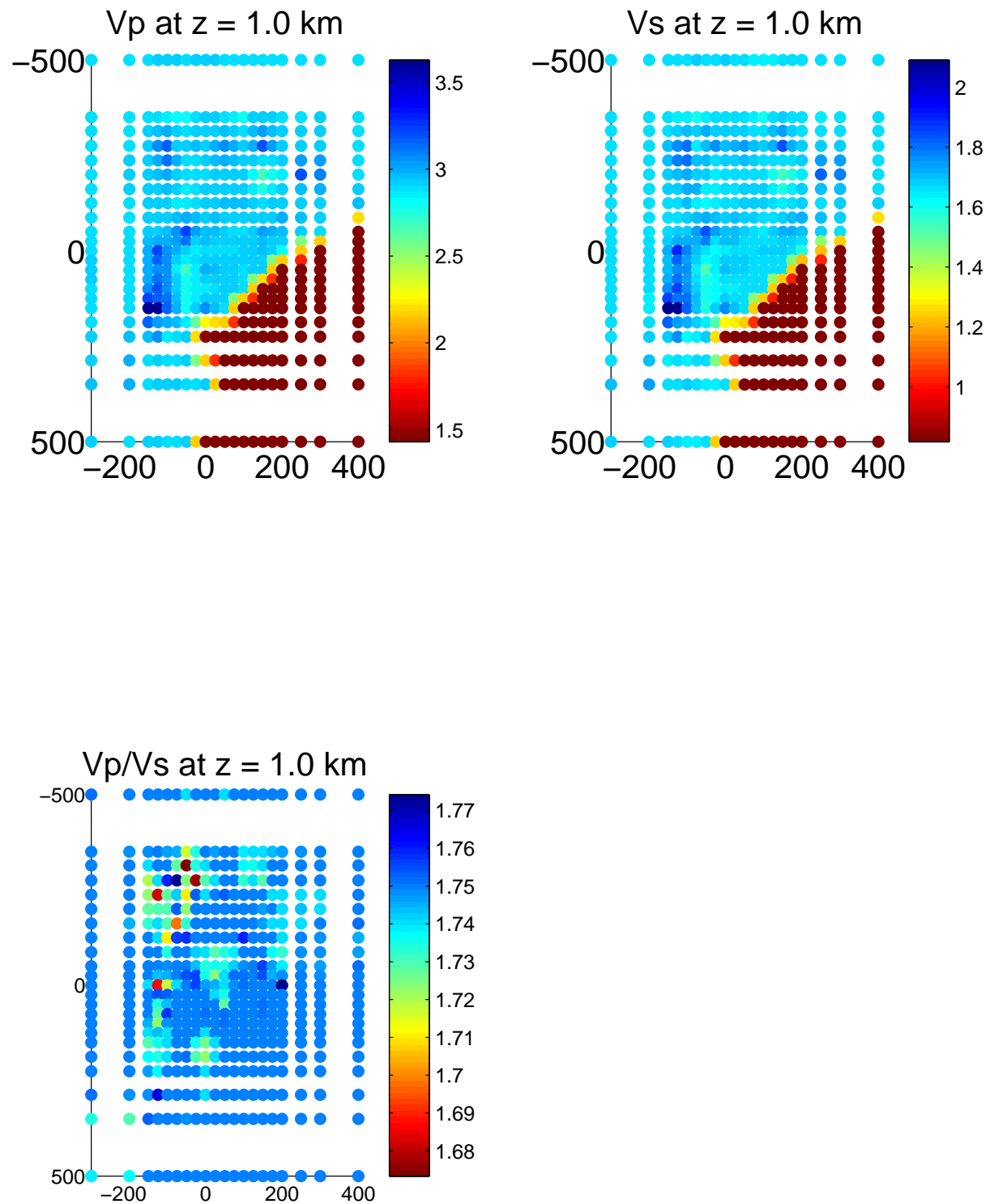


Figure C.6: V_p and V_s at E2006 nodes in layer 1, depth = 1 km above the sea level.

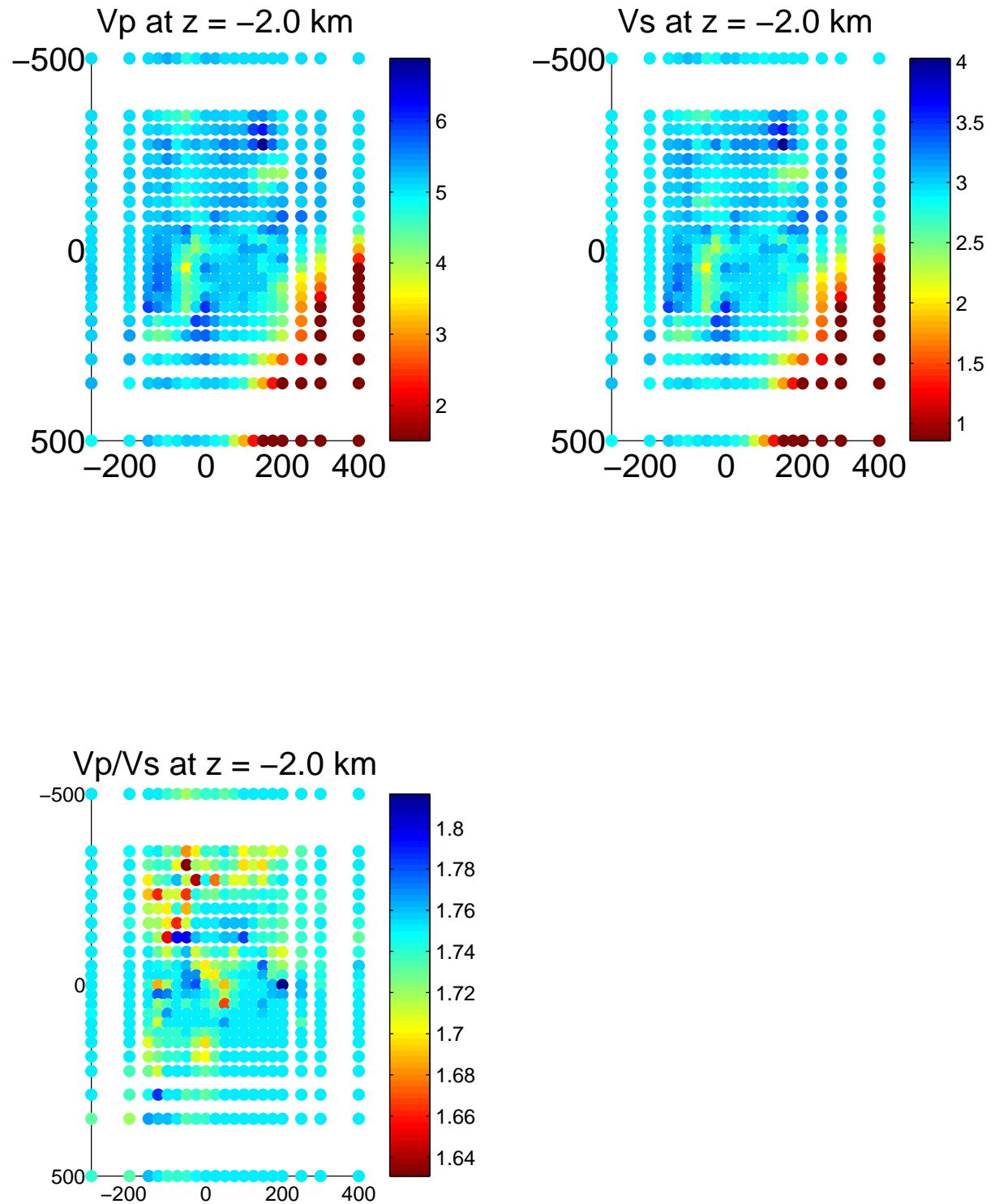


Figure C.7: Vp and Vs at E2006 nodes in layer 2, depth = 2 km below the sea level.

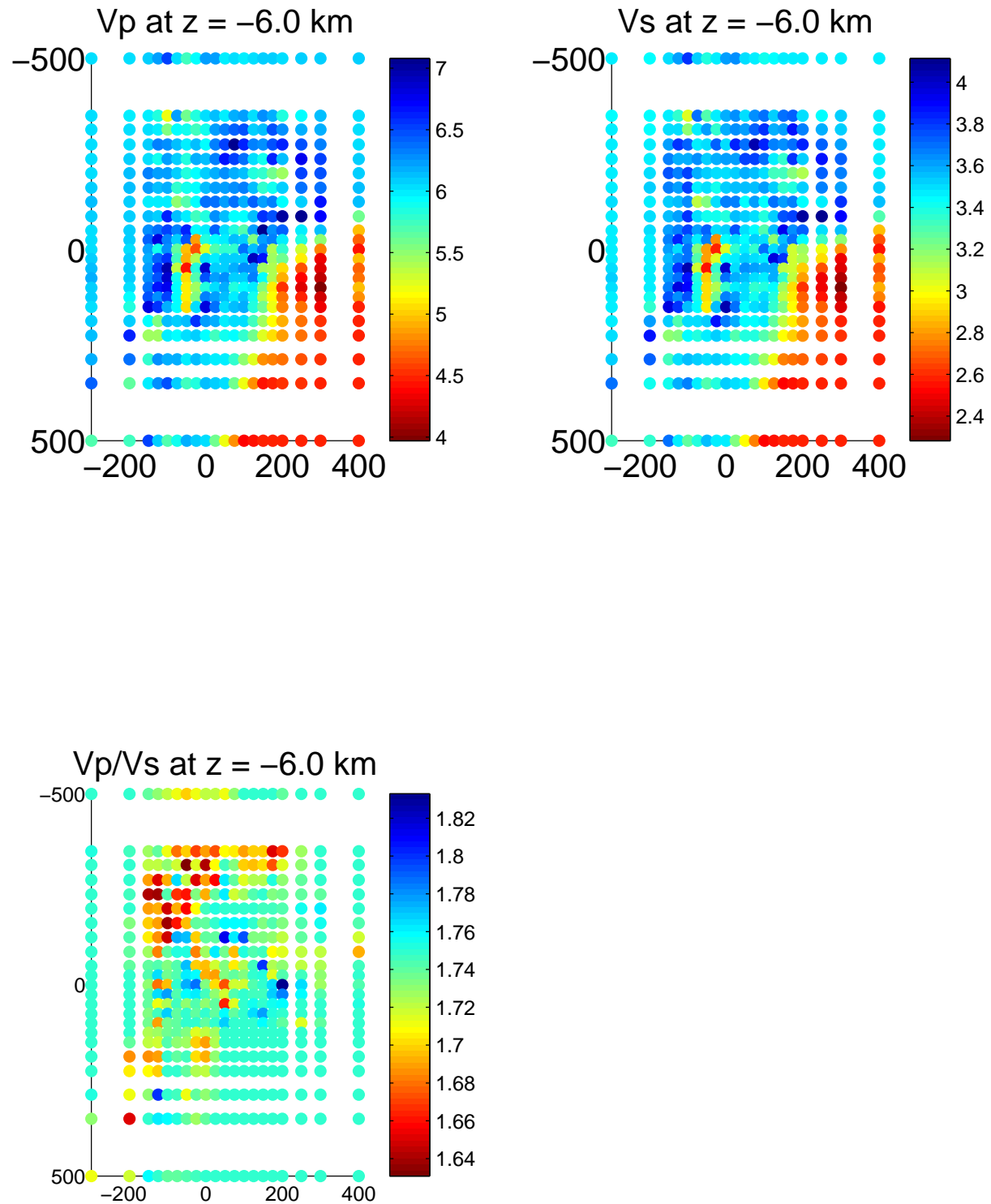


Figure C.8: V_p and V_s at E2006 nodes in layer 3, depth = 6 km below the sea level.

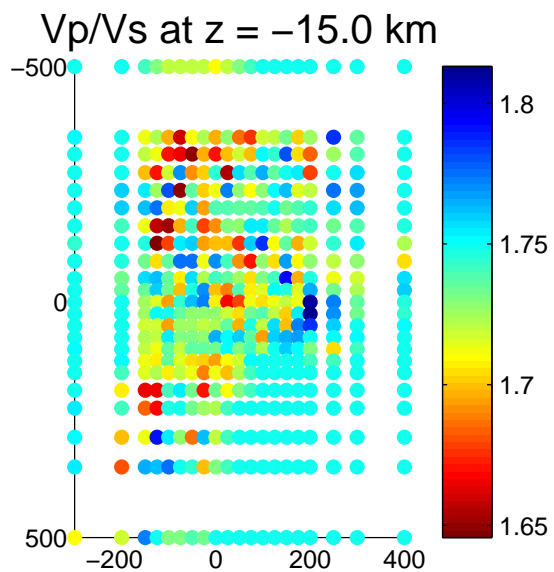
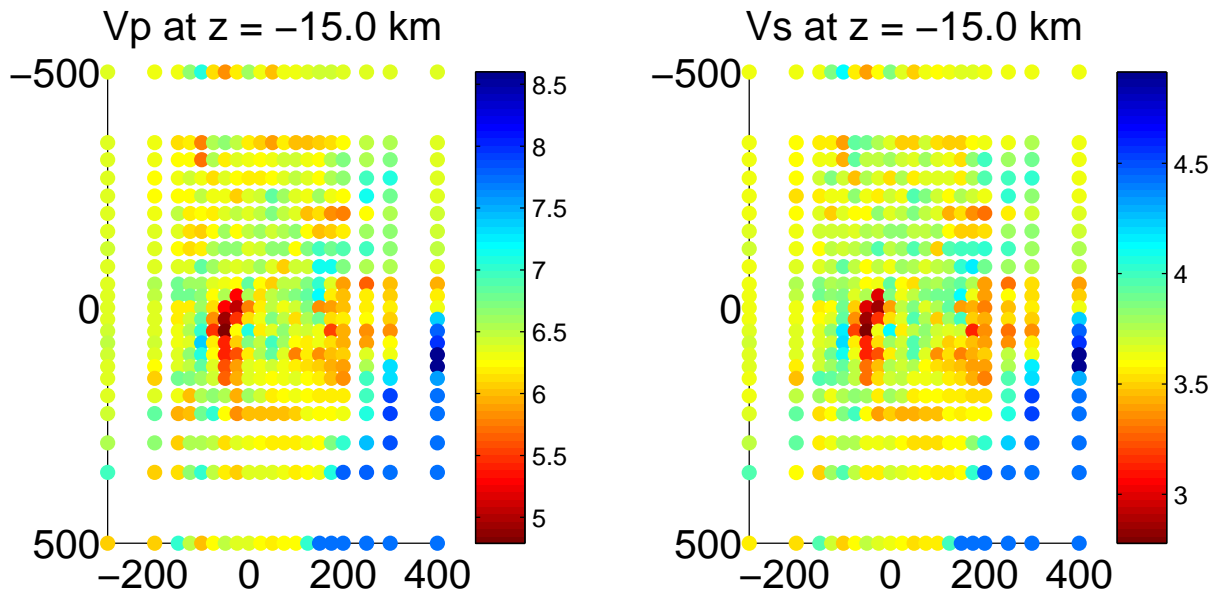


Figure C.9: Vp and Vs at E2006 nodes in layer 4, depth = 15 km below the sea level.

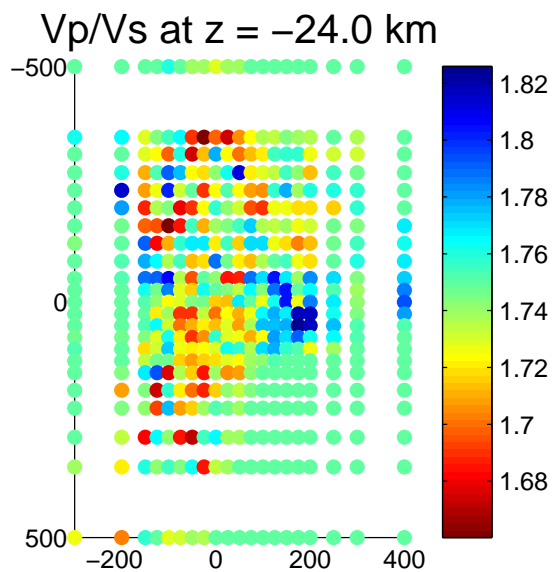
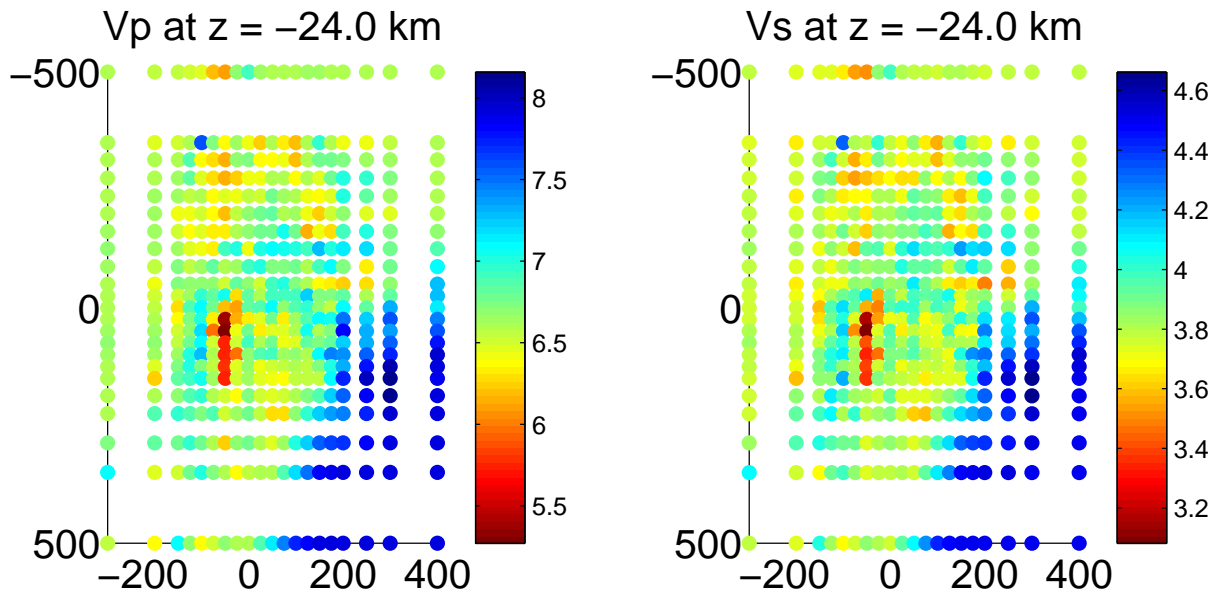


Figure C.10: Vp and Vs at E2006 nodes in layer 5, depth = 24 km below the sea level.

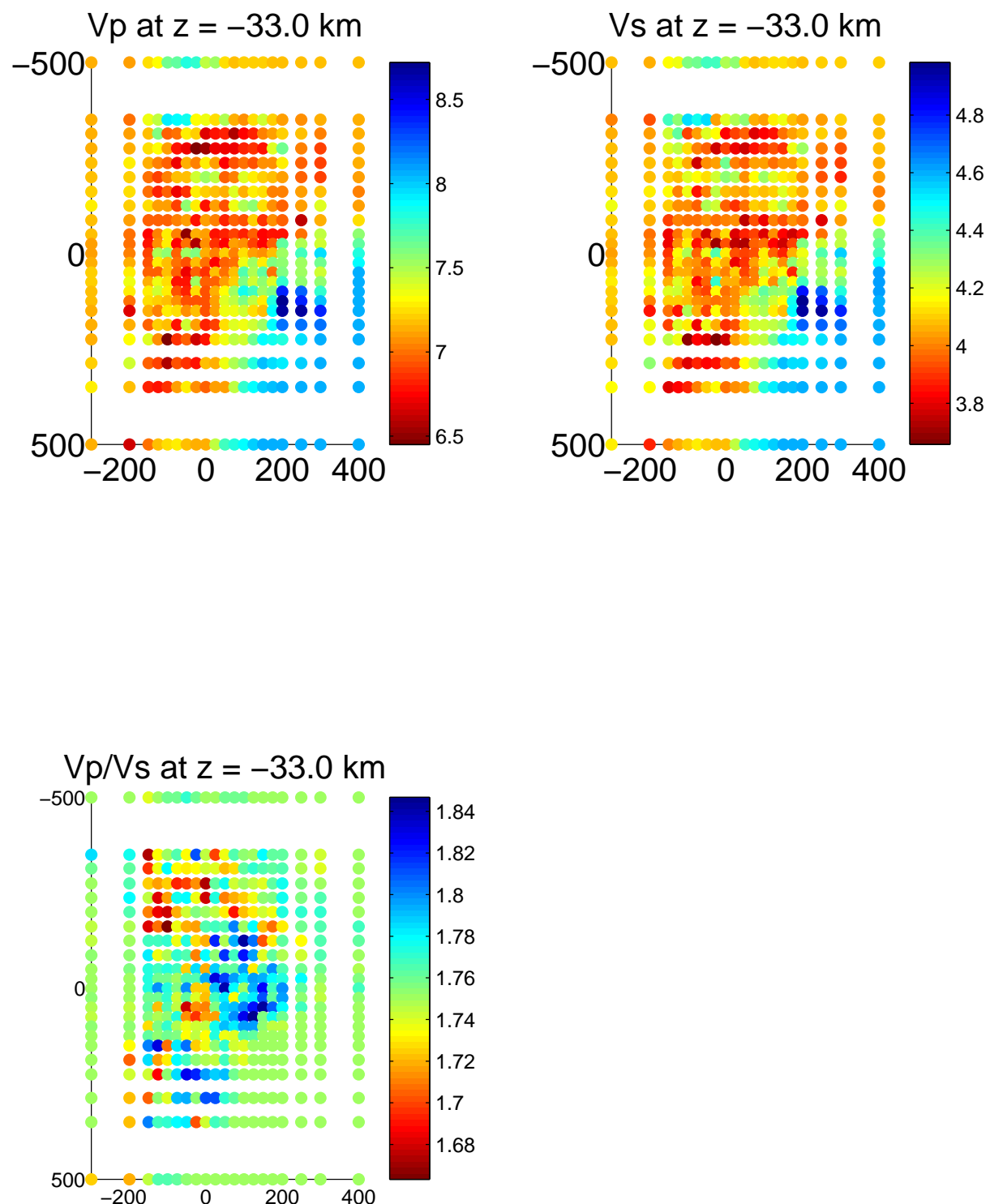


Figure C.11: V_p and V_s at E2006 nodes in layer 6, depth = 33 km below the sea level.

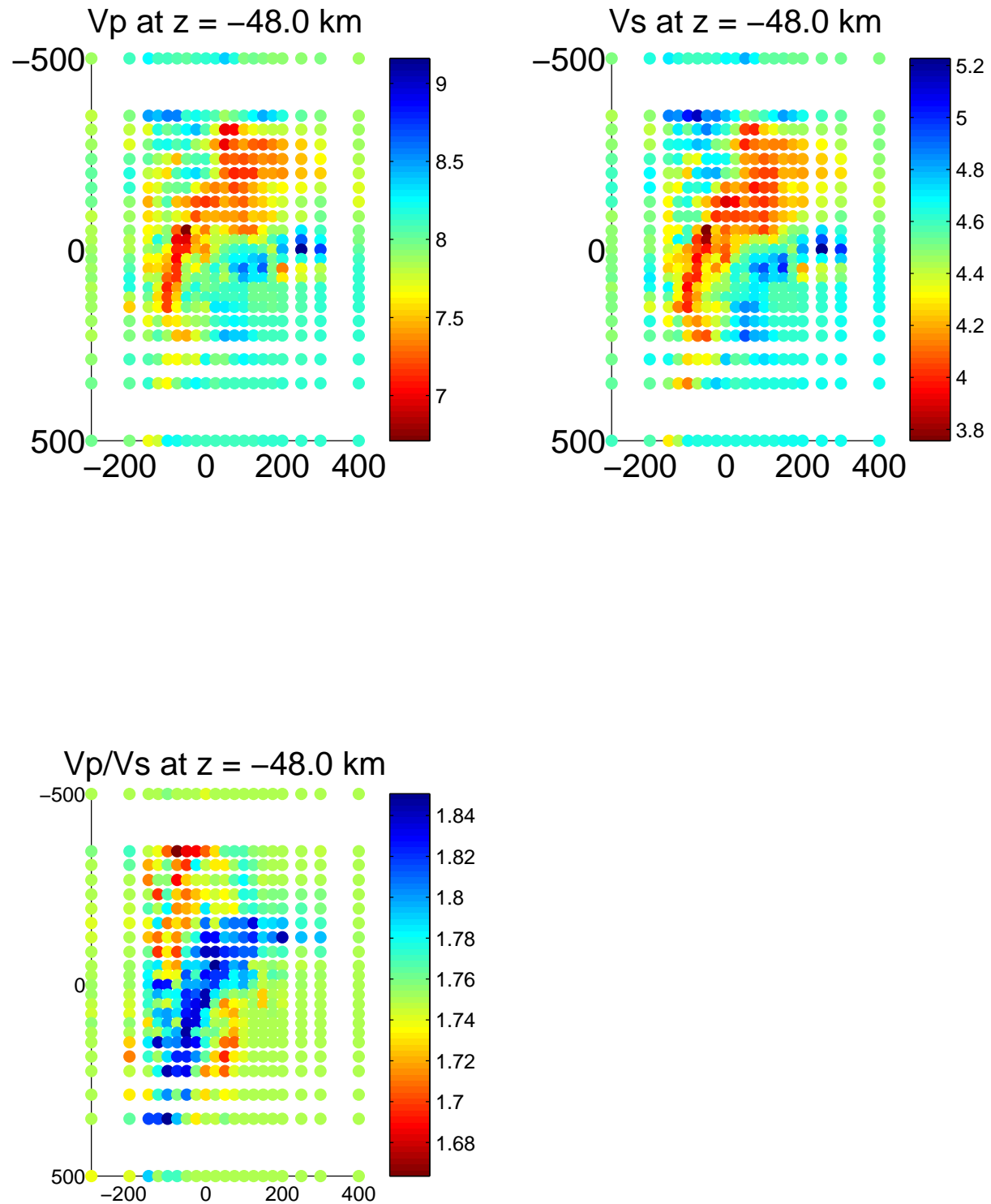


Figure C.12: V_p and V_s at E2006 nodes in layer 7, depth = 48 km below the sea level.

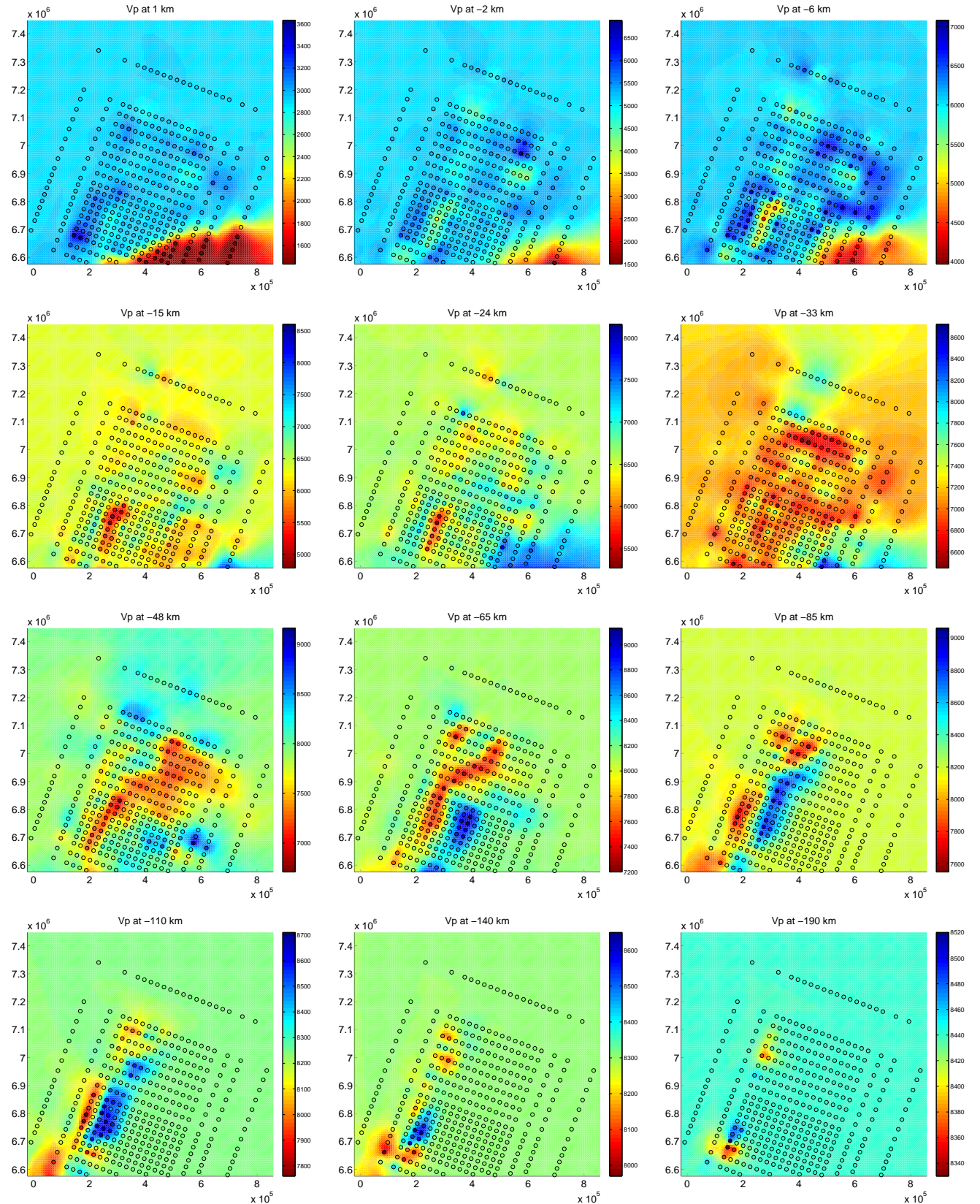
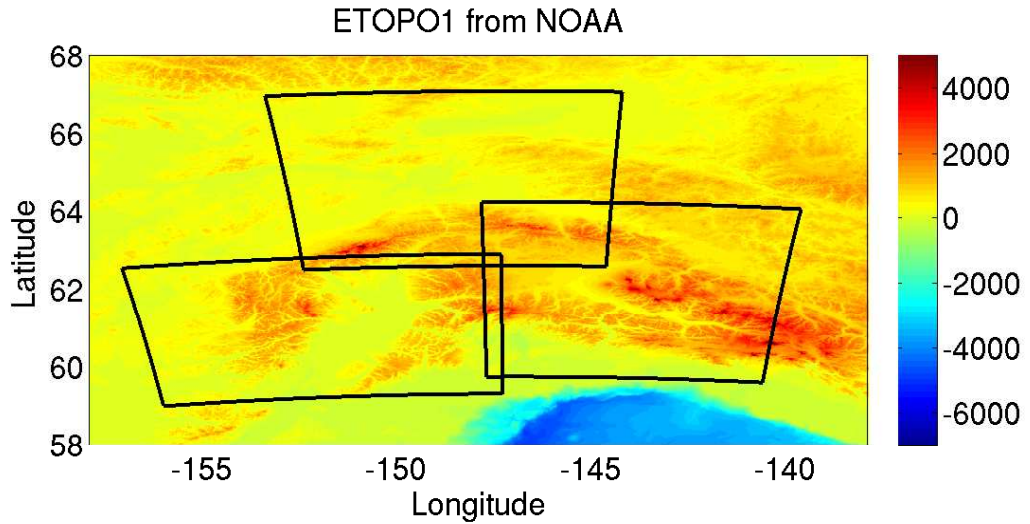


Figure C.13: Horizontal interpolation of V_p at E2006 nodes.

(a)



(b)

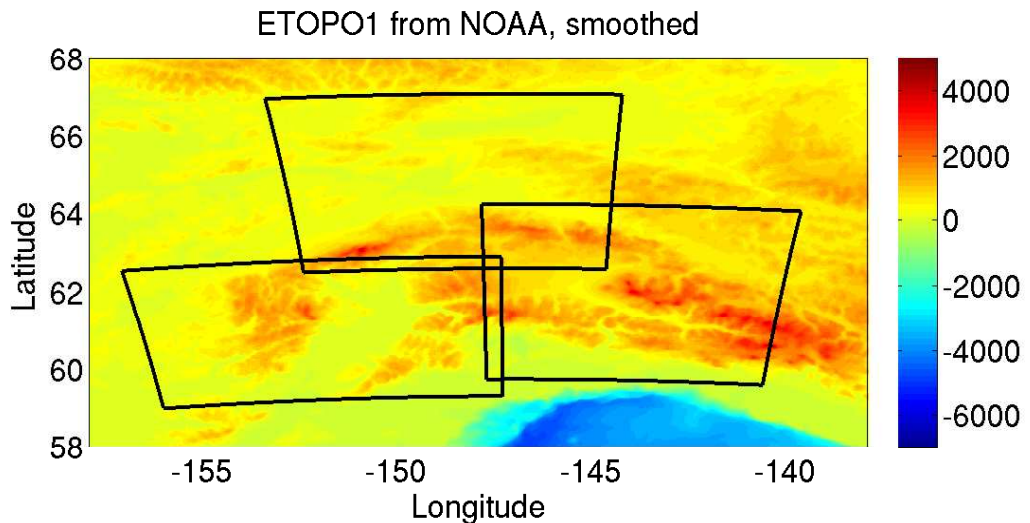


Figure C.14: Effect of smoothing the topography in three simulation regions. (a) Unsmoothed topography, from ETOPO-1 (Amante & Eakins, 2009). (b) Smoothed version of (a).

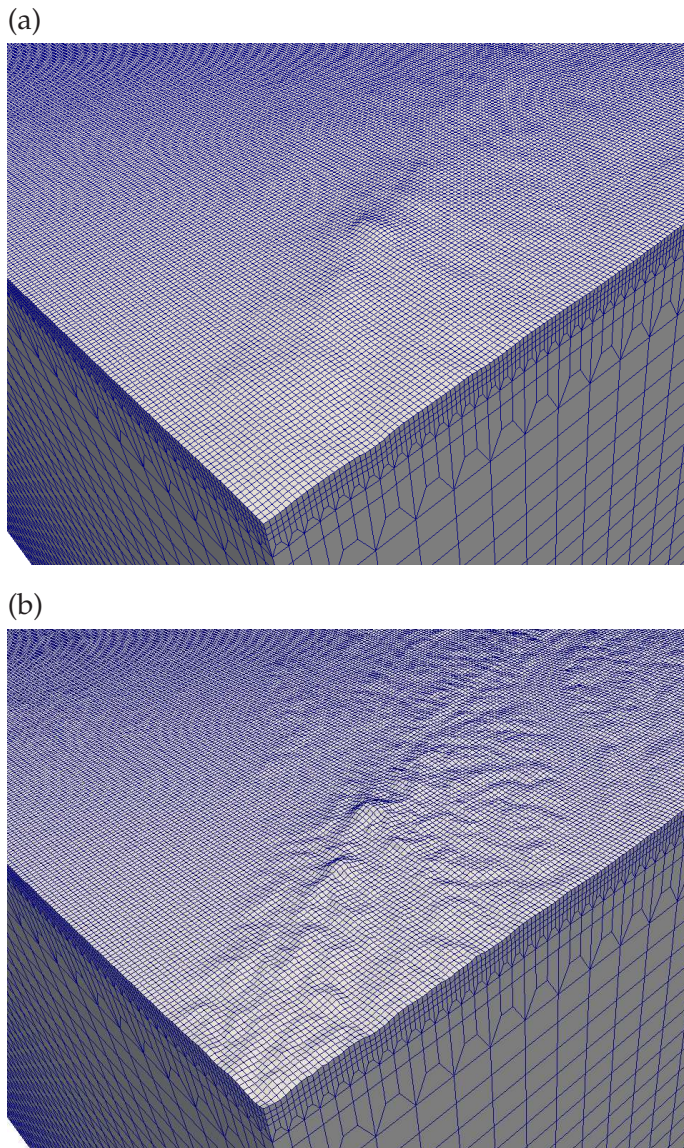


Figure C.15: Effect of topographic smoothing on the Interior mesh. (a) Hexahedral mesh generated using unsmoothed topography. (b) Hexahedral mesh generated using smoothed topography.

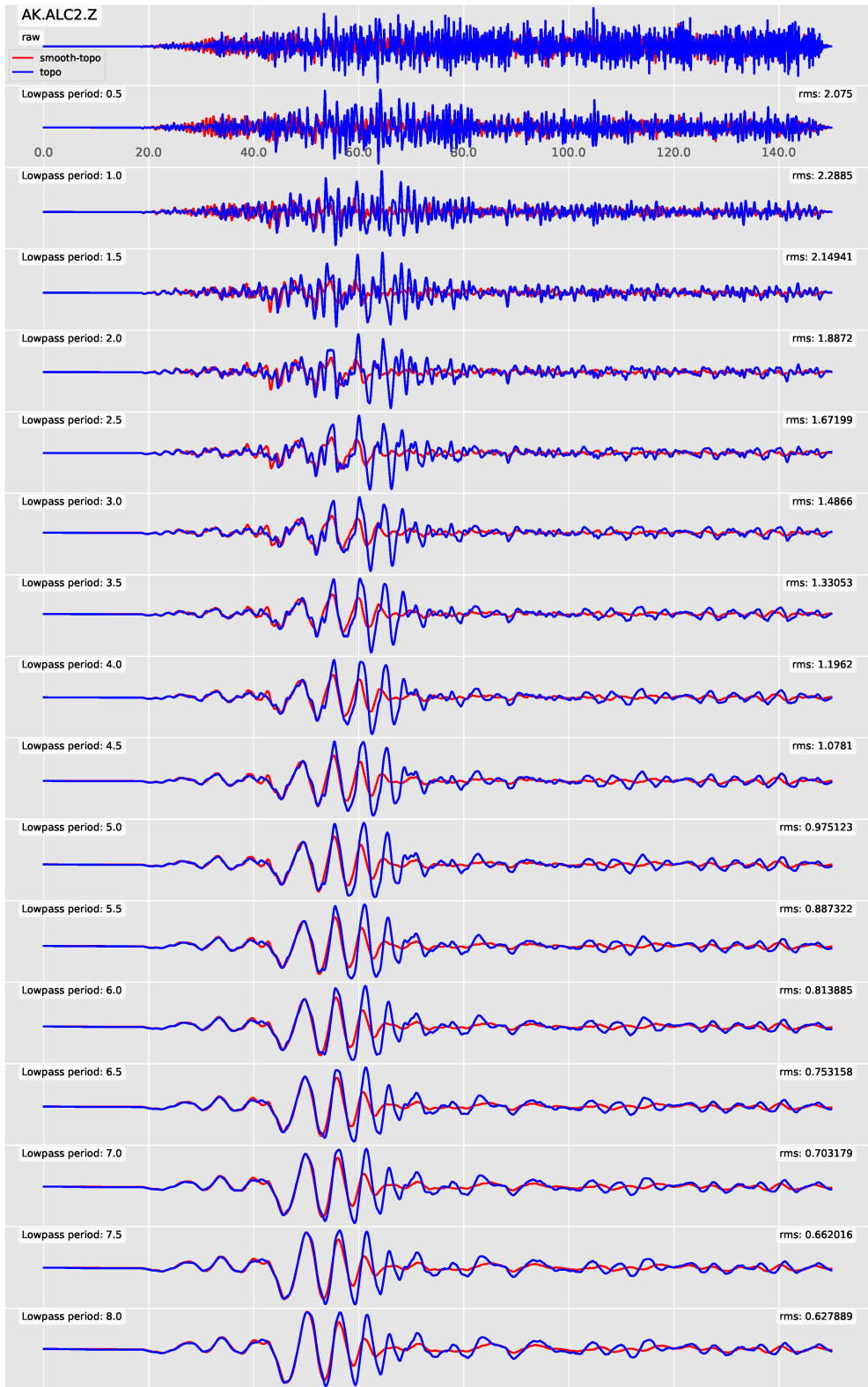


Figure C.16: Effect of topography smoothing on the Wrangell mesh after velocity thresholding has been applied. Shown are the synthetic waveforms at AK.ALC2.Z generated using unsmoothed (blue) and smoothed (red) topography, and filtered at varying low-pass periods.

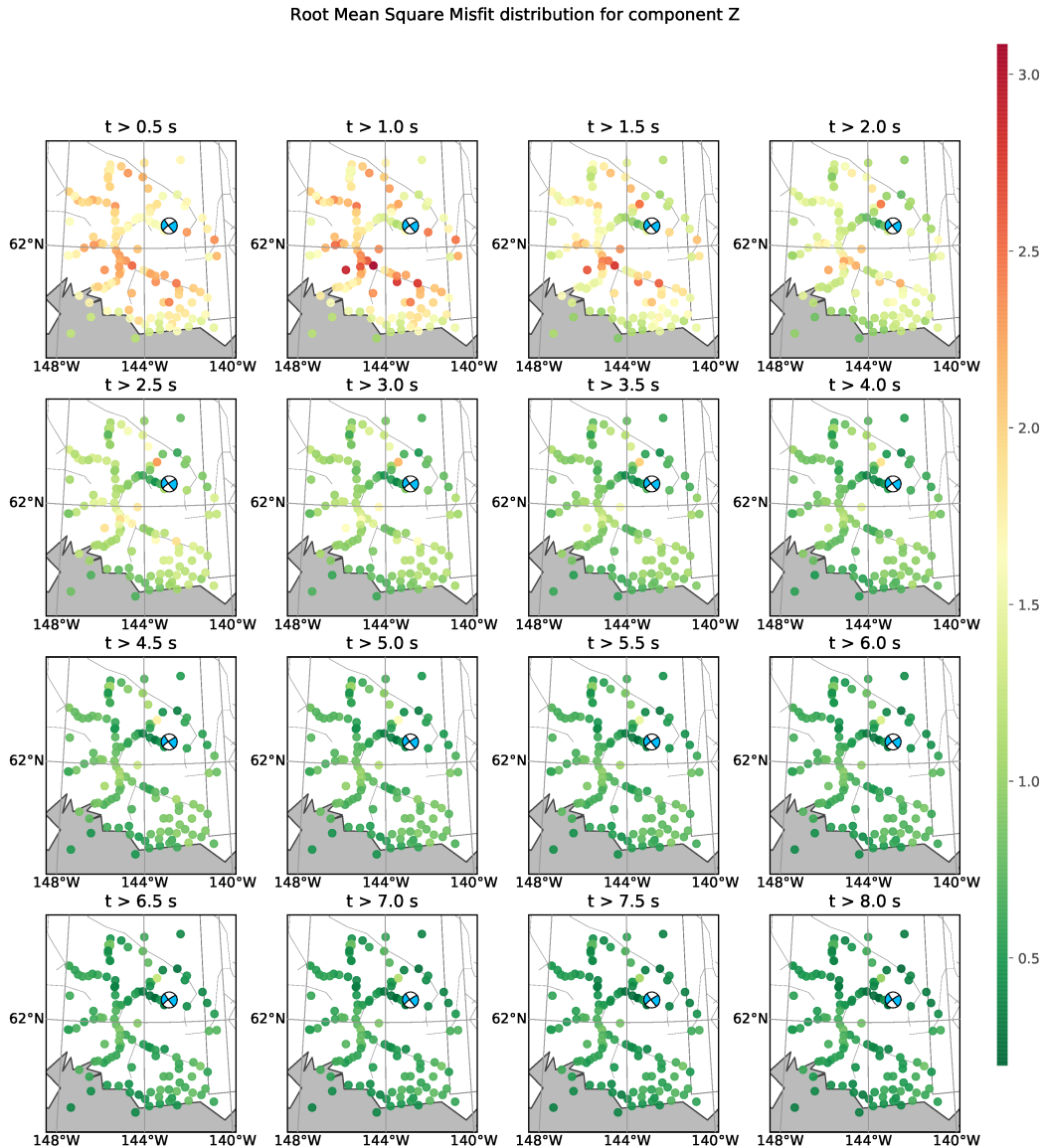


Figure C.17: Effect of topography smoothing on the Wrangell mesh after velocity thresholding has been applied. Colors represents the rms value between waveforms generated with smoothing and without smoothing the topography.

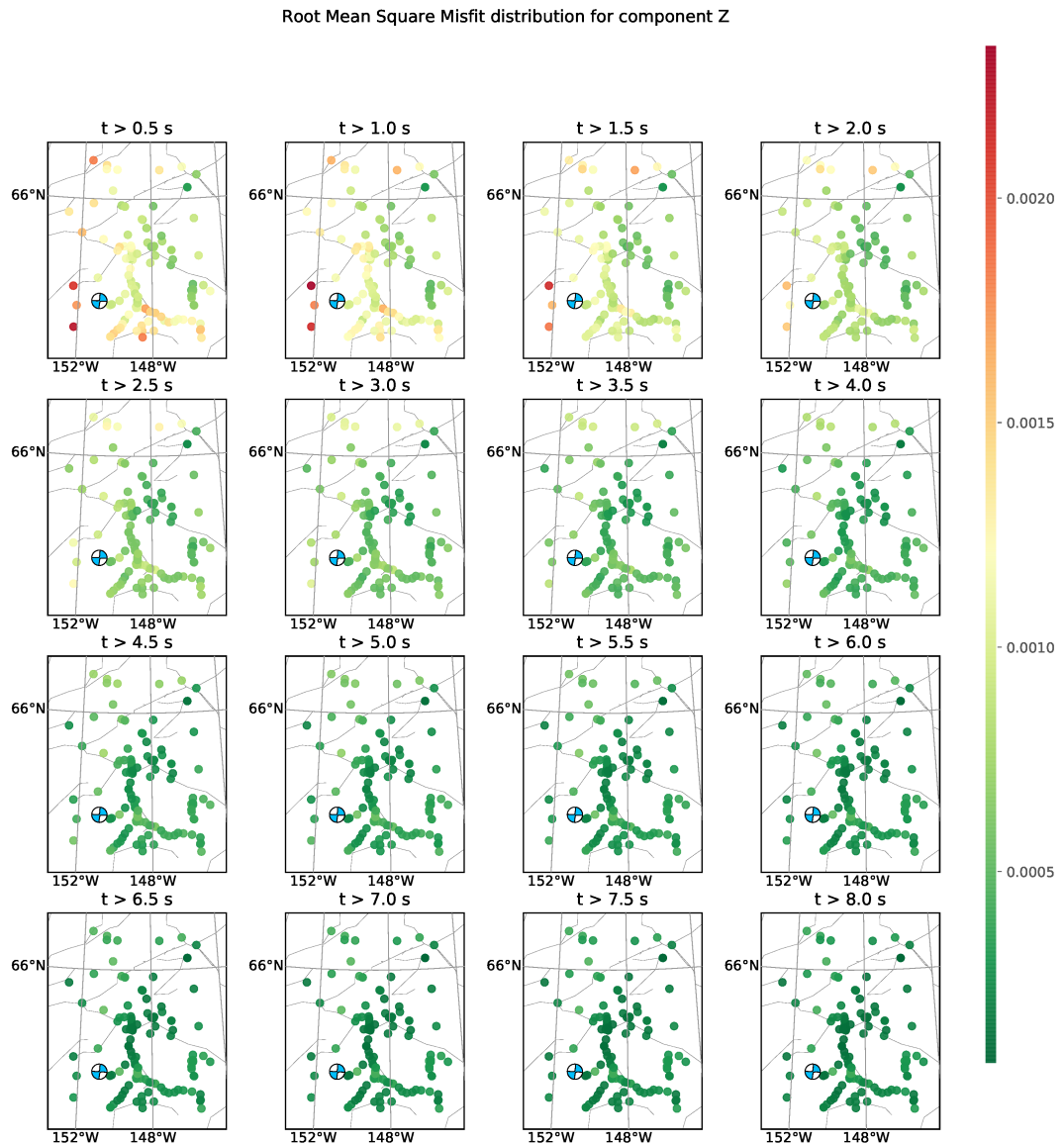


Figure C.18: Effect of velocity thresholding on the Interior mesh without any embedded basin in the model. Colors represents the rms value between waveforms generated with and without velocity thresholding.

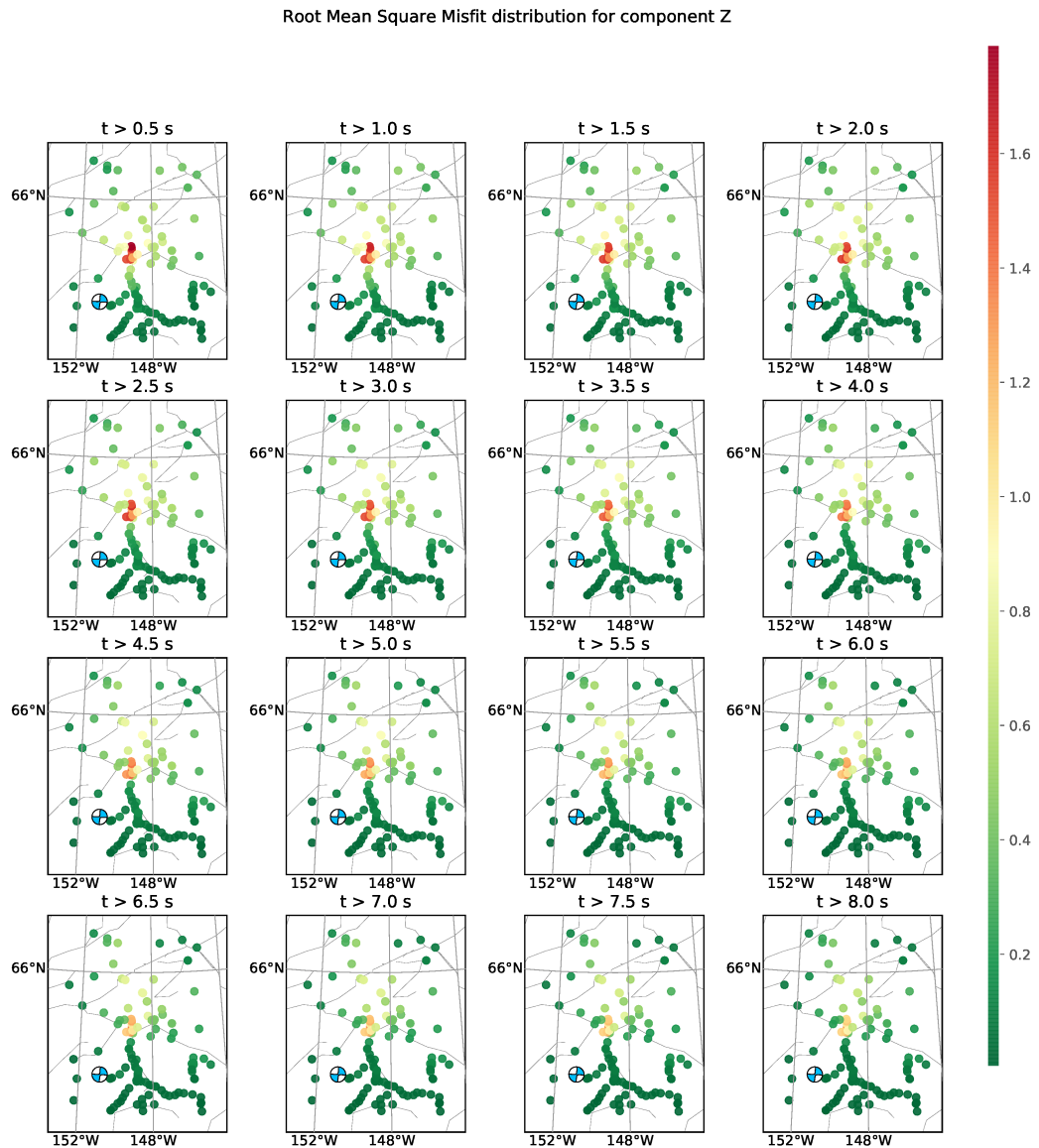


Figure C.19: Effect of velocity thresholding on the Interior mesh after Nenana basin is embedded in the model. Colors represents the rms value between waveforms generated with and without velocity thresholding.

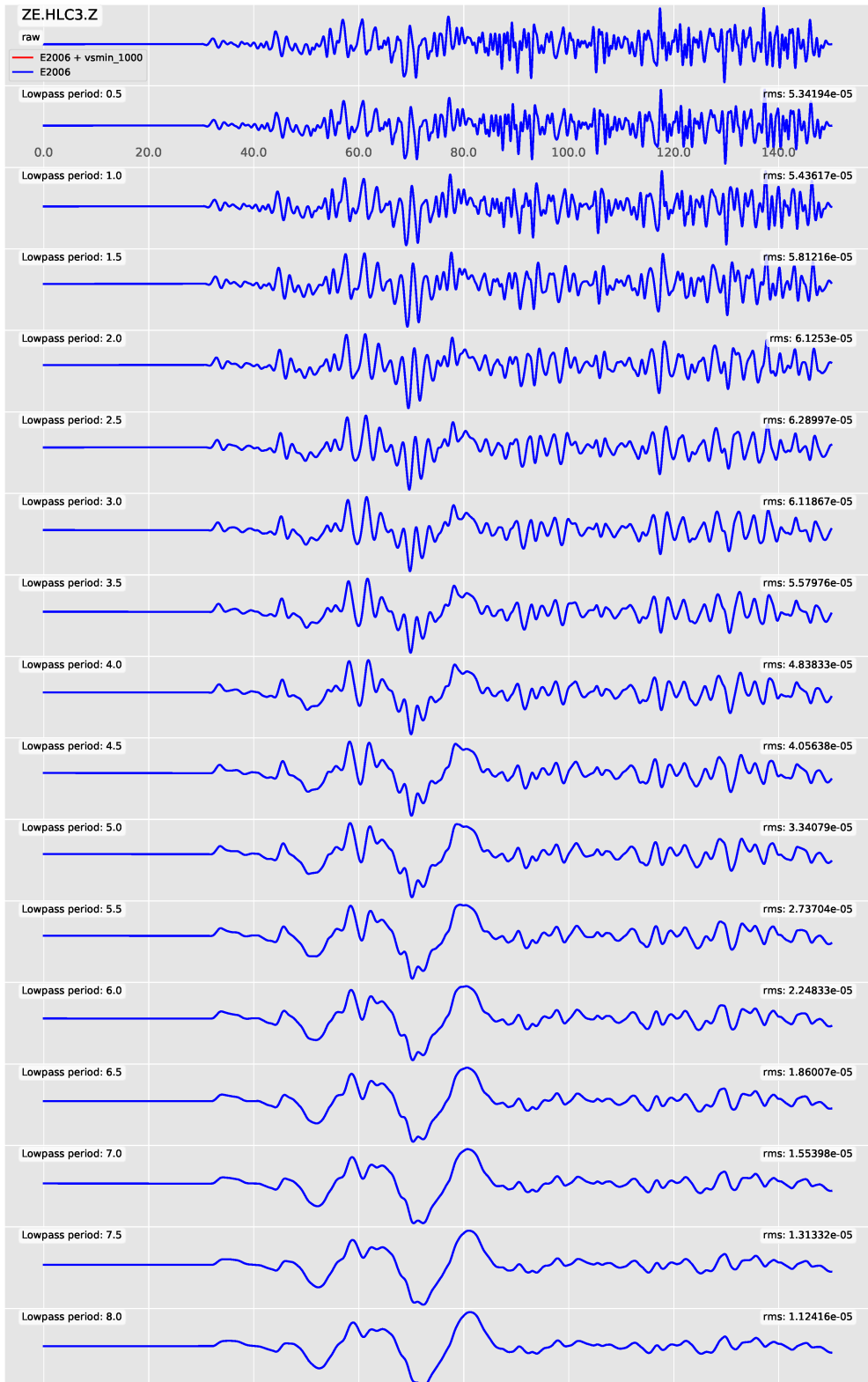


Figure C.20: Effect of velocity thresholding on the Cook Inlet mesh without any embedded basin in the model. Shown are the synthetic waveforms at ZE.HLC3.Z generated without $vsmin=1000$ m/s threshold (blue) and with threshold(red), and filtered at varying low-pass periods.

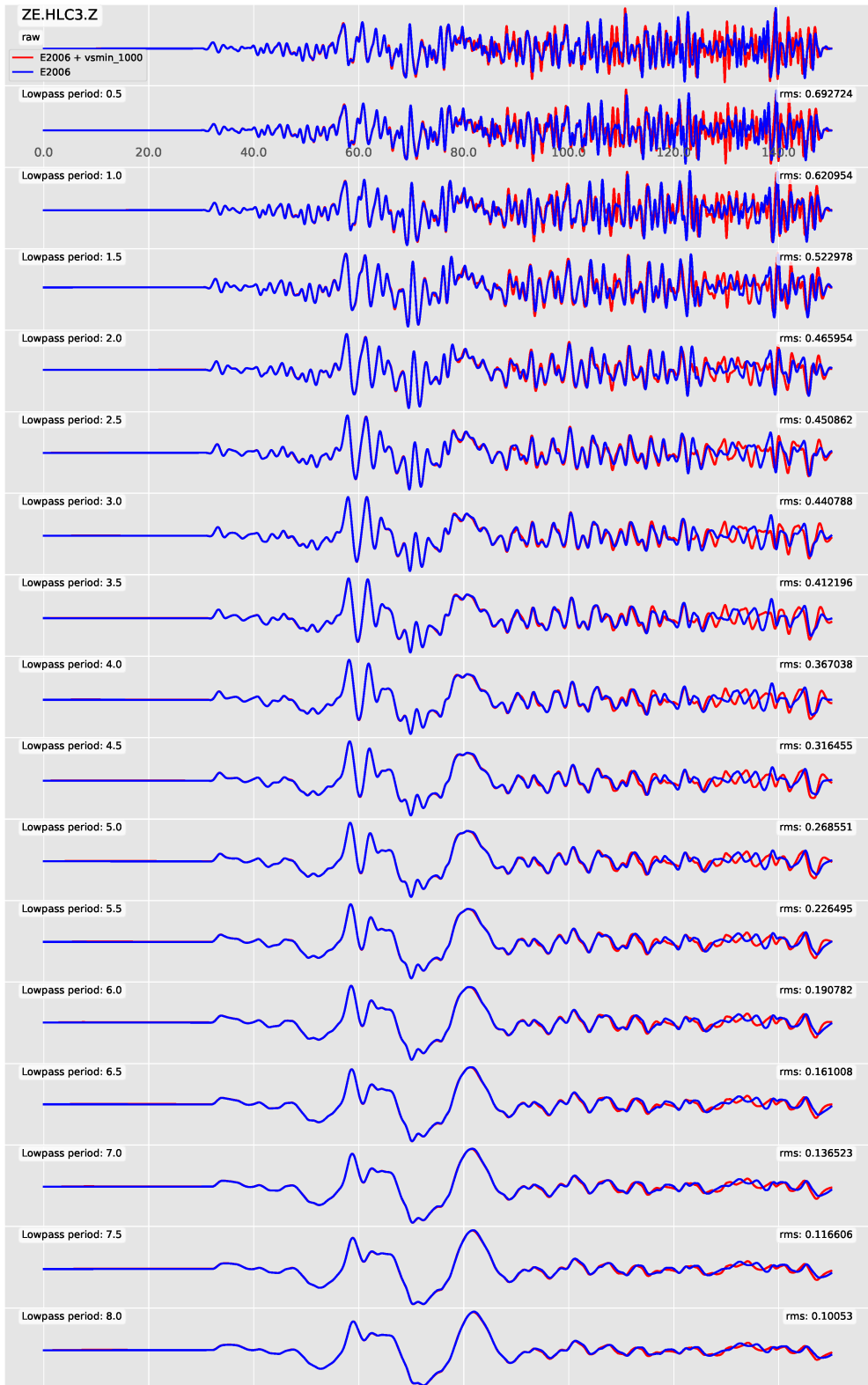


Figure C.21: Effect of velocity thresholding on the Cook Inlet mesh after Cook Inlet, Susitna, and Yentna basins are embedded basin in the model. Shown are the synthetic waveforms at ZE.HLC3.Z generated without $\text{vsmin}=1000$ m/s threshold (blue) and with threshold (red), and filtered at varying low-pass periods.

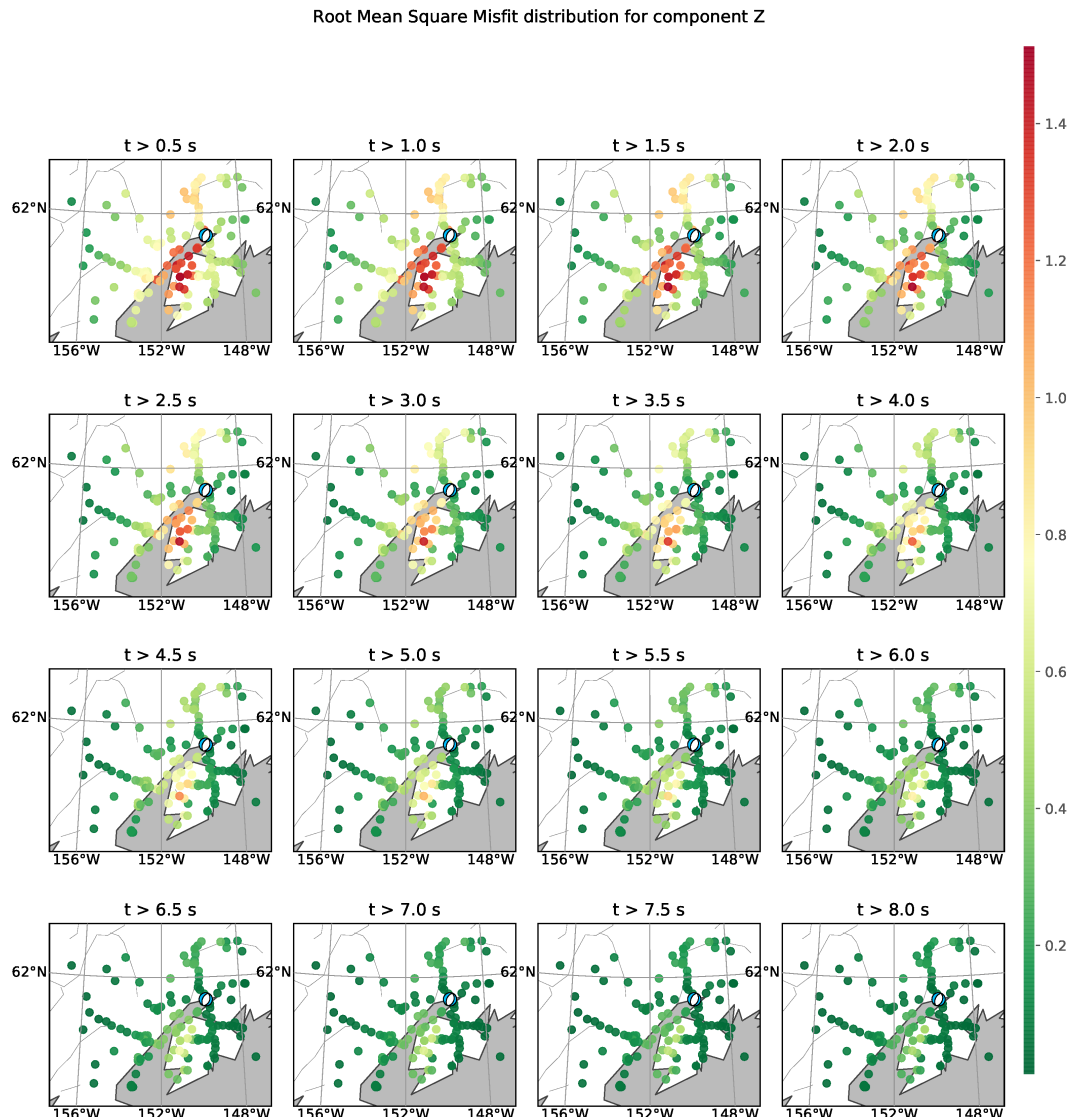


Figure C.22: Effect of velocity thresholding on the Cook Inlet mesh after Cook Inlet, Susitna, and Yentna basins are embedded in the model. Colors represents the rms value between waveforms generated with and without velocity thresholding.

References

Amante, C. & Eakins, B. W., 2009. ETOPO1 1 Arc-Minute Global Relief Model: Procedures, Data Sources and Analysis, NOAA Technical Memorandum NESDIS NGDC-24, 19 pp.

Eberhart-Phillips, D., Christensen, D. H., Brocher, T. M., Hansen, R., Ruppert, N. A., Haeussler, P. J., & Abers, G. A., 2006. Imaging the transition from Aleutian subduction to Yakutat collision in central Alaska, with local earthquakes and active source data, *J. Geophys. Res.*, **111**, B11303, doi:10.1029/2005JB004240.